Carbon-Based Nanomaterials for Electrochemical Sensing of Small Biomolecules

Submitted by

Peng Lei

In fulfilment of the requirements for the degree of

Doctor of Philosophy

College of Science and Engineering

James Cook University

September 2024

Supervisors: Dr. Yang Liu & Prof. Yinghe He

DECLARATION

I declare that the work presented in the thesis titled "*Carbon-based nanomaterials for electrochemical sensing of small biomolecules*" represents my work and has not been submitted to any university for another degree in any form. Information obtained from the published works of others has been acknowledged in this thesis and the related references have been provided.

STATEMENT OF ACCESS TO THIS THESIS

I fully acknowledge the regulations of James Cook University regarding the retention and use of the thesis: the university allows the thesis to be accessed and borrowed, agrees that it may be reproduced in different forms elsewhere, and retains the intellectual property rights of the thesis.

I have appropriately acknowledged the owner for using any third-party copyright material in this thesis and have provided relevant references in the images.

ACKNOWLEDGMENTS

Firstly, I would like to appreciate my primary advisor, Dr. Yang Liu for the guidance of my research and personal life. When faced with research challenges, Dr. Liu actively helped me by promptly analyzing and solving problems, which deepened my understanding and passion for research. Dr. Liu also showed genuine consideration for my daily life, introducing me to Australian customs and enriching my experience with diverse cultures. I am equally grateful to my co-supervisor, Professor Yinghe He, who is approachable and witty, and helped me overcome my fear of speaking and listening skills. I extend my heartfelt thanks to both of my supervisors for their invaluable guidance and support throughout my work.

I would like to express my gratitude to Professor Shaomin Shuang and Professor Chuan Dong from Shanxi University for their collaboration with us. I also appreciate the assistance of all staff at James Cook University and Shanxi University.

I want to thank my family and colleagues for their support, encouragement, understanding, and silent dedication. They are my strongest support, driving me forward, and giving me the courage and hope to pursue my dreams. I'm particularly grateful to my wife Minglu Li. Her appearance has added a ray of light to my life and every loss is her encouragement and companionship, which has helped me regain confidence and set off again.

STATEMENT OF CONTRIBUTION OF OTHERS

This thesis involved the following contributions from others:

Financial assistance: The financial assistance to cover the tuition fees and stipend for this course was provided by James Cook University, Australia, and Shanxi University, China, respectively. The funding for the procurement of consumables, sample characterizations, and to attend conferences was provided by the Graduate Research School, the College of Science and Engineering and the Eric Both grants in James Cook University.

Experimental and editorial assistance: Dr. Liu assisted with experiment planning and data analysis. Dr. Liu and Prof. He provided assistance with editing journal articles and the thesis.

Contribution to co-authored publications: The assistance in materials characterization was provided by Prof. Shuang Shaomin and Prof. Dong Chuan from Shanxi University, China.

ABSTRACT

With the rapid advancement of society, scientific and technological progress has surged, leading to a growing interest in the easy and rapid detection of small biomolecules. Electrochemical sensors are highly valued for their advantages such as high sensitivity, good selectivity, low cost, fast analysis, and ease of operation. They have found wide-ranging applications in clinical analysis, diagnostics, food testing, environmental monitoring, and biopharmaceuticals. However, unmodified electrodes suffer from poor conductivity, slow electron conduction rate, and poor selectivity. Therefore, the modification of electrodes with high-performance sensing materials has attracted increasing interest in enhancement of the analytical performance of electrochemical sensors. Carbon-based nanomaterials offer tremendous potential for electrode modification in construction of electrochemical sensors, owing to their high surface area, excellent conductivity and chemical stability. The work presented in this thesis aimed to develop novel carbon-based nanocomposites through simple synthetic approaches, for construction of high-performance and low-cost electrochemical sensors to detect small biomolecules.

For this purpose, carbon nanospheres (CNs) using glucose as the raw material through a simple hydrothermal method were synthesized for the highly sensitive detection of dopamine. The unique structure of CNs provides a high specific surface area and rapid electron transfer capability, which enables CNs-modified electrodes to achieve superior sensitivity compared to previously reported dopamine sensors Furthermore, a one-pot synthetic method was employed to prepare the Au-Pd/polyaniline/graphene (Au/Pd-PPy/GR) nanocomposites, which exhibit high sensitivity and good selectivity for simultaneous detection of multiple analytes including guanine (G), adenine (A), thymine (T), and cytosine (C). The Au/Pd-PPy/GR modified electrodes exhibited good anti-interference ability, stability, and reproducibility, enabling simultaneous detection of the four DNA bases in calf-thymus DNA. It was found that the enhancement in sensing performance can be attributed to the combined benefits of high catalytic activity and large electroactive surface area, which are associated with Au/Pd-PPy and GR, respectively.

In addition to single-function nanomaterials, efforts were subsequently made to develop multifunctional nanomaterials capable of simultaneously providing supervior sensing performance and wastewater treatment property. Novel cobalt-nickel metal-organic framework/graphene (CNMs-GR) magnetic multifunctional nanocomposites were synthesized via a simple hydrothermal method for applications in enzyme-free glucose detection and dye removal. Due to synergistic effects, CNMs-GR greatly enhanced the electrocatalytic activity towards glucose oxidation, eliminating the need for enzymes in glucose detection. The proposed sensing material exhbits good selectivity, stability, and reproducibility for determination of glucose in human serum samples. Meanwhile, it was found that the material can be used for removal of three organic dyes effectively by leveraging its adsorption and magnetic separability properties. The dual functionality of the CNMs-GR makes it a promising candidate for developing integrated platforms of sensing devices and wastewater treatment systems.

Finally, a dual-mode sensing platform that combines colorimetric and electrochemical methods was developed to detect hydrogen peroxide, along with a smartphone-based monitoring system. Copper/zirconium metal-organic framework (Cu/Zr-MOF), synthesized by a straightforward solvothermal method, exhibits high electrochemical performance and peroxidase-like activity, enabling the dual-mode analytical strategy. The proposed method effectively enhances detection accuracy by minimizing influence factors such as background noise and instrument fluctuations, as demonstrated through intra- and extracellular analyses. It was demonstrated that dual-mode detection is more reliable and accurate compared to traditional single-mode detection, effectively overcoming the limitations of single-mode approaches.

CONTENTS

LIST OF FIGURES

LIST OF TABLES

LIST OF PUBLICATIONS

Candidate published the following publications during this thesis:

1. Lei, P., Zhou, Y., Li, B., Liu, Y., Dong, C., and Shuang, S. (2022). Gold/palladium-polypyrrole/graphene nanocomposites for simultaneous electrochemical detection of DNA bases. ACS Applied Nano Materials, 5, 1635-1643.

2. Lei, P., Zhou, Y., Sun, X., Dong, C., He, Y., Liu, Y., and Shuang, S. (2023). Green synthesis of carbon nanospheres for enhanced electrochemical sensing of dopamine. ChemElectroChem, 10, e202201129 (1 of 8).

3. Lei, P., Zhou, Y., Dong, C., Liu, Y., and Shuang, S. (2023). CoNi-MOF-graphene nagnetic nanocomposites for the electrocatalytic detection of glucose and the efficient removal of organic dyes. ACS Applied Nano Materials, 6, 9369-9375.

4. Lei, P., Wu, N., Zhou, Y., Dong, C., Liu, Y., and Shuang, S. (2024). Cu/Zr metal-organic frameworks with high peroxidase-like activity for sensitive electrochemical and colorimetric dual-mode detection of hydrogen peroxide released from living cells. ACS Applied Nano Materials, 7, 6556-6563.

Chapter 1 Introduction

1.1 Background

Small biomolecules, as fundamental substances in the human body, play crucial roles in gene expression, physiological stress responses, bodily movements, and other physiological processes [1, 2]. Their structural and quantitative variations significantly impact human behavior and function. Imbalances in small biomolecule levels can disrupt bodily processes, leading to various diseases. Therefore, establishing sensitive, accurate, and efficient methods to detect these biomolecules within the body is critically important, particularly for disease prevention and diagnosis.

Electrochemical sensing is a technology that utilizes electrochemical methods to detect chemical substances, widely applied in many fields such as environmental monitoring, biomedical sciences, and food safety. For instance, electrochemical sensors have been employed to detect heavy metal ions in water, glucose in blood, and methane in exhaled breath [3]. They can also be integrated with other analytical separation techniques such as capillary electrophoresis and high-performance liquid chromatography to enhance detection sensitivity and selectivity [4]. With its wide range of applications and diverse detection capabilities, electrochemical sensing technology continues to be a focus of current research in analytical chemistry, offering significant advantages as follows: (1) high sensitivity-detection limits as low as parts per billion (ppb) or parts per million (ppm) can be achieved [5]; (2) high selectivity-electrodes can be modified by recognition elements to eliminate interference [6]; (3) portability-devices are easily miniaturized, enabling for rapid on-site detection [7]; (4) low cost-sensor designs are simple, with straightforward manufacturing processes.

With the advancement of modern technology, the rapid development of carbon-based nanomaterials has propelled progress in electrochemical sensing, paving the way for the design of sensitive and efficient electrochemical sensing platforms. Commonly used carbon-based nanomaterials include graphene, conductive polymers, carbon nanospheres, and metal-organic frameworks (MOFs), which have been widely employed in constructing electrochemical sensors [8]. Graphene is a single layer of carbon atoms arranged in a two-dimensional hexagonal lattice. It is known for its exceptional electrical, thermal, and

mechanical properties. Graphene exhibits high electrical conductivity due to the mobility of its charge carriers. Additionally, graphene is nearly transparent, flexible, and has a high surface area, which makes it useful for a wide range of applications. Carbon nanospheres with uniform spherical shape, tunable size, and large surface area, exhibit unique properties including high electrical conductivity, thermal stability, and mechanical strength. In electrochemical sensing applications, their high surface area and conductivity can improve the analytical performance such as sensitivity and response time. Conductive polymers are organic materials that conduct electricity, combining properties of traditional polymers with electronic conductivity. This is achieved through a conjugated system of alternating single and double bonds, which allows for the movement of electrons along the polymer chain. The properties of conductive polymers can be tuned by chemical doping or by altering their polymerization process, making them versatile materials for electrochemical sensing. MOFs are crystalline porous materials with permanent porosity, high specific surface area, and uniform open channels. These features enable target analytes to be concentrated within MOFs and facilitate rapid mass transfer, highlighting their strong potential for applications in electrochemical detection.

Despite the development of various nanocomposites for electrochemical detection of small biomolecules, research on several key issues remains insufficient. The current research gaps include: (1) Most methods for preparing nanocomposites typically involve multiple steps, making the preparation process complex. Moreover, during the preparation, various toxic and harmful chemical reagents are often used, which pose potential pollution risks to the environment; (2) Single-function nanomaterials only achieve specific functions, making it difficult for them to meet the diverse needs of complex systems, which limits their flexibility and applicability in practical applications; (3) Single-mode detection often only recognizes specific types of signals and may be affected by background noise and instrument fluctuations, making it difficult to ensure accurate results. This thesis focuses on addressing the aforementioned challenges by synthesis of novel nanocomposites using methods such as hydrothermal reduction and chemical reduction to integrate carbon-based nanomaterials with metals known for their excellent electrocatalytic properties and MOFs with effective enrichment capabilities. These nanocomposites not only retain their inherent excellent properties but also significantly enhance the

electrocatalytic activity of the materials, enabling simultaneous, multifunctional, and dual-mode detection of various small biomolecules with improved sensing performance including sensitivity, selectivity and accuracy.

1.2 Research Objectives

This work aims to use environmentally friendly methods for the development of novel carbon-based nanocomposites, namely gold-palladium/polyaniline/graphene (Au-Pd/PPy/GR), carbon nanospheres (CNs), cobalt/nickel metal-organic framework/graphene (CNMs-GR), and copper/zirconium metal-organic frameworks (Cu/Zr-MOFs), as well as demonstrating their applications in electrochemical sensing of small biological molecules. The connections between chapters are shown in Fig. 1.1. Moreover, the detection of multiple biomolecules, the development of multifunctional nanomaterials, and the application of multimodal detection are closely interconnected, collectively driving the advancement of biosensing technology, making it more efficient, flexible, and adaptable in practical applications. The specific objectives of this thesis are:

(1) Synthesize CNs using glucose as a raw material, and investigate the electrochemical properties and response mechanisms of CNs-modified electrodes to enhance their sensing performance in the determination of dopamine (DA) in human serum samples.

(2) Prepare Au-Pd/PPy/GR nanocomposites to develop an electrochemical sensor for simultaneous detection of guanine (G), adenine (A), thymine (T), and cytosine (C) in calf-thymus DNA with good accuracy and high reliability.

(3) Develop CNMs-GR nanocomposites using bimetallic precursors and investigate their multifunctional properties for detection of glucose and dye removal.

(4) Synthesize Cu/Zr-MOFs via a hydrothermal method, and study their electrochemical properties and peroxidase-like activities to fabricate highly-sensitive electrochemical sensors for the determination of hydrogen peroxide in cancer cells.

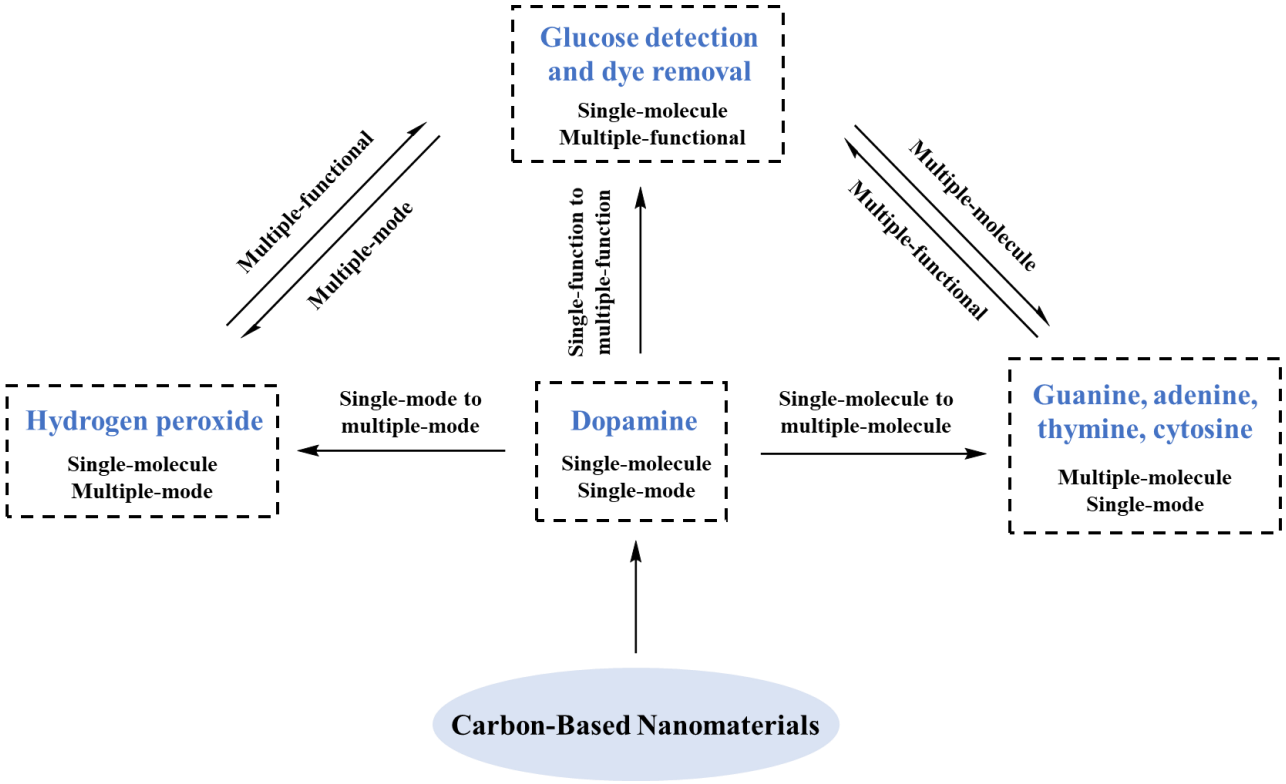

Fig. 1.1: The connections between chapters

1.3 Document Organization

Chapter 1 provides a brief introduction to the research background and objectives of this thesis.

Chapter 2 gives an overview and discusses research progress on small biomolecules, electrochemical sensors, as well as the properties of carbon nanomaterials and their applications in electrochemical sensing.

Chapter 3 focuses on the synthesis of carbon nanospheres (CNs) for constructing a dopamine (DA) electrochemical sensing platform. The structure, morphology, composition, and electrochemical properties of the CNs have been studied. The electrocatalytic mechanism for the detection of DA on the proposed sensing platform has been investigated, along with its feasibility studies for serum sample analysis.

Chapter 4 demonstrates the synthesis of gold-palladium/polyaniline/graphene (Au-Pd/PPy/GR) nanocomposites, which exhibits high selectivity for the simultaneous electrochemical detection of guanine (G), adenine (A), thymine (T), and cytosine (C). The applicability of the developed

electrochemical sensors has been evaluated for the detection of G, A, T and C in calf-thymus DNA samples.

Chapter 5 describes the hydrothermal synthesis of cobalt-nickel metal-organic framework/graphene (CNMs-GR) nanocomposites using bimetallic precursors, characterized by FESEM, TEM and XPS. The CNMs-GR nanocomposites have been explored for enzyme-free detection of glucose and dye removal, as confirmed by practical usability evaluations.

Chapter 6 presents an analytical strategy for dual-mode detection of hydrogen peroxide based on a copper/zirconium metal-organic framework (Cu/Zr-MOF). The electrochemical performance of the Cu/Zr-MOF and its peroxidase-like activity have been investigated via electrochemical methods and UV-visible absorption spectroscopy. The capability of the proposed strategy for real-time monitoring of hydrogen peroxide in cancer cells has also been explored.

Chapter 7 summarizes the research presented in this thesis and provides an outlook for future work.

References

1. Goodchild, S.A.; Hubble, L.J.; Mishra, R.K.; Li, Z.; Yugender Goud, K.; Barfidokht, A.; Shah, R.; Bagot, K.S.; McIntosh, A.J.S.; Wang, J. Ionic Liquid-Modified Disposable Electrochemical Sensor Strip for Analysis of Fentanyl. *Anal. Chem.* **2019**, *91,* 3747-3753.
2. Ji, W.; Wu, D.; Tang, W.; Xi, X.; Su, Y.; Guo, X.; Liu, R. Carbonized Silk Fabric-Based Flexible Organic Electrochemical Transistors for Highly Sensitive and Selective Dopamine Detection. *Sensor. Actuat. B: Chem.* **2020**, *304*, 127414.
3. Zhou, Z.; Shu, T.; Sun, Y.; Si, H.; Peng, P.; Su, L.; Zhang, X. Luminescent Wearable Biosensors Based on Gold Nanocluster Networks for "Turn-On" Detection of Uric Acid, Glucose and Alcohol in Sweat. *Biosen. Bioelectron.* **2021**, *192*, 113530.
4. Qin, C.; Wang, B.; Li, P.; Sun, L.; Han, C.; Wu, N.; Wang, Y. Metal-Organic Framework-Derived Highly Dispersed Pt Nanoparticles-Functionalized ZnO Polyhedrons for ppb-Level CO Detection. *Sensor. Actuat. B: Chem.* **2021**, *331*, 129433.

5. Elizabeth, I.; Nair, A.K.; Singh, B.P.; Gopukumar, S. Multifunctional Ni-NiO-CNT Composite as High Performing Free Standing Anode for Li Ion Batteries and Advanced Electro Catalyst for Oxygen Evolution Reaction. *Electrochim. Acta* **2017**, *230*, 98-105.

6. Adeniyi, O.; Nwahara, N.; Mwanza, D.; Nyokong, T.; Mashazi, P. Nanohybrid Electrocatalyst Based on Cobalt Phthalocyanine-Carbon Nanotube-Reduced Graphene Oxide for Ultrasensitive Detection of Glucose in Human Saliva. *Sensor. Actuat. B: Chem.* **2021**, *348*, 130723.

7. Lang, X.; Fu, H.; Hou, C.; Han, G.; Yang, P.; Liu, Y.; Jiang, Q. Nanoporous Gold Supported Cobalt Oxide Microelectrodes as High-Performance Electrochemical Biosensors. *Nat. Commun.* **2013**, *4*, 2169.

8. Üğe, A.; Zeybek, D.K.; Zeybek, B. An Electrochemical Sensor Forsensitive Detection of Dopamine Based on MWCNTs/CeO_2-PEDOT Composite. *J. Electroanal. Chem.* **2018**, *813*, 134-142.

Chapter 2: Literature Review

This chapter provides a brief overview of the major advancements in the sensing of small biomolecules, with a focus on electrochemical sensors developed using carbon-based nanocomposites. Section 2.1 introduces the significance of the target small biomolecules in this study. Section 2.2 presents the current methods for detecting these small biomolecules. Section 2.3 describes type of electrochemical measurement and principles of electrochemical sensors. Section 2.4 showcases the carbon-based nanomaterials and their applications in electrochemical sensors. Section 2.5 highlights the significance of the research in this thesis.

2.1 Small Biomolecules

Small biomolecules are typically simple monomeric substances with molecular weights less than 500, which constitute essential substances for life [1]. These small biomolecules are continuously produced, diffused, and consumed under normal physiological conditions to regulate gene expression, cellular metabolism, neurological functions, physiological stress, and other processes essential for maintaining normal bodily functions [2]. Deviations in the levels of these small biomolecules within organisms can disrupt normal physiological states and directly reflect the health status of the body [3]. Furthermore, as the focus on physiological health intensifies and advancements in biomedical engineering and diagnostic applications continue, the development of rapid, accurate, and reliable quantitative analysis methods for small molecules becomes increasingly important. Among them, DNA bases, dopamine, glucose and hydrogen peroxide have significant importance in biology and medicine.

2.1.1 DNA Bases

Deoxyribonucleic acid (DNA) is an indispensable substance for the development and normal operation of an organism. The double helix of DNA is stabilized by hydrogen bonds established between the nitrogen-containing bases on the two strands [4]. As shown in Fig. 2.1, two complementary base pairs (adenine (A) and thymine (T), cytosine (C) and guanine (G)) are heterocyclic aromatic biomolecules that play a critical role in the replication and transcription of genetic information. However, variations in these sequences can lead to genetic mutations that contribute to various diseases. For instance, specific mutations in genes can result in hereditary conditions like cystic fibrosis and sickle cell anemia; chromosomal abnormalities can disrupt gene function and also lead to conditions like Down syndrome; the accumulation of mutations in critical genes can activate oncogenes or deactivate tumor suppressor genes, promoting cancer development [5, 6]. Therefore, many methods including chemiluminescence, fluorescence, surface plasmon resonance, resonance spectroscopy, and electrochemistry have been proposed for DNA base detection [7, 8].

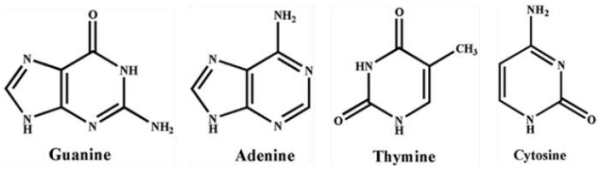

Fig. 2.1: The structures of guanine, adenine, thymine and cytosine

2.1.2 Dopamine

Dopamine (DA), primarily found in neural tissues, is an essential catecholamine neurotransmitter that plays a crucial role in regulating various physiological functions of the central nervous system [9]. As shown in Fig. 2.2, DA is a catechol group (a benzene ring with two hydroxyl groups) attached to an ethylamine side chain. Normal dopamine levels in human serum range from 10^{-6} to 10^{-9} mol/L, with plasma concentrations around 20 ng mL^{-1} and salivary concentrations at 18.9 pg mL^{-1} [10]. However, abnormal DA levels are closely associated with neurological and physiological disorders, particularly Parkinson's disease, Alzheimer's disease, and schizophrenia [11]. Various analytical methods, such as fluorescence imaging, spectroscopy, surface-enhanced Raman spectroscopy, chromatography–mass spectrometry, and electrochemical sensing, have been successfully employed for the determination of DA [12, 13].

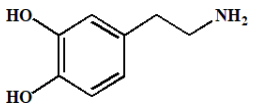

Fig. 2.2: The structure of dopamine

2.1.3 Glucose

Glucose is the primary energy source for normal cellular function in the human body, and maintaining stable blood glucose levels is crucial for health [14]. As indicated in Fig. 2.3, its structure consists of a six-carbon chain with a hydroxyl group attached to each carbon except for one. The normal range of blood glucose levels is typically between 6.1 and 7.0 mmol/L when fasting. After eating, blood glucose levels can rise, but they should generally remain below 7.0 mmol/L within two hours after a meal [15]. Persistent glucose levels above these ranges may indicate conditions such as prediabetes or diabetes. Diabetes is a metabolic disorder characterized by significantly elevated blood sugar levels, which can lead to complications such as kidney failure, diabetic foot, and cardiovascular diseases [18-20]. The

severe complications caused by diabetes are difficult to fully cure, making the monitoring and control of individual blood glucose levels an urgent societal concern. Nowadays, various detection technologies, including colorimetry, chromatography, microfluidic paper-based analysis, capillary electrophoresis, electrochemical sensing, have been reported for glucose detection [16, 17].

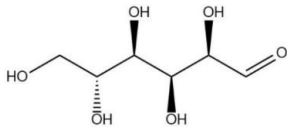

Fig. 2.3: The structure of glucose

2.1.4 Hydrogen Peroxide

Hydrogen peroxide (H_2O_2) is one of the most stable and abundant reactive oxygen species (ROS) within biological organisms, which is characterized by mild nature, high specificity, strong diffusivity, and membrane permeability [21]. It plays a significant role in regulating cell growth, differentiation, apoptosis, immune cell activation, and other biological signal transduction processes [22]. Typically, the concentration of H_2O_2 in human tissues is very low, ranging from nanomolar (nM) to micromolar (μM) [23]. Excessive production of H_2O_2 easily leads to oxidative stress, aging and various diseases, such as cardiovascular diseases, atherosclerosis, Parkinson's disease, diabetes, and cancer [24]. Therefore, high-sensitivity, quantitative monitoring of H_2O_2 levels is essential for understanding its pathological, physiological, and biomedical functions, providing theoretical guidance for health monitoring and disease diagnosis. Various approaches, including fluorescence and colorimetric sensing, chemical and electrochemical luminescence, surface-enhanced Raman scattering, capillary electrophoresis, electrochemical sensing, have been utilized to detect H_2O_2 [25].

2.2 Methods for Small Biomolecules Detection

In the human body, the small biomolecules play crucial roles in regulating physiological functions [26-29]. However, the inherent physiological balance of cells will be disrupted after being stimulated, causing changes in the concentration levels. The disruption can cause functional disturbances in the body and may even trigger various serious diseases [30, 31]. Therefore, establishing sensitive, accurate, and rapid analytical methods for detection of these bioactive small molecules is particularly important. In recent

years, with the rapid development of society, science and technology have greatly advanced, lead to increased attention on the detection of small biomolecules. The detection technology requires a simple process, fast response, environmental friendliness, and portability. Currently, many methods such as fluorescence spectrometry [32, 33], high performance liquid chromatography [34-36], inductively coupled plasma-mass spectrometry [37, 38], colorimetry [39-41], and electrochemistry [42-45] have been commonly used to detect small biomolecules.

2.2.1 Fluorescence Spectrometry

Fluorescence spectrometry is considered an effective and rapid method for determination of small biomolecules in the fields of supramolecular, biological, and medical chemistry. This method enables sensitive and selective detection of small biomolecules in vitro and in vivo, evaluation of biocompatibility and cell permeability [46, 47]. Small biomolecules can undergo changes in fluorescence signals, making them easy to be detected in analytical environments. For example, Guo's group [48] synthesized a near-infrared fluorescent probe, Cy-PFS, which enabled two-photon near-infrared ratio detection of hydrogen peroxide (H_2O_2), as indicated in Fig. 2.4. The detection limit of Cy-PFS reached 50 nM, and kinetic studies demonstrated its rapid response to H_2O_2 within 200 seconds, along with excellent selectivity. Importantly, Cy-PFS exhibited strong fluorescence signals in response to endogenous H_2O_2, making it a promising tool for studying changes in H_2O_2 levels during biological processes. However, the preparation of fluorescence probes typically requires exposure to organic solvents, which may have negative impact on analysis of cells or tissues.

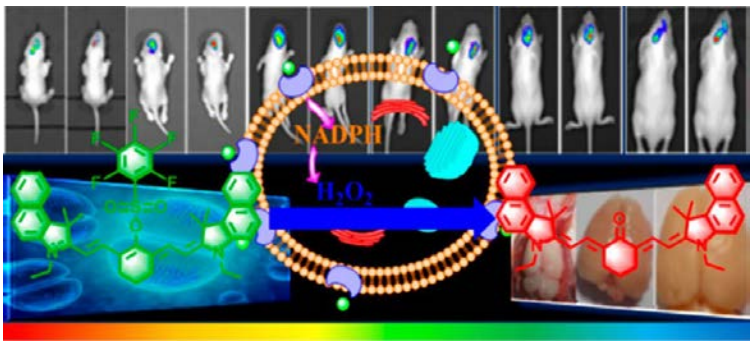

Fig. 2.4: Cy-PFS for the detection of H_2O_2 [48]

2.2.2 High Performance Liquid Chromatography

High-performance liquid chromatography (HPLC) employs a liquid mobile phase to achieve the separation of different components within a column [49, 50]. It allows simultaneous detection of multiple target molecules, thus achieving significant advancements. As indicated in Fig. 2.5, Zhang et al. [51] developed a 5-minute ultra-high-performance liquid chromatography-electrospray ionization mass spectrometry (UHPLC-ESI-MS) method for separation and detection of levodopa, ascorbic acid, and convicine in fava beans. This method has been applied to analyze various fava bean samples, offering a potential dietary therapeutic approach for treating Parkinson's disease. However, this technique requires complex sample preparation steps and may encounter co-elution during experimentation, especially for structurally and polarity-similar compounds, which have limited its applications.

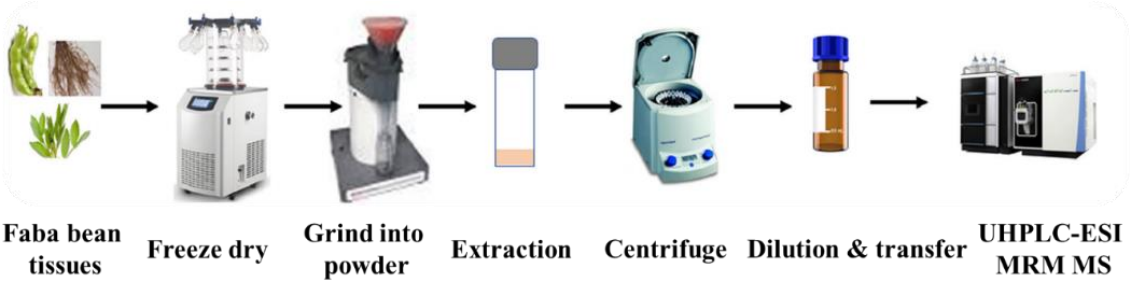

Fig. 2.5: Rapid separation and quantitative detection of UHPLC-ESI-MS [51]

2.2.3 Surface-Enhanced Raman Spectroscopy

Surface-Enhanced Raman Spectroscopy (SERS) utilizes ordinary Raman scattering to detect samples adsorbed on surfaces of metals such as Au, Ag, and Cu, thereby achieving an enhancement of the Raman signal [52, 53]. SERS overcomes the limitations of conventional Raman spectroscopy (weak signals, low sensitivity, etc.), making it applicable in the detection of small biomolecules [54]. Lu et al. [55] prepared nanostructured silver films through silver mirror reactions, followed by functionalization with mercaptopropionic acid (MPA) for accurate capture of DA, as shown in Fig. 2.6. In addition, silver colloids, synthesized via solvothermal methods, were modified with 4-mercaptophenylboronic acid (4-MPBA). Subsequently, the coupling of the two yielded a SERS substrate that ultimately achieved ultrasensitive detection of DA. However, most small biomolecules have relatively low Raman cross-

sections, which weakens their affinity for plasmas, and thus hindering the ability of SERS to detect them effectively [64].

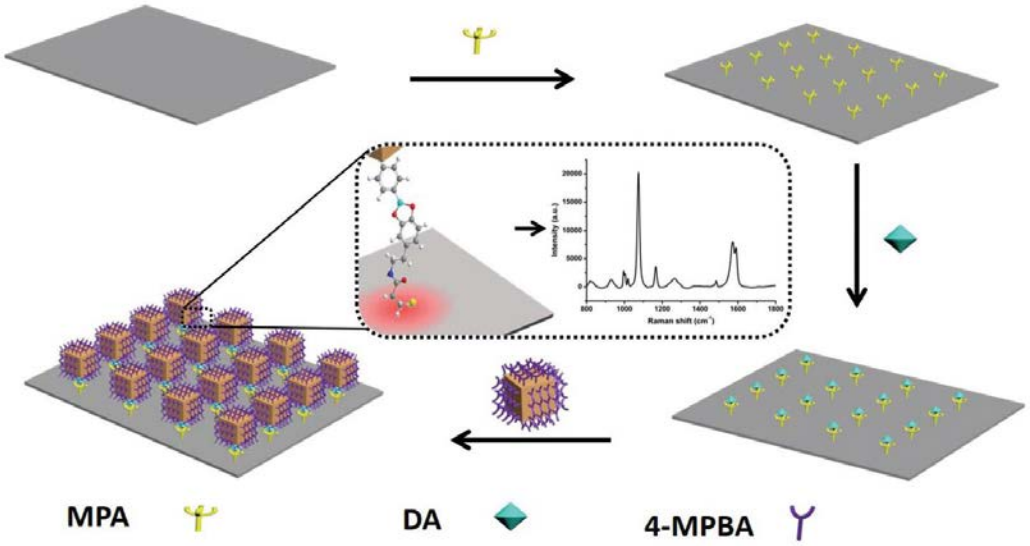

Fig. 2.6: The coupled SERS substrates for detection of DA [66]

2.2.4 Colorimetry

Colorimetry is a method for detecting substances based on their inherent color or color changes upon reaction with reagents, which can be observed visually or measured with instruments. [66]. In recent years, numerous colorimetric methods have been developed for detecting various small biomolecules due to their high accuracy, broad applicability, simplicity of operation, and rapid response [67, 68]. As indicated in Fig. 2.7, Lee et al. [69] constructed a sensing platform based on glucose oxidase-oxidized graphene oxide/manganese dioxide nanoenzyme (GOD-GO/MnO_2), which enabled direct detection of glucose in blood samples. The results indicated that a detection limit of 3.1 mg/dL and a linear range from 25 mg/dL to 300 mg/dL were achieved, which paves the way for the clinical application of blood glucose monitoring in diabetes patients.

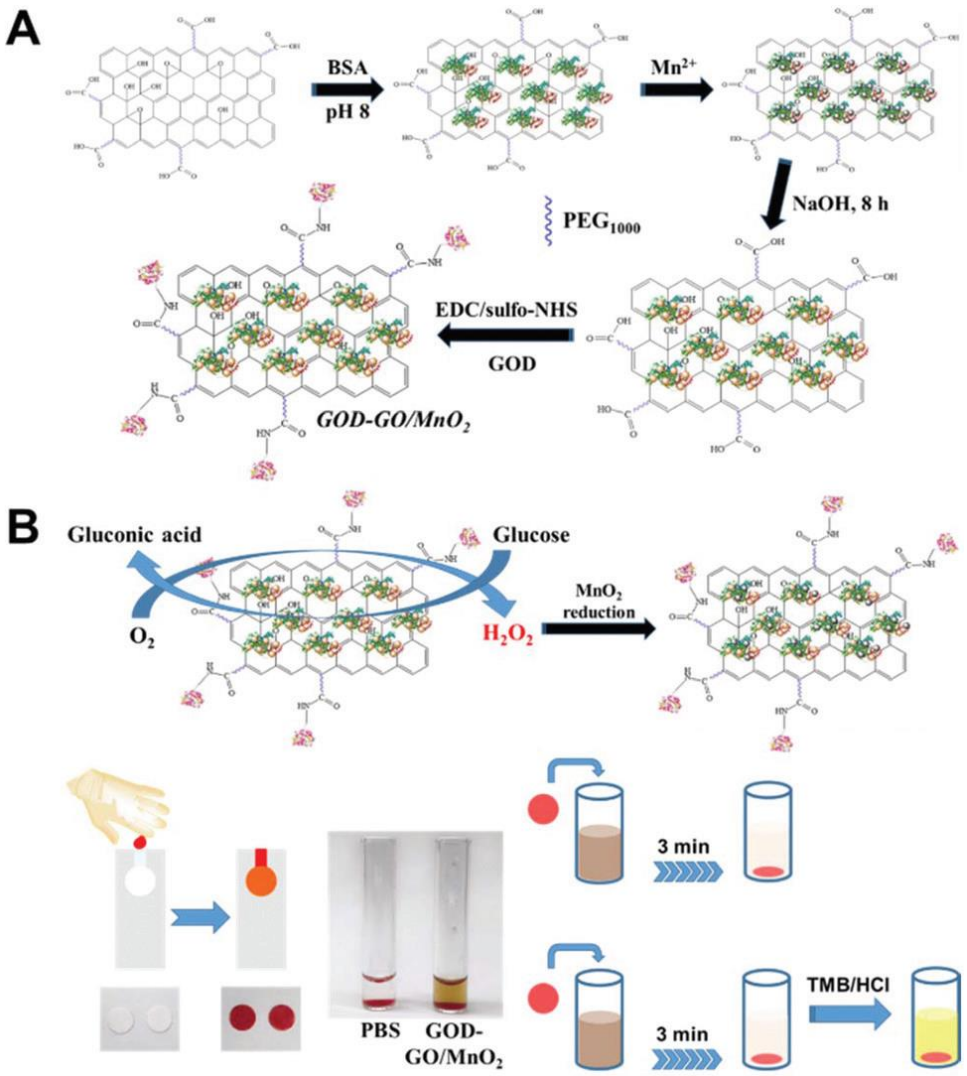

Fig. 2.7: Colorimetric method for the detection of glucose [69]

2.2.5 Electrochemistry

Electrochemical sensor transforms the physical or chemical signals of target molecules into electrical signals [70]. It typically consists of a molecular recognition system, signal transduction system, signal transmission system, and signal processing system. As illustrated in Fig. 2.8, the molecular recognition system is usually connected to the signal transduction system. It selectively interacts with target molecules, converting resulting chemical or physical changes into electrochemical signals such as resistance, current, or voltage. The electrochemical signals are then transmitted via the signal transmission system to the signal processing system to achieve the detection of target molecules [71]. In electrochemical sensors, the molecular recognition system is crucial for determining sensor effectiveness. Therefore, the successful construction of electrochemical sensors primarily involves

addressing issues related to the preparation and selection of the molecular recognition system, as well as effectively linking it with the signal transduction system.

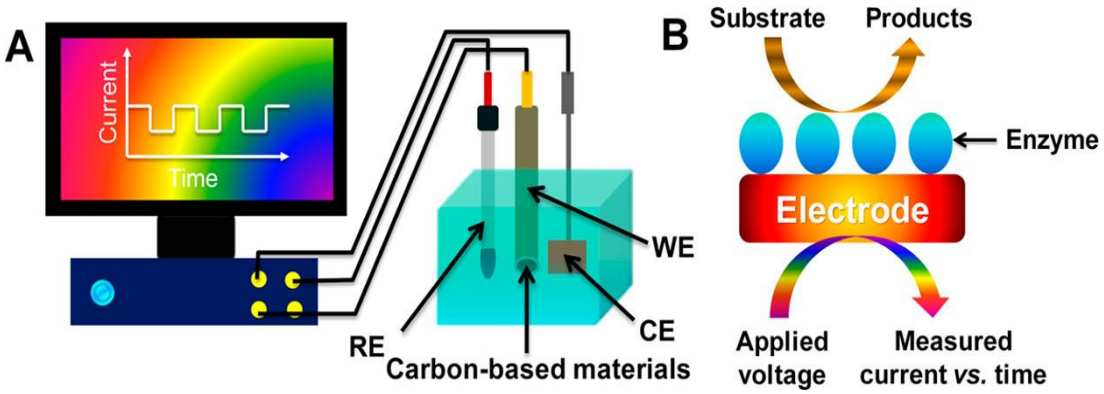

Fig. 2.8: The working principle of electrochemical sensor [71]

Due to their high sensitivity, low detection limit, and easy miniaturization, electrochemical methods have been widely used in the analysis of small biomolecules [72,73]. As illustrated in Fig. 2.9, Kokulnathan [74] exploited a new electrocatalyst for DA detection using a composite of yttrium vanadate (YVO) and graphene aerogel (GA), which provides a large specific surface area and high conductivity. This new composite exhibited excellent catalytic activity and synergistic effect for DA detection, making it suitable for creating effective sensors that can analyze human serum samples.

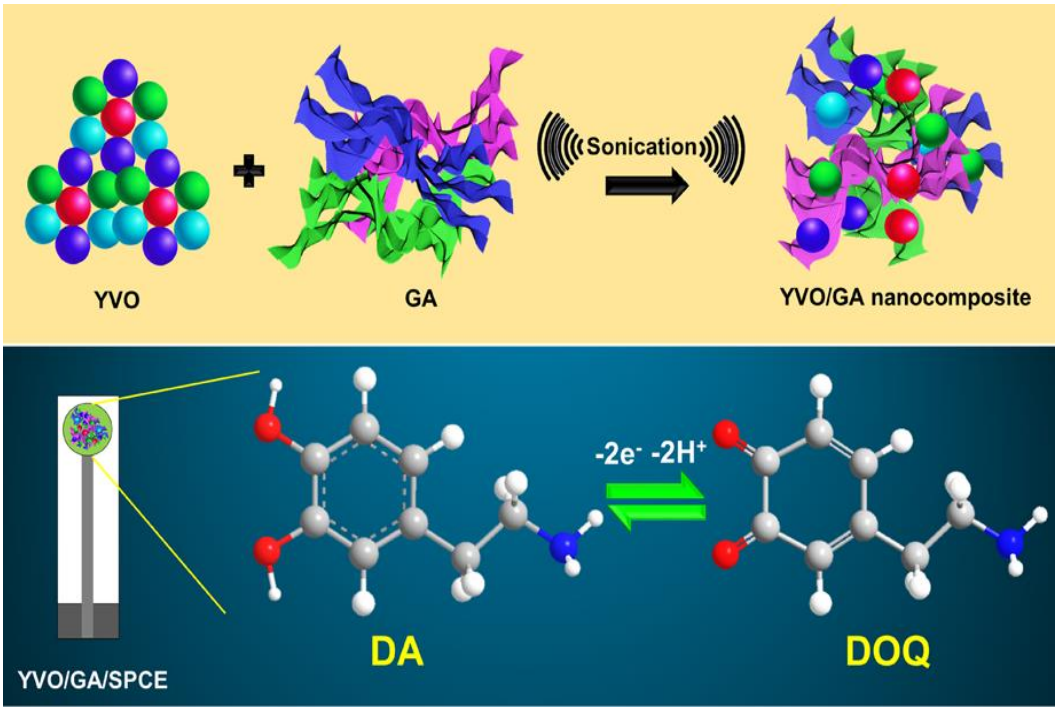

Fig. 2.9: YVO/GA nanocomposites for the detection of DA [74]

2.3 Electrochemical Sensors

Electrochemical sensors can be classified based on various criteria such as signal transduction, target analyte and sensing mechanism. Based on signal transduction, electrochemical sensors can be classified into potentiometry, voltammetry, amperometry and conductometry sensors.

2.3.1 Potentiometry Sensors

Potentiometry sensors detect the concentration of a specific ion or analyte by monitoring potential difference between a reference electrode and a working electrode [75]. For instance, an ion-selective electrode (ISE), which is a type of potentiometric sensors, is made up of a membrane that is selectively permeable to the ion of interest, allowing it to generate a potential difference across the membrane that is dependent on the ion's concentration. The ISE sensors are suitable for the following two situations: (i) when the selective membrane is infinitely large or the concentration of interfering ions is constant or sufficiently low; (ii) when the potential difference at different phase boundaries can be neglected, apart from the membrane/sample-solution interface. Potentiometric sensors are commonly used in fields such as electronic devices and industrial automation.

2.3.2 Voltammetry Sensors

Voltammetry sensors are based on the relationship between current and voltage. By applying different voltages and measuring the current response, these sensors can obtain the qualitative and quantitative information of an analyte [76]. Voltammetry techniques can be classified into different types including cyclic voltammetry, square wave voltammetry and differential pulse voltammetry, which have been widely applied in chemical analysis, electrochemical reaction research, materials science, and environmental monitoring [7,16,74].

2.3.3 Amperometry Sensors

Amperometry sensors detect currents generated from the electrochemical oxidation or reduction of target analytes. They operate by maintaining a constant voltage relative to a reference electrode on a working electrode or an array of electrodes [77]. The reference electrode can also serve as an auxiliary

electrode if the current is low. As shown in Fig. 2.10, current is typically measured under constant voltage, known as amperometry, or under varying voltage, known as voltammetry. Furthermore, the current signal measured within a linear range is proportional to the concentration of the target molecules. Amperometry sensors are capable of significantly reducing background current signals and offer advantages such as high sensitivity, low detection limits, and fast response times. However, unmodified working electrodes suffer from drawbacks such as poor conductivity, slow electron transfer rates, and inadequate selectivity towards target substances, which hinder sensitive and accurate detection of target molecules [78]. Therefore, for the detection of small biomolecules in complex samples, it is highly desirable to design electrochemical sensors with high sensitivity and strong interference resistance for simultaneous, real-time, and in vivo determination of multiple target analytes.

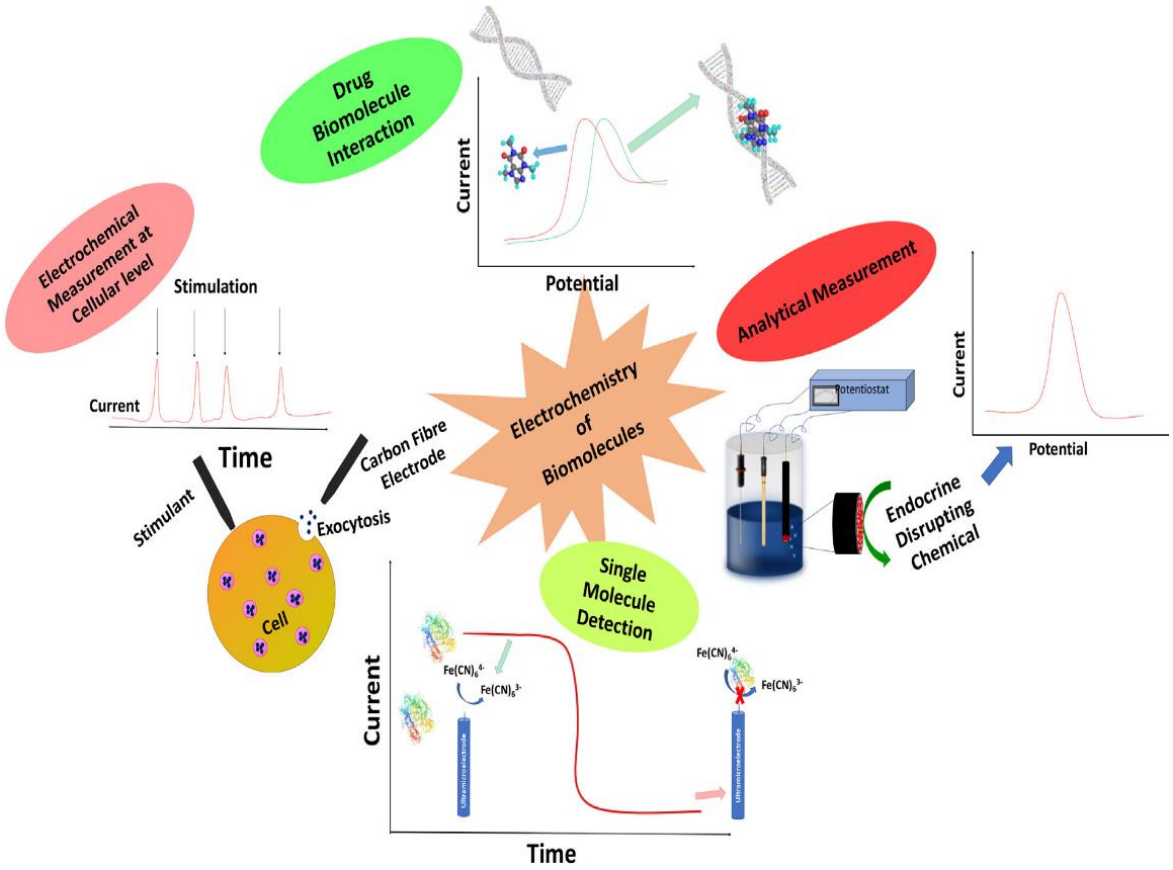

Fig. 2.10: The electrochemical method for the detection of small biomolecules [79]

2.3.4 Conductometry Sensors

Conductometry sensors can detect the ability of target molecules or media to conduct electrical current between electrodes [80]. Conductivity measures a solution's ability to conduct electrical current, the

electrical conductivity of a solution is directly related to the concentration of analytes present in it. Conductometry sensors can provide real-time data on conductivity, allowing for immediate adjustments in processes. They are widely used in various fields, including chemistry, environmental monitoring, and industrial processes.

2.4 Carbon-Based Nanomaterials in Electrochemical Sensing Applications

With the rapid advancement of nanotechnology, various nanomaterials with unique properties and functions have been synthesized and widely applied across many fields [88-90]. For electrochemical sensing applications, single-function nanomaterials are insufficient to fully enhance the sensing capabilities of electrodes. Therefore, nanomaterials with multiple functionalities are highly desirable to improve the analytical performance of electrochemical sensors through synergistic effects. The continual emergence and evolution of carbon-based nanomaterials have provided a broad development platform for electrochemical sensors. As reported previously, carbon-based nanomaterials have significantly enhanced the performance due to their good conductivity and biological characteristics, controllable morphology, and large specific surface area [91, 92]. Specifically, in biosensing applications, they can amply signals by increasing the electroactive area of the sensing electrode and maintain biomolecule activities due to their excellent biocompatibility.

Typical carbon-based nanomaterials include graphene, conductive polymers, carbon nanospheres, and metal-organic frameworks. Electrochemical sensors based on these carbon-based nanomaterials have made significant advances in nanotechnology and science, with tremendous potential in enhancing the performance for the detection of small biomolecules [97-100].

2.4.1 Graphene

In 2004, physicists Geim et al. [101] utilized micromechanical exfoliation techniques to first extract graphene from graphite. Graphene (GR) exhibits a honeycomb structure, though it has a certain degree of rippling, with lateral dimensions reaching up to millimeters or even micrometers, as shown in Fig. 2.11 [102]. The unique structure of graphene ensures its stability [103]and imparts excellent physical

and chemical properties, including superb electrical conductivity, thermal conductivity, high specific surface area, and mechanical strength.

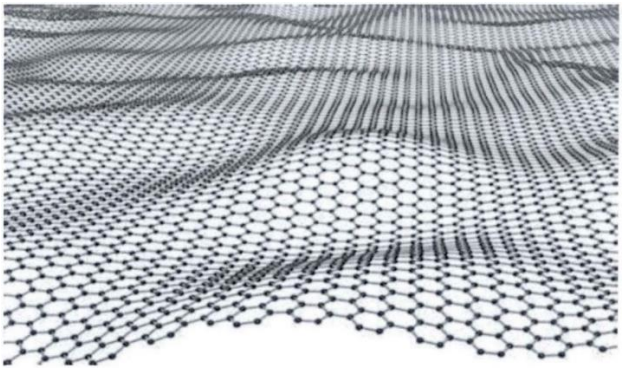

Fig. 2.11: The honeycomb structure of graphene [102]

2.4.1.1 Preparation of Graphene. Since graphene was discovered, optimization studies for graphene preparation have been conducted for many years, summarized into top-down and bottom-up approaches [104], as shown in Fig. 2.12.

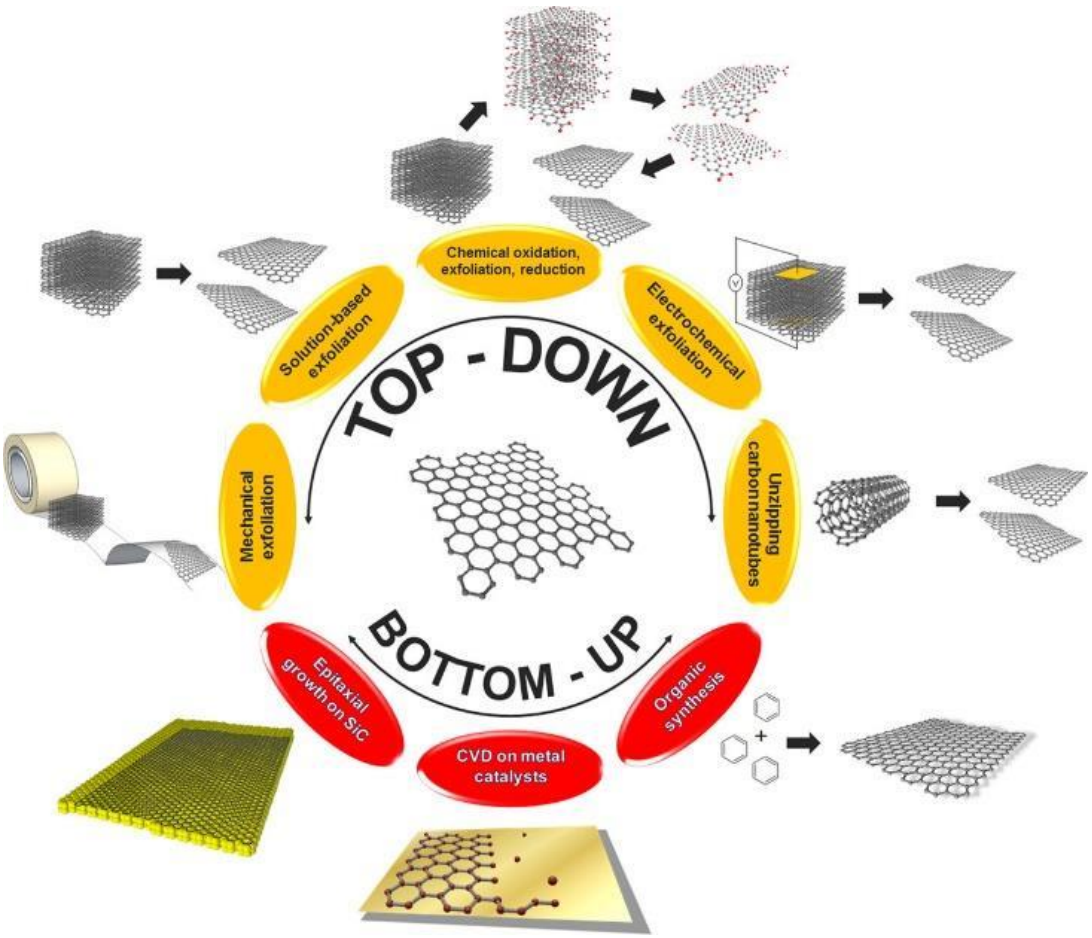

Fig. 2.12: Preparation of graphene: top-down and bottom-up approaches [104]

(1) The top-down approach involves physically processing powdered graphite to exfoliate it into graphene. Mechanical exfoliation and chemical reduction are both examples of top-down methods [105].

(a) Mechanical exfoliation. Single-layer graphene sheets are obtained through mechanical cleavage of graphite [106]. Pristine single-layer graphene is a semimetal with a zero bandgap, characterized by extremely high carrier density, room temperature Hall effect, low intrinsic noise, and bipolar field effect properties [107]. These outstanding characteristics play a crucial role in the development of electronic sensors. However, a drawback of the mechanical exfoliation method is its low yield and inability to produce large-sized graphene sheets.

(b) Chemical reduction. Graphene can be obtained by reducing oxidized graphene using reducing agents [108]. Compared to pristine graphene, reduced graphene oxide has abundant reactive sites on its edges and defect-rich surfaces, enhancing its electrochemical activity. This makes reduced graphene oxide promising for the development of electrochemical sensors.

(2) The bottom-up approach utilizes carbon-containing gases to generate graphene. It typically allows for better control over the number of layers of graphene, reduction of defects, increased surface area, and enhanced material orderliness. Chemical vapor deposition and epitaxial growth methods are examples of the bottom-up approach.

(a) Chemical vapor deposition. Graphene can be grown using chemical vapor deposition (CVD) on transition metal substrates such as nickel, copper, and palladium [109]. The advantage of CVD growth is the ability to directly prepare doped graphene by introducing dopant atoms into the carbon lattice with control over the type and degree of doping. However, due to its complexity, limited scalability,, and high costs, this method has not been widely adopted.

(b) Epitaxial growth. Silicon carbide serves as the substrate, with silicon atoms sublimating and carbon atoms reorganizing themselves at high temperatures, to obtain graphene [110]. However, the graphene produced by this method lacks uniformity and is difficult to separate from the substrate, limiting its scalability for widespread applications.

2.4.1.2 Electrochemical sensing applications of graphene. Graphene possesses outstanding electrochemical properties and unique structural advantages, and its use in electrochemical sensors significantly enhances the performance for the detection of various substances [111, 112]. Its high surface area and functionalized surface enhance the binding of target molecules, promoting the development of novel sensing interfaces. As shown in Fig. 2.13, Biswas et al. [113] successfully synthesized NOGG nanocomposites by ultrasound treatment of neodymium oxide (Nd_2O_3) nanoparticles and graphene for simultaneous detection of adrenaline (AD) and tyrosine (TY). NOGG/GP exhibited excellent electrocatalytic performance towards AD and TY. The results confirmed the irreversible oxidation of AD and TY on the electrode surface via an adsorption-controlled process. The electrochemical signals of NOGG/GP had no significant changes in the presence of various interferents. AD and TY in biological and pharmaceutical samples were detected via standard addition method, with results consistent with those obtained from HPLC, further confirming the reliability of this approach.

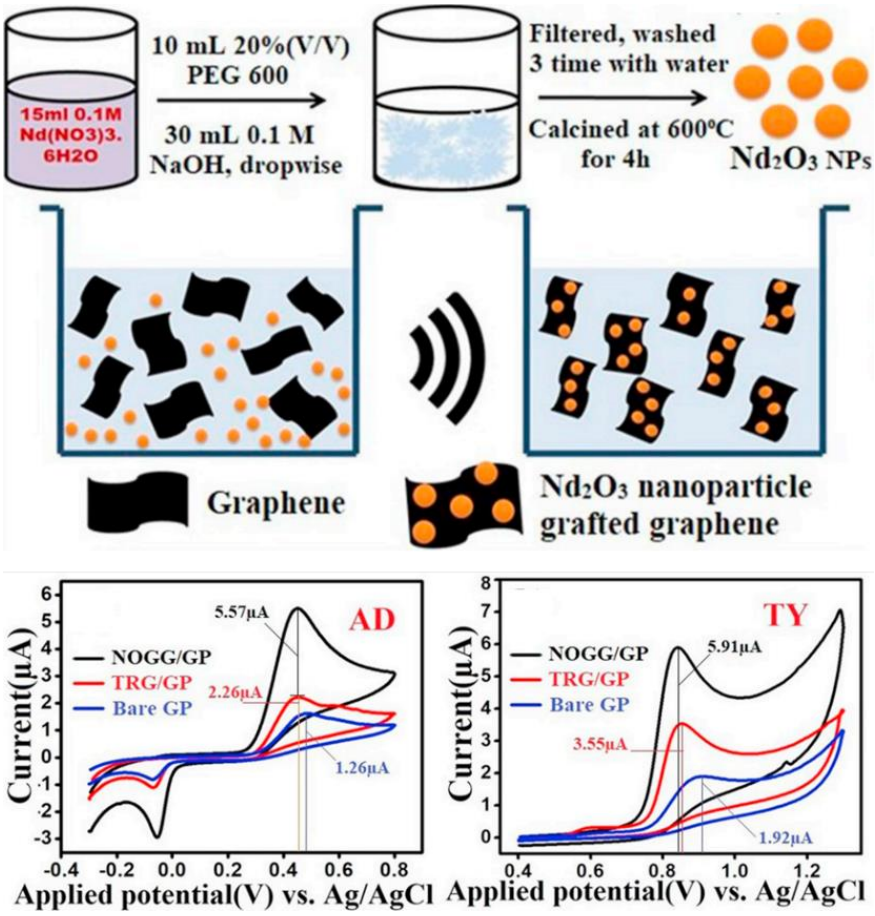

Fig. 2.13: Preparation NOGG nanocomposites for the detection of AD and TY [113]

Balu et al. [114] synthesized tin disulfide (SnS_2) nanorods modified graphene-β-cyclodextrin (SnS_2/GR-β-CD) nanocomposites through ultrasound and hydrothermal methods, and investigated their electrocatalytic activity towards dopamine (DA), as shown in Fig. 2.14. The synergistic effect enhanced sensitivity and reduced the detection potential for DA compared to the use of individual materials. SnS_2/GR-β-CD/GCE exhibited a linear current response to DA within the concentration range of 0.01-150.76 μM, with a detection limit of 4 nM. In the presence of various interferents, there was little effect on the response current of DA. Ultimately, SnS_2/GR-β-CD/GCE was successfully applied to detect DA in rat brains and human serum samples.

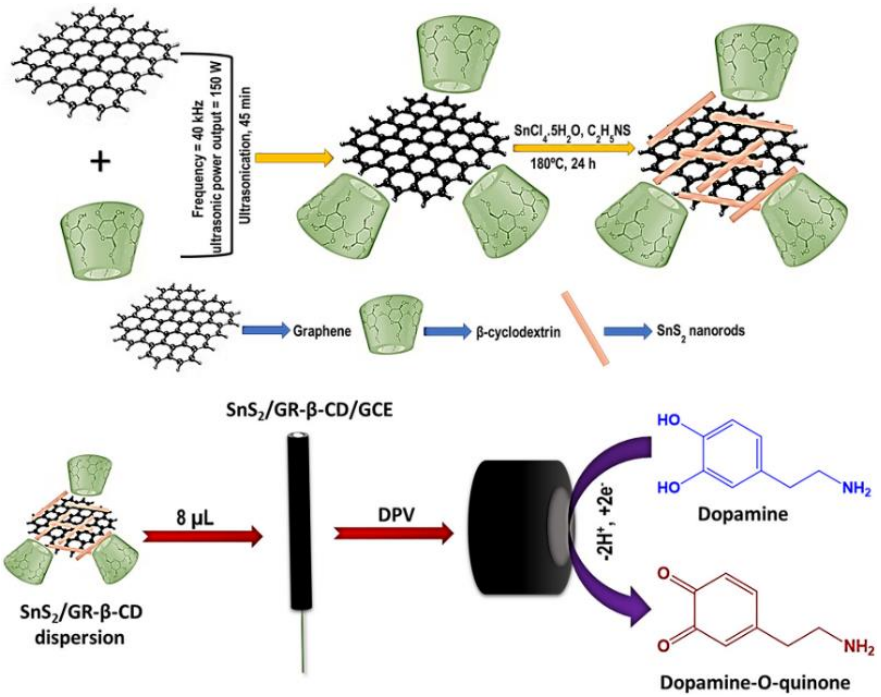

Fig. 2.14: Preparation of SnS_2/GR-β-CD nanocomposites for the detection of DA [114]

Graphene nanomaterials exhibit high biocompatibility and provide a favorable environment for natural enzymes. Since combining them with enzymes to form composites as probes can enhance the sensitivity of immunosensors, many graphene-based sensors have been employed for biomarker detection. Fan et al. [115] designed graphene capsules (GR-CAPS) as carriers for horseradish peroxidase to detect hydrogen peroxide, as shown in Fig. 2.15. The sensor exhibited outstanding reproducibility and selectivity in the presence of interference, indicating its promising potential for medical analysis.

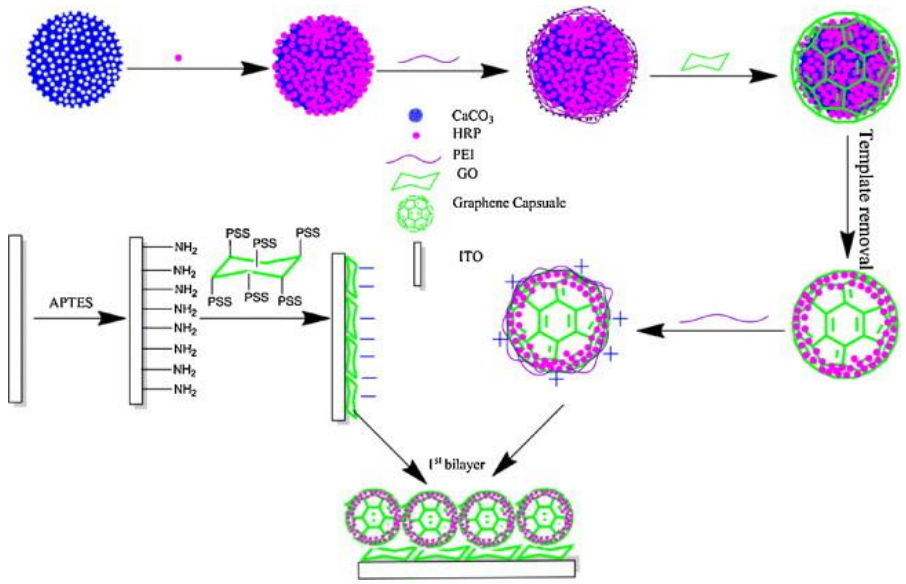

Fig. 2.15: Electrochemical biosensors based on GRCAPS for H_2O_2 detection [115]

Combining graphene with various functional nanomaterials leverages their synergistic effects in developing advanced sensors with signal amplification capabilities [116]. Noble metals (Pt, Pd, and Au), known for their excellent conductivity and catalytic activity, are beneficial for constructing electrochemical sensors. Moreover, these nanoscale noble metals effectively prevent graphene aggregation, thereby enhancing its electroactive area. As shown in Fig. 2.16, Qi et al. [117] have pioneered a highly sensitive electrochemical sensor for detecting alpha-fetoprotein (AFP) based on immune reactions with Pd-graphene nanocomposites (Pd-rGO). It was found that Pd nanoparticles loaded onto graphene effectively improved electron transfer efficiency and catalytic performance, resulting in a pronounced amplification of electrochemical signals. Upon binding the target molecule with antibodies on the electrode surface, electron transfer obstruction altered the current signal. Additionally, graphene serves as an active carrier, providing a robust platform for electrochemical sensing by immobilizing signal probes related to target molecules via π-π stacking interactions. Compared to graphene, graphene nanocomposites exhibit certain advantages in catalyzing the oxidation of small biomolecules, promising applications in developing novel electrochemical biosensing platforms for sensitive and selective detection of small biomolecules.

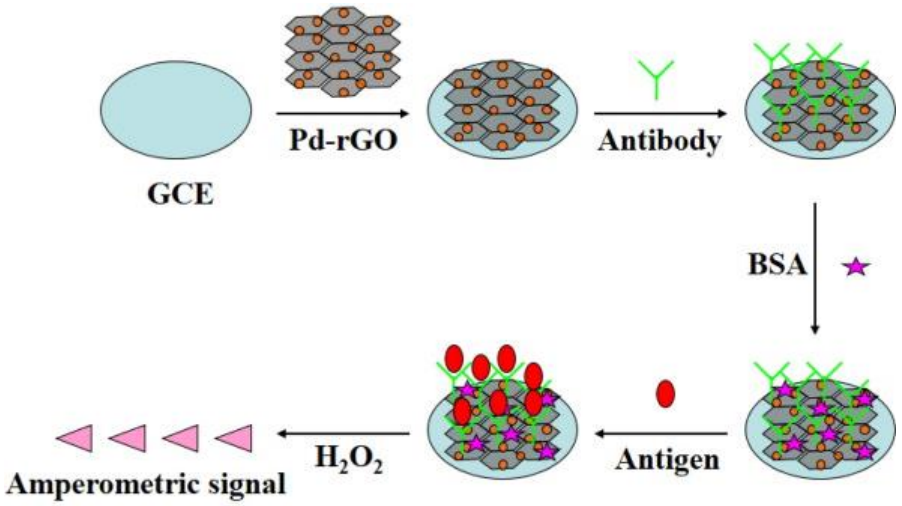

Fig. 2.16: Electrochemical immunosensor based on Pd-rGO for AFP detection [117]

2.4.2 Conductive Polymers

Conductive polymers are a type of polymer material that exhibits conductivity either inherently or after doping with other materials, including polypyrrole [118], polyaniline [119], and poly(3,4-ethylenedioxythiophene) [120]. Conductive polymers offer several advantages: (1) They possess good electrical conductivity, facilitating rapid charge transfer; (2) They exhibit excellent chemical stability, allowing operation across a wide range of pH values and solution environments; (3) Their conductivity can be tuned by modifying the chemical structure and synthesis conditions of the polymer, enabling selective detection of target molecules to meet diverse sensing requirements. Conductive polymers are widely used in electrochemical detection, serving as electrode materials, electrolyte materials, and auxiliary components. Some studies employ conductive polymers-modified electrodes for electrochemical detection of environmental pollutants, biomarkers, drugs, and other target molecules [121, 122].

Conductive polymers can serve independently as signal probes, and their unique structures play a crucial role in electrochemical catalysis. Lu et al. [123] developed a novel electrochemical sensor based on PPI by a simple electrochemical method, as indicated in Fig. 2.17. The bromophenyl moiety in PPI extended its aromatic plane, which enhanced charge transfer and π-π interactions. PPI with π-electron-enriched conjugated structure achieved simultaneous detection of G, A, T, and C in neutral solutions, with oxidation peak potentials observed at 0.714 V, 1.004 V, 1.177 V, and 1.353 V, respectively. PPI/GCE

exhibited strong electrochemical responses towards the determination of G (3-300 μM), A (1-300 μM), T (30-800 μM), and C (20-750 μM) within their respective concentration ranges. The prepared sensor demonstrated excellent selectivity, stability, and reproducibility, making it a promising candidate for the detection of DNA bases in practical samples.

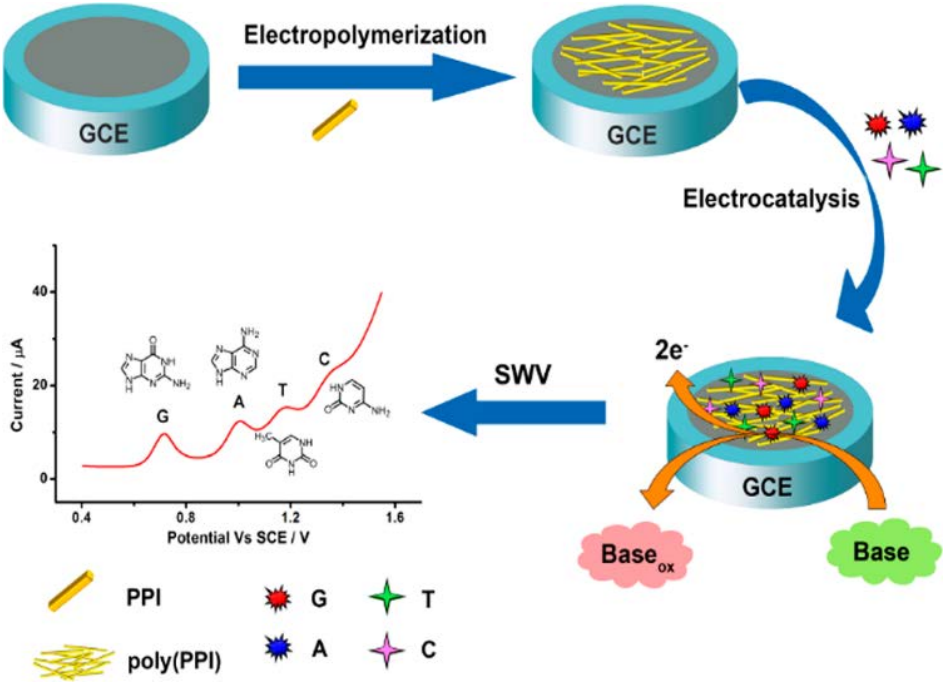

Fig. 2.17: Fabrication of the PPI/GCE for the sensing of DNA bases [123]

Due to the excellent performance, conductive polymers can serve as carriers for other nanomaterials, enabling the preparation of novel nanomaterials with enhanced properties. As indicated in Fig. 2.18, Pan et al. [124] synthesized PEDOT-Au NPs-GO nanocomposites, which were applied for the simultaneous detection of DA and uric acid (UA). PEDOT-Au NPs-GO/GCE exhibited excellent electrocatalytic activity towards DA and UA under physiological conditions, while effectively suppressing the oxidation of ascorbic acid (AA). This method enabled the detection of DA and UA in urine with satisfactory recovery rates (96.7%-105.0%). The study demonstrates that PEDOT-Au NPs-GO exhibits outstanding electrocatalytic properties and holds great promise as a nanocomposite for electroanalytical and clinical applications.

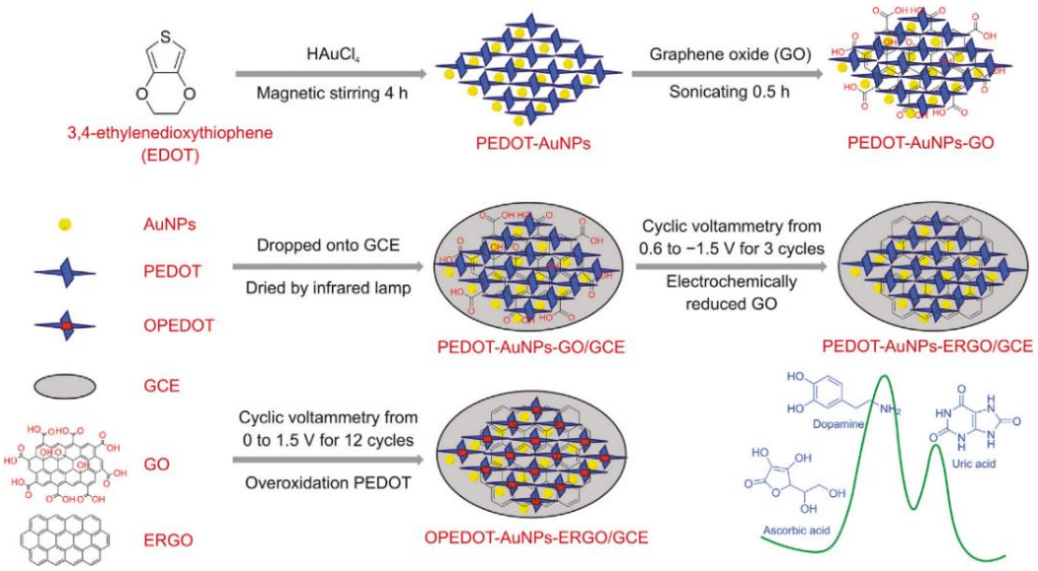

Fig. 2.18: Fabrication of PEDOT-Au NPs-GO/GCE for DA and UA detection [124]

Eryiğit et al. [120] used electrodeposition to modify a gold electrode surface with PEDOT and electrochemically reduced graphene oxide (ERGO) for non-enzymatic glucose detection, as indicated in Fig. 2.19. Compared to individual materials, Au-PEDOT-ERGO exhibited the highest electrocatalytic activity for glucose detection, highlighting the synergistic effect between PEDOT and ERGO in catalyzing glucose oxidation. Au-PEDOT-ERGO showed lower detection limits and higher sensitivity toward glucose compared to previous reports. The remarkable catalytic performance of Au-PEDOT-ERGO is primarily attributed to well-dispersed PEDOT-ERGO, increased surface area, and enhanced conductivity. Additionally, interference tests conducted in the presence of substances such as AA, UA DA, and H_2O_2 revealed excellent selectivity of this sensor.

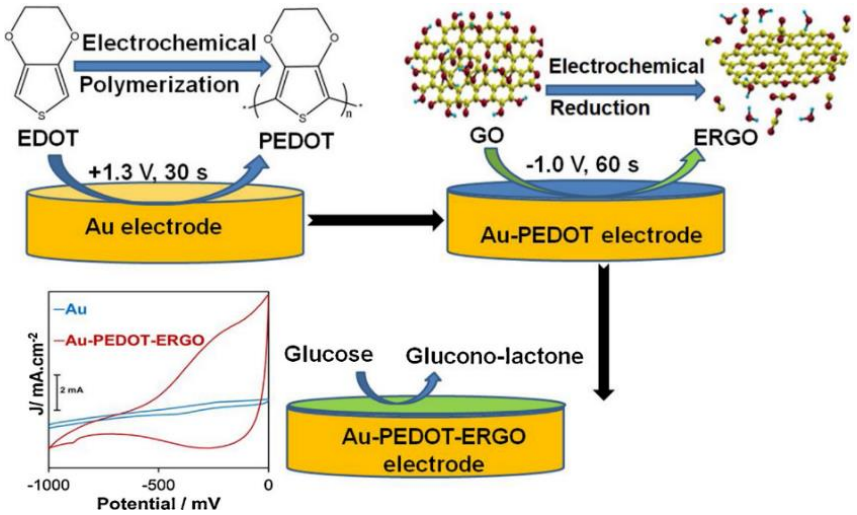

Fig. 2.19: Fabrication of Au-PEDOT-ERGO for detecting glucose [120]

Furthermore, Chen et al. [125] synthesized Co-Ni(Fe)-MOF/PPy nanocomposites by combining PPy with Co-Ni(Fe)-MOF nanosheets, and developed a glucose sensing platform, as shown in Fig. 2.20. The unique porous structure of Co-Ni(Fe)-MOF, combined with its multi-component metal ions, provided abundant electrochemical active sites for glucose oxidation. Additionally, the incorporation of PPy enhanced the electron transfer kinetics. Therefore, Co-Ni(Fe)-MOF/PPy nanocomposites exhibited superior electrocatalytic activity.

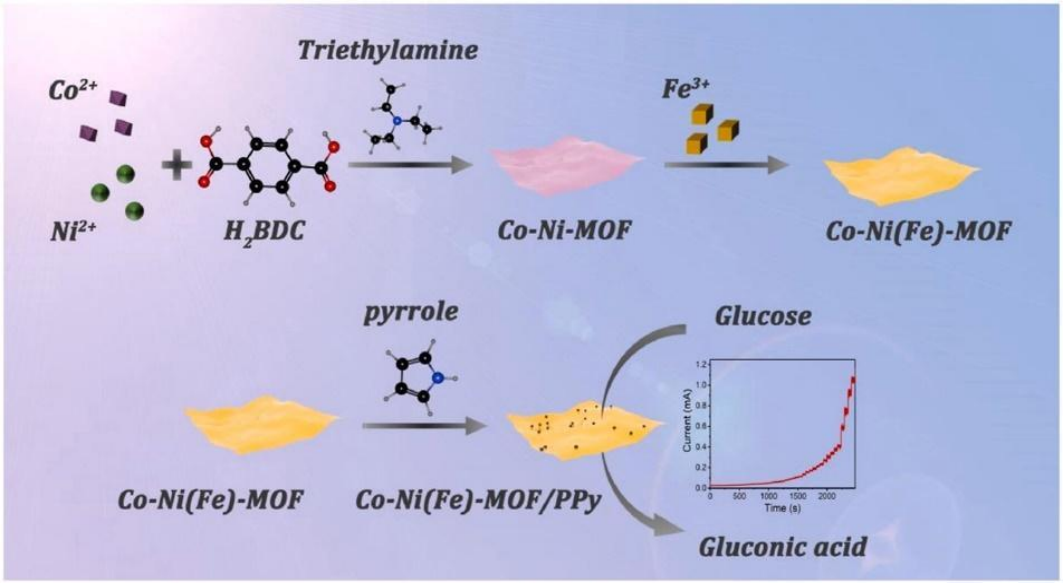

Fig. 2.20: Fabrication of Co-Ni(Fe)-MOF/PPy for detecting glucose [125]

2.4.3 Carbon Nanospheres

Carbon nanospheres exhibit excellent biocompatibility, low cost, and low toxicity, making them essential for applications such as supercapacitors, drug carriers, and lithium-ion batteries [126]. In the field of electrochemical sensing, their abundant nanoporous structure, unique spherical morphology, and tunable pore sizes ensure a large specific surface area, rich functional surfaces, and high conductivity, qualifying them as high-performance electrode materials [127].

2.4.3.1 Preparation of carbon nanospheres. Various methods have been developed for synthesizing carbon nanospheres, including template methods, chemical vapor deposition, and solvothermal methods [128-130].

(1) Template methods, commonly used for synthesizing nanostructured composites, mainly include soft template and hard template methods. Soft template methods involve modifying materials within the template to prepare nanostructures with excellent performance. However, due to the instability of some emulsions, strict control of experimental parameters is necessary. In contrast, morphologies synthesized by hard template-assisted strategies exhibit higher stability and allow precise control over parameters to adjust the morphology and shell thickness of carbon spheres. Chen et al. [131] synthesized hollow mesoporous carbon nanospheres loaded with Pt nanoparticles (Pt-HMCNs) to mimic peroxidase enzymes through calcination and etching, as indicated in Fig. 2.21. The hollow cavity structure and mesoporous nature of Pt-HMCNs demonstrated high activity towards H_2O_2 and TMB substrates. However, removing the template typically involves a complex and time-consuming procedures, which can potentially cause structural damage to the carbon spheres and lead to chemical contamination issues.

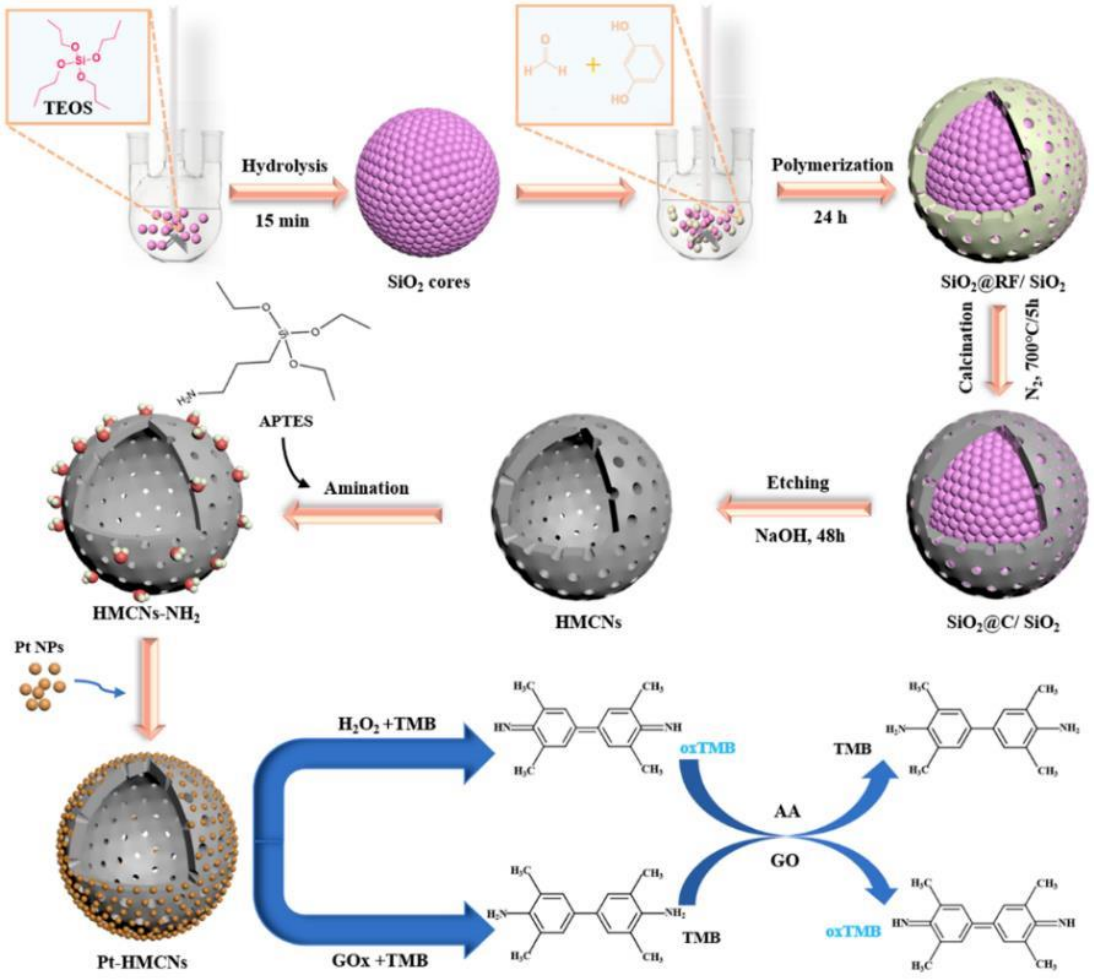

Fig. 2.21: Preparation and detection application of Pt HMCNs [131]

(2) Chemical vapor deposition (CVD) primarily encompasses two types: catalytic CVD and non-catalytic CVD. The catalytic route of CVD can produce pure carbon nanospheres, but it requires a complex process to remove catalyst residues from the final product. In contrast, non-catalytic CVD does not use any catalyst and can produce relatively uniform and highly graphitized carbon nanospheres. It offers advantages such as high efficiency and the potential for large-scale production. As indicated in Fig. 2.22, Li's group [132] employed non-metallic catalyst methane CVD to synthesize graphitized hollow carbon nanospheres (HCS) and Au@HCS nanoeggshell structures. This method provides a strategy for producing high-quality HCS. However, it also has drawbacks, including high cost, the use of toxic or flammable gases, and the need for high-temperature synthesis.

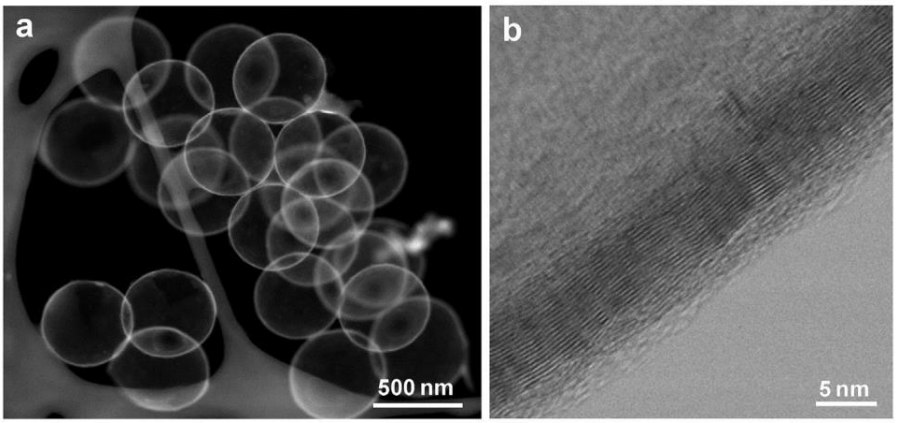

Fig. 2.22: TEM images of HCSs [132]

(3) Solvothermal method is a technique for producing high-purity, high-performance nanocomposites. It is an ideal route for synthesizing carbon sphere materials due to its low cost, simple synthesis method, and high yield. By adjusting variables such as temperature, time, and solvent type, it is possible to alter the size, morphology, and pore size of the spheres, thereby producing carbon nanospheres with various shapes and forms [133]. Therefore, this method has been widely used for preparing carbon nanospheres. Yao et al. [134] developed a simple and environmentally friendly method to prepare structurally uniform carbon spheres (CS), as indicated in Fig. 2.23. The optimized synthesis method produces CS with high pore volume, which demonstrates outstanding rate capability and excellent stability in alkaline solutions, making it an ideal electrode material.

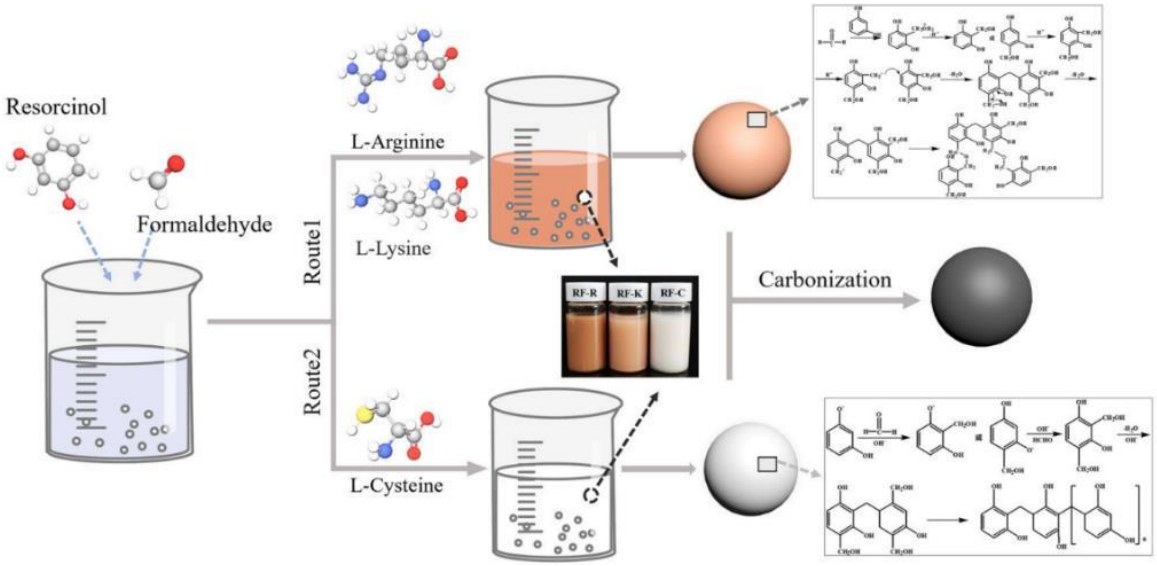

Fig. 2.23: Preparation and mechanism of CS [134]

2.4.3.2 Electrochemical sensing applications of carbon nanospheres. Surface-enriched functional groups and excellent conductivity of carbon nanospheres are advantageous for their use in electrochemical sensing applications. As shown in Fig. 2.24, Mahanthappa et al. [135] developed an electrochemical sensor based on nitrogen-phosphorus co-doped hollow mesoporous carbon spheres (NPHMCS). The platform exhibited excellent electrocatalytic performance suitable for AA, AC, UA, and DA detection. Carbon substrates doped with dual atoms (N, P) showed defects, numerous catalytic active sites and rapid heterogeneous electron transfer rates, thereby enhancing the sensing capabilities of the electrochemical analysis platform. NPHMCS/GCE demonstrated outstanding electrocatalytic performance in the simultaneous detection of multiple analytes and was effectively validated in real samples.

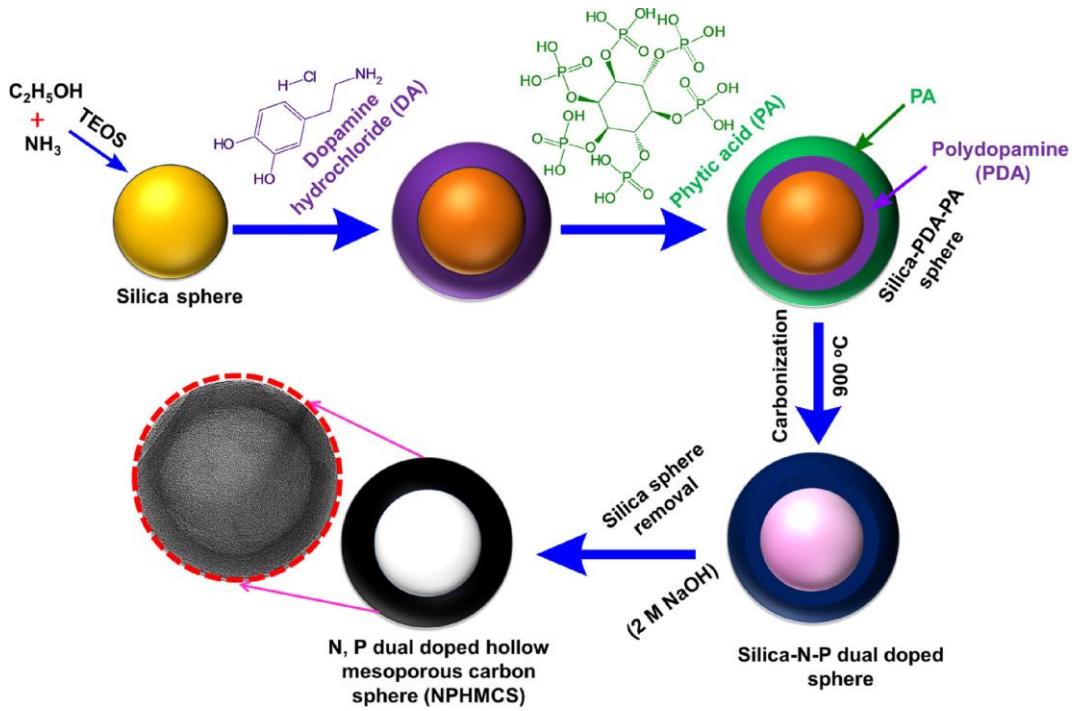

Fig. 2.24: Preparation principle of NPHMCS [135]

As shown in Fig. 2.25, Wang et al. [136] employed an electrochemical sensing platform based on Pd/POMs/NHCSs. The hollow structure of NHCSs enhanced chemical stability, increased internal porosity, and facilitated mass transfer of analytes. Additionally, N atoms exhibited strong electron-donating properties, contributing to enhanced electrocatalytic activity in NHCSs after doping. This sensor demonstrated excellent electrocatalytic performance in the detection of acetaminophen (AP).

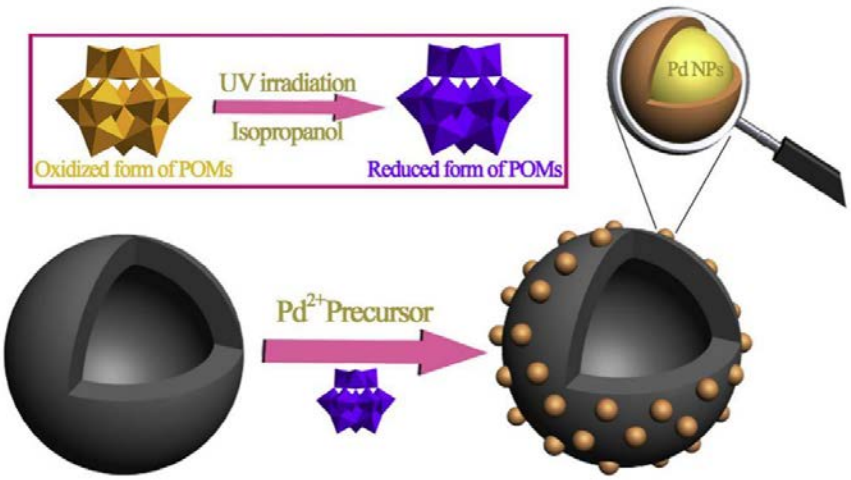

Fig. 2.25: Preparation principle of Pd/POMs/NHCSs [136]

Liu et al. [137] prepared a non-enzyme and metal-free electrochemical sensor using nitrogen-doped hollow mesoporous carbon spheres (N-HMCS) rapidly and sensitively detect superoxide anions, as shown in Fig. 2.26. N-HMCS exhibited excellent electrochemical properties due to its enriched electroactive sites and higher conductivity, which facilitate faster electron transfer during the electrochemical reduction of superoxide anions. Furthermore, N-HMCS/SPCE is capable of detecting superoxide anions released by live cells, demonstrating significant potential for practical applications in real sample analysis. Electrochemical sensors based on carbon nanospheres have found widespread applications in enhancing sensitivity, selectivity, and detection range for various chemical and biological substances.

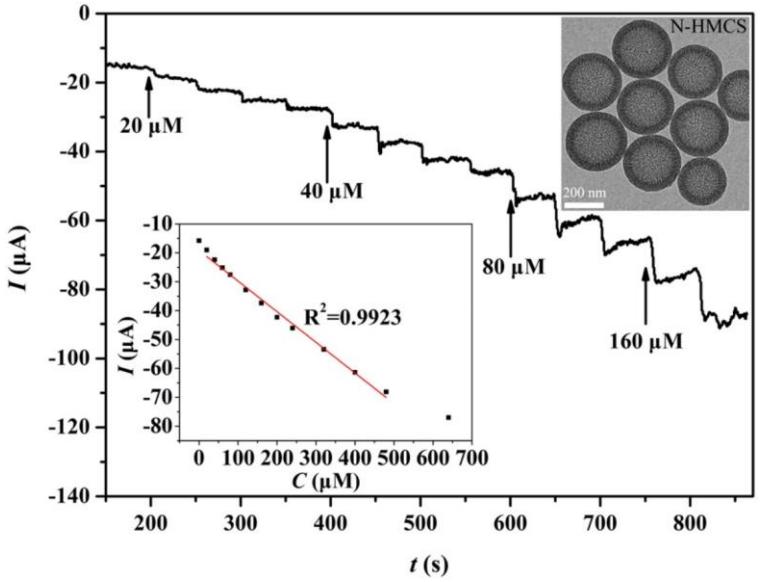

Fig. 2.26: N-HMCS/SPCE for detecting superoxide anions [137]

2.4.4 Metal-Organic Frameworks

Metal-organic frameworks (MOFs) are a novel class of porous crystalline materials formed through the self-assembly of inorganic metal ions with organic ligands via coordination bonds [138, 139], as shown in Fig. 2.27. MOFs exhibit highly ordered pore structures, ultrahigh surface areas, and uniform pore apertures. The structure of MOFs is determined by the characteristics of the metal ions and the spatial topology of the organic ligands [140, 141]. Due to their high surface area and pore structures, MOFs can accommodate multiple guest molecules, providing high adsorption capacity and excellent selectivity.

Modifying the organic ligands by grafting different functional groups can alter the physicochemical properties of MOFs, resulting in larger surface areas and more stable structures [142, 143].

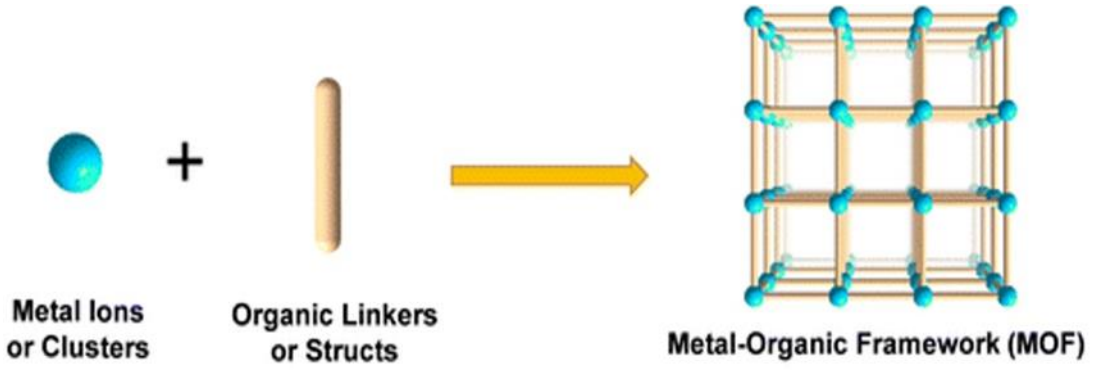

Fig. 2.27: Schematic diagram of MOFs construction [144]

2.4.4.1 Preparation of metal-organic frameworks. MOFs with various structures and properties have been synthesized due to the diversity of available metal ions and organic ligands. The properties of MOFs depend on factors such as their morphology and crystal size. By varying reaction conditions such as solvents [145], pH [146], substituents [147], and concentrations of metal ions [148], the growth and nucleation rates of MOF crystals can be controlled at the nanoscale to obtain MOFs with specific performance. Therefore, the selection of appropriate methods for synthesizing specific MOF materials is crucial. Common methods for synthesizing MOFs include solvothermal, electrochemical, microwave, and sonochemical techniques [149-151].

(1) Hydrothermal/solvothermal method [152-154] is a commonly employed method for preparing MOFs, as indicated in Fig. 2.28. Hydrothermal method, a subset of solvothermal synthesis, involves dissolving metal salts and organic ligands in water, transferring them to a reaction vessel, and using controlled reaction time and temperature to effectively produce MOFs. The solvothermal method, on the other hand, uses organic solvents instead of water, allowing for higher pressures during MOF preparation.

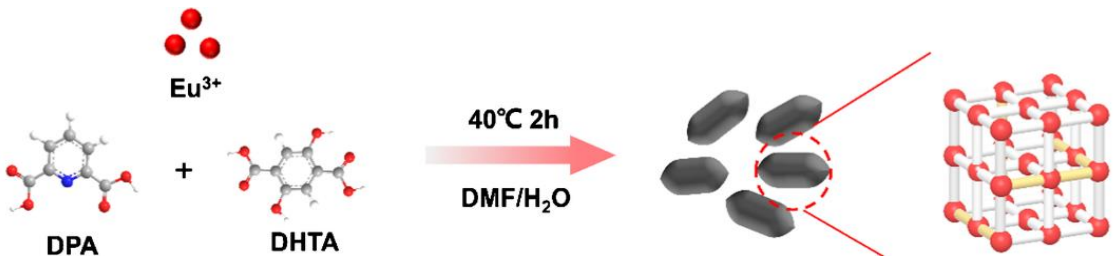

Fig. 2.28: Preparation of MOF through hydrothermal/solvothermal method [155]

(2) Electrochemical method is highly favorable due to its mild reaction conditions, simplicity, high yield, and rapid crystallization, addressing issues associated with large MOF sizes [156, 157], as shown in Fig. 2.29. Electrochemical method is divided into anodic and cathodic processes. Factors such as electrolyte concentration, voltage and current density, temperature, and synthesis time can influence the morphology and crystal size of MOFs, requiring careful attention to the synthesis process.

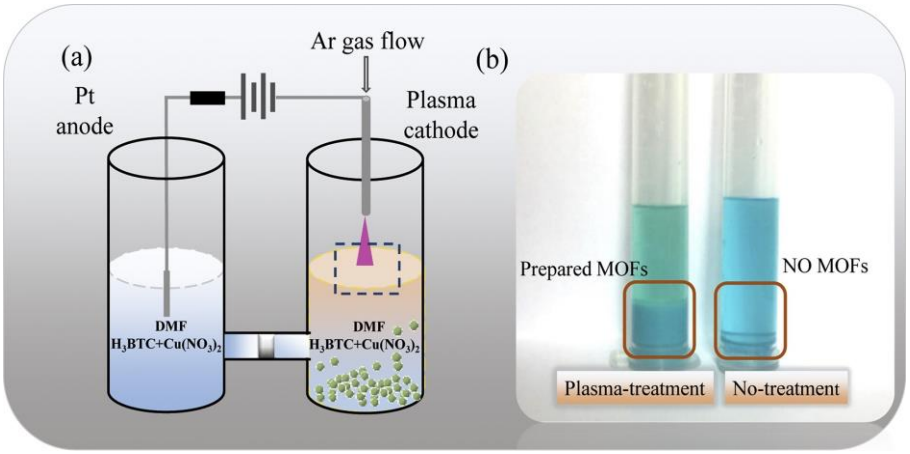

Fig. 2.29: Preparation of MOF through electrochemical method [157]

(3) Microwave method [158-160] utilizes microwave radiation for rapid MOF preparation, as shown in Fig. 2.30. Localized overheating can create hot spots that act as nucleation sites, producing products similar to those from solvothermal methods. This method offers advantages such as high efficiency, controllable structures, small particle size, good selectivity, fast reactions, and environmental friendliness. The morphology and crystal size of MOFs are closely related to the initial concentration and reaction time.

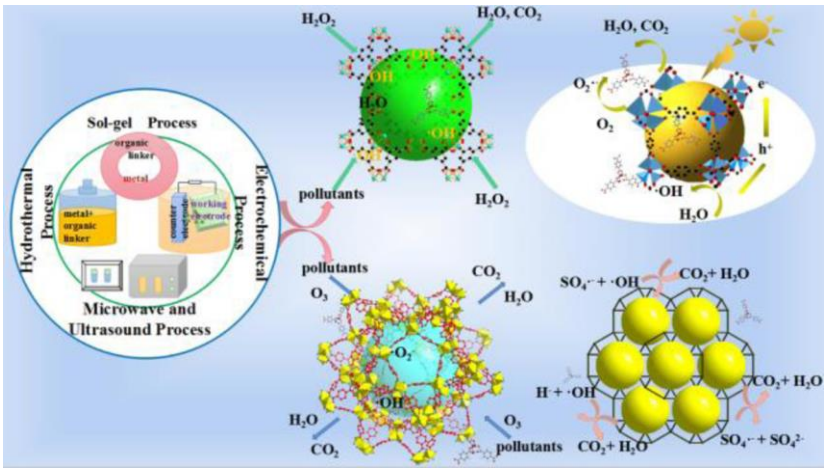

Fig. 2.30: Preparation of MOF through microwave method [158]

(4) Sonochemical method [161, 162] employs ultrasound to activate chemical reactions, effectively promoting interactions between metal ions and organic ligands, as indicated in Fig. 2.31. This method significantly shortens the crystallization period of MOFs, facilitating rapid and uniform nucleation to produce MOFs with consistent size and high crystallinity. However, volatile solvents should be avoided during the preparation process.

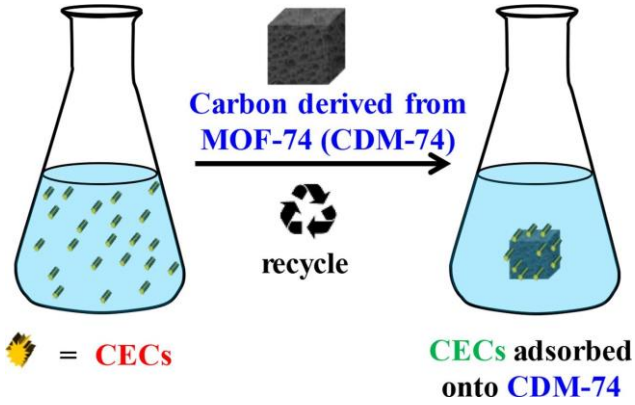

Fig. 2.31: Preparation of MOF through microwave method [162]

2.4.4.2 Electrochemical sensing applications of metal-organic frameworks. Although MOFs demonstrate significant potential in various fields [163-166], their limited conductivity has been a major barrier to their use as electrode materials in electrochemical devices, resulting in relatively fewer studies and reports in electrochemical sensing. To overcome this limitation, strategies of integrating MOFs with highly conductive materials to form composites have been explored [167-169], expanding the applications of MOFs via significant enhancement of their conductivity. By designing composite materials, MOFs are expected to be explored more extensively and deeply in the field of electrochemical sensing.

Compared to single-metal MOFs, the optimized bimetallic MOFs exhibit superior performance [170]. They have been applied in constructing enzyme-free electrochemical sensors for detecting various small biomolecules. For instance, Huang's group [171] studied cobalt-doped nickel-MOFs, which were used to construct an electrochemical sensor for detecting L-tryptophan (Trp), as indicated in Fig. 2.32. After detailed optimization of the ratio, Co-Ni-MOFs-1% demonstrate high catalytic activity in Trp oxidation.

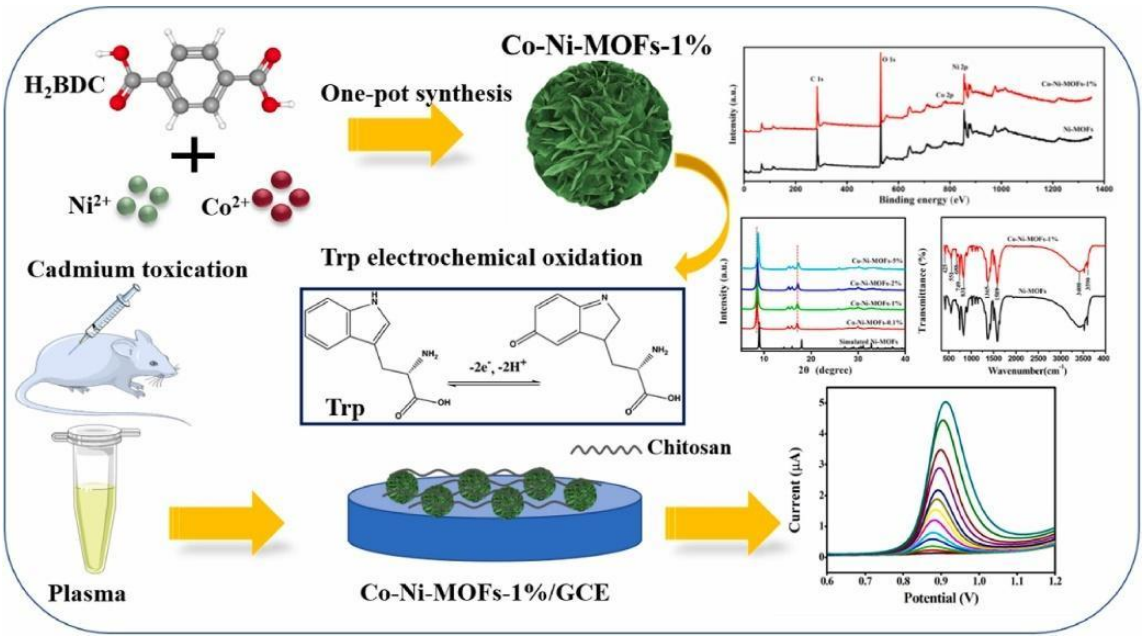

Fig. 2.32: Preparation of Co-Ni-MOF-1% for sensing of Trp [171]

Combining graphene and its derivatives with MOFs can enhance the performance of MOFs [172, 173]. Composites of MOFs with graphene and its derivatives have been used in sensor construction.As indicated in Fig. 2.33, Dong et.al [174] synthesized a composite of ZIF-67 with reduced graphene oxide (ZIF-67/rGO) for detecting hydrogen peroxide and dopamine. The synergistic effect between ZIF-67 and rGO resulted in excellent electrochemical performance for the detection of hydrogen peroxide and dopamine.

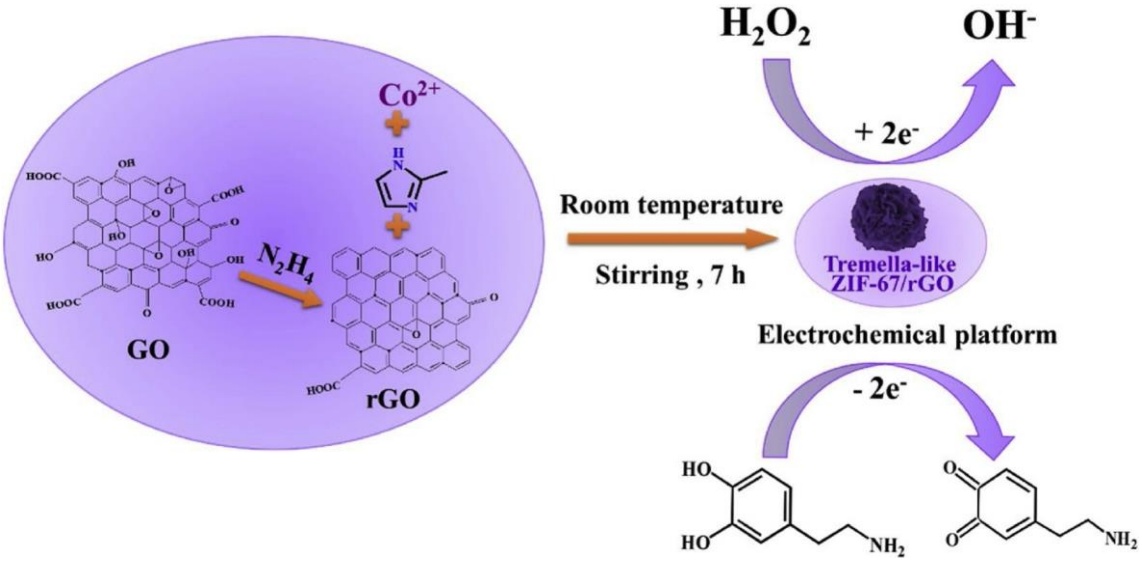

Fig. 2.33: Preparation of ZIF-67/rGO for sensing of DA [174]

Guo et al. [175] prepared JUC-62@pOMC composites via a simple one-step solvothermal reaction. The synergistic effect between JUC-62 and pOMC demonstrated excellent electrochemical catalytic performance, as shown in Fig. 2.34. The results showed that JUC-62@pOMC/GCE exhibited higher potentials and current responses in the reduction of nitroaromatic compounds, with good linear ranges and lower detection limits for the individual detection of five nitroaromatic compounds, surpassing most previously reported catalysts.

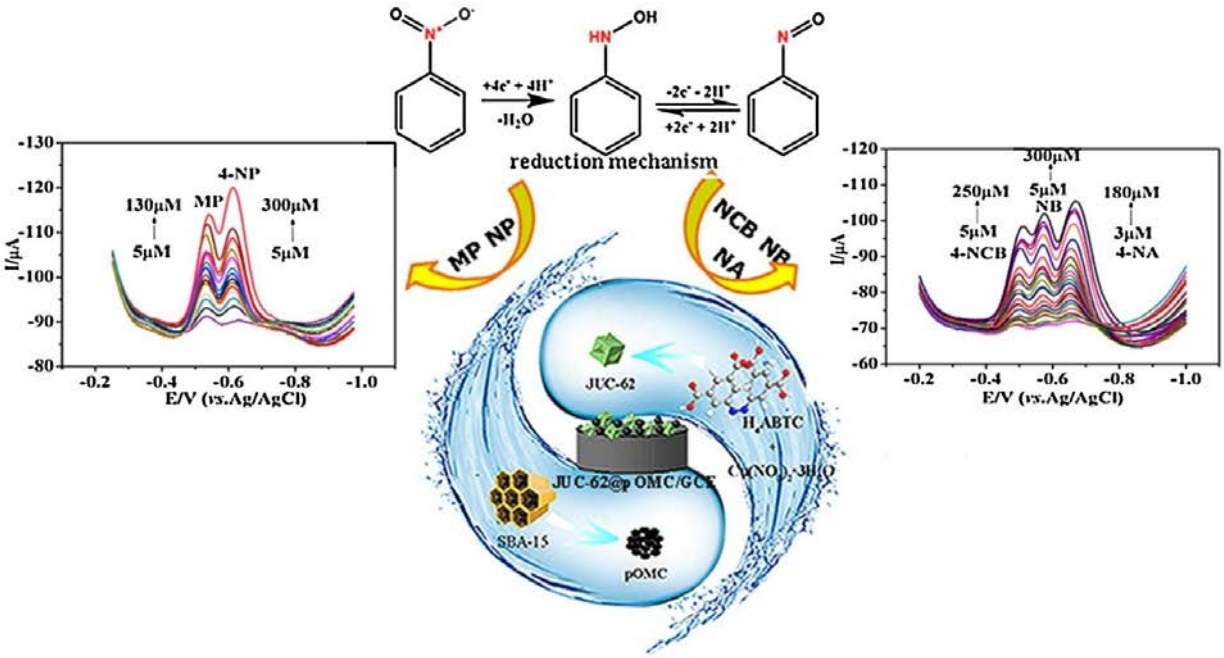

Fig. 2.34: Preparation of JUC-62@pOMC for detection of nitroaromatic [175]

2.5 Conclusion

Carbon-based nanomaterials exhibit unique advantages such as distinctive nanostructures, excellent biocompatibility, abundant active sites, and strong catalytic capabilities. Therefore, they play a crucial role in the development of novel nanocomposites and biosensing research. Carbon-based nanocomposites, formed by combining with other nanomaterials, not only retain their inherent excellent properties but also enhance the electrocatalytic activity and achieve precise targeting in sensing applications.

In recent years, carbon-based electrochemical sensors designed for detecting small biomolecules have faced several challenges. Firstly, achieving rapid, reliable, and highly sensitive detection requires careful

selection and optimization of electrode materials to design superior functional nanocomposites. Secondly, enhancing detection stability and interference resistance is crucial for enabling rapid detection of small biomolecules in complex samples. Additionally, simultaneous detection and dynamic analysis of multiple small biomolecules in complex biological systems are highly desirable to broaden the application scope. Therefore, the development of advanced nanomaterials for electrode modification has been brought into focus to meet various detection requirements.

References

1. Wang, Y.; Li, Y.M.; Tang, L.H.; Lu, J.; Li, J.H. Application of Graphene-Modified Electrode for Selective Detection of Dopamine. *Electrochem. Commun.* **2009**, *11*, 889-892.
2. He, W.Z.; Liu, R.T.; Zhou, P.; Liu, Q.Y.; Cui, T.H. Flexible Micro-Sensors with Self-Assembled Graphene on a Polyolefin Substrate for Dopamine Detection. *Biosens. Bioelectron.* **2020**, *167*, 112473.
3. Wang, J.; Yang, B.B.; Zhong, J.T.; Yan, B.; Zhang, K.; Zhai, C.Y.; Shiraishi, Y.; Du, Y.K.; Yang, P. Dopamine and Uric Acid Electrochemical Sensor Based on a Glassy Carbon Electrode Modified with Cubic Pd and Reduced Graphene Oxide Nanocomposite. *J. Colloid Interf. Sci.* **2017**, *497*, 172-180.
4. Shahrokhian, S.; Ghalkhani, M.; Amini, M.K. Application of Carbon-Paste Electrode Modified with Iron Phthalocyanine for Voltammetric Determination of Epinephrine in the Presence of Ascorbic Acid and Uric Acid. *Sensor. Actuat. B-Chem.* **2009**, *137*, 669-675.
5. Vishnu, N.; Badhulika, S. Single Step Grown MoS_2 on Pencil Graphite as an Electrochemical Sensor for Guanine and Adenine: A Novel and Low Cost Electrode for DNA Studies. *Biosens. Bioelectron.* **2019**, *124*, 122-128.
6. Ng, K.L.; Khor, S.M. Graphite-Based Nanocomposite Electrochemical Sensor for Multiplex Detection of Adenine, Guanine, Thymine, and Cytosine: a Biomedical Prospect for Studying DNA Damage. *Anal. Chem.* **2017**, *89*, 10004-10012.

7. Ensafi, A.A.; Abarghoui, M.M.; Rezaei, B. A New Electrochemical Sensor Based on Porous Silicon Supported Pt–Pd Nanoalloy for Simultaneous Determination of Adenine and Guanine. *Sensor. Actuat. B: Chem.* **2014**, *204,* 528-535.

8. Kato, D.; Sumimoto, M.; Ueda, A.; Hirono, S.; Niwa, O. Evaluation of Electrokinetic Parameters for All DNA Bases with Sputter Deposited Nanocarbon Film Electrode. *Anal. Chem.* **2012**, *84*, 10607-10613.

9. Post, M.R.; Lee, W.L.; Guo, J.; Sames, D.; Sulzer, D. Development of a Dual Fluorescent and Magnetic Resonance False Neurotransmitter That Reports Accumulation and Release from Dopaminergic Synaptic Vesicles. *ACS Chem. Neurosci.* **2021**, *12*, 4546-4553.

10. Bostick, D.T.; Hercules, D.M. Quantitative Determination of Blood Glucose Using Enzyme Induced Chemiluminescence of Luminol. *Anal. Chem.* **1975**, *47*, 447-452.

11. Wightman, R.M.; May, L.J.; Michael, A.C. Detection of Dopamine Dynamics in the Brain. *Anal. Chem.* **1988**, *60*, 769A-793A.

12. Xie, W.Y.; Yin, Y.Y.; Gu, R.H.; Xu, J.Y.; Su, X.; Wang, Y.; Liu, R.A.; Liu, X.Z.; Huang, J.Y. Label-Free and Highly Selective MOFs-Based Dopamine Detection in Urine of Parkinson's Patients. *Chem. Eng. J.* **2022**, *443*, 136371.

13. Savransky, A.; Chiappelli, J.; Du, X.M.; Carino, K.; Kvarta, M.; Bruce, H.; Kochunov, P.; Goldwaser, E.; Tan, Y.L.; Hare, S.; Hong, L.E. Association of Working Memory and Elevated Overnight Urinary Norepinephrine in Patients with Schizophrenia. *J. Psychiatr. Res.* **2021**, *137*, 89-95.

14. Lee, H.; Hong, Y.J.; Baik, S.; Hyeon, T.; Kim, D.H. Enzyme-Based Glucose Sensor: from Invasive to Wearable Device. *Adv. Healthc. mater.* **2018**, *7*, 1701150.

15. Adeel, M.; Rahman, M.M.; Caligiuri, I.; Canzonieri, V.; Rizzolio, F.; Daniele, S. Recent Advances of Electrochemical and Optical Enzyme-Free Glucose Sensors Operating at Physiological Conditions. *Biosens. Bioelectron.* **2020**, *165*, 112331.

16. Wei, M.; Qiao, Y.X.; Zhao, H.T.; Liang, J.; Li, T.S; Luo, Y.L.; Lu, S.Y.; Shi, X.F.; Lu, W.B.; Sun, X.P. Electrochemical Non-Enzymatic Glucose Sensors: Recent Progress and Perspectives. *Chem. Commun.* **2020**, *56*, 14553-14569.

17. Lovic, D.; Piperidou, A.; Zografou, A.M.A. The Growing Epidemic of Diabetes Mellitus. *Curr. Vasc. pharmacol.* **2020**, *18*, 104-109.

18. Nery, E.W.; Kundys, M.; Jelen, P.S.; Jönsson-Niedziólka, M. Electrochemical Glucose Sensing: Is There Still Room for Improvement. *Anal. Chem.* **2016**, *88*, 11271-11282.

19. Annalakshmi, M.; Kumaravel, S.; Chen, T.W.; Chen, S.M.; Lou, B.S. 3D Flower-like NiCo Layered Double Hydroxides: An Efficient Electrocatalyst for Non-Enzymatic Electrochemical Biosensing of Hydrogen Peroxide in Live Cells and Glucose in Biofluids. *ACS Appl. Bio Mater*. **2021**, *4*, 3203-3213.

20. Dong, Q.Y.; Yang, L.; He, Z.Y.; Zhang, Y.; Tang, X.; Tang, J.Y.; Huang, K.; Zou, Z.R.; Xiong, X.L. Co-Based Transition Metal Hydroxide Nanosheet Arrays on Carbon Cloth for Sensing Glucose and Formaldehyde. *ACS Appl. Nano Mater.* **2021**, *4*, 5076-5083.

21. Montezano, A.C.; Dulak, L.M.; Tsiropoulou, S.; Harvey, A.; Briones, A.M.; Touyz, R.M. Oxidative Stress and Human Hypertension: Vascular Mechanisms, Biomarkers, and Novel Therapies. *Can. J. Cardiol.* **2015**, *31*, 631-641.

22. Sies, H. Hydrogen Peroxide as a Central Redox Signaling Molecule in Physiological Oxidative Stress: Oxidative Eustress. *Redox Biol.* **2017**, *11*, 613-619.

23. Mohammadi, S.S.; Vaezi, Z.; Hossein, N.M. Chemiluminescent Liposomes as a Theranostic Carrier for Detection of Tumor Cells Under Oxidative Stress. *Anal. Chim. Acta* **2019**, *1059*, 113-123.

24. Daemi, S.; Ghasemi, S.; Ashkarran, A.A. Electrospun CuO-ZnO Nanohybrid: Tuning the Nanostructure for Improved Amperometric Detection of Hydrogen Peroxide as a Non-Enzymatic Sensor. *J. Colloid Interface Sci.* **2019**, *550*, 180-189.

25. Liu, H.; Chen, Q.; Cheng, X.; Wang, Y.; Zhang, Y.; Fan, G. Sustainable and Scalable In-Situ Fabrication of Au Nanoparticles and Fe_3O_4 Hybrids as Highly Efficient Electrocatalysts for the EnzymeFree Sensing of H_2O_2 in Neutral and Basic Solutions. *Sensor. Actuat. B: Chem.* **2020**, *314*, 128067.

26. Kanjana K.; Traipop S.; Chailapakul O.; Chuanuwatanakul, S. Simultaneous Determination of Ascorbic Acid, Dopamine, and Uric Acid Using Graphene Quantum Dots/Ionic Liquid Modified Screen-Printed Carbon Electrode. *Sensor. Actuat. B-Chem.* **2020**, *314*, 128059.

27. Gupta, P.; Tsai, K.; Ruhunage, C.K.; Gupta, V.K.; Rahm, C.E.; Jiang, D.H.; Alvarez, N.T. True Picomolar Neurotransmitter Sensor Based on Open-Ended Carbon Nanotubes. *Anal. Chem.* **2020**, *92*, 8536-8545.

28. Lei, P.; Zhou, Y.; Zhu, R.Q.; Liu, Y.; Dong, C.; Shuang, S.M. Facile Synthesis of Iron Phthalocyanine Functionalized N,B-Doped Reduced Graphene Oxide Nanocomposites and Sensitive Electrochemical Detection for Glutathione. *Sensor. Actuat. B-Chem.* **2019**, *297*, 126756.

29. Yang, T.; Chen, M.J.; Nan, F.X.; Chen, L.H.; Luo, X.L.; Jiao, K. Enhanced Electropolymerization of Poly(xanthurenic acid)-MoS2 Film for Specific Electrocatalytic Detection of Guanine and Adenine. *J. Mater. Chem. B* **2015**, *3*, 4884-4891.

30. Waqas, M.; Wu, L.Y.; Tang, H.G.; Liu, C.Z.; Fan, Y.J.; Jiang, Z.; Wang, X.Q.; Zhong, J.P.; Chen, W. Cu_2O Microspheres Supported on Sulfur-Doped Carbon Nanotubes for Glucose Sensing. *ACS Appl. Nano Mater.* **2020**, *3*, 4788-4798.

31. Ji, W.; Wu, D.Q.; Tang, W.; Xi, X.; Su, Y.Z.; Guo, X.J.; Liu, R.L. Carbonized Silk Fabric-Based Flexible Organic Electrochemical Transistors for Highly Sensitive and Selective Dopamine Detection. *Sensor. Actuat. B-Chem.* **2020**, *304*, 127414.

32. Lin, Y.J.; Huang, X.Q.; Hu, L.P.; Zhou, H.L.; Yang, A.N.; Xu, J.; Chen, W.J.; Zeng, X.Y.; Sun, P.H.; Zhong, X. Self-Assembly MoS_2@MnO_2 Nanoflowers for the Fluorescence/Magnetic Resonance Dual-Modal Sensing of H_2O_2 and Photothermal Therapy. *ACS Appl. Nano Mater.* **2023**, *6*, 22265-22274

33. Fang, C.; Deng, Q.; Zhao, K.C.; Zhou, Z.L.; Zhu, X.H.; Liu, F.; Yin, P.; Liu, M.L.; Li, H.T.; Zhang, Y.Y.; Yao, S.Z. Fluorescent Probe for Investigating the Mitochondrial Viscosity and Hydrogen Peroxide Changes in Cerebral Ischemia/Reperfusion Injury. *Anal. Chem.* **2024**, *96*, 3436-3444.

34. Rodiguez, A.; Gomila, R.M.; Martorell, G.; Costa-Bauza, A.; Grases, F. Quantification of Xanthine- and Uric Acidrelated Compounds in Urine Using a “Dilute-and-Shoot” Technique Coupling Ultra-High-Performance Liquid Chromatography and High-Resolution Orbitrap Mass Spectrometry. *J. Chromatogr. B* **2017**, *1067*, 53-60.

35. Habib, A.; Mabrouk, M.M.; Fekry, M.; Mansour, F.R. Glycerol as a New Mobile Phase Modifier for Green Liquid Chromatographic Determination of Ascorbic Acid and Glutathione in Pharmaceutical Tablets. *Journal of Pharm. Biomed. Anal*. **2022**, *219*, 114870.

36. Yu, S.L.; Yin, Y.C.; Li, Q.Q.; Yu, J.L.; Liu, W.J.; Wang, D.C.; Cheng, Q.; Xie, S.W.; Cheng, X.Q.; Qiu, L. Validation of an Improved Liquid Chromatography Tandem Mass Spectrometry Method for Rapid and Simultaneous Analysis of Plasma Catecholamine and Their Metabolites. *J. Chromatogr. B* **2019**, *1129*, 121805.

37. Lores-Padín, A.; Menero-Valdés, P.; Fernández, B.; Pereiro, R. Nanoparticles as Labels of Specific-Recognition Reactions for the Determination of Biomolecules by Inductively Coupled Plasma-Mass Spectrometry. *Anal. Chim. Acta* **2020**, *1128*, 251-268.

38. Liu, Z.R.; Li, X.T.; Xiao, G.Y.; Chen, B.B.; He, M.; Hu, B. Application of Inductively Coupled Plasma Mass Spectrometry in the Quantitative Analysis of Biomolecules with Exogenous Tags: a Review. *Trends Anal. Chem.* **2017**, *93*, 78-101.

39. Xing, Y.Y.; Chen, M.L.; Zhao, Y.K.; Xu, J.B.; Hou, X.H. Triple-Enzyme Mimetic Activity of Fe_3O_4@C@MnO_2 Composites Derived from Metal-Organic Frameworks and Their Application to Colorimetric Biosensing of Dopamine. *Microchim. Acta* **2021**, *189*, 1-10.

40. Liu D.L.; Chen G.F.; Fang G.Q. A Near-Infrared, Colorimetric and Ratiometric Fluorescent Sensor with High Sensitivity to Hydrogen Peroxide and Viscosity for Solutions Detection and Imaging Living Cells. *Bioorg. Chem.* **2022**, *119*, 105513.

41. Zhang, W.C.; Sharma, G.; Kumar, A.; Shekh, M.I.; Stadler, F.J. Fabrication and Characterization of Ni/Ag/Zn Trimetal Oxide Nanocomposites and Its Application in Dopamine Sensing. *Mater. Today Commun.* **2021**, *29*, 102726.

42. Liu, Y.D.; Liu, X.H.; Guo, Z.P.; Hu, Z.G.; Xue, Z.H.; Lu, X.Q. Horseradish Peroxidase Supported on Porous Graphene as a Novel Sensing Platform for Detection of Hydrogen Peroxide in Living Cells Sensitively. *Biosens. Bioelectron.* **2017**, *87*, 101-107.

43. Ye, M.F.; Yang, C.; Sun, Y.; Wang, J.Y.; Wang, D.D.; Zhao, Y.J.; Zhu, Z.; Liu, P.C.; Zhu, J.H.; Li, C.S.; Peng, W.X.; Zhang, N.; Dong, Y.P. $ZnFe_2O_4$/Graphitic Carbon Nitride

Nano/Microcomposites for the Enhanced Electrochemical Sensing of H_2O_2. *ACS Appl. Nano Mater.* **2022**, *5*, 10922-10932.

44. Fatima, B.; Hussain, D.; Bashir, S.; Hussain, H.T.; Aslam, R.; Nawaz, R.; Rashid, H.N.; Bashir, N.; Majeed, S.; Ashiq, M.N.; Najam-ul-Haq, M. Catalase Immobilized Antimonene Quantum Dots Used as an Electrochemical Biosensor for Quantitative Determination of H_2O_2 from CA-125 Diagnosed Ovarian Cancer Samples. *Mat. Sci. Eng. C-Mater.* **2020**, *117*, 111296.

45. Luo, C.X.; Liu, X.H.; Liu, F.X.; He, N.; Yu, R.; Liu, X.H. AgNPs Doping the Fold Carbon Nanoflower Composite for Highly Sensitive Electrochemical Detection of Hydrogen Peroxide. *J. Electroanal. Chem*. **2022**, *904*, 115930.

46. Jia, D.L.; Li, Z.; Ma, H.Y.; Ji, H.Y.; Qi, H.L.; Zhang, C.X. Near-Infrared Fluorescence Probe with a New Recognition Moiety for the Specific Detection of Cysteine to Study the Corresponding Physiological Processes in Cells, Zebrafish, and Arabidopsis Thaliana. *Anal. Chem.* **2024**, *96*, 6030-6036.

47. Li, N.; Li, X.P.; Li, J.J.; Li, Y.; Zhang, T. An AND-Gate Photoacoustic Probe for Cys and H_2S Precise Photoacoustic Sensing in Localized Tumors. *Anal. Chem.* **2024**, *96*, 7342-7347.

48. Guo, H.L.; Chen, G.; Gao, M.; Wang, R.; Liu, Y.X.; Yu, F.B. Imaging of Endogenous Hydrogen Peroxide during the Process of Cell Mitosis and Mouse Brain Development with a Near-Infrared Ratiometric Fluorescent Probe. *Anal. Chem.* **2019**, *91*, 1203-1210.

49. Zhao, X.J.; Wang, N.; Zhang, M.J.; Liu, S.S.; Yu, H.; Tang, M.H.; Liu, Z.Y. Simultaneous Determination of Five Amino Acid Neurotransmitters in Rat and Porcine Blood and Brain by Two-Dimensional Liquid Chromatography. *J. Chromatogr. B* **2021**, *1163*, 122507.

50. Fang, W.L.; Xia, L.J.; Huang, X.; Guo, X.F.; Ding, J.; Wang, H.; Feng, Y.Q. Highly Sensitive Determination for Catecholamines Using Boronate Affinity Polymer Monolith Microextraction with In-Situ Derivatization and HPLC Fluorescence Detection. *Chromatographia* **2018**, *81*, 1381-1389.

51. De Silva, D.; Liu, Y.; A Smit, M.; Vandenberg, A.; Zhang, H.X. Distribution of Vicine, Convicine and Levodopa in Faba Bean Plant Tissues Determined by UltraHigh Performance Liquid

Chromatography-Electrospray Ionization Mass Spectrometry. *J. Chromatogr. Open* **2024**, *5*, 100127.

52. Chio, W.I.K.; Davison, G.; Jones, T.; Liu, J.; Parkin, I.P.; Lee, T.C. Quantitative SERS Detection of Uric Acid via Formation of Precise Plasmonic Nanojunctions within Aggregates of Gold Nanoparticles and Cucurbit[n]uril. *Jove-J. Vis. Exp.* **2020**, *164*, 61682.

53. Bhattacharjee, G.; Majumder, S.; Senapati, D.; Banerjee, S.; Satpati, B. Core-Shell Gold @Silver Hollow Nanocubes for Higher SERS Enhancement and Non-Enzymatic Biosensor. *Mater. Chem. Phys.* **2020**, *239*, 122113.

64. Sun X. Glucose Detection Through Surface-Enhanced Raman Spectroscopy: A Review. *Anal. Chim. Acta* **2022**, *1206*, 339226.

65. Lu, D.C.; Fan, M.; Cai R.Y.; Huang, Z.F.; You, R.Y.; Huang, L.Q.; Feng, S.Y.; Lu, Y.D. Silver Nanocube Coupling with a Nano Porous Silver Film for Dual-Molecule Recognition based Ultrasensitive SERS Detection of Dopamine. *Analyst* **2020**, *145*, 3009-3016.

66. Devi, N.R.; Sasidharan, M.; Sundramoorthy, A.K. Gold Nanoparticles-Thiol-Functionalized Reduced Graphene Oxide Coated Electrochemical Sensor System for Selective Detection of Mercury Ion. *J. Electrochem. Soc.* **2018**, *165*, 3046-3053.

67. Zhang, W.C.; Sharma, G.; Kumar, A.; Shekh, M.I.; Stadler, F.J. Fabrication and Characterization of Ni/Ag/Zn Trimetal Oxide Nanocomposites and Its Application in Dopamine Sensing. *Mater. Today Commun.* **2021**, *29*, 102726.

68. Rostami, S.; Mehdinia, A.; Niroumand, R.; Jabbari, A. Enhanced LSPR Performance of Graphene Nanoribbons-Silver Nanoparticles Hybrid as a Colorimetric Sensor for Sequential Detection of Dopamine and Glutathione. *Anal. Chim. Acta* **2020**, *1120*, 11-23.

69. Lee, P.C.; Li, N.S.; Hsu, Y.P.; Peng, C.; Yang, H.W. Direct Glucose Detection in Whole Blood by Colorimetric Assay Based on Glucose Oxidase-Conjugated Graphene Oxide/MnO_2 nanozymes. *Analyst* **2019**, *144*, 3038-3044.

70. Liang, M.M.; Jia, S.P.; Zhu, S.C.; Guo, L.H. Photoelectrochemical Sensor or the Rapid Detection of in situ DNA Damage Induced by Enzyme-Catalyzed Fenton Reaction. *Environ. Sci. Technol*. **2008**, *42*, 635-639.

71. Tiwari, J.N.; Vij, V.; Kemp, K.C.; Kim, K.S. Engineered Carbon-Nanomaterial-Based Electrochemical Sensors for Biomolecules. *ACS Nano* **2016**, *10*, 46-80.

72. Zhao, Q.; Faraj, Y.; Liu, L.Y.; Wang, W.; Xie, R.; Liu, Z.; Ju, X.J.; Wei, J.; Chu, L.Y. Simultaneous Determination of Dopamine, Uric Acid and Estriol in Maternal Urine Samples Based on the Synergetic Effect of Reduced Graphene Oxide, Silver Nanowires and Silver Nanoparticles in Their Ternary 3D Nanocomposite. *Microchem. J.* **2020,** *158*, 105185.

73. Quan, D.P.; Thao, B.T.P.; Trang, N.V.; Huy, N.L.; Dung, N.Q.; Ahmed, M.U.; Lam, T.D. The Role of Copper Nanoparticles Decorating Polydopamine/Graphene Film as Catalyst in the Enhancement of Uric Acid Sensing. *J. Electroanal. Chem.* **2021**, *893*, 115322.

74. Kokulnathan, T.; Ahmed, F.; Chen, S.M.; Chen, T.W.; Hasan, P.M.Z.; Bilgrami, A.L.; Darwesh, R. Rational Confinement of Yttrium Vanadate Within Three-Dimensional Graphene Aerogel: Electrochemical Analysis of Monoamine Neurotransmitter (Dopamine). *ACS Appl. Mater. Interfaces* **2021**, *13*, 10987-10995.

75. Prodromidis, M.I. Impedimetric Immunosensors-A Review. *Electrochim. Acta* **2010**, *55*, 4227-4233.

76. Zdrachek, E.; Bakker, E. Potentiometric Sensing. *Anal. Chem.* **2018**, *91*, 2-26.

77. Hoyos-Arbeláez, J.; Vázquez, M.; Contreras-Calderón, J. Electrochemical Methods as a Tool for Determining the Antioxidant Capacity of Dood and Beverages: A Review. *Food Chem.* **2017**, *221*, 1371-81.

78. Bai, J.; Wang, X.J.; Meng, Y.N.; Zhang, H.M.; Qu, L.T. Fabrication of Graphene Coated Carbon Fiber Microelectrode for Highly Sensitive Detection Application. *Anal. Sci.* **2014**, *30(9)*, 903-909.

79. Manna, S.; Sharma, A.; Satpati, A.K. Electrochemical Methods in Understanding the Redox Processes of Drugs and Biomolecules and Their Sensing. *Curr. Opin. Electrochem.* **2022**, *32*, 100886.

80. Chen, Y.; Zhao, P.; Liang, Y. A Sensitive Electrochemical Sensor Based on 3D Porous Melamine-Doped rGO/MXene Composite Aerogel for the Detection of Heavy Metal Ions in the Environment. *Talanta* **2023**, *256*, 124294.

81. Stradiotto, N.R.; Yamanaka, H.; Zanoni, M.V.B. Electrochemical Sensors: A Powerful Tool in Analytical Chemistry. *J. Brazil. Chem. Soc.* **2003**, *14*, 159-173.

82. Kim, S.K.; Lee, G.H.; Jeon, C.; Bimetallic Nanocatalysts Immobilized in Nanoporous Hydrogels for Long-Term Robust Continuous Glucose Monitoring of Smart Contact Lens. *Adv. Mater.* **2022**, e2110536.

83. Soto, D.; Alzate, M.; Gallego, J. Hybrid Nanomaterial/Catalase-Modified Electrode for Hydrogen Peroxide Sensing. *J. Electroanal. Chem.* **2021**, *880*, 114826.

84. Liang, M.M.; Jia, S.P.; Zhu, S.C.; Guo, L.H. Photoelectrochemical Sensor or the Rapid Detection of in situ DNA Damage Induced by Enzyme-Catalyzed Fenton Reaction. *Environ. Sci. Technol*. **2008**, *42*, 635-639.

85. Fatima, B.; Hussain, D.; Bashir, S. Catalase Immobilized Antimonene Quantum Dots Used as an Electrochemical Biosensor for Quantitative Determination of H_2O_2 from CA-125 Diagnosed Ovarian Cancer Samples. *Mater. Sci. Eng. C* **2020**, *117*, 111296.

86. Chen, P.; Hua, X.; Liu, J. A Dual Amplification Electrochemical Immunosensor Based on HRPAu@Ag NPs for Carcinoembryonic Antigen Detection. *Anal. Biochem.* **2019**, *574*, 23-30.

87. Yang, Y.; Wei H.; Wang X. MOF/COF Heterostructure Hybrid Composite-Based Molecularly Imprinted Photoelectrochemical Sensing Platform for Determination of Dibutyl Phthalate: A Further Expansion for MOF/COF Application. *Biosens. Bioelectron.* **2023**, *223*, 115017.

88. Mohan, B.; Kumari, R.; Virender.; Singh, K.; Pombeiro, A.J.L.; Yang, X.M.; Ren, P. Covalent Organic Frameworks (COFs) and Metalorganic Frameworks (MOFs) as Electrochemical Sensors for the Efficient Detection of Pharmaceutical Residues. *Environ. Int.* **2023**, *175*, 107928.

89. Lee, J.; Farha, O.K.; Roberts, J.; Scheidt, K.A.; Hupp, J.T. Metal-Organic Framework Materials as Catalysts. *Chem. Soc. Rev*. **2009**, *38*, 1450-1459.

90. Radhika, M.G.; Byatarayappa, G.; Ingale, D.V.; Bhatta, L.K.G.; Venkatesh, K.; Kamath, M.K.S.; Nagaraju, K. High Performance of Asymmetric Coin Cells Designed Using Optimized Weight Percentage of Multiwalled Carbon Nanotubes in Ni/Co-MOFs Nanocomposites. *Mater. Res. Bull.* **2022**, *156*, 111996.

91. Abdel-Salam, A.I.; Awad, M.M.; Soliman, T.S.; Khalid, A. The Effect of Graphene on Structure and Optical Properties of CdSe Nanoparticles for Optoelectronic Application. *J. Alloys Compd.* **2022**, *898*, 162946.

92. Wu, H.R.; Wang, J.J.; Yang, Q.; Qin, S.X.; Li, Z.X.; Zhang, Y.; Pan, J.Q.; Li, C.R. Ultrasensitive and Stable SERS Detection by Defect Engineering Constructed Ag@Ga-doped ZnO Core-Shell Nanoparticles. *Appl. Surf. Sci.* **2023**, *621*, 156873.

93. Zhu, C.Z.; Yang, G.H.; Li, H.; Du, D.; Lin, Y.H. Electrochemical Sensors and Biosensors Based on Nanomaterials and Nanostructures. *Anal. Chem.* **2015**, *87*, 230-49.

94. Hu, W.H.; Li, C.M. Nanomaterial-Based Advanced Immunoassays. *Wires. Nanomed. Nanobi.* **2011**, *3*, 119-33.

95. Zhong, Z.Y.; Wu, W.; Wang, D.; Wang, D.; Shan, J.L.; Qing, Y.; Zhang, Z.M. Nanogold-Enwrapped Graphene Nanocomposites as Trace Labels for Sensitivity Enhancement of Electrochemical Immunosensors in Clinical Immunoassays: Carcinoembryonic Antigen as a Model. *Biosens. Bioelectron.* **2010**, *25*, 2379-2783.

96. Zhang, J.; Ting, B.P.; Khan, M.; Pearce, M.C.; Yang, Y.Y.; Gao, Z.Q.; Ying, J.Y. Pt Nanoparticle Label-Mediated Deposition of Pt Catalyst for Ultrasensitive Electrochemical Immunosensors. *Biosens. Bioelectron.* **2010**, *26*, 418.

97. Yang, L.Q.; Huang, N.; Lu, Q.J.; Liu, M.L.; Li, H.T.; Zhang, Y.Y.; Yao, S.Z. A Quadruplet Electrochemical Platform for Ultrasensitive and Simultaneous Detection of Ascorbic Acid, Dopamine, Uric Acid and Acetaminophen Based on a Ferrocene Derivative Functional Au NPs/Carbon Dots Nanocomposite and Graphene. *Anal. Chim. Acta* **2016**, *903*, 69-80.

98. Cheng, J.Y.; Wang, X.D.; Nie, T.Y.; Yin, L.; Wang, S.M.; Zhao, Y.C.; Wu, H.M.; Mei, H. A Novel Electrochemical Sensing Platform for Detection of Dopamine Based on Gold Nanobipyramid/Multi-Walled Carbon Nanotube Hybrids. *Anal. Bioanal. Chem.* **2020**, *412*, 2433-2441.

99. Wu, R.; Yu, S.; Chen, S.Y.; Dang, Y.; Wen, S.H.; Tang, J.L.; Zhou, Y.Z.; Zhu, J.J. A Carbon Dots-Enhanced Laccase-Based Electrochemical Sensor for Highly Sensitive Detection of Dopamine in Human Serum. *Anal. Chim. Acta* **2022**, *1229*, 340365.

100. Silva, V.N.C.; Farias, E.A.D.; Araújo, A.R.; Magalhaes, F.E.X.; Fernandes, J.R.N.; Souza, J.M.T.; Eiras, C.; da Silva, D.A.; Bastos, V.H.D.; Teixeira, S.S. Rapid and Selective Detection of Dopamine in Human Serum Using an Electrochemical Sensor Based on Zinc Oxide Nanoparticles, Nickel Phthalocyanines, and Carbon Nanotubes. *Biosens. Bioelectron.* **2022**, *210*, 114211.

101. Novoselov, K.S.; Geim, A.K.; Morozov, S.V.; Jiang, D.; Zhang, Y.; Dubonos, S.V.; Grigorieva, I.V.; Firsov, A.A. Electric Field Effect in Atomically Thin Carbon Films. *Science* **2004**, *306*, 666-669.

102. Jiang, Z.X.; Feng, B.; Xu, J.; Qing, T.P.; Zhang, P.; Qing, Z.H. Graphene Biosensors for Bacterial and Viral Pathogens. *Biosens. Bioelectron.* **2020**, *166*, 112471.

103. Zhang, T.; Xue, Q.Z.; Zhang, S.; Dong, M.D. Theoretical Approaches to Graphene and Graphene-Based Materials. *Nano Today* **2012**, *7*, 180-200.

104. Edwards, R.S.; Coleman, K.S. Graphene Synthesis: Relationship to Applications. *Nanoscale* **2013**, *5*, 38-51.

105. Bhuyan, M.S.A.; Uddin, M.N.; Islam, M.M.; Bipasha, F.A.; Hossain, S.S. Synthesis of Graphene. *International Nano Letters* **2016**, *6*, 65.

106. Zhang, Y.B.; Small, J.P.; Pontius, W.V.; Kim, P. Fabrication and Electric-Field-Dependent Transport Measurements of Mesoscopic Graphite Devices. *Appl. Phys. Lett*. **2005**, *86*, 073104.

107. Rao, C.; Sood, A. Graphene: Synthesis, Properties and Phenomena. *Wiley-VCH Verlag GmbH & Co. KGaA* **2012**, 49-90.

108. Wu, Y.H.; Yu, T.; Shen, Z.X. Two-Dimensional Carbon Nanostructures: Fundamental Properties, Synthesis, Characterization, and Potential Applications. *J. Appl. Phys.* **2010**, *108*, 1301-1338.

109. Zhu, Y.W.; Murali, S.; Cai, W.W.; Li, X.S.; Suk, J.W.; Potts, J.R.; Ruoff, R.S. Graphene and Grapheneoxide: Synthesis, Properties, and Applications. *Adv. Mater.* **2010**, *22*, 3906-3924.

110. Mattevi, C.; Kim, H.; Chhowalla, M. A Review of Chemical Vapour Deposition of Graphene on Copper. *J. Mater. Chem. A* **2011**, *21*, 3324-3334.

111. Gahouari, T.; Bodkhe, G.; Sayyad, P.; Ingle, N.; Mahadik, M.; Shirsat, S.M.; Deshmukh, M.; Musahwar, N.; Shirsat, M. Electrochemical Sensor: L-Cysteine Induced Selectivity Enhancement

of Electrochemically Reduced Graphene Oxide-Multiwalled Carbon Nanotubes Hybrid for Detection of Lead (Pb^{2+}) Ions. *Front. Mater*. **2020**, *7*, 68

112. Chen, Y.Y.; Zhao, P.; Liang, Y.; Liu, Y.Y.; Zhao, J.S.; Hou, J.Z.; Hou, C.J.; Huo, D.Q. A Sensitive Electrochemical Sensor Based on 3D Porous Melamine-Doped rGO/MXene Composite Aerogel for the Detection of Heavy Metal Ions in the Environment. *Talanta* **2023**, *256*, 124294.
113. Biswas, S.; Naskar, H.; Pradhan, S.; Wang, Y.; Bandyopadhyay, R.; Pramanik, P. Simultaneous Voltammetric Determination of Adrenaline and Tyrosine in Real Samples by Neodymium Oxide Nanoparticles Grafted Graphene. *Talanta* **2020**, *206*, 120176.
114. Balu, S.; Palanisamy, S.; Velusamy, V.; Yang, T.C.K.; El-Shafey, E.S.I. Tin Disulfide Nanorod-Graphene-β-Cyclodextrin Nanocomposites for Sensing Dopamine in Rat Brains and Human Blood Serum. *Mater. Sci. Eng. C* **2020**, *108*, 110367.
115. Fan, Z.J.; Lin, Q.Q.; Gong, P.W.; Liu, B.; Wang, J.Q.; Yang, S.R. A New Enzymatic Immobilization Carrier Based on Graphene Capsule for Hydrogen Peroxide Biosensors. *Electrochim. Acta* **2015**, *151*, 186-194.
116. Han, J.M.; Ma, J.; Ma, Z.F. One-Step Synthesis of Graphene Oxide-Thionine-Au Nanocomposites and Its Application for Electrochemical Immunosensing. *Biosens. Bioelectron.* **2013**, *47*, 243-247
117. Qi, T.T.; Liao, J.F.; Li, Y.S.; Peng, J.R.; Li, W.T.; Chu, B.Y.; Li, H.; Wei, Y.Q.; Qian, Z.Y. Label-Free Alpha Fetoprotein Immunosensor Established by the Facile Synthesis of a Palladium-Graphene Nanocomposite. *Biosens. Bioelectron.* **2014**, *61*, 245-250.
118. Rehman, A.U.; Ikram, M.; Kan, K.; Zhao, Y.M.; Zhang, W.J.; Zhang, J.W.; Liu, Y.; Wang, Y.; Du, L.J.; Shi, K.Y. 3D Interlayer Nanohybrids Composed of Reduced Graphenescheme Oxide/SnO_2/PPy Grown from Expanded Graphite for the Detection of Ultra-Trace Cd^{2+}, Cu^{2+}, Hg^{2+} and Pb^{2+} ions. *Sensor. Actuat. B-Chem.* **2018**, *274*, 285-95.
119. Song, N.N.; Wang, Y.Z.; Yang, X.Y.; Zong, H.L.; Chen, Y.X.; Ma, Z.; Chen, C.X. A Novel Electrochemical Bbiosensor for the Determination of Dopamine and Ascorbic Acid Based on Graphene Oxide/Poly(aniline-co-thionine) Nanocomposite. *J. Electroanal. Chem.* **2020**, *873*, 114352.

120. Eryigit, M.; Çepni, E.; Urhan, B.K.; Dogan, H.Ö.; Özer, T.Ö. Nonenzymatic Glucose Sensor Based on Poly(3,4-ethylene dioxythiophene)/Electroreduced Graphene Oxide Modified Gold Electrode. *Synth. Met.* **2020**, *268*, 116488.

121. Rikukawa, M.; Nakagawa, M.; Nishizawa, N.; Sanui, K.; Ogata, N. Electrochemical and Sensing Properties of Enzyme-Polypyrrole Multicomponent Electrodes. *Synth. Met.* **1997**, *85*, 1377-1378.

122. Li, H.B.; Li, J.; Xu, Q.; Hu, X.Y. Poly(3-hexylthiophene)/TiO_2 Nanoparticle-Functionalized Electrodes for Visible Light and Low Potential Photoelectrochemical Sensing of Organophosphorus Pesticide Chlopyrifos. *Anal. Chem.* **2011**, *83*, 9681-9686.

123. Lu, N.N.; Liu, H.; Huang, R.; Gu, Y.; Yan, X.Y.; Zhang, T.G.; Xu, Z.Q.; Xu, H.X.; Xing, Y.; Song, Y.; Li, X.W.; Zhang, Z.Q. Charge Transfer Platform and Catalytic Amplification of Phenanthroimidazole Derivative: A New Strategy for DNA Bases Recognition. *Anal. Chem.* **2019**, *91*, 11938-11945.

124. Pan, J.; Liu, M.; Li, D.; Zheng, H.; Zhang, D. Overoxidized Poly (3,4-Ethylenedioxythiophene)-Gold Nanoparticlese Graphene-Modified Electrode for the Simultaneous Detection of Dopamine and Uric Acid in the Presence of Ascorbic Acid. *J. Pharm. Anal.* **2021**, *11*, 699-708.

125. Chen, S.H.; Liu, D.; Song, N.; Wang, C.; Lu, X.F. Promoting Non-Enzymatic Electrochemical Sensing Performance Toward Glucose by the Integration of Conducting Polypyrrole with Metal-Organic Framework. *Compos. Commun.* **2022**, *30*, 1-5.

126. Egbedina, A. O.; Bolade, O.P.; Ewuzie, U.; Lima, E.C. Emerging Trends in the Application of Carbonbased Materials: A Review. *J. Environ. Chem. Eng.* **2022**, *10*, 107260.

127. Fu, S.S.; Zhu, Y.; Zhang, Y.; Zhang, M.J.; Zhang, Y.Y.; Qiao, L.; Yin, N.; Song, K.X.; Liu, M.S.; Wang, D.B. Recent Advances in Carbon Nanomaterials-Based Electrochemical Sensors for Phenolic Compounds Detection. *Microchem. J.* **2021**, *171*, 106776.

128. Jang, J.; Lim B. Selective Fabrication of Carbon Nanocapsules and Mesocellular Foams by Surface-Modified Colloidal Silica Templating. *Adv. Mater.* **2002**, *14*, 1390-1393.

129. Yang, X.G.; Li, C.; Wang, W.; Yang, B.J.; Zhang, S.Y.; Qian, Y.T. A Chemical Route from PTFE to Amorphous Carbon Nanospheres in Supercritical Water. *Chem. Commun.* **2004**, *3*, 342-343.

130. Jin, Y.Z.; Gao, C.; Hsu, W.K.; Zhu, Y.Q.; Huczko, A.; Bystrzejewski, M.; Roe, M.; Lee, C.Y.; Acquah, S.; Kroto, H.; Walton, D.R.M. Large-Scale Synthesis and Characterization of Carbon Spheres Prepared by Direct Pyrolysis of Hydrocarbons. *Carbon* **2005**, *43*, 1944-1953.

131. Chen, H.T.; Yuan, C.Y.; Yang, X.Y.; Cheng, X.W.; Elzatahry, A.A.; Alghamdi, A.; Su, J.C.; He, X.; Deng, Y.H. Hollow Mesoporous Carbon Nanospheres Loaded with Pt Nanoparticles for Colorimetric Detection of Ascorbic Acid and Glucose. *ACS Appl. Nano Mater.* **2020**, *3*, 4586-4598.

132. Li, X.F.; Chi, M.F.; Mahurin, S.M.; Liu, R.; Chuang, Y.J.; Dai, S.; Pan, Z.W. Graphitized Hollow Carbon Spheres and Yolk-Structured Carbon Spheres Fabricated by Metal-Catalyst-Free Chemical Vapor Deposition. *Carbon* **2016**, *101*, 57-61.

133. Sudha, V.; Duraisamy, V.; Arumugam, N.; Almansour, A.I.; Liu, T.X.; Dharuman, V.; Kumar, S.M.S. Ultrasensitive Dopamine Detection at Co_3O_4-Anchored N-Doped Hollow Mesoporous Carbon Nanospheres. *ACS Appl. Nano Mater.* **2023**, *6*, 13013-13026.

134. Yao, H.H.; Zhang, J.Q.; Du, J.; Li, B.; Zong, S.; Chen, A.B. Carbon Spheres Prepared by Amino Acid-Catalyzed Resorcinolformaldehyde Polymerization for Supercapacitors. *J. Alloys Compd.* **2022**, *926*, 166948.

135. Mahanthappa, M.; Duraisamy, V.; Arumugam, P.; Kumar, S.M.S. Simultaneous Determination of Ascorbic Acid, Dopamine, Uric Acid, and Acetaminophen on N, P-Doped Hollow Mesoporous Carbon Nanospheres. *ACS Appl. Nano Mater.* **2022**, *5*, 18417-18426.

136. Mansoor, S.; Ali Wani, O.; Lone, J.K.; Manhas, S.; Kour, N.; Alam, P.; Ahmad, A.; Ahmad, P. Reactive Oxygen Species in Plants: From Source to Sink. *Antioxidants* **2022**, *11*, 225.

137. Liu, L.; Zhao, H.L.; Shi, L.B.; Lan, M.B.; Zhang, H.W.; Yu, C.Z. Enzyme- and Metal-Free Electrochemical Sensor for Highly Sensitive Superoxide Anion Detection Based on Nitrogen Doped Hollow Mesoporous Carbon Spheres. *Electrochim. Acta* **2017**, *227*, 69-76.

138. Shi, W.; Li, W.T.; Nguyen, W.; Chen, W.; Wang, J.H.; Chen, M.L. Advances of Metal Organic Frameworks in Analytical Applications. *Mater. Today Adv.* **2022**, *15*, 100273.

139. Zhang, S.X.; Xiao, J.Y.; Zhong, G.; Xu, T.L.; Zhang, X.J. Design and Application of Dual-Emission Metal-Organic Framework-Based Ratiometric Fluorescence Sensors. *Analyst* **2024**, *149*, 1381-1397.

140. Jiang, M.; Liao, J.; Liu, C.H.; Liu, J.; Chen, P.X.; Zhou, J.; Du, Z.Z.; Liu, Y.; Luo, Y.; Liu, Y.B.; Chen, F.; Fang, X.J.; Lin, X.F. Metal-Organic Frameworks/Metal Nanoparticles as Smart Nanosensing Interfaces for Electrochemical Sensors Applications: A Mini-Review. Front. Bioeng. Biotechnol. **2023**, *11*, 1251713.

141. Mukherjee, D.; Van der Bruggen, B.; Mandal, B. Advancements in Visible Light Responsive MOF Composites for Photocatalytic Decontamination of Textile Wastewater: A Review. *Chemosphere* **2022**, *295*, 133835.

142. Furukawa, H.; Gándara, F.; Zhang Y.B.; Jiang, J.C.; Queen, W.L.; Hudson, M.R.; Yaghi, O.M. Water Adsorption in Porous Metal-Organic Frameworks and Related Materials. *J. Am. Chem. Soc.* **2014**, *136*, 4369-4381.

143. Jiang, H.L.; Feng, D.W.; Liu, T.F.; Li, J.R.; Zhou, H.C. Pore Surface Engineering with Controlled Loadings of Functional Groups via Click Chemistry in Highly Stable Metal-Organic Frameworks. *J. Am. Chem. Soc.* **2012**, *134*, 14690- 14693.

144. Chen, Z.J.; Kirlikovali, K.O.; Shi, L.; Farha, O.K. Rational Design of Stable Functional Metal-Organic Frameworks. *Mater. Horiz.* **2023**, *10*, 3257-3268.

145. Yuan, S.; Qin, J.S.; Lollar, C.T.; Zhou, H.C. Stable Metal-Organic Frameworks with Group 4 Metals: Current Status and Trends. *ACS Cent. Sci.* **2018**, *4*, 440-450.

146. Cavka, J.H.; Jakobsen, S.; Olsbye, U.; Guillou, N.; Lamberti, C.; Bordiga, S.; Lillerud, K.P. A New Zirconium Inorganic Building Brick Forming Metal Organic Frameworks with Exceptional Stability. *J. Am. Chem. Soc.* **2008**, *130*, 13850-13851.

147. Llewellyn, P.L.; Bourrelly, S.; Serre, C.; Vimont, A.; Daturi, M.; Hamon, L.; De Weireld, G.; Chang, J.S.; Hong, D.Y.; Hwang, Y.K.; Jhung, S.H.; Férey, G. High Uptakes of CO_2 and CH_4 in Mesoporous Metal-Organic Frameworks MIL-100 and MIL-101. *Langmuir* **2008**, *24*, 7245-7250.

148. Guan, W.X.; Dai, Y.; Dong, C.Y.; Yang, X.C.; Xi, Y. Zeolite Imidazolate Framework (ZIF)-Based Mixed Matrix Membranes for CO_2 Separation: A Review. *J. Appl. Polym.* **2020**, *137*, 48968.

149. Li, S.M.; Tan, L.F.; Meng, X.W. Nanoscale Metal-Organic Frameworks: Synthesis, Biocompatibility, Imaging Applications, and Thermal and Dynamic Therapy of Tumors. *Adv. Funct. Mater.* **2020**, *30*, 1908924.

150. Yuan, S.; Feng, L.; Wang K.C.; Pang, J.D.; Bosch, M.; Lollar, C.; Sun, Y.J.; Qin, J.S.; Yang, X.Y.; Zhang, P.; Wang, Q.; Zou, L.F.; Zhang, Y.M.; Zhang, L.L.; Fang, Y.; Li, J.L.; Zhou, H.C. Stable Metal-Organic Frameworks: Design, Synthesis, and Applications. *Adv. Mater.* **2018**, *30*, 1704303.

151. Zhang, X.; Peng, F.; Wang, D.H. MOFs and MOF-Derived Materials for Antibacterial Application. *J. Funct. Biomater.* **2022**, *13*, 215.

152. Cohen, S.M. Postsynthetic Methods for the Functionalization of Metal-Organic Frameworks. *Chem. Rev.* **2012**, *112*, 970-1000.

153. Li, B.Y.; Zhang, Y.M.; Ma, D.X.; Li, L.; Li, G.H.; Li, G.D.; Shi, Z.; Feng, S.H. A Strategy Toward Constructing a Bifunctionalized MOF Catalyst: Post-Synthetic Modification of MOFs on Organic Ligands and Coordinatively Unsaturated Metal Sites. *Chem. Commun.* **2012**, *48*, 6151-6153.

154. Yin, F.; Wang, C.; Lin, K.; Tong, S. Persulfate Activation for Efficient Degradation of Norfloxacin by a rGO-Fe_3O_4 Composite. *J. Taiwan Inst. Chem. Eng.* **2019**, *102*, 163-169.

155. Wang, M.; Guan, J.; Liu, S. Dual-Ligand Lanthanide Metal-Organic Framework Probe for Ratiometric Fluorescence Detection of Mercury Ions in Wastewater. *Microchim. Acta* **2023**, *190*, 359-369.

156. Varsha, M.V.; Nageswaran, G. Review-Direct Electrochemical Synthesis of Metal Organic Frameworks. *J. Electrochem. Soc.* **2020**, *167*, 155527.

157. Wei, G.; Lu, Y.; Liu, S.; Li, H.; Liu, X.; Ye, G.; Chen, J. Microplasma Electrochemistry (MIPEC) Strategy for Accelerating the Synthesis of Metal Organic Frameworks at Room Temperature. *Chinese Chem. Lett.* **2021**, *32*, 497-500.

158. Zheng, H.; Hou, Y.; Li, S.; Ma, J.; Nan, J.; Li, T. Recent Advances in the Application of Metal Organic Frameworks Using in Advanced Oxidation Progresses for Pollutants Degradation. *Chinese Chem. Lett.* **2022**, *33*, 5013-5022.

159. Sabouni, R.; Kazemian, H.; Rohani, S. Microwave Synthesis of the CPM-5 Metal Organic Framework. *Chem. Eng. Technol.* **2012**, *35*, 1085-1092.

160. Burgaz, E.; Erciyes, A.; Andac, M.; Omer, A. Synthesis and Characterization of Nano-Sized Metal Organic Framework-5 (MOF-5) by Using Consecutive Combination of Ultrasound and Microwave Irradiation Methods. *Inorg. Chim. Acta* **2019**, *485*, 118-124.

161. Zhang, Y.; Zhou, J.; Chen, J.; Feng, X.; Cai, W. Rapid Degradation of Tetracycline Hydrochloride by Heterogeneous Pphotocatalysis Coupling Persulfate Oxidation with MIL-53(Fe) Under Visible Light Irradiation. *J. Hazard. Mater.* **2020**, *392*, 122315.

162. Bhadra, B.N.; Yoo, D.K.; Jhung, S.H. Carbon-Derived from Metal-Organic Framework MOF-74: A Remarkable Adsorbent to Remove a Wide Range of Contaminants of Emerging Concern from Water. *Appl. Surf. Sci.* **2020**, *504*, 144348.

163. Wang, R.; Liu, B.; Zhang, S.; Huang, X.; Xie, L.; Liu, T.; Cao, R. Design of a Metal-Organic Framework with Preset Binding Sites for Crystallographic Visualized Metalation. *Small Struct.* **2022**, *3*, 1025-1028.

164. Feng, D.; Gu, Z.; Li, J.; Jiang, H.; Wei, Z.; Zhou, H. Zirconium-Metalloporphyrin PCN-222: Mesoporous Metal-Organic Frameworks with Ultrahigh Stability as Biomimetic Catalysts. *Angew. Chem. Internat. Ed.* **2012**, *51*, 10307-10310.

165. Millward, A.R.; Yaghi, O.M. Metal-Organic Frameworks with Exceptionally High Capacity for Storage of Carbon Dioxide at Room Temperature. *J. Am. Chem. Soc.* **2005**, *127*, 17998-17999.

166. Cadiau, A.; Adil, K.; Bhatt, P.M.; Belmabkhout, Y.; Eddaoudi, M. A. Metal-Organic Framework-Based Splitter for Separating Propylene From Propane. *Science* **2016**, *353*, 137-140.

167. Guo, H.; Fan, T.; Yao, W.; Yang, W.; Wu, N.; Liu, H.; Wang, M.; Yang, W. Simultaneous Determination of 4-Aminophenol and Acetaminophen Based On High Electrochemical Performance of ZIF-67/MWCNTCOOH/Nafion Composite. *Microchem. J.* **2020**, *158*, 105262.

168. Zhou, Z.; Mukherjee, S.; Hou, S.; Li, W.; Elsner, M. Porphyrinic MOF Film for Multifaceted Electrochemical Sensing. *Angew. Chem. Internat. Ed.* **2021**, *60*, 20551-20557.

169. Liu, S.; Xiang, Z.; Hu, Z. Cao, D. Zeolitic Imidazolate Framework-8 As A Luminescent Material for The Sensing of Metal Ions and Small Molecules. J. Mater. Chem. **2011**, *21*, 6649-6653.

170. Zhou, Y.; Abazari, R.; Chen, J.; Kumar, A.; Ikreedeegh, R.R.; Rani, E.; Singh, H.; Kirillov, A.M. Bimetallic Metal-Organic Frameworks and MOF-Derived Composites: Recent Progress on Electro- and Photoelectrocatalytic Applications. *Coordin. Chem. Rev.* **2022**, *451*: 1-43.

171. Huang, W.; Chen, Y.; Wu, L.; Long, M.; Lin, Z.; Su, Q.; Zheng, F.; Wu, S.; Li, H.; Yu, G. 3D Co-Doped Ni-Based Conductive MOFs Modified Electrochemical Sensor for Highly Sensitive Detection of L-Tryptophan. *Talanta* **2022**, *247*, 1-10.

172. Zeng, Y.; Camarada, M.B.; Lu, X; Tang, K.; Li, W.; Qiu, D.; Wen, Y.; Wu, G.; Luo, Q.; Bai, L. Detection and Electrocatalytic Mechanism of Zearalenone Using Nanohybrid Sensor Based on Copper-Based Metal-Organic Framework/Magnetic Fe_3O_4-Graphene Oxide Modified Electrode. *Food Chem.* **2022**, *370*, 1-10.

173. Li, X.; Li, C.; Wu, C.; Wu, K. Strategy for Highly Sensitive Electrochemical Sensing: In Situ Coupling of a Metal-Organic Framework with Ball-Mill-Exfoliated Graphene. *Anal. Chem.* **2019**, *91*, 6043-6050.

174. Fang, X.; Chen X.; Liu, Y. Li, Q.; Zeng, Z.; Maiyalagan, T. Mao, S. Nanocomposites of Zr(IV)-Based Metal-Organic Frameworks and Reduced Graphene Oxide for Electrochemically Sensing Ciprofloxacin in Water. *ACS Appl. Nano Mater.* **2019**, *2*, 2367-2376.

175. Liu, C.; Bo, X.; Guo, L. A Novel Electrochemical Sensing Platform of JUC-62 Metal Organic Framework/Platelet Ordered Mesoporous Carbon for High Selective Detection of Nitro-Aromatic Compounds. *Sensor. Actuat. B-Chem.* **2019**, *297*, 126741.

Chapter 3: CNs for the detection of dopamine

This chapter presents a simple and environmentally friendly method for the synthesis of carbon nanospheres (CNs). The results indicate that the CNs can be successfully prepared via a hydrothermal reaction using glucose as a precursor, as demonstrated through various characterization methods. An electrochemical sensing platform was developed based on the CNs, and its analytical performance for the determination of dopamine was evaluated.

This Chapter is published to the journal "ChemElectroChem":

Lei, P., Zhou, Y., Sun, X., Dong, C., He, Y., Liu, Y., and Shuang, S. (2023). Green synthesis of carbon nanospheres for enhanced electrochemical sensing of dopamine. ChemElectroChem, 10, e202201129 (1 of 8).

Green synthesis of carbon nanospheres for enhanced electrochemical sensing of dopamine

Abstract

The specific detection of dopamine (DA) has received enormous attention since it is universally acknowledged as an important neurotransmitter associated with nerve signaling and some diseases. In this work, glucose−derived carbon nanospheres (CNs) are synthesized by the green hydrothermal approach and served to modify electrodes for the detection of DA. The CNs were successfully synthesized and purposely investigated in detail by the kinds of characterization technologies. The CNs modified glassy carbon electrode (CNs/GCE) exhibits better electrochemical sensing performances with a wide linear range of 0.05 – 1600 μM and a low limit of 8.3 nM toward determination of dopamine, as compared with the modified electrodes reported previously. The CNs/GCE is successfully applied to detect DA in human serum samples, which makes it promising for biomedical applications. More importantly, this work shows a novel green and simple strategy for the design of an effective electrode nanomaterial, which provides more opportunities for modifying the design of electrodes in electrochemical sensing applications.

Keywords: Green synthesis, carbon nanospheres, dopamine detection, human serum samples

3.1 Introduction

Dopamine (DA) is an essential catecholamine neurotransmitter and plays a significant role in regulating various physiological functions of the central nervous system [1]. The content of DA is the highest (50 nmol g^{-1}) in the caudate nucleus of the human brain [2]. However, the abnormal concentration of DA is closely related to neurological and physiological diseases, particularly Parkinson's disease [3,4]. Since DA is the main neurotransmitter used for disease diagnosis, the detection of DA in vivo and in vitro is of clinical significance. A variety of biosensing methods, such as flow-injection analysis [5], fluorescence spectrophotometry [6], and capillary electrophoresis [7], have been successfully employed for the determination of DA. However, the application of these methods is limited by the complicated operation processes, insufficient anti–interference ability, and high cost [8,9]. The electrochemical analysis method has attracted more and more attention owing to its advantages of easy operation, low specific investment cost, and high sensitivity [10]. Therefore, the development of green, non-toxic, high catalytic activity electrochemical sensing materials is especially critical.

The application of nanomaterials in electrochemical sensing has opened up a new path to better understanding the redox process for the detection of analytes through the electrochemical method. Carbon nanomaterials, including multi–walled carbon nanotubes [11], graphene [12], nanorods [13], fullerenes [14], and carbon nanospheres [15], have aroused extensive attention due to their outstanding electrochemical performances. Among these nanomaterials, carbon nanospheres have a reasonable prospect to play a crucial part in imaging [16], water splitting [17], supercapacitors [18], and electrochemical sensing [19] owing to their ordered structures, excellent mechanical stability, and easy dispersion [20]. For example, Zhang and co-workers [16] designed hollow carbon nanospheres (HCSs) dotted with Gd-Fe nanoparticles to achieve magnetic resonance and photoacoustic imaging in vivo. Li et al. [17] prepared Co-Mo-P carbon nanospheres derived from metal–organic frameworks as a high–performance electrocatalyst towards efficient water splitting, which exhibited excellent electrocatalytic performance. Ultrasmall carbon nanospheres with tailored sizes and textural properties were designed by the miniemulsion polymerization technique, which demonstrated excellent supercapacitive performances [18]. Pd nanoparticles decorated N-doped graphene quantum dots@N-doped carbon

hollow nanospheres with high electrochemical sensing performance were constructed and explored their clinical application in ultrasensitive and highly specific detection of H_2O_2 secreted from living cancer cells [19]. Although carbon nanospheres (CNs) have been used in many fields according to previous reports, the CNs synthesized in this chapter using green and nontoxic glucose as a carbon source have never been separately used as an electrochemical modification nanomaterial for direct electroanalytical detection, including the development of electrochemical sensors. The glucose-derived CNs offer more benefits as electrode modification nanomaterial including (a) They exhibit good hydrophilicity and biocompatibility due to a large number of hydroxyl groups; (b) The preparation process of the CNs are completely "green" and non-toxic. (c) The glucose-derived CNs are favorable to improve the electron transfer efficiency and enhance the sensitivity of electrochemical sensors. These properties are conducive to the further electrochemical application of the CNs.

In this chapter, a simple hydrothermal method was employed for the preparation of uniform and mesoporous CNs with large active surface areas using glucose as raw material. The unique structure of the CNs provided a large specific surface area and fast electron transfer capacity, which were expected to achieve high electrochemical performances for the electrocatalysis of DA, as indicated in Fig. 3.1. The experimental results showed that the sensing system exhibited good linearity in a broad range with a low detection limit. In addition, the satisfactory results were obtained when the CNs/GCE was applied to determinate DA in serum, demonstrating the practical applicability of the proposed analytical method.

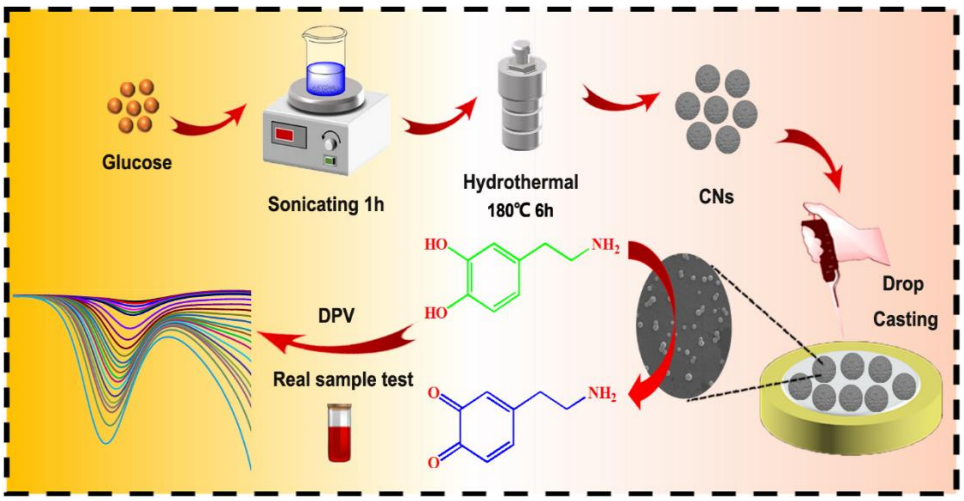

Fig. 3.1: Preparation of the CNs and the fabrication of CNs/GCE

3.2 Materials and Methods

3.2.1 Reagents

Glucose, DA, epinephrine (EP), ascorbic acid (AA), uric acid (UA), glutathione (GSH), tryptophan (Trp), hydrogen peroxide (H_2O_2) were purchased from Aladdin Chemistry Co., Ltd. (Shanghai, China).

3.2.2 Instrumentation

The surface morphology and the elemental composition were studied by field-emission scanning electron microscopy (FESEM, JSM-7900F, Japan), high resolution (HR) transmission electron microscopy (TEM, Tecnai G2 F20 S-Twin, USA), and energy−dispersive spectroscopy (EDS). XRD patterns were obtained an X-ray diffractometer (XRD, Bruker D8 ADVANCE A25). The N_2 adsorption/desorption curves were obtained using a Tristar II (3020) (Micromeritics, USA) volumetric absorption analyzer. The X-ray photoelectron spectroscopy (XPS, AXIS ULTRA DLD, UK) was applied to analyze the chemical composition of the composite. The Fourier transform infrared (FT-IR) and dynamic light scattering (DLS) patterns were obtained from a Bruker TENSOR II. Cyclic voltammetry (CV) and differential pulse voltammetry (DPV) techniques were carried out at the CHI 660E electrochemical workstation (Shanghai CH Instrument Co. Ltd., China).

3.2.3 Preparation of the CNs and CNs/GCE

5.0 g glucose was dissolved in 80 mL ultrapure water and sonicated for 60 min. Then, the obtained solution was transferred into a 100 mL autoclave, and the hydrothermal reaction was executed at 180 ℃ for 6 h. The puce products were spearated by centrifugation at 10000 rpm for 15 min and washed with ethanol and deionized water for 4 times. Then, the solution was dialyzed with ultrapure water for 24 h to produce uniformly sized CNs. The CNs were harvested by freeze-drying the aforesaid solutions. Before each electrochemical test, a glassy carbon electrode (GCE) was polished with 0.05 μm alumina slurry and then cleaned ultrasonically in ultrapure water and ethanol to give a clean surface. The CNs were dispersed in ultrapure water (2 mg mL^{-1}). The dispersed solution was drip-coated onto the cleaned GCE, then vacuum dried to produce the CNs/GCE.

3.2.4 Electrochemical Methods

The working electrode was the CNs modified GCE, the reference electrode was Ag/AgCl electrode and the counter electrode was platinum wire electrode. CV was carried on a voltage range of -0.2-0.6 V with a scan rate of 50 mV s^{-1} in 5 mM $[Fe(CN)_6]^{3-/4-}$ including 0.1 M KCl. DPV: increment potential, 0.004 V; pulse amplitude, 0.05 V; pulse width, 0.06 s; pulse period, 0.2 s; quiet time, 2 s.

3.3 Results and Discussions

3.3.1 Characterization of CNs

The XRD pattern obtained from the powdered forms of CNs was depicted in Fig. 3.2A. The XRD pattern showed two peaks at 20.5º and 40.3º, which can be assigned to the [002] and [100] planes of the carbon material [21]. The characteristic FT-IR bands of the CNs at 1703 cm^{-1} and 1612 cm^{-1} in Fig. 3.2B were assigned to C=O and C=C groups, respectively [22]. The bands in range from 1000 cm^{-1} to 1300 cm^{-1} for C-OH stretching and -OH bending vibrations implied the existence of numerous residual hydroxyl groups, which can improve the hydrophilicity and the biocompatibility of CNs. The porosity of CNs was evaluated by nitrogen adsorption-desorption measurement. Fig. 3.2C shows a type-IV isotherm with a hysteresis loop behavior, indicating the mesoporous nature of CNs. The obtained BET surface area of CNs was 58.6 m^2 g^{-1} with a total pore volume of 0.30 cm^3 g^{-1}. The mean particle size of CNs was found to be 200 nm, measured by the DLS system. (Fig. 3.3D). The zeta potential of the CN was -41.3 ± 2.01 mV in an aqueous solution (Fig. 3.2E).

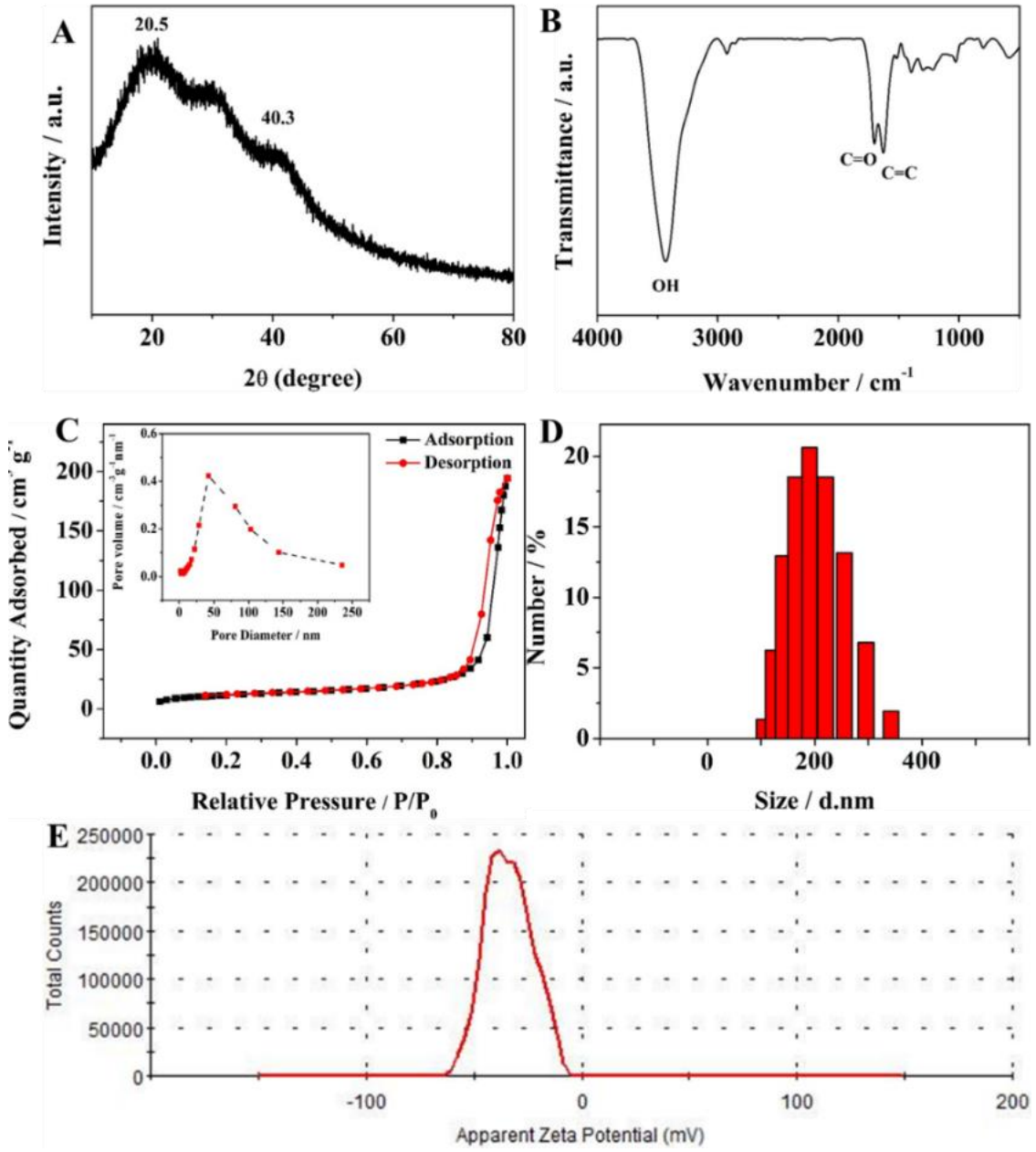

Fig. 3.2: (A) XRD pattern, (B) FT-IR spectra, (C) N_2 adsorption-desorption isotherms, corresponding pore size distribution, (D) DLS, and (E) zeta potential of CNs

Fig. 3.3A shows the XPS spectra for the CNs over a wide binding energy range, demonstrating that CNs are composed of C 1s and O 1s. In the C 1s spectra (Fig. 3.3B), the peaks observed at 284.7 eV, 285.9 eV, and 288.4 eV can be attributed to C-C, C=C, and C=O, respectively [23]. Fig. 3.3C shows the high-resolution XPS spectra of O 1s, which includes two peaks at 532.2 eV and 533.1 eV, corresponding to C-OH and C=O, respectively. The UV-visible absorption spectra of the CNs exhibited a wide characteristic peak at 348 nm (Fig. S1). The morphological features of CNs were captured using FESEM

and TEM measurements. The images demonstrated the spherical shape of CNs, with the diameter ranging from 50 to 100 nm (Fig. 3.3D and E). CNs were observed to be highly monodispersed with distinct shape boundaries. Fig. 3.3F shows the EDS spectra of CNs, indicating that the nanomaterial is composed of 88.24% C and 11.76% O. To assess the low toxicity of CNs, PC12 cells were co-cultured with varying concentrations of CNs. As shown in Fig. S2, even when CNs reached a concentration of 200 µg/mL, the cell viability of PC12 cells remains above 95%, indicating excellent biocompatibility of CNs with minimal toxicity towards normal cells.

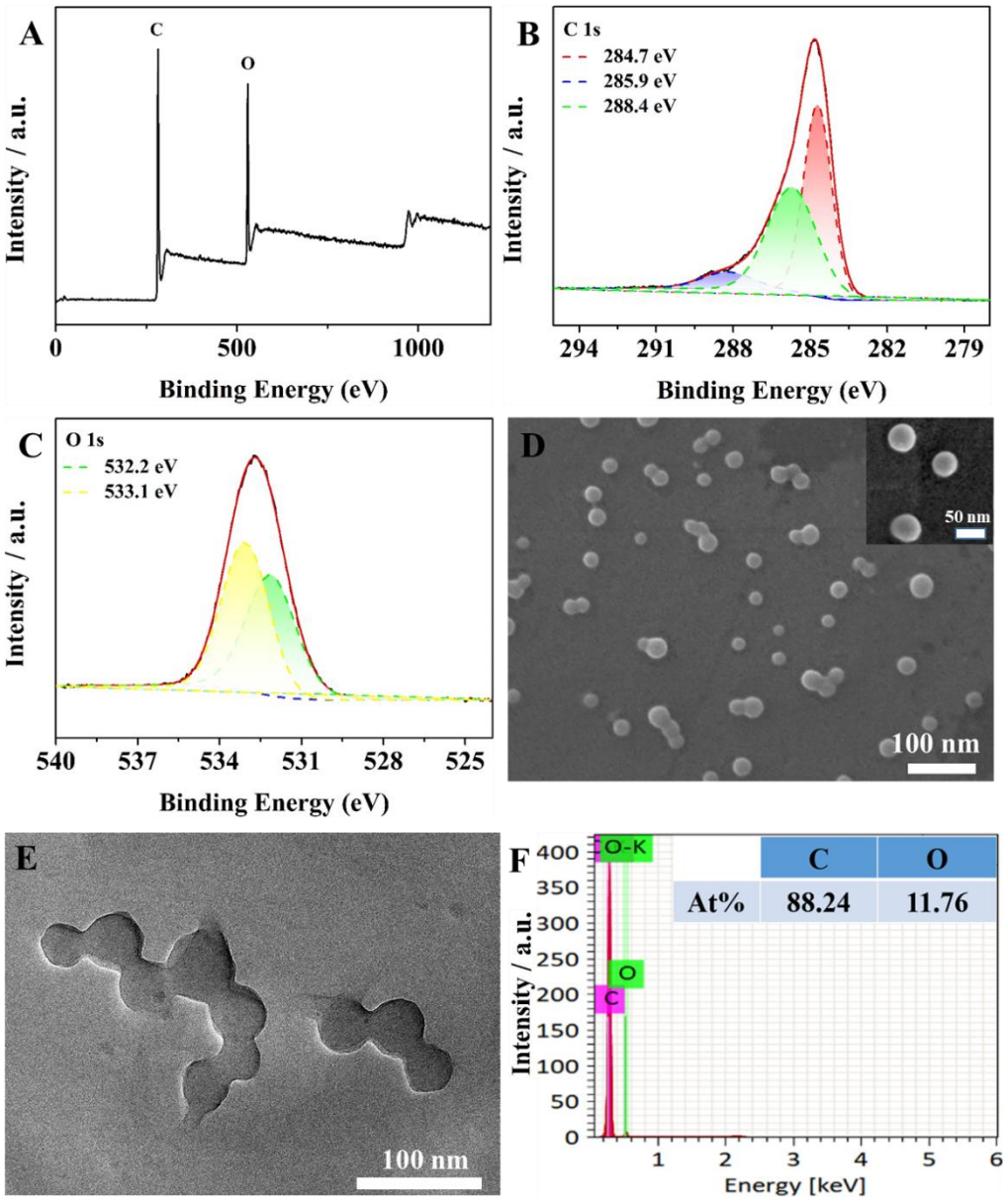

Fig. 3.3: XPS survey (A), C 1s (B) and O 1s (C) spectra of the CNs. FESEM (D) and TEM (E) images of the CNs, insets show the high-magnification images; (F) EDS analysis of CNs

3.3.2 Electrochemical Performance of CNs/GCE

The characterization of the bare GCE and CNs/GCE have been carried out using the CV and EIS techniques. The well-defined reversible redox peaks were observed on both bare GCE and CNs/GCE, while the peak current increased significantly after modification of -CNs due to the increase of electroactive surface area (Fig. 3.4A). The electroactive surface area of CNs/GCE was calculated to investigate the electrochemical behavior of the sensing system. CV was performed with different scan rates from 20 to 100 mV/s in 5.0 mM $[Fe(CN)_6]^{3-/4-}$ (Fig. 3.4B). The redox peak current (I_p) followed the linear equation: I_{pa} (μA)=0.2868+9.471$v^{1/2}$ $(mV/s)^{1/2}$， R^2=0.9983 and I_{pc} (μA)=−22.35−7.374$v^{1/2}$ $(mV/s)^{1/2}$， R^2=0.9979, indicating that the electrochemical sensing system followed the diffusion control mechanism [24]. The electroactive surface area was calculated by the Randles-Sevcik equation [25]:

$$I_p = 268600n^{3/2}AD^{1/2}Cv^{1/2} \qquad (1)$$

in which I_p (A) represented peak current and the electron transfer number of $[Fe(CN)_6]^{3-/4-}$ redox process was represented by n (n=1), A (cm^2) was electroactive surface area of the sensing system, the diffusion coefficient and concentration of the $[Fe(CN)_6]^{3-/4-}$ were represented by D (cm^2 s^{-1}), and C ($mol \cdot cm^{-3}$). v was the scan rate (V s^{-1}). With the concentration of $[Fe(CN)_6]^{3-/4-}$ being 5.0 mM, n = 1, C=5×10^{-6} $mol \cdot cm^{-3}$, D=0.67×10^{-5} cm^2 s^{-1}, the average electroactive surface area of CNs/GCE without template incubation was calculated to be 0.0349 cm^2. As shown in Fig. S3, the resistance (Ret) of CNs/GCE decreases significantly compared with bare GCE, which further confirmed the good electronic conductivity of the CNs. Fig. 3.4C compares the CV responses to 0.1 mM DA at the bare GCE and CNs/GCE. CNs/GCE displayed much better DA oxidation capability in comparison with the bare GCE. It can be seen that almost no peak current was observed on CNs/GCE without DA. The results strongly illustrated the enhanced performance of the CNs for the electrochemical detection of DA. Fig. 3.4D shows the CVs of DA on the CNs/GCE at different scan rates, the linear regression equation is I_{pc} (μA)=−0.9863$v^{1/2}$ $(mV/s)^{1/2}$−4.324, R^2=0.9941. It is found that the peak current is proportional to the square root of scan rate, indicating that the electrochemical sensing system followed the diffusion control mechanism.

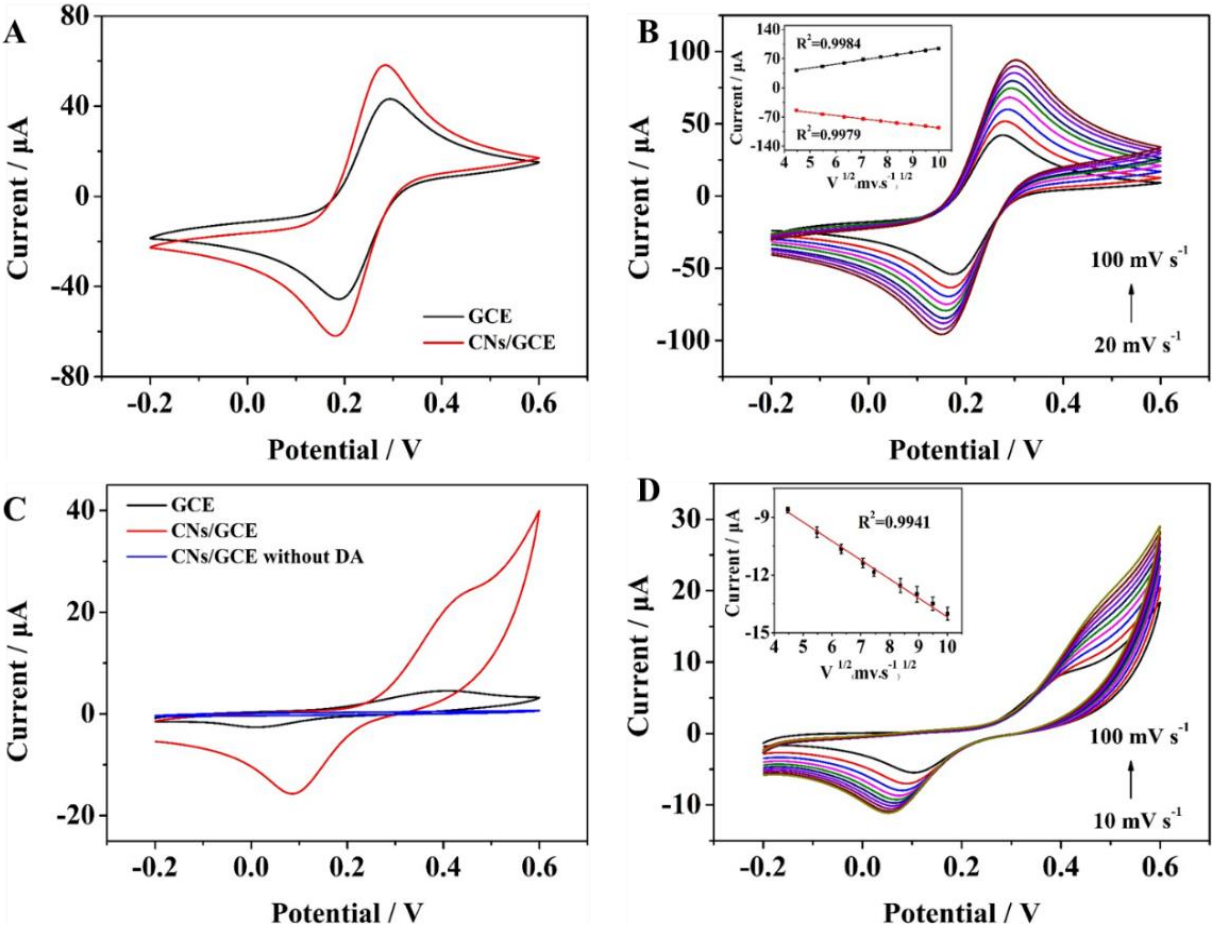

Fig. 3.4: (A) CVs of bare GCE and CNs/GCE in 5.0 mM $[Fe(CN)_6]^{3-/4-}$ containing 0.1 M KCl; (B) CVs of CNs/GCE with different scan rates in 5.0 mM $[Fe(CN)_6]^{3-/4-}$ containing 0.1 M KCl (inset: variation of the peak currents with the square root of scan rate); (C) CVs of bare GCE and CNs/GCE in 0.01 M PBS (pH 7.0) containing 0.1 mM DA, and CVs of CNs/GCE without 0.1 mM DA; (D) CVs of CNs/GCE in 0.01 M PBS (pH 7.0) containing 0.1 mM DA at various scan rates 10-100 mV s^{-1} (inset: variation of cathodic peak current (I_{pc}) with the square root of scan rate)

In order to maximize the performance of CNs/GCE towards DA determination, the amount of the CNs coated on the GCE must be optimized. In Fig. 3.5A, the response current is seen to increase with increasing volume of CNs from 6-10 µL, and then decreased with further increase of CNs volume. The change of response current can be attributed to that a change in the effective electrode surface area, which initially increased with increasing CN volume to reach the maximum, while further increase in CNs volume maybe block the electron transfer caused by the thick modification layer at the electrode surface. Therefore, 10 µL was chosen for the electrode modification in the following measurements. The pH value of the supporting electrolyte solution directly affects the sensitivity of CNs/GCE for the detection of DA [26]. Fig. 3.5B shows the CV response of CNs/GCE to 0.1 mM DA in 0.01 M PBS

with the pH ranging from 5.0 to 9.0. The results indicate that the peak current increased rapidly as the pH increased, reaching a plateau at pH 7.0, which was selected as the optimal pH for the determination of DA. Fig. 3.5C shows that the reduction potential of DA is linear to the pH value ranging from 5.0 to 9.0, with the linear regression equation of E_p (V)=–0.0536pH+0.281 (R^2=0.9911). The attained slope was close to -0.059, indicating that the electrochemical oxidization reaction on CNs/GCE was a two-electron transfer process for DA [27-29]. The reaction was shown in Fig. 3.5D.

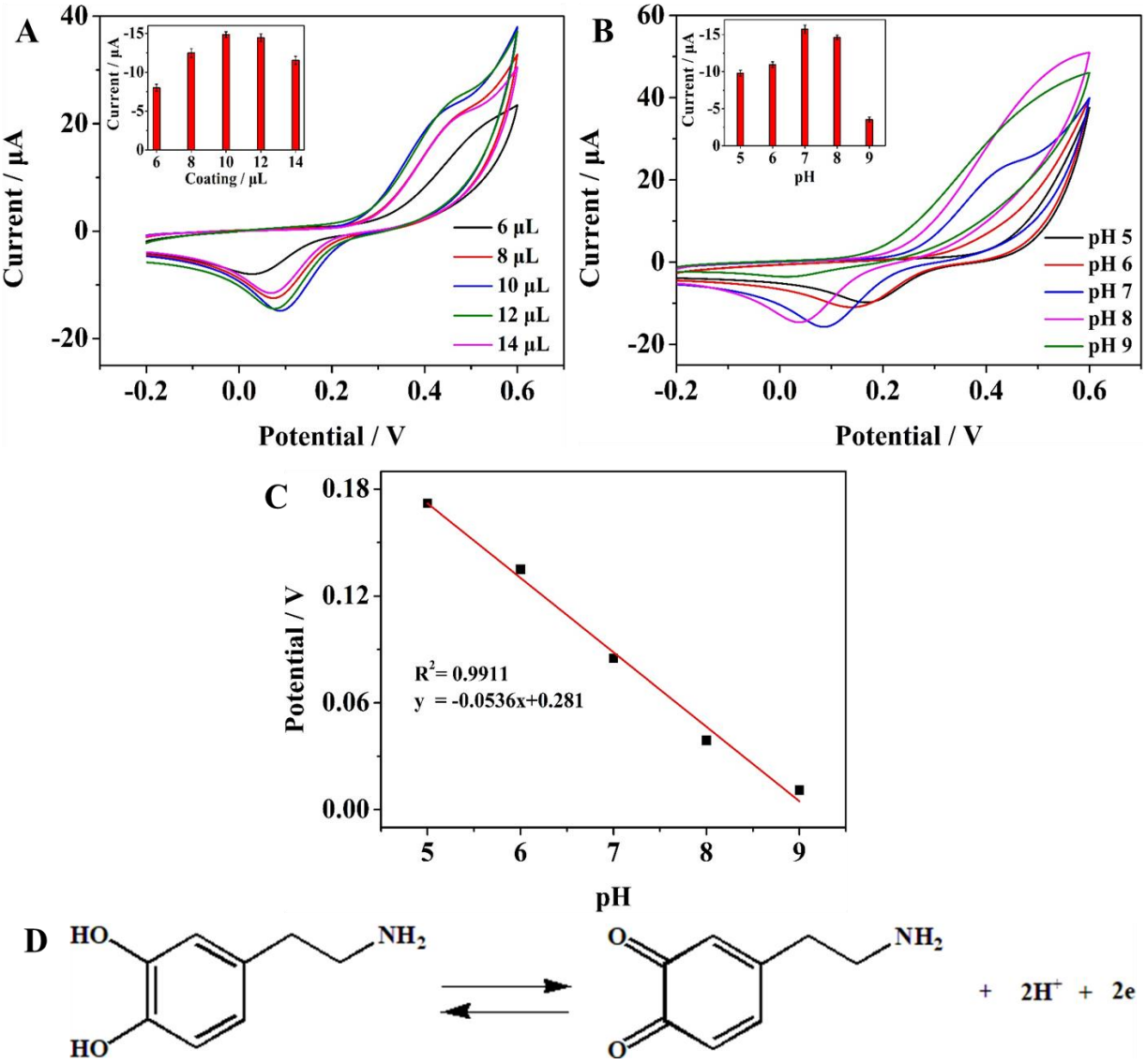

Fig. 3.5: Effect of the amount of CNs (A) and the pH values (B) on the peak currents of 0.1 mM DA at the CNs/GCE; (C) The value of reduction potential of DA versus pH; (D) Mechanistic pathway for the electrochemical reaction of DA

DPV was employed to investigate the current signals of different concentrations of DA on CN/GCE. As shown in Fig. 3.6A, the CNs exhibit excellent electrocatalytic activity towards the oxidation of DA with the peak current response increasing monotonously with the DA concentration. In Fig. 3.6B, the peak current response and the concentrations showed good linearity, with regression equations $I_{pc}(\mu A)=-0.0754C(\mu M)-3.02$, $R^2=0.9947$ for the low DA concentration region (0.05-150 μM) and $I_{pc}(\mu A)=-0.0226C(\mu M)-13.03$, $R^2=0.9958$ for the DA concentration range of 150-1600 μM. The limit of detection was determined to be 8.3 nM using the first linear segment according to the LOD=3Sb/k (where, Sb was the standard deviation of the blank solution, and k was slope of the regression). Table 3.1 compares the analytical performances obtained with the CNs/GCE and some other modified electrodes reported previously for DA detection. Obviously, CNs/GCE displays a better sensing performance with a wider linear range in comparison with those obtained in the previous reports. It was due to the unique structure of the CNs providing a large specific surface area and fast electron transfer capacity achieved high electrochemical performances for the electrocatalysis of DA.

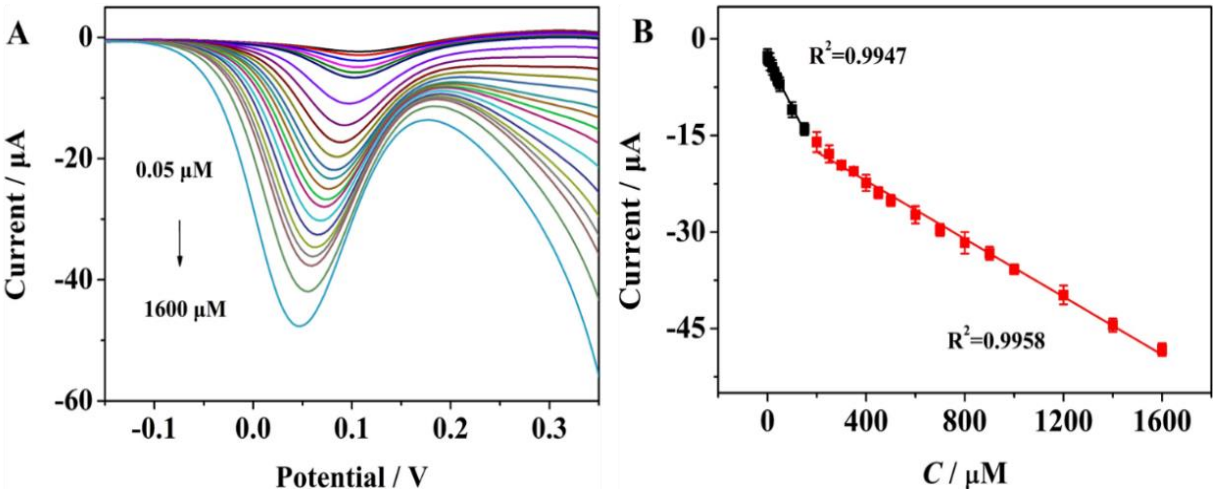

Fig. 3.6: (A) DPV curves of CNs/GCE with the variation of the DA concentrations from 0.05 to 1600 μM; (B) Calibration curves of DPV peak currents versus the concentrations of DA from 0.05 to1600 μM at the CNs/GCE

Table 3.1: The detection performances of recently reported electrochemical DA sensors

Electrode	Method	Linear range (μM)	Detection limit (μM)	Ref.
Fe_3O_4/SnO_2/Gr/CPE	DPV	0.02-2.8	0.0071	[30]
Cu/Cu_2O-OA/MWCNTs/GC	DPV	0.02-0.159	0.00327	[31]
L-cys ZnS:Mn QDs	Phospho rescence	0.15-3.00	0.0078	[32]
G-30	DPV	3-140	1.44	[33]
β-CD@AuNCs	Fluoresc ence	0.1-80	0.02	[34]
rGO/Co_3O_4/GCE	CA	0-30	0.277	[35]
Ti_3C_2-MXene-FET	DPV	0.1-50	0.1	[36]
HNP-PtTi	DPV	4-500	3.2	[37]
GQDs/IL-SPCE	DPV	0.2-15	0.06	[38]
TiO_2 microtube	DPV	0.4-80	0.025	[39]
NACP film electrode	DPV	0.05-15	0.01	[40]
CNs/GCE	DPV	0.05-1600	0.0083	This work

Selectivity was a critical property indicator for CNs/GCE. Some electroactive substances were usually present in human body fluids and affect dopamine detection. Fig. 3.7A illustrates that none of these interferons yielded a significant current response compared with DA. The satisfactory result manifested the efficient performance of CNs/GCE toward selective electrochemical detection of DA. The

reproducibility of CNs/GCE was assessed using six independent CNs/GCEs under identical fabrication and measurement conditions for DA detection. The results are shown in Fig. 3.7B. The relative standard deviation (RSD) value of intraday reproducibility was 4.1%, which indicated the good reproducibility of this developed CNs/GCE. The repeatability of CNs/GCE was tested for 20 times in 0.01 M PBS containing 20 μM DA, and results are presented in Fig. 3.7C. The current response still retained 89.87 % of the original value after 20 times of continuous measurement. Moreover, the stability of the CNs/GCE was also examined by measuring the current response in 20 μM DA on a daily basis for 15 days. CNs/GCE displayed a relatively stable performance for repeated measurements, showing a 97.2% retention of the initial response. The response decreased further to 89.6% upon consecutive scans after 15 days (Fig. 3.7D). Overall, CNs/GCE displayed good selectivity, reproducibility, repeatability, and stability, which are the essential features required of an effective sensor in practical applications, for the determination of DA.

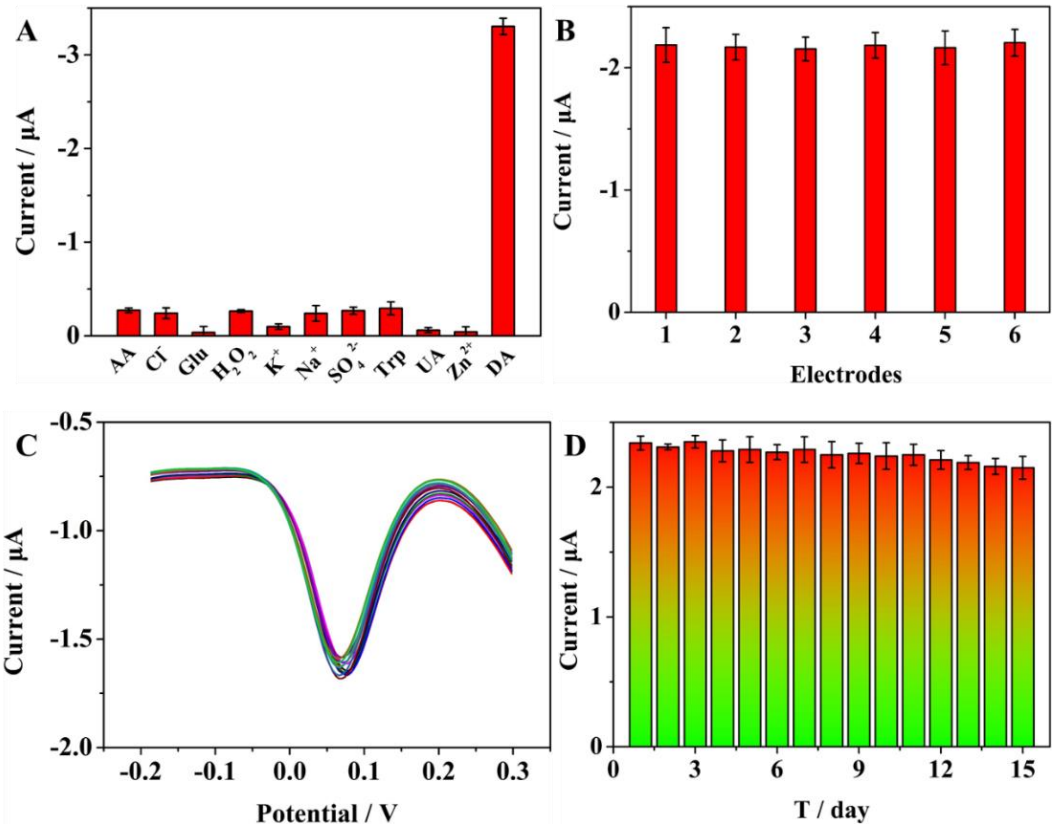

Fig. 3.7: (A) Selectivity of CNs/GCE for the detection of 20 μM DA in the presence of 10-fold excess of different interferents; (B) Reproducibility of CNs/GCE for the detection of 20 μM DA at 6 different electrodes; (C) Repeatability of the same CNs/GCE for 20 consecutive measurements of 20 μM DA; (D) Stability of CNs/GCE for measuring DA over 15 days

3.3.3 Spiked Serum Sample Studies

To demonstrate the potential of CNs/GCE in clinical applications, its responses to spiked DA in serum samples at different concentrations (5 μM, 100 μM, 500 μM) were measured. The average percentage of recovery values for the spiked DA concentrations varied from 99.71% to 105.60% with a relative standard deviation (RSD) less than 3.57% (Table 3.2), suggesting that the CNs/GCE can be effectively applied to the real samples with a high DA concentration.

Table 3.2: The DA detection results obtained at the CNs/GCE in human serum samples

Sample	Added (μM)	Detected (μM)	Recovery (%)	RSD (%)
Human serum	5	5.28	105.60	2.57
	100	101.64	101.64	3.21
	500	498.53	99.71	3.57

3.4 Conclusion

The CNs, synthesized through a facile green hydrothermal synthesis procedure, were found to exhibit outstanding electrocatalytic activities for the determination of DA with a wide linear response range, low LOD, good stability, excellent selectivity, and reproducibility. CNs were also employed to study its practicability for analysis of different concentrations of DA in human blood serum samples and achieved satisfactory recoveries of 99.71% to 105.60%. The proposed approach provides an interesting and important method for improving the detection performance of the electrochemical sensor.

References

1. Li, H.; Zhou, K.; Cao, J.; Wei, Q.; Lin, C.; Pei, S. E.; Ma, L.; Hu, N.; Guo, Y.; Deng, Z.; Yu, Z.; Zeng, S.; Yang, W.; Meng. L. A Novel Modification to Boron-Doped Diamond Electrode for Enhanced, Selective Detection of Dopamine in Human Serum. *Carbon* **2021**, *171*, 16-28.

2. Subramaniam, T.; Kesavan, G.; Venkatachalam, G. Development of $CuAlO_2$-Encapsulated Reduced Graphene Oxide Nanocomposites: an Efficient and Selective Electrocatalyst for Detection of Neurodegenerative Disorders. *ACS Appl. Bio Mater.* **2020**, *3*, 7769-7778.

3. Qu, Z.; Muhammad, Y.; He, W.; Li, J.; Gao, Z.; Fu, J.; Shah, S. J.; Sun, H.; Wang, J.; Huang, Z.; Zhao Z. Designing C-Fe-O Bonded MIL-88B(Fe)/Jasmine Petal-Derived-Carbon Composite Biosensor for the Simultaneous Detection of Dopamine and Uric Acid. *Chem. Eng. J.* **2021**, *404*, 126570.

4. Jia, W.; Wu, D.; Tang, W.; Xia, X.; Su, Y.; Guo, X.; Liu, R. Carbonized Silk Fabric-Based Flexible Organic Electrochemical Transistors for Highly Sensitive and Selective Dopamine Detection. *Sensor. Actuat. B-Chem.* **2020**, *304*, 127414.

5. Staden, J. F.; Staden, R. I. S. Flow-Injection Analysis Systems with Different Detection Devices and Other Related Techniques for the in Vitro and in Vivo Determination of Dopamine as Neurotransmitter, A review. *Talanta* **2012**, *102*, 34-43.

6. Zhao, C.; Jiao, Y.; Hua, J.; Yang, J.; Yang, Y. Hydrothermal Synthesis of Nitrogendoped Carbon Quantum Dots as Fluorescent Probes for the Detection of Dopamine. *J. Fluoresc.* **2018**, *28*, 269-276.

7. Li, X.; Pan, J.; Yang, F.; Feng, J.; Mo, J.; Chen, Z. Simple Amperometric Detector for Microchip Capillary Electrophoresis, and its Application to the Analysis of Dopamine and Catechol. *Microchim. Acta* **2011**, *174*, 123-130.

8. He, W.; Liu, R.; Zhou, P.; Liu, Q.; Cui, T. Flexible Micro-Sensors with Self-Assembled Graphene on a Polyolefin Substrate for Dopamine Detection. *Biosens. Bioelectron.* **2020**, *167*, 112473.

9. Lu, Z.; Li, Y.; Liu, T.; Wang, G.; Sun, M.; Jiang, Y.; He, H.; Wang, Y.; Zou, P.; Wang, X.; Zhao, Q.; Rao, H. A Dual-Template Imprinted Polymer Electrochemical Sensor Based on AuNPs and Nitrogen-Doped Graphene Oxide Quantum Dots Coated on NiS_2/Biomass Carbon for Simultaneous Determination of Dopamine and Chlorpromazine. *Chem. Eng. J.* **2020**, *389*, 124417.

10. Liu, W.; Cui, F.; Li, H.; Wang, S.; Zhuo, B.; Wang, S. Three-Dimensional Hybrid Networks of Molecularly Imprinted Poly (9-Carbazoleacetic Acid) and MWCNTs for Simultaneous Voltammetric Determination of Dopamine and Epinephrine in Plasma Sample. *Sensor. Actuat. B-Chem.* **2020**, *323*, 128669.

11. Lei, P.; Zhou, Y.; Zhang, G.; Zhang, Y.; Zhang, C.; Hong, S.; Yang, Y.; Dong, C.; Shuang, S. A Highly Efficient Chiral Sensing Platform for Tryptophan Isomers Based on a Coordination Self-Assembly. *Talanta* **2019**, *195*, 306-312.

12. Lei, P.; Zhou, Y.; Zhu, R.; Liu, Y.; Dong, C.; Shuang, S. Novel Strategy of Electrochemical Analysis of DNA Bases with Enhanced Performance Based on Copper Nickel Nanosphere Decorated N,B Doped Reduced Graphene Oxide. *Biosens. Bioelectron.* **2020**, *147*, 111735.

13. Xiong, J.; Bian, Q.; Lei, S.; Deng, Y.; Zhao, K.; Sun, S.; Fu, Q.; Xiao, Y.; Cheng, B. $Bi_{19}S_{27}I_3$ Nanorods: A New Candidate for Photothermal Therapy in the First and Second Biological Near-Infrared Windows. *Nanoscale* **2021**, *13*, 5369-5382.

14. Hashikawa, Y.; Fushino, T.; Murata, Y. Double-Holed Fullerenes. *J. Am. Chem. Soc.* **2020**, *142*, 20572-20576.

15. Tsai, C.; Tai, H.; Su, C.; Chiang, L.; Li, Y. Activated Microporous Carbon Nanospheres for Use in Supercapacitors. *ACS Appl. Nano Mater.* **2020**, *3*, 10380-10388.

16. Zhang, H.; Wu, T.; Chen, Y.; Zhang, Q.; Chen, Z.; Ling, Y.; Jia, Y.; Yang, Y.; Liu, X.; Zhou, Y.; Hollow Carbon Nanospheres Dotted with Gd-Fe Nanoparticles for Magnetic Resonance and Photoacoustic Imaging. *Nanoscale* **2021**, *13*, 10943-10952.

17. Li, N.; Guan, Y.; Li, Y.; Mi, H.; Deng, L.; Sun, L.; Zhang, Q.; He, C.; Ren, X. Co–Mo–P Carbon Nanospheres Derived from Metal-Organic Frameworks as a High-Performance Electrocatalyst Towards Efficient Water Splitting. *J. Mater. Chem. A* **2021**, *9*, 1143-1149.

18. Liu, X.; Vadiyar, M. M.; Kwon Oh, J.; Ye, Z. Designing Ultrasmall Carbon Nanospheres with Tailored Sizes and Textural Properties for High-Rate High-Energy Supercapacitors. *ACS Appl. Mater. Interfaces* **2021**, *13*, 32916-32929.

19. Xi, J.; Xie, C.; Zhang, Y.; Wang, L.; Xiao, J.; Duan, X.; Ren, J.; Xiao, F.; Wang, S. Pd Nanoparticles Decorated N-Doped Graphene Quantum Dots@N-Doped Carbon Hollow Nanospheres with High Electrochemical Sensing Performance in Cancer Detection. *ACS Appl. Mater. Interfaces* **2016**, *8*, 22563-22573.

20. Yan, J.; Duan, H.; Miao, L.; Ruhlmann, L.; Lv, Y.; Xiong, W.; Zhu, D.; Li, L.; Gan, L.; Liu, M. Core-Shell Hierarchical Porous Carbon Spheres with N/O Doping for Efficient Energy Storage.

Electrochim. Acta **2020**, *358*, 136899-136908.

21. Wen, X.; Zhang, D.; Shi, L.; Yan, T.; Wang, H.; Zhang, J. Three-Dimensional Hierarchical Porous Carbon with a Bimodal Pore Arrangement for Capacitive Deionization. *J. Mater. Chem.* **2012**, *22*, 23835-23844.
22. Selvi, B. R.; Jagadeesan, D.; Suma, B. S.; Nagashankar, G.; Arif, M.; Balasubramanyam, K.; Eswaramoorthy, M.; Kundu, T. K. Intrinsically Fluorescent Carbon Nanospheres as a Nuclear Targeting Vector: Delivery of Membrane-Impermeable Molecule to Modulate Gene Expression in Vivo. *Nano Lett.* **2008**, *8*, 10.
23. Lei, P.; Zhou, Y.; Zhu, R.; Dong, C.; Wu, S.; Shuang, S. Facilely Synthesized Ultrathin Ni_6MnO_8@C Nanosheets: Excellent Electrochemical Performance and Enhanced Electrocatalytic Epinephrine Sensing. *Sensor. Actuat. B-Chem.* **2021**, *326*, 128863.
24. Liu, Y.; Zhang, L.; Zhao, N.; Han, Y.; Zhao, F.; Peng, Z.; Li, Y. Preparation of Molecularly Imprinted Polymeric Microspheres Based on Distillation-Precipitation Polymerization for an Ultrasensitive Electrochemical Sensor. *Analyst* **2017**, *142*, 1091-1098.
25. Prasad, B. B.; Kumar, A.; Singh, R. Synthesis of Novel Monomeric Graphene Quantum Dots and Corresponding Nanocomposite with Molecularly Imprinted Polymer for Electrochemical Detection of an Anticancerous Ifosfamide Drug. *Biosens. Bioelectron.* **2017**, *94*, 1-9.
26. Huang, J.; Liu, Y.; Hou, H.; You, T. Simultaneous Electrochemical Determination of Dopamine, Uric Acid and Ascorbic Acid Using Palladium Nanoparticle-Loaded Carbon Nanofibers Modified Electrode. *Biosens. Bioelectron.* **2008**, *24*, 632-637.
27. Wang, J.; Yang, B.; Zhong, J.; Yan, B.; Zhang, K.; Zhai, C.; Shiraishi, Y.; Du, Y.; Yang, P. Dopamine and Uric Acid Electrochemical Sensor Based on a Glassy Carbon Electrode Modified with Cubic Pd and Reduced Graphene Oxide Nanocomposite. *J. Colloid Interface Sci.* **2017**, *497*, 172-180.
28. Xu, Z.; Liu, F.; Zhang, T.; Gu, Y.; Lu, N.; Xu, H.; Yan, X.; Song, Y.; Xing, Y.; Yu, D.; Zhang, Z.; Lu, P. Density Functional Theory-Assisted Electrochemical Assay Manipulated by a Donor-Acceptor Structure Toward Pharmaceutical Diagnostic. *Anal. Chem.* **2020**, *92*, 15297-15305.
29. Dong, Y.; Zheng, J. Tremella-Like ZIF-67/rGO as Electrode Material for Hydrogen Peroxide and Dopamine Sensing Applications. *Sensor. Actuat. B-Chem.* **2020**, *311*, 127918.

30. Bagheri, H.; Pajooheshpour, N.; Jamali, B.; Amidi, S.; Hajian, A.; Khoshsafar, H. A Novel Electrochemical Platform for Sensitive and Simultaneous Determination of Dopamine, Uric Acid and Ascorbic Acid Based on Fe_3O_4-SnO_2-Gr Ternary Nanocomposite. *Microchem. J.* **2017**, *131*, 120-129.

31. Devaraj, M.; Saravanan, R.; Deivasigamani, R.; Gupta, V. K.; Gracia, F.; Jayadevan, S. Fabrication of Novel shape Cu and Cu/Cu_2O Nanoparticles Modified Electrode for the Determination of Dopamine and Paracetamol. *J. Mol. Liq.* **2016**, *221*, 930-941.

32. Diaz-Diestra, D.; Thapa, B.; Beltran-Huarac, J.; Weiner, B. R.; Morell, G. L-cysteine Capped ZnS:Mn Quantum Dots for Room-Temperature Detection of Dopamine with High Sensitivity and Selectivity. *Biosens. Bioelectron.* **2017**, *87*, 693-700.

33. Fu, L.; Wang, A.; Lai, G.; Su, W.; Malherbe, F.; Yu, J.; Lin, C.; Yu, A. Defects Regulating of Graphene Ink for Electrochemical Determination of Ascorbic Acid, Dopamine and Uric Acid. *Talanta* **2018**, *180*, 248-253.

34. Halawa, M. I.; Wu, F.; Fereja, T. H.; Lou, B.; Xu, G. One-Pot Green Synthesis of Supramolecular Beta-Cyclodextrin Functionalized Gold Nanoclusters and their Application for Highly Selective and Sensitive Fluorescent Detection of Dopamine. *Sensor. Actuat. B-Chem.* **2018**, *254*, 1017-1024.

35. Numan, A.; Shahid, M. M.; Omar, F. S.; Ramesh, K.; Ramesh, S. Facile Fabrication of Cobalt Oxide Nanograin-Decorated Reduced Graphene Oxide Composite as Ultrasensitive Platform for Dopamine Detection. *Sensor. Actuat. B-Chem.* **2017**, *238*, 1043-1051.

36. Xu, B.; Zhu, M.; Zhang, W.; Zhen, X.; Pei, Z.; Xue, Q.; Zhi, C.; Shi, P. Ultrathin MXene-Micropattern-Based Field-Effect Transistor for Probing Neural Activity. *Adv. Mater.* **2016**, *28*, 3333-3339.

37. Zhao, D.; Yu, G.; Tian, K.; Xu, C. A Highly Sensitive and Stable Electrochemical Sensor for Simultaneous Detection towards Ascorbic Acid, Dopamine, and Uric Acid Based on the Hierarchical Nanoporous PtTi Alloy. *Biosens. Bioelectron.* **2016**, *82*, 119-126.

38. Kunpatee, K.; Traipop, S.; Chailapakul, O.; Chuanuwatanakul, S. Simultaneous Determination of Ascorbic Acid, Dopamine, and Uric Acid Using Graphene Quantum Dots/Ionic Liquid Modified Screen-Printed Carbon Electrode. *Sensor. Actuat. B-Chem.* **2020**, *314*, 128059.

39. Ma, F.; Yang, B.; Zhao, Z.; Zhao, Y.; Pan, R.; Wang, D.; Kong, Y.; Chen, Y.; Huang, G.; Kong, J.; Mei, Y. Sonication-Triggered Rolling of Janus Porous Nanomembranes for Electrochemical Sensing of Dopamine and Ascorbic Acid. *ACS Appl. Nano Mater.* **2020**, *3*, 10032-10039

40. Shu, Y.; Lu, Q.; Yuan, F.; Tao, Q.; Jin, D.; Yao, H.; Xu, Q.; Hu, X. Stretchable Electrochemical Biosensing Platform Based on Ni-MOF Composite/Au Nanoparticle-Coated Carbon Nanotubes for Real-Time Monitoring of Dopamine Released From Living Cells. *ACS Appl. Mater. Interfaces* **2020**, *12*, 49480-49488.

Chapter 4: Au/Pd-PPy/GR for simultaneous detection of DNA bases

This chapter demonstrates the preparation of gold/palladium-polyaniline/graphene nanocomposites (Au/Pd-PPy/GR) based on in-situ reduction reaction, and non-covalent interactions between gold/palladium-polyaniline and graphene. The successful fabrication of the nanocomposites was confirmed through various characterization techniques. Additionally, the chapter showcases the application of Au/Pd-PPy/GR nanocomposites, modified onto a glassy carbon electrode surface, for the simultaneous detection of four DNA bases.

This Chapter is published to the journal "ACS Applied Nano Materials":

Lei, P., Zhou, Y., Li, B., Liu, Y., Dong, C., and Shuang, S. (2022). Gold/palladium-polypyrrole/graphene nanocomposites for simultaneous electrochemical detection of DNA bases. ACS Applied Nano Materials, 5, 1635-1643.

Gold/palladium-polypyrrole/graphene nanocomposites for simultaneous electrochemical detection of DNA bases

Abstract

The unique combination of DNA bases is essential for storing genetic information. A reliable and accurate electrochemical sensor based on gold/palladium-polypyrrole/graphene nanocomposite (Au/Pd-PPy/GR) has been prepared to individually and simultaneously detect guanine (G), adenine (A), thymine (T), and cytosine (C). The bimetallic nanomaterial (Au/Pd-PPy) is used to enhance the sensing performance of DNA bases, and the GR could further increase the electroactive area and amplify the electrochemical response. As expected, the electrochemical sensor shows excellent electrocatalytic activity with well-separated current responses at 0.704 V (G), 0.976 (A), 1.164 (T), and 1.348 V (C). The prepared sensor exhibits the linear range of 1-350 μM for G, 5-300 μM for A, 20-900 μM for T, and 10-700 μM for C, respectively. The developed device is also demonstrated as an excellently sensitive and highly selective sensor to identify the four bases in calf thymus DNA, which provides the application of electrochemical sensors in bioscience.

Keywords: Synergistic catalyst, Electrochemical sensor, Simultaneous determination, DNA bases, Calf-thymus DNA

4.1 Introduction

Deoxyribonucleic acid (DNA) is an indispensable substance for the development and normal operation of an organism. The double helix of DNA is stabilized by hydrogen bonds established between the nitrogen-containing bases on the two strands [1]. Two complementary base pairs (adenine (A) and thymine (T), cytosine (C) and guanine (G)) play a critical role in the replication and transcription of genetic information [2,3]. However, abnormal changes or incorrect expression of base pairs may cause gene mutations, decreased immunity, and various diseases [4]. Therefore, developing a sensitive, accurate, and reliable method for the individual and simultaneous detection of four bases in biological DNA is more imperative for biological science and clinical diagnosis. Recently, various methods including capillary electrophoresis, spectrophotometry, chemiluminescence, and flow injection chemiluminescence have been proposed for bases detection [5-8]. Although these methods show certain advantages, they usually involve complex, time-consuming, and tedious sample preparation procedures, which greatly limit their further applications [9].

The electrochemical method presents the advantages of fast response, high sensitivity, and inexpensive, which is an ideal choice for direct measurement of targets. According to the reports, G and A could be determined on the traditional modified electrode. Vishnu and Badhulika [2] prepared a MoS_2-pencil graphite electrode for the reliable detection of G and A with well−separated oxidation peaks. Zhang's group [10] reported a novel electrochemical sensing platform based on the Mo_xC@C nanospheres for the detection of G and A, which displayed highly sensitive electrochemical responses. However, it is difficult to directly detect T or C because their oxidation potential is too high and also tends to overlap [11]. Besides, the electron transfer of T or C is slow on the electrode and the background current is too large, and T or C will be adsorbed on the electrode surface after oxidation, which causes a decrease in sensitivity and repeatability [12]. To the best of our knowledge, there is little literature on the electrochemical simultaneous detection of G, A, T, and C. Thus, it is highly desirable to develop the nanocomposite with the low detection limit, excellent electrocatalytic activity, and great sensitivity for the comprehensive analysis of four DNA bases.

The superior electrical conductivity, significant electron transport capability, ultrahigh specific surface area, and good chemical stability are favorable to the electrocatalytic properties of graphene (GR) [13]. Over the decades, GR has attracted widespread attention in the application of (bio)sensors owing to its unique characteristics [14-16]. Nonaka et al. [17] described the crumpled graphene-based nanocomposites electrode and explored it for application in nonenzymatic electrochemical H_2O_2 determination. Gong et al. [18] prepared a novel nanomaterial frompolyaniline/GR and also investigated its electrochemical properties for the sensitive detection of the HIV-1 gene. However, since GR is extremely susceptible to agglomerate owing to van der Waals force, it is particularly significant to modify GR for the improvement of the dispersibility.

It has been found that Au NPs exhibits outstanding electrocatalytic activity for detecting ascorbic acid, dopamine, urea, and other biological molecules [19-21]. It is reported that the bimetallic catalysts present higher catalytic performance than their single metal catalysts [22]. Many attempts have been made to explore bimetallic catalysts for the electrocatalytic reactions to further improve the electrocatalytic activity of Au NPs [23,24]. However, the surface effect and the small size effect lead to the agglomeration of the bimetallic catalysts, which limit its practical application. To overcome these shortcomings, bimetallic catalysts are loaded onto other supporting nanomaterials, such as carbon nanotubes and metal-organic frameworks [25,26]. As a conductive polymer, polypyrrole (PPy) has become a potentially useful nanomaterial in the field of sensors due to its good electrochemical response characteristics. PPy has been successfully used in various types of electrochemical sensors [27-29]. The negatively charged imino groups on the PPy nanoparticles surface are beneficial to effectively avoid the aggregation of metal nanoparticles and provide an excellent biosensing matrix for the quantification of bases in this study.

Au/Pd-PPy/GR nanocomposite has been successfully synthesized and applied to individually and simultaneously detect the four DNA bases. The high electrical conductivity of PPy was beneficial to enhance the conductivity of the electrode surface. Au/Pd were loaded onto the PPy surface forming a bimetal nanomaterial to improve the sensing capability. GR was utilized to further amplify the electrochemical signal and improve the electroactive area. Surprisingly, the synergistic effect of the

nanocomposite exhibited effectively excellent electrocatalytic performance with outstanding sensitivity, selectivity, and stability toward DNA bases. The prepared sensor created a new opportunity for the development of new reliable biological detection systems.

4.2 Materials and Methods

4.2.1 Materials

Carboxylated graphene (GR) was ordered from Chengdu Organic Chemicals Co. Ltd., Chinese Academy of Sciences. G, A, T, C, pyrrole (99%), anhydrous ferric chloride ($FeCl_3$, AR), sodium borohydride ($NaBH_4$, 98%), chloroauric acid ($HAuCl_4 \cdot 4H_2O$, ≥99.9%), palladium chloride ($PdCl_2$, 99.99%), and calf-thymus DNA were purchased from Aladdin Chemistry Co., Ltd. (Shanghai, China).

4.2.2 Instruments

Field-emission scanning electron microscopy (FESEM), energy-dispersive spectroscopy (EDS) and high-resolution transmission electron microscopy (HRTEM) were acquired using the JSM-7900F (JEOL, Tokyo, Japan) and (JEM-2100F). X-ray diffraction (XRD) patterns were measured with a Bruker D8 Venture advanced powder X-ray diffraction system. X-ray photoelectron spectroscopy (XPS) were acquired on an AXIS ULTRA DLD X-ray photoelectron spectrometer (Kratos, Tokyo, Japan). Electrochemical investigations were carried out using a CHI660E (Chenhua Instrument company, Shanghai, China) electrochemical workstation.

4.2.3 Electrochemical Measurements

Cyclic voltammetry (CV) measurements were carried out in above solution at 0.05 V s^{-1}. Electrochemical impedance spectroscopy (EIS) was performed on an CHI660E in the frequency range from 1 Hz to 100 kHz in 5 mM $[Fe(CN)_6]^{3-/4-}$ including 0.1 M KCl. Differential pulse voltammetry (DPV): increment potential, 0.004 V; pulse amplitude, 0.05 V; pulse width, 0.06 s; pulse period, 0.2 s; quiet time, 2 s.

4.2.4 Synthesis of the Au/Pd-PPy/GR

0.25 mL pyrrole was injected into 50 mL H_2O stirring for 15 min at 5 °C to distribute pyrrole evenly scattered in H_2O. After slowly adding 1.0 mL of a 0.1 M $FeCl_3$ solution, the reaction was continued for 5 h. Subsequently, 3 mL of 5.0 mM $HAuCl_4$ and 3 mL of 5.0 mM $PdCl_2$ were added to the solution and stirred for 30 min. 10 mL of 0.05 M $NaBH_4$ was slowly transferred to the above mixture using a pipette and the mixture was stirred for 2 h. After adding 0.5 mg of GR and stirring for 30 min, the product was centrifuged and washed with ethanol and water several times, and dried under vacuum at 50 °C overnight.

4.2.5 Fabrication of the Sensor

The glassy carbon electrode (GCE) was repeatedly polished with Al_2O_3, successively rinsed with ultrapure water and ethanol， and dried at room temperature prior to experimentation. 1.0 mg Au/Pd-PPy/GR nanocomposite were dispersed in 1 mL ultrapure water and sonicated for 15 min, and then 6.0 μL of the suspension was carefully transferred onto the GCE surface. After drying under an infrared lamp for 8 min, the obtained Au/Pd-PPy/GR modified GCE was marked as Au/Pd-PPy/GR/GCE. Using the same procedure, other modified GCEs were obtained. The preparation scheme of Au/Pd-PPy/GR/GCE to detect the four bases is illustrated in Fig. 4.1.

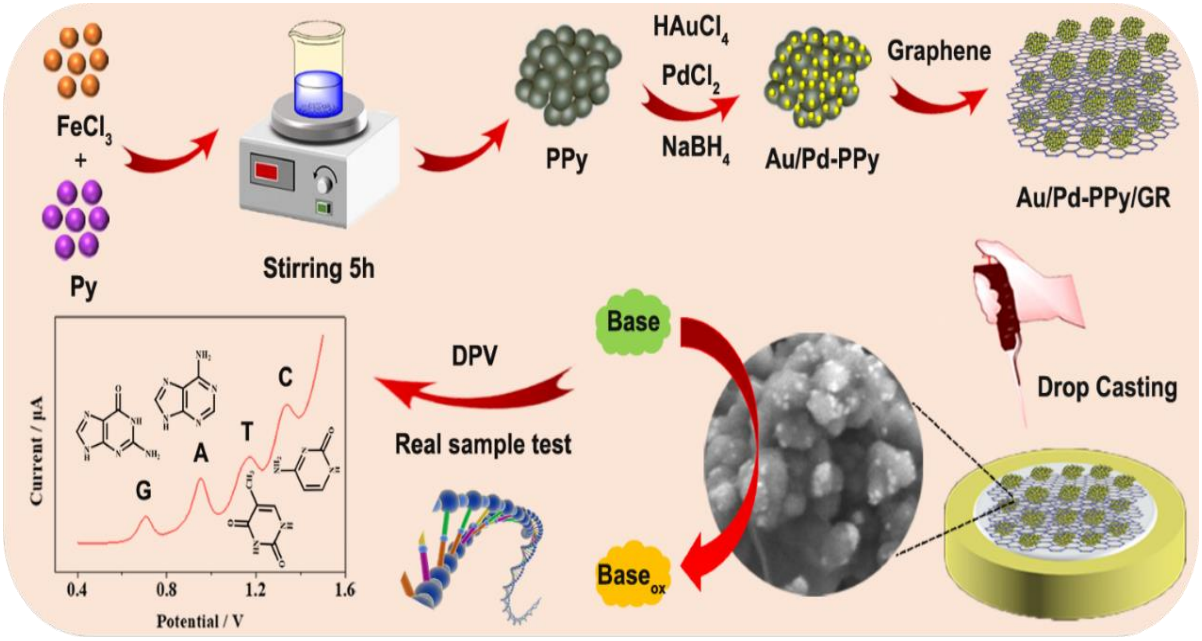

Fig. 4.1: The fabrication of Au/Pd-PPy/GR/GCE for DNA bases determination

4.3 Results and Discussions

4.3.1 Structural and Physical Features of Au/Pd-PPy/GR

FESEM, EDS, and elemental mapping were applied to characterize the structural morphology of the synthesized Au/Pd-PPy/GR nanocomposite. The FESEM image of PPy shows an aggregated and small sphere structure in Fig. 4.2A, and the diameters are mainly distributed in the range of 200-400 nm. When $HAuCl_4$ and $PdCl_2$ are used to modify PPy, the images clearly show that the Au/Pd are formed on the surface of PPy and the Au/Pd-PPy is obtained. There is no obvious agglomeration of Au/Pd on the PPy surface, due to the negatively charged imino groups on the PPy surface, which are beneficial to effectively avoid the aggregation of Au/Pd in Fig. 4.2B. Wrinkles of GR nanosheets are clearly observed, and Au/Pd-PPy is dispersed on the GR surface or embedded in the layer with close interfacial contact in Fig. 4.2C and D. The GR nanosheets could effectively enhance the conductivity of the composites and increase the specific surface area. The element mapping of Au/Pd-PPy/GR nanocomposite demonstrates the homogeneous distribution of elements, including C, O, N, Pd, and Au in Fig. 4.2E. The distribution of different elements in Au/Pd-PPy/GR nanocomposite is investigated by EDS in Fig. 4.2F. As expected, the appearance of C, O, N, Pd, and Au elements could be observed without any other discernible impurities.

HRTEM images depict the morphology of Au/Pd–PPy/GR. Fig. S4A and S4B confirm spherical PPy aggregates and sheet-like GR at different magnifications. Fig. S4C and S4D clearly show the atomic lattices of Pd and Au. The EDX spectrum of Au/Pd-PPy/GR in Fig. S4E exhibits characteristic peaks of C, O, N, Pd, and Au elements. Additionally, the EDX mapping in Fig. S4F demonstrates the presence of C, O, N, Pd, and Au elements in Au/Pd-PPy/GR.

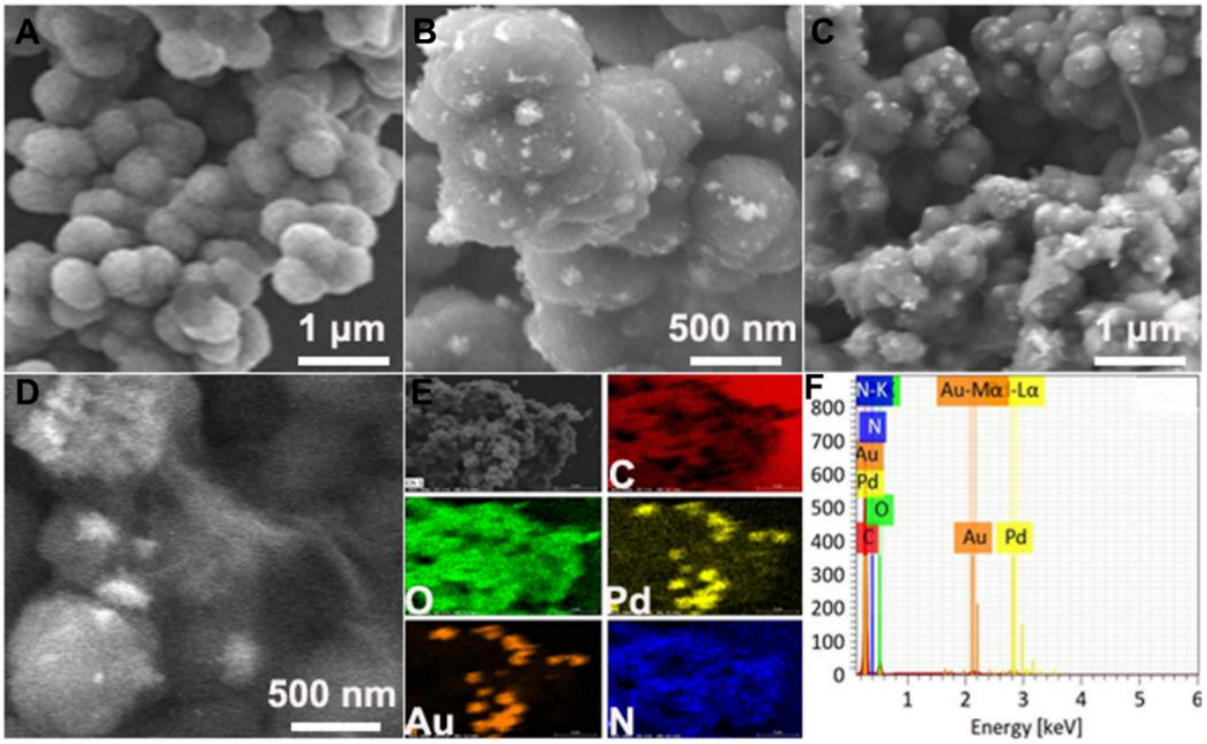

Fig. 4.2: FESEM images of (A) PPy, (B) Au/Pd-PPy, and (C, D) Au/Pd-PPy/GR; the element mapping (E) and the EDS spectra (F) of Au/Pd-PPy/GR nanocomposite

To further confirm the element content, the nanocomposite were studied by XPS. The wide spectrum of Au/Pd-PPy/GR shows the existence of C, O, N, Pd, and Au in Fig. 4.3A. The C 1s core-level spectrum shows four single binding energies which corresponded to C=C (284.6 eV), C-N (285.1 eV), C-C (285.8 eV), and C=O (288.1 eV) in Fig. 4.3B, originating from the PPy and the GR nanosheets [29,18]. The peaks at 533.6 eV and 532.0 eV in the O 1s spectra refere to the carboxyl group in the GR nanosheets in Fig. 4.3C [14]. Furthermore, the N 1s spectra could be divided into two peaks at 339.1 eV and 400.4 eV in Fig. 4.3D, which are mainly attributed to pyrrolic-N [29]. The Pd 3d spectra reveales strong diffraction peaks at 335.7 eV ($3d_{5/2}$) and 341.0 eV ($3d_{3/2}$) [30] in Fig. 4.3E. The peak separation is approximately 5.3 eV, demonstrating that Pd^0 is successfully formed by chemical reduction of $PdCl_2$ in Fig. 4.3F. The Au 4f core-level spectrum exhibits two characteristic peaks corresponding to Au $4f_{7/2}$ (83.8) and Au $4f_{5/2}$ (87.5), and the weaker peaks at 85.0 and 89.1 eV are assigned to Au (I) and Au (III) oxide, respectively [31]. The above XPS spectrum indicated that C, O, N, Pd, and Au were present in Au/Pd-PPy/GR nanocomposite.

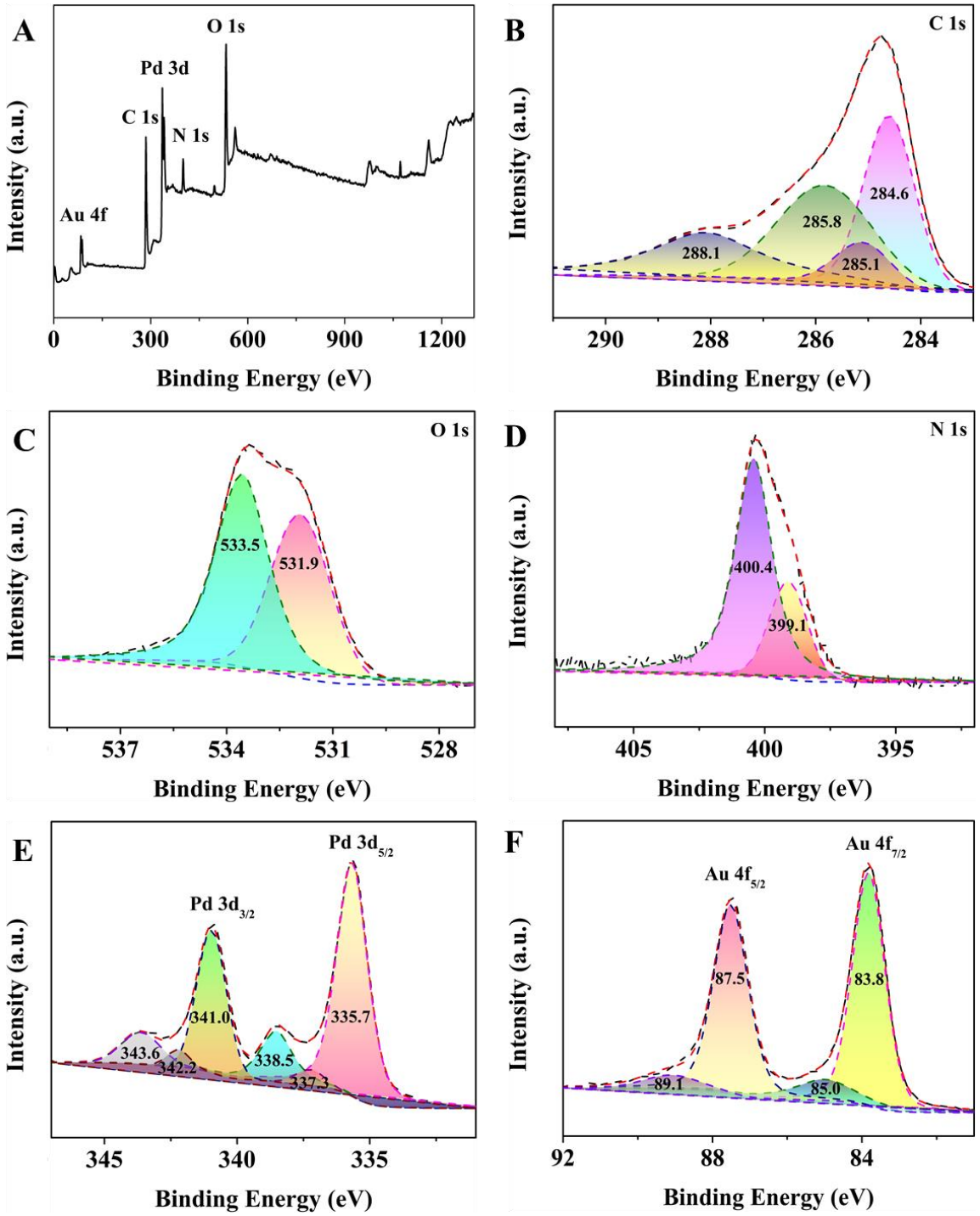

Fig. 4.3: XPS spectra of Au/Pd-PPy/GR: (A) wide spectrum; (B) C1s; (C) O1s; (D) N1s; (E) Pd 3d; (F) Au 4f

The bonding characterization for PPy, GR, and Au/Pd-PPy/GR were recorded via FT-IR spectra (Fig. 4.4A). The PPy characteristic peaks are found at 1544, 1296, and 1201 cm^{-1}, which referred to the C=C, C-C, and C-N stretching, respectively [29]. The peaks at 1460, 1400, 916, and 780 cm^{-1} are attributed to Py ring stretching, and the band at 3390 cm^{-1} is assigned to N-H stretching [32]. The characteristic peaks

of GR at 1743, 1630, and 1116 cm^{-1} are attributed to C=O (-COOH), C=C, and C-O, respectively [18]. The FT-IR spectra of the Au/Pd-PPy/GR nanocomposite showes slight shifts and retained characteristic peaks of the pure GR and PPy. Further, the crystal phase of PPy, GR, and Au/Pd-PPy/GR were investigated via XRD analysis in Fig. 4.4B. The diffraction characteristic peak appear at 10.3° and 24.6° corresponding to the amorphous structure of PPy [32]. Typically, the strongest peak for GR located at 2θ=25.1° reveals the characteristic interlayer stacking of the aromatic system (002) [15]. For the Au/Pd-PPy/GR, the characteristic peaks located at 38.4°, 44.6°, 65.1°, and 77.9° are corresponding to (111), (200), (220), and (311) planes of the Au/Pd [21,33]. The above characterization results confirmed that the Au/Pd-PPy/GR nanocomposite have been successfully synthesized.

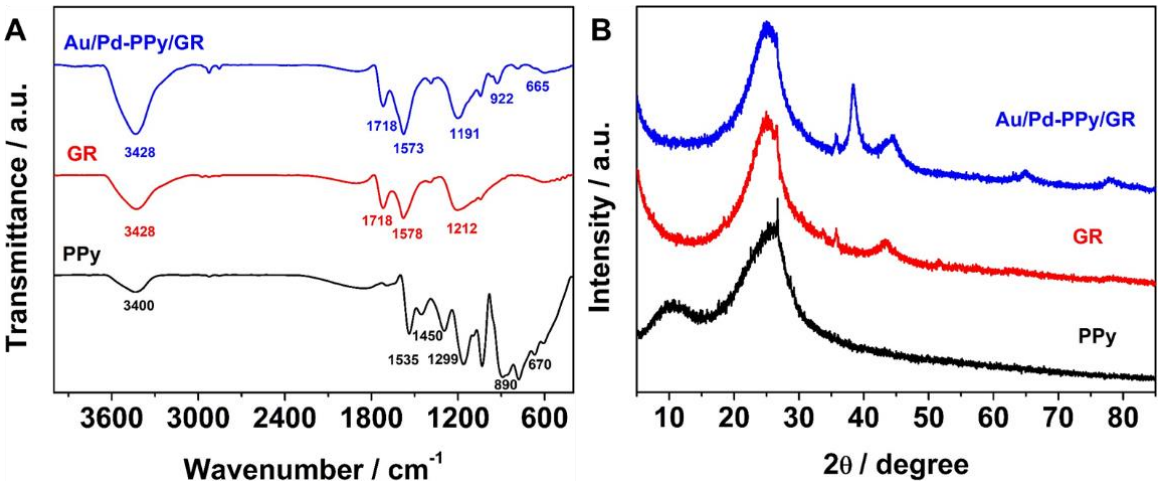

Fig 4.4: (A) FT-IR spectra and (B) XRD of PPy, GR, and Au/Pd-PPy/GR

4.3.2 Electrochemical Performance

The electrochemical properties of modified electrodes was explored through CV and EIS in the $[Fe(CN)_6]^{3-/4-}$ redox system. The redox peak current of the PPy/GCE increases as compared with the bare GCE owing to the introduction of the highly conductive PPy in Fig. 4.5A. After the modification of GR, the peak current obviously increases with a peak separation of 86 mV, indicating GR can enhance the conductivity and enlarge the specific surface area. The redox peak current from Au/Pd-PPy/GR/GCE is higher than that of the other electrodes, which is attributed to the increase of available active sites and faster electron transfer efficiency caused by the co-contribution of Au/Pd and PPy/GR. The EIS measurement was applied to measure the interfacial properties. Fig. 4.5B demonstrates that the electron

transfer resistance (Rct) of Au/Pd-PPy/GR/GCE is lower than that of bare GCE (232.8 Ω), PPy/GR/GCE (85.5 Ω), and PPy/GCE (10.7 Ω). It is mainly attributed to the synergistic effect of PPy, GR, and Au/Pd, which promotes electron transfer during the redox process.

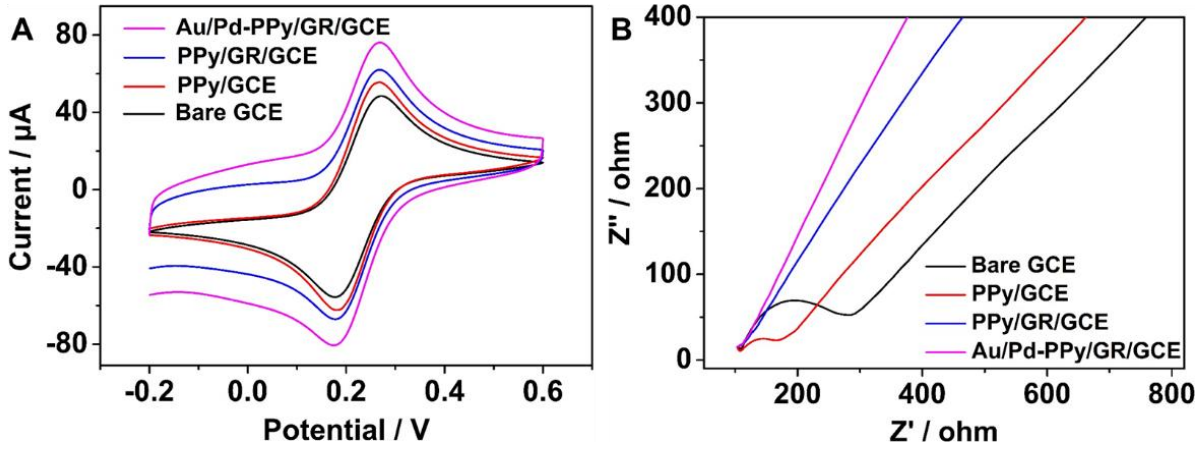

Fig.4.5: (A) The CVs and (B) EIS of bare GCE, PPy/GCE, PPy/GR/GCE, and Au/Pd-PPy/GR/GCE in 5.0 mM $Fe(CN)_6^{3-/4-}$ containing 0.1 M KCl

The electrochemical responses of Au/Pd-PPy/GR/GCE with and without DNA bases were studied by CV. There are no peaks in the blank scan without DNA bases, indicating that the electrochemical responses of Au/Pd-PPy/GR/GCE are definitely from the oxidation of DNA bases in Fig. 4.6A-D. Only the oxidation peaks can be observed, revealing that the redox process is irreversible. It is worth noting that the highest oxidation peaks are found at 0.704 V, 0.976, 1.164, and 1.348 V in Fig. 4.6E, respectively, indicating the proposed Au/Pd-PPy/GR nanocomposite exhibited excellent electrocatalytic performance towards the oxidation of DNA bases. The differential pulse voltammetry (DPV) diagrams of bare GCE, Au/Pd/GCE, PPy/GCE, Au/Pd-PPy/GCE, and Au/Pd-PPy/GR/GCE in mixed solutions are investigated in Fig. 4.6F. No oxidation peaks are observed at the bare GCE. In contrast, the clearly defined oxidation peaks and enhanced current responses are observed at other modified electrodes. Amazingly, compared with Au/Pd/GCE, Au/Pd-PPy/GCE and PPy/GCE, the Au/Pd-PPy/GR/GCE enhances the electrochemical responses approximately by factor 2 and 4, respectively. The excellent performance of Au/Pd-PPy/GR/GCE towards the electrochemical oxidation of four DNA bases might be attributed to the following reasons: (a) The nanocomposite exhibits excellent conductivity; (b) PPy with large specific

surface area provids abundant reaction site, which was beneficial to the formation of Au/Pd; (c) The effective structural integration of GR, PPy, and Au/Pd causes a synergistic effect.

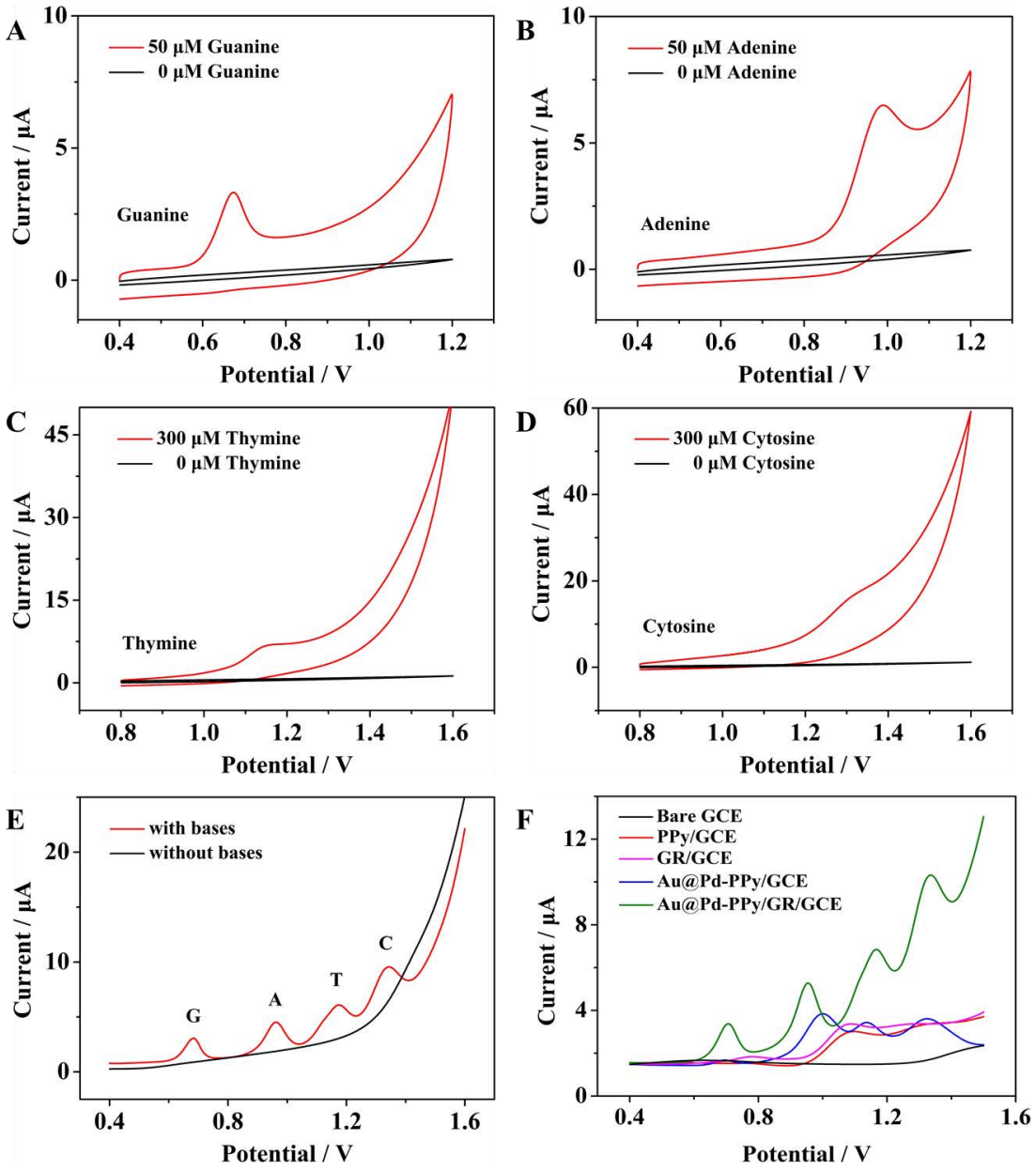

Fig. 4.6: CV and DPV curves of Au/Pd-PPy/GR/GCE with and without the (A) G, (B) A, (C) T, and (D) C; (E) DPV curves of Au/Pd-PPy/GR/GCE with and without G, A, T, and C; (F) DPV curves of different modified electrodes in a mixture including G, A, T, and C

Meanwhile, the electrochemical responses at bare GCE and Au/Pd-PPy/GR/GCE with DNA bases are studied by CV in Fig. 4.7. A weak peak current can be observed at bare GCE. The enhancement of current signal and the left shift of spike potential can be observed at Au/Pd-PPy/GR/GCE, which illustrates that Au/Pd-PPy/GR displays excellent electrocatalytic activity for DNA bases.

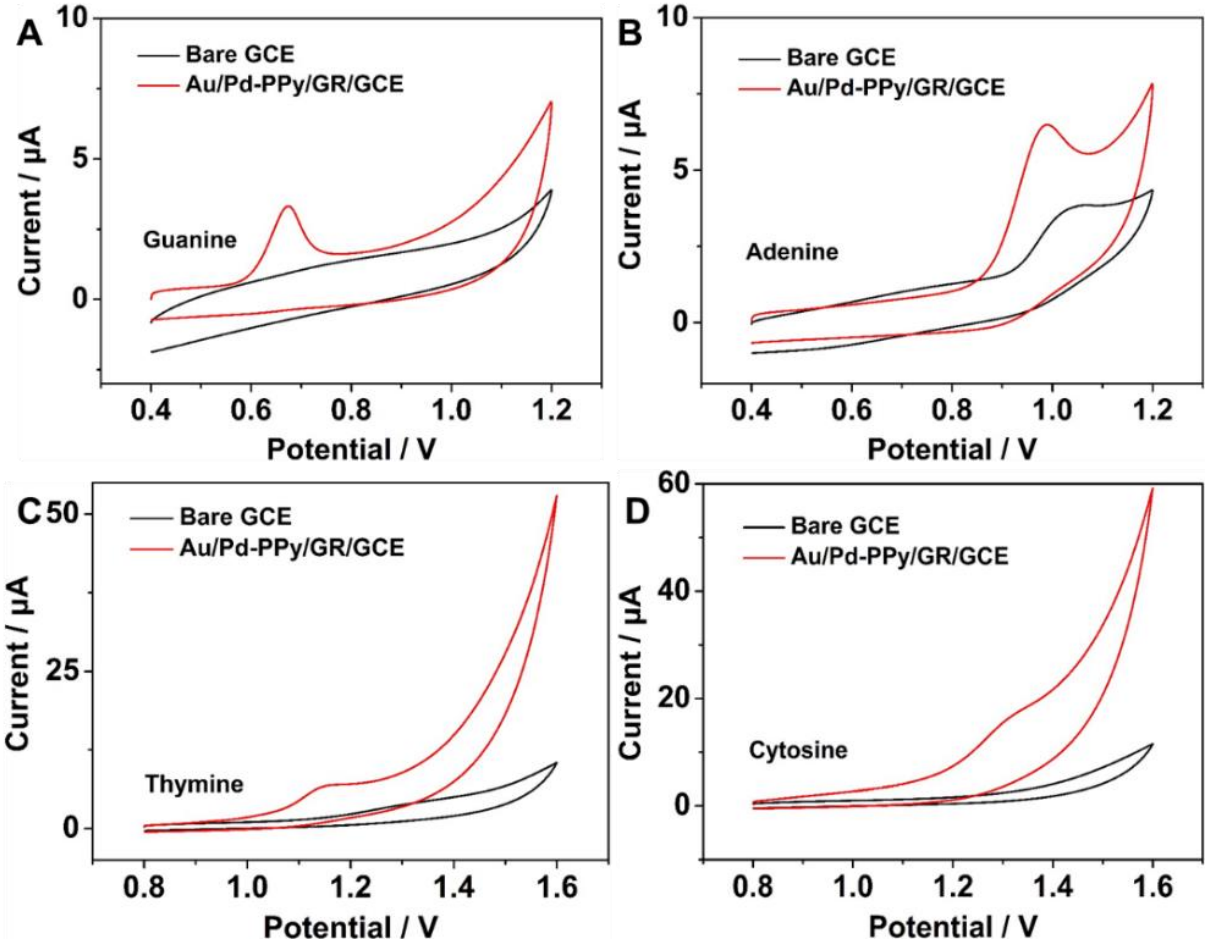

Fig. 4.7: CV curves of (A) 50 µM G, (B) 50 µM A, (C) 300 µM T, and (D) 300 µM C in 0.1 M PBS (pH 7.0) at bare GCE and Au/Pd-PPy/GR/GCE

4.3.3 Effects of pH, Accumulation Condition, and Scan Rate on Detection of DNA Bases

Previous reports, indicate that the adsorption of DNA bases at the electrode surface is independent on the accumulation potential and that the accumulation process could be carried out under open-circuit conditions [9, 34-36]. Therefore, the effect of accumulation time is evaluated with the accumulation potential of 0.4 V. The oxidation peak currents increase with extending the accumulation time and leveled off after 80 s, which indicates that the adsorption of DNA bases at Au/Pd-PPy/GR/GCE is saturated in Fig. 4.8.

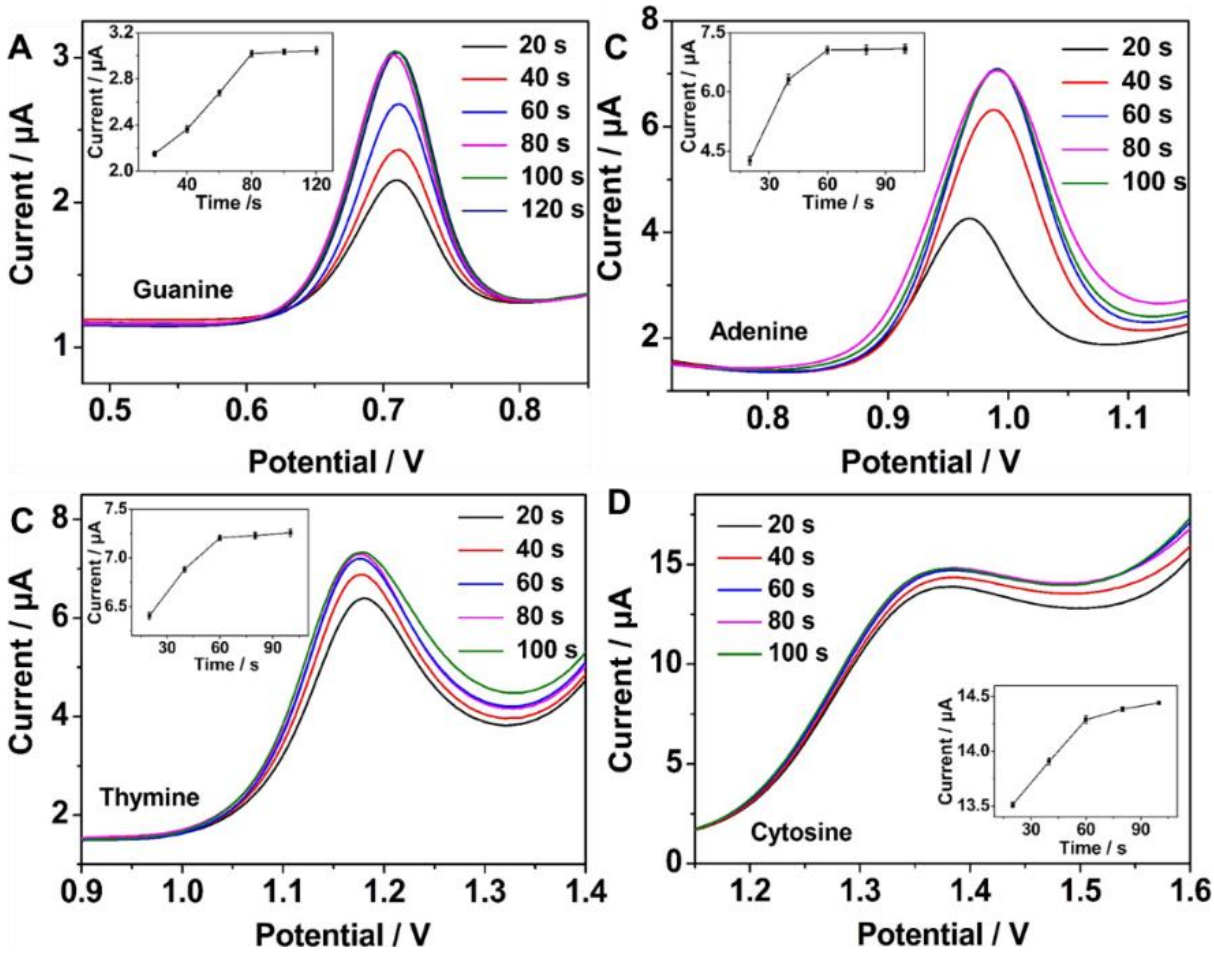

Fig. 4.8: The DPVs of DNA bases at Au/Pd–PPy/GR/GCE with different accumulation time from solutions containing (A) 50 μM G, (B) 50 μM A, (C) 300 μM T, and (D) 300 μM C in 0.1 M PBS (pH 7.0) at the accumulation potential of 0.4 V

The effect of different pH (3.0-9.0) towards the electrochemical responses of DNA bases at Au/Pd-PPy/GR/GCE is investigated in Fig. 4.9. For G and A, the maximum electrochemical responses are observed at pH 3.0, and the electrochemical responses decreased with increasing pH. The phenomenon may be caused by protonation of G and A. G and A are more easily oxidized after protonation under acidic conditions, which led to an increase of the electrochemical response. The oxidation of T and C at Au/Pd-PPy/GR/GCE is favorable in neutral solution. To obtain the ideal results, pH 7.0 is chosen as the optimum pH for further investigations to simulate the physiological conditions of actual samples.

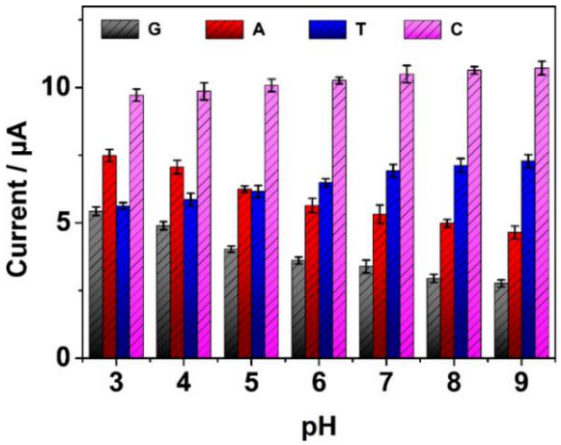

Fig. 4.9: The current of 50 µM G and A, 300 µM T and C *vs* pH to explore the preference pH

The effect of different scan rate at Au/Pd-PPy/GR/GCE was investigated via the LSV. In Fig. 3.10A-D, the well-defined oxidation peak currents increase with the increase of scan rate (20-240 mV s^{-1}). The corresponding linear regression equations are expressed in inset Fig. 4.10A-D. The consequences demonstrate that the electrode reactions of DNA bases at Au/Pd-PPy/GR/GCE are an adsorption-controlled irreversible process [36].

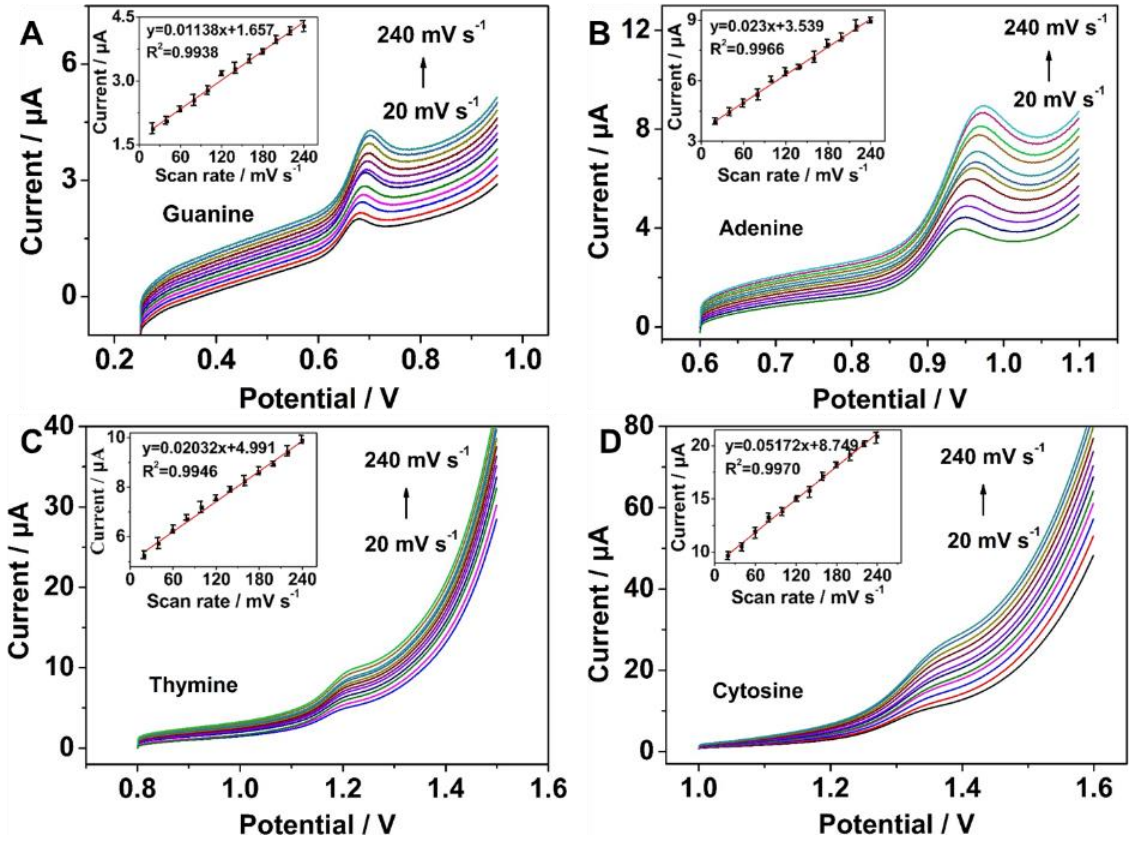

Fig. 4.10: LSV curves of Au/Pd-PPy/GR/GCE (A) 50 µM G, (B) 50 µM A, (C) 300 µM T, and (D) 300 µM C with different scan rate. Insets: the plots of current *vs* scan rate

4.3.4 Determining the DNA Bases

The individual determination of G, A, T, and C in different concentrations are studied at Au/Pd-PPy/GR/GCE using DPV in Fig. 4.11. The detection limits are calculated from the linear regression to be 0.067 μM (G), 0.18 μM (A), 2.42 μM (T), and 1.84 μM (C) (LOD=3Sb/k), respectively. As can be seen from Figure S8, the oxidation reactions of DNA bases at Au/Pd-PPy/GR/GCE are an adsorption-controlled irreversible process. When DNA bases concentration is low, a small amount of DNA bases were adsorbed on the surface of Au/Pd-PPy/GR/GCE, and they lost electrons and undergo oxidation reactions, thereby generating lower peak currents. The peak currents gradually increase along with DNA bases concentration increasing. The possible electrochemical oxidation mechanism was presented in the supporting information (Fig. S5)

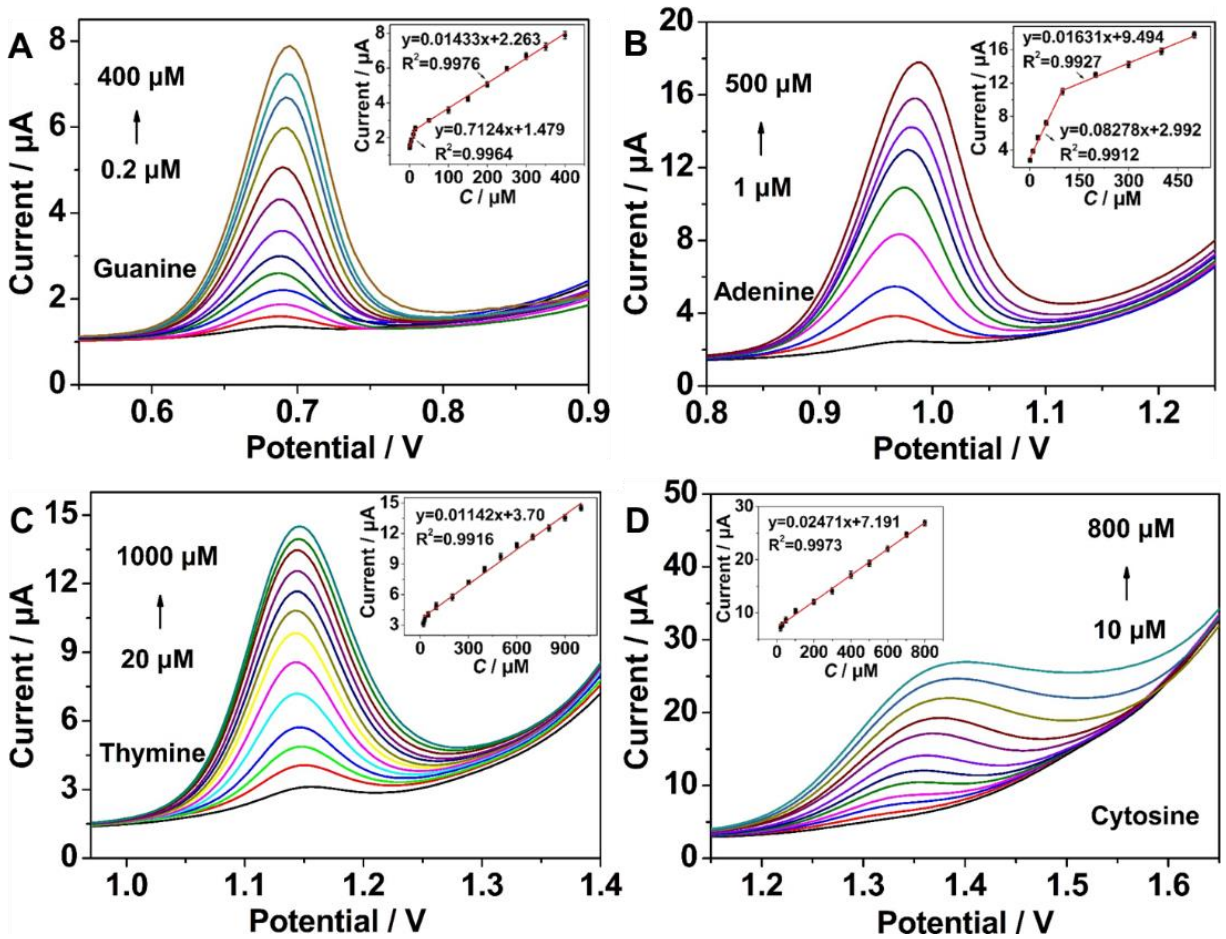

Fig. 4.11: DPV curves for the Au/Pd-PPy/GR/GCE in the presence of different concentrations of (A) G, (B) A, (C) T, and (D) C and their corresponding calibration plots

The individual determination in a mixture was investigated by changing the concentration of the target substance while keeping another substance constant. The peak currents increase along with G concentration increasing in the presence of 50 µM A in Fig. 4.12A. Similarly, the peak currents of A, T, and C increase with the concentration, then reach the maximum in Fig. 4.12B-D. The corresponding linear regression equations are expressed in inset Fig. 4.12A-D. The linear concentration ranges of DNA bases are 1-350 µM, 5-300 µM, 20-900 µM, and 10-700 µM, respectively. The LODs are 0.13 µM (G), 0.21 µM (A), 3.57 µM (T), and 2.69 µM (C).

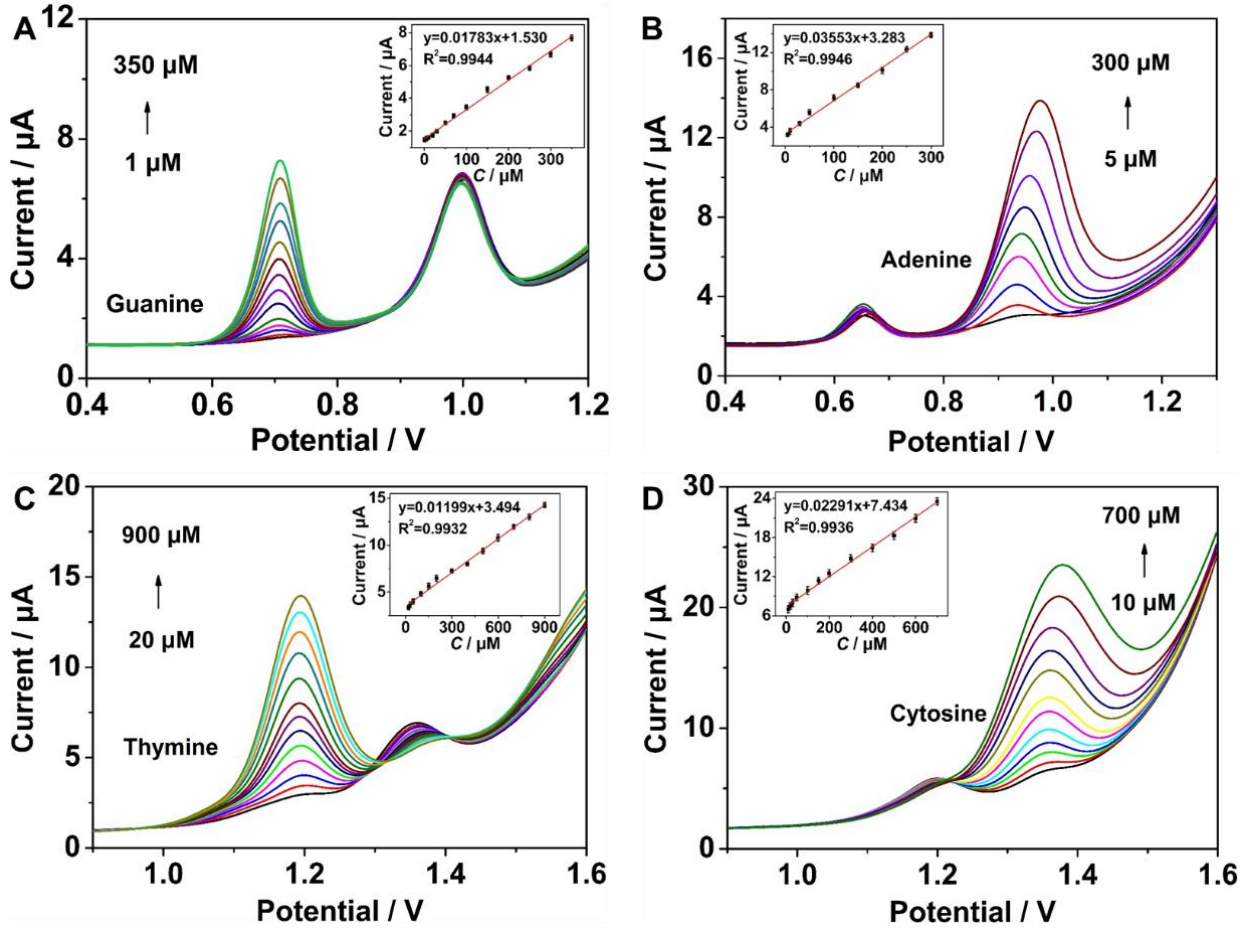

Fig. 4.12: DPV curves of different concentrations of (A) G in the presence of 50 µM A; (B) A in the presence of 50 µM G; (C) T in the presence of 150 µM C; and (D) C in the presence of 150 µM T at Au/Pd-PPy/GR/GCE

The prepared Au/Pd-PPy/GR/GCE is evaluated the simultaneous detection of DNA bases in Fig. 4.13A. The DPV diagrams show well-defined peaks at 0.704 V (G), 0.976 V (A), 1.164 V (T), and 1.348 V (C).

As expected, all of the peak currents increase with the increase of DNA bases concentrations (inset Fig. 4.13A). On the basis of the results, the obtained linear regression equations are written as follows:

G: I_{pa} (μA) = 0.01335 C (μM) + 2.638 (R^2 = 0.9912)

A: I_{pa} (μA) = 0.02343 C (μM) + 4.488 (R^2 = 0.9920)

T: I_{pa} (μA) = 0.01417 C (μM) + 45776 (R^2 = 0.9933)

C: I_{pa} (μA) = 0.01937 C (μM) + 7.340 (R^2 = 0.9906)

The results indicates that the simultaneous determination of four DNA bases in the mixed solutions is feasible. The linear ranges of the DNA bases are different from that obtained in the individual determination, which may be attributed to the competitive adsorption of the DNA bases on the Au/Pd-PPy/GR/GCE surface. Compared with the previously reported results, the performance of the present sensor exhibits a wider linear range and lower detection limit in Table 4.1.

4.3.5 DNA Base Detection from Calf-Thymus DNA

The application reliability and potential of the sensor were evaluated in the pretreated calf-thymus DNA. The well-defined peaks of DNA bases are measured by DPV in Fig. 4.13B. The contents are calculated to be 21.92 (G), 27.28 (A), 28.26 (T), and 22.54 (C) mol%. For the pretreated calf-thymus DNA, the value of (G + C)/(A + T) is calculated as 0.80, which is close to the standard value of 0.77 [34].

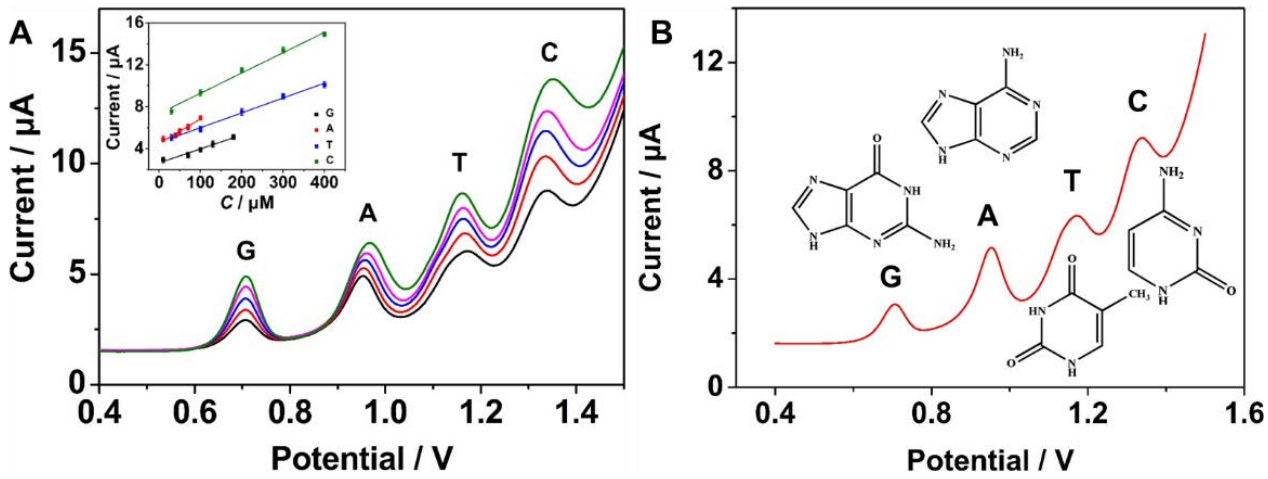

Fig. 4.13: (A) DPV curves of Au/Pd-PPy/GR/GCE in different concentrations of G, A, T, and C; (B) DPV of calf-thymus DNA on Au/Pd-PPy/GR/GCE

Table 4.1: Comparison of various DNA bases sensors

Electrode	Method	DNA bases	Linear range (μM)	LOD (μM)	Ref.
poly(PPI)/GCE	SWV	G	3-300	0.28	[37]
		A	1-300	0.24	
		T	30-800	3.2	
		C	20-750	6.8	
polyaniline/MnO_2/GCE	DPV	G	10-240	7.80	[38]
		A	10-150	7.70	
		T	10-1100	4.90	
		C	10-500	4.10	
MWCNT/Ch/GCE	DPV	G	0.20-450	0.06	[39]
		A	0.4-500	0.15	
		T	1-550	0.35	
		C	1.5-600	0.4	

		G	1.0-94	0.687	
CuO NPs/MCPE	DPV	A	1.0-94	0.472	[40]
		T	1.0-244	0.111	
		G	1.0-180	0.17	
Cu@Ni/MWCNTs/GCE	DPV				[41]
		A	2.0-150	0.33	
		G	100-280	0.033	
B-cyclodectrin/MWCNTs/GCE	DPV	A	4.0-30	0.0007	[42]
		T	80-400	0.006	
		G	8.0-130	4.80	
MWCNT-Fe_2O_3@PDA-Ag/CPE	DPV				[43]
		A	10-120	2.90	
		G	0.03-122	0.0085	
Mo_xC@C/GCE	DPV				[10]
		A	0.02-122	0.008	

		G	1-350	0.13	
		A	5-300	0.21	
Au/Pd-PPy/GR/GCE	DPV				This work
		T	20-900	3.57	
		C	10-700	2.69	

4.3.6 Stability, Reproducibility and Anti-interference Ability

Au/Pd-PPy/GR/GCE is stored at room temperature for 17 days, and the DPV electrochemical responses of DNA bases are recorded every 2 days to study its stability in Fig. 4.14A. Au/Pd-PPy/GR/GCE has the ability to maintain 95.8% of its initial current response, so it has good stability. The reproducibility of the results is analyzed by recording the DPV electrochemical responses of DNA bases via 20 successive measurements at the same Au/Pd-PPy/GR/GCE. No obvious changes are observed in Fig. 4.14B. The obtained results demonstrated the high reproducibility of the sensor.

Several compounds from other biologically relevant molecules have been examined to investigate the anti-interference ability of the sensor in the presence of DNA bases. The results manifested that there was almost no interference from $CaCl_2$, $CuSO_4$, KCl, KNO_3, Na_2SO_4, ascorbic acid, lactose, sucrose, glucose, glycine, glutathione, uracil, and cytosine (Table S1). Thus, the sensor showed a high anti-interference ability.

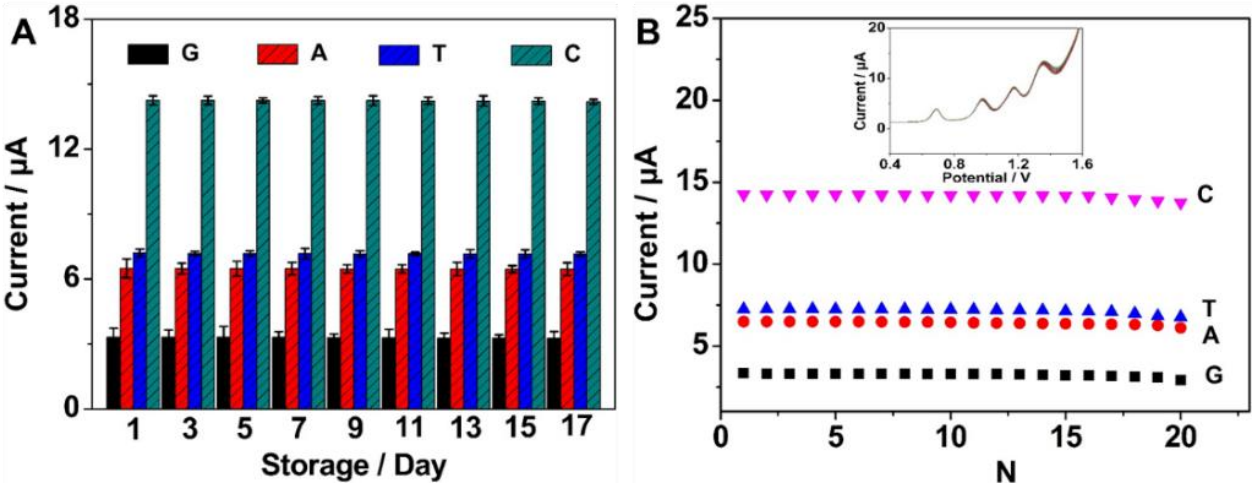

Fig. 4.14: The stability (A) and reproducibility (B) of Au/Pd-PPy/GR/GCE in determination of 50 μM G, 50 μM A, 300 μM T and 300 μM C

4.4 Conclusion

Au/Pd-PPy/GR nanocomposite have been successfully prepared and confirmed by various characterization methods (FESEM, EDS, XPS, XRD, and FT-IR). The nanocomposite were used to fabricate an electrochemical electrode for simultaneously detect G, A, T, and C. The introduction of electrochemically active Au/Pd, conductive PPy, and the signal amplification of GR played positive roles in accelerating charge transfer, resulting in excellent electrochemical performance of the Au/Pd-PPy/GR. Au/Pd-PPy/GR/GCE demonstrated a competitive sensitivity and selectivity for detection of the four DNA bases. The good accuracy of Au/Pd-PPy/GR/GCE has been confirmed by detecting four bases in calf-thymus DNA. This study showed a simple preparation process and provided remarkable electrocatalytic property in comparison with the previous reports. More importantly, this study not only presented a novel vision for DNA base determination but also could be expanded to more nanocomposites to develop their applications in electrochemical detection technology and biotechnology.

References

1. Kato, D.; Sumimoto, M. Ueda, A. Hirono, S. Niwa, O. Evaluation of Electrokinetic Parameters for All DNA Bases with Sputter Deposited Nanocarbon Film Electrode. *Anal. Chem.* **2012**, *84*, 10607-10613.

2. Vishnu, N.; Badhulika, S. Single Step Grown MoS_2 on Pencil Graphite as an Electrochemical Sensor for Guanine and Adenine: A Novel and Low Cost Electrode for DNA Studies. *Biosens. Bioelectron.* **2019**, *124*, 122-128.

3. Ng, K.L.; Khor, S.M. Graphite-Based Nanocomposite Electrochemical Sensor for Multiplex Detection of Adenine, Guanine, Thymine, and Cytosine: a Biomedical Prospect for Studying DNA Damage. *Anal. Chem.* **2017**, *89*, 10004-10012.

4. Siuzdak, K.; Ficek, M.; Sobaszek, M.; Ryl, J.; Gnyba, M.; Niedziałkowski, P.; Malinowska, N.; Karczewski, J.; Bogdanowicz, R. Boron-Enhanced Growth of Micron-Scale Carbon-Based Nanowalls: a Route Toward High Rates of Electrochemical Biosensing. *ACS Appl. Mater. Interfaces* **2017**, *9*, 12982-12992.

5. Yang, F.; Ge, L.; Yong, J. W.; Tan, S.; Li, S. Determination of Nucleosides and Nucleobases in Different Species of Cordyceps by Capillary Electrophoresis-Mass Spectrometry. *J. Pharm. Biomed. Anal.* **2009**, *50*, 307-314.

6. Pang, S.; Zhang, Y.; Wu, C.; Feng, S. Fluorescent Carbon Dots Sensor for Highly Sensitive Detection of Guanine. *Sensor. Actuat. B-Chem.* **2016**, *222*, 857-863.

7. Li, T.; Li, B.; Dong, S. Aptamer-Based Label-Free Method for Hemin Recognition and DNA Assay by Capillary Electrophoresis with Chemiluminescence Detection. *Anal. Bioanal. Chem.* **2007**, *389*, 887-893.

8. Liu, E.; Xue, B. Flow Injection Determination of Adenine at Trace Level Based on Luminol-$K_2Cr_2O_7$ Chemiluminescence in a Micellar Medium. *J. Pharm. Biomed. Anal.* **2006**, *41*, 649-653.

9. Sun, S.; Liu, H.; Zhou, Y.; Wang, F.; Xia, X. Copper-Nitrogen-Doped Graphene Hybrid as an Electrochemical Sensing Platform for Distinguishing DNA Bases. *Anal. Chem.* **2017**, *89*, 10858-10865.

10. Zhang, L.; Zhang, J. Multiporous Molybdenum Carbide Nanosphere as a New Charming Electrode Material for Highly Sensitive Simultaneous Detection of Guanine and Adenine. *Biosens. Bioelectron.* **2018**, *110*, 218-224.

11. Wang, Q.; Zhang, J.; Li, Q.; Guo, X.; Zhang, L. Fabrication of WO_2/W@C Core-Shell Nanospheres for Voltammetric Simultaneous Determination of Thymine and Cytosine. *Microchim. Acta* **2020**,

187, 62-71.

12. Deng, C.; Xia, Y.; Xiao, C.; Nie, Z.; Yang, M.; Si, S. Electrochemical Oxidation of Purine and Pyrimidine Bases Based on the Boron-Doped Nanotubes Modified Electrode. *Biosens. Bioelectron.* **2012**, *31*, 469-474.
13. Zhou, H.; Ren, M.; Zhai, H. Enhanced Supercapacitive Behaviors of Poly(3,4-Ethylenedioxythiophene)/Graphene Oxide Hybrids Prepared Under Optimized Electropolymerization Conditions. *Electrochim. Acta* **2021**, *372*, 137861.
14. Li, Q; Wu, J.; Liu, Y.; Qi, X.; Jin, H.; Yang, C.; Liu, J.; Li, G.; He, Q. Recent Advances in Black Phosphorus-Based Electrochemical Sensors: A Review. *Anal. Chim. Acta* **2021**, *1170*, 338480.
15. Li, Q.; Xia, Y.; Wan, X.; Yang, S.; Cai, Z.; Ye, Y.; Li, G. Morphology-Dependent MnO_2/Nitrogen-Doped Graphene Nanocomposites for Simultaneous Detection of Trace Dopamine and Uric Acid. *Mater. Sci. Eng. C* **2020**, *109*, 110615.
16. Liu, H.; Xiong, R.; Zhong, P.; Li, G.; Liu, J.; Wu, J.; Liu, Y.; He, Q. Nanohybrids of Shuttle-Like α-Fe_2O_3 Nanoparticles and Nitrogen-Doped Graphene for Simultaneous Voltammetric Detection of Dopamine and Uric Acid. *New J. Chem.* **2020**, *44*, 20797-20805.
17. Nonaka, L.; Almeida, T.S.D.; Aquino, C.B.; Domingues, S.H.; Salvatierra, R.V.; Souza, V.H.R. Crumpled Graphene Decorated with Manganese Ferrite Nanoparticles for Hydrogen Peroxide Sensing and Electrochemical Supercapacitors. *ACS Appl. Nano Mater.* **2020**, *3*, 4859-4869.
18. Gong, Q.; Han, H.; Yang, H.; Zhang, M.; Sun, X.; Liang, Y.; Liu, Z.; Zhang, W.; Qiao, J. Sensitive Electrochemical DNA Sensor for the Detection of HIV Based on a Polyaniline/Graphene Nanocomposite. *J. Materiomics* **2019**, *5*, 313-319.
19. Tsierkezos, N.G.; Othman, S.H.; Ritter, U.; Hafermann, L.; Knauer, A.; Köhler, M.; Downing, C.; McCarthy, E.K. Electrochemical Analysis of Ascorbic Acid, Dopamine, and Uric Acid on Nobel Metal Modified Nitrogen-Doped Carbon Nanotubes. *Sensor. Actuat. B-Chem.* **2016**, *231*, 218-229.
20. Wu, X.; Xing, Y.; Pierce, D.; Zhao, J. One-pot Synthesis of Reduced Graphene oOxide/Metal (Oxide) Composites. *ACS Appl. Mater. Interfaces* **2017**, *9*, 37962-37971.
21. Zhang, T.; Xing, Y.; Song, Y.; Gu, Y.; Yan, X.; Lu, N.; Liu, H.; Xu, Z.; Xu, H.; Zhang, Z.; Yang, M. AuPt/MOF-Graphene: A Synergistic Catalyst with Surprisingly High Peroxidase-Like Activity

and Its Application for H_2O_2 Detection. *Anal. Chem.* **2019**, *91*, 10589-10595.

22. Fu, L.; Zhang, D.; Yang, Z.; Chen, T.; Zhai, J. PtAuCo Trimetallic Nanoalloys as Highly Efficient Catalysts Toward Dehydrogenation of Ammonia Borane. *ACS Sustainable Chem. Eng.* **2020**, *8*, 3734-3742.
23. Kim, D.; Nam, H.; Cho, Y.H.; Yeo, B.C.; Cho, S.H.; Ahn, J.P.; Lee, K.Y.; Lee, S.Y.; Han, S. Unlocking the Potential of Nanoparticles Composed of Immiscible Elements for Direct H_2O_2 Synthesis. *ACS Catal.* **2019**, *9*, 8702-8711.
24. Yang, J.; Ji, X.; Liu, L.; Xiang, Y.; Zhu, Y. One Step Fabrication of Graphene/Polypyrrole/Ag Composite Electrode Towards Compressible Supercapacitor. *J. Alloy. Compd.* **2020**, *820*, 153081-153089.
25. Maitya, D.; Kumar, R.T.R. Highly Sensitive Amperometric Detection of Glutamate by Glutamic Oxidase Immobilized Pt Nanoparticle Decorated Multiwalled Carbon Nanotubes (MWCNTs)/Polypyrrole Composite. *Biosens. Bioelectron.* **2019**, *130*, 307-314.
26. Wang, N.; Zhao, W.; Shen, Z.; Sun, S.; Dai, H.; Ma, H.; Lin, M. Sensitive and Selective Detection of Pb (II) and Cu (II) Using a Metal-Organic Framework/Polypyrrole Nanocomposite Functionalized Electrode. *Sensor. Actuat. B-Chem.* **2020**, *304*, 127286-127292.
27. Li, Z.; Chen, G.; Chen, L.; Guo, M.; Wu, Y.; Wei, Y.; Wang, J.; Wang, X. Hollow Au/Polypyrrole Capsules to Form Porous and Neural Network-Like Nanofibrous Film for Wearable, Super-Rapid, and Ultrasensitive NH_3 Sensor at Room Temperature. *ACS Appl. Mater. Interfaces* **2020**, *12*, 55056-55063.
28. Shahmoradi, A.; Hosseini, A.; Akbarinejad, A.; Alizadeh, N. Noninvasive Detection of Ammonia in the Breath of Hemodialysis Patients Using a Highly Sensitive Ammonia Sensor Based on a Polypyrrole/Sulfonated Graphene Nanocomposite. *Anal. Chem.* **2021**, *93*, 6706-6714.
29. Abinaya, M.; Rajakumaran, R.; Chen, S.M.; Karthik, R.; Muthuraj, V. In Situ Synthesis, Characterization, and Catalytic Performance of Polypyrrole Polymer-Incorporated Ag_2MoO_4 Nanocomposite for Detection and Degradation of Environmental Pollutants and Pharmaceutical Drugs. *ACS Appl. Mater. Interfaces* **2019**, *11*, 38321-38335.
30. Chen, Y.; Ge, X.; Cen, S.; Wang, A.; Luo, X.; Feng, J. Ultrasensitive Dual-Signal Ratiometric

Electrochemical Aptasensor for Neuron-Specific Enolase Based on Au Nanoparticles@Pd Nanoclusters-Poly (Bismarck Brown Y) and Dendritic AuPt Nanoassemblies. *Sensor. Actuat. B-Chem.* **2020**, *311*, 127931.

31. Zhang Q.; Fu, M.; Lu, H.; Fan, X.; Wang, H.; Zhang, Y.; Wang, H. Novel Potential and Current Type Chiral Amino Acids Biosensor Based on L/D-Handed Double Helix Carbon Nanotubes@Polypyrrole@Au Nanoparticles@L/D-Cysteine. *Sensor. Actuat. B-Chem.* **2019**, *296*, 126667.
32. Maruthapandi, M.; Nagvenkar, A.P.; Perelshtein, I.; Gedanken, A. Carbon-Dot Initiated Synthesis of Polypyrrole and Polypyrrole@CuO Micro/Nanoparticles with Enhanced Antibacterial Activity. *ACS Appl. Polym. Mater.* **2019**, *1*, 1181-1186.
33. Bao, Y.; Liu, H.; Liu, Z.; Wang, F.; Feng, L. Pd/FeP Catalyst Engineering via Thermal Annealing for Improved Formic Acid Electrochemical Oxidation. *Appl. Catal. B: Environ.* **2020**, *274*, 119106.
34. Arvand, M.; Motaghed Mazhabi, R.; Niazi, A. Simultaneous Determination of Guanine, Adenine and Thymine Using a Modified Carbon Paste Electrode by TiO_2 Nanoparticles-Magnesium(II) Doped Natrolite Zeolite. *Electrochim. Acta* **2013**, *89*, 669-679.
35. Ensafi, A.A.; Abarghoui, M.M.; Rezaei, B. A New Electrochemical Sensor Based on Porous Silicon Supported Pt-Pd Nanoalloy for Simultaneous Determination of Adenine and Guanine. *Sensor. Actuat. B-Chem.* **2014**, *204*, 528-535.
36. Gao, Y.; Xu, J.; Lu, L.; Wu, L.; Zhang, K.; Nie, T.; Zhu, X.; Wu, Y. Overoxidized Polypyrrole/Graphene Nanocomposite with Good Electrochemical Performance as Novel Electrode Material for the Detection of Adenine and Guanine. *Biosens. Bioelectron.* **2014**, *62*, 261-267
37. Lu, N.; Liu, H.; Huang, R.; Gu, Y.; Yan, X.; Zhang, T.; Xu, Z.; Xu, H.; Xing, Y.; Song, Y.; Li, X.; Zhang, Z. Charge Transfer Platform and Catalytic Amplification of Phenanthroimidazole Derivative: A New Strategy for DNA Bases Recognition. *Anal. Chem.* **2019**, *91*, 11938-11945.
38. Anu Prathap, M.U.; Srivastava, R.; Satpati, B. Simultaneous Detection of Guanine, Adenine, Thymine, and Cytosine at Polyaniline/MnO_2 Modified Electrode. *Electrochim. Acta* **2013**, *114*,

285-295.

39. Wang, P.; Wu, H.; Dai, Z.; Zou, X. Simultaneous Detection of Guanine, Adenine, Thymine and Cytosine at Choline Monolayer Supported Multiwalled Carbon Nanotubes Film. *Biosens. Bioelectron.* **2011**, *26*, 3339-3345.

40. Siddegowda, K.S.; Mahesh, B.; Swamy, K.N. Fabrication of Copper Oxide Nanoparticles Modified Carbon Paste Electrode and Its Application in Simultaneous Electroanalysis of Guanine, Adenine, and Thymine. *Sensor. Actuat. A* **2018**, *280*, 277-286.

41. Wang, D.; Huang, B.; Liu, J.; Guo, X.; Abudukeyoumu, G.; Zhang, Y.; Ye, B. C.; Li, Y. A Novel Electrochemical Sensor based on Cu@Ni/MWCNTs Nanocomposite for Simultaneous Determination of Guanine and Adenine. *Biosens. Bioelectron.* **2018**, *102*, 389-395.

42. Shen, Q.; Wang, X. Simultaneous Determination of Adenine, Guanine and Thymine Based on β-cyclodextrin/MWNTs Modified Electrode. *J. Electroanal. Chem.* **2009**, *632*, 149-153.

43. Yari, A.; Derki, S. New MWCNT-Fe_3O_4@PDA-Ag Nanocomposite as a Novel Sensing Element of an Electrochemical Sensor for Determination of Guanine and Adenine Contents of DNA. *Sensor. Actuat. B-Chem.* **2016**, *227*, 456-466.

Chapter 5: CNMs-GR for electrocatalytic detection of glucose and removal of organic dyes

This chapter reports on the synthesis of magnetic CNMs-GR nanocomposites using a hydrothermal method. The formation of the CNMs-GR was confirmed through various characterization techniques. Furthermore, the electrocatalytic activity of the CNMs-GR nanocomposites towards glucose oxidation and their effectiveness in the removal of three organic dyes (Methylene Blue (MB), Congo Red (CR), and Neutral Red (NR)) are investigated.

This Chapter is published to the journal "ACS Applied Nano Materials":

Lei, P., Zhou, Y., Dong, C., Liu, Y., and Shuang, S. (2023). CoNi-MOF-graphene nagnetic nanocomposites for the electrocatalytic detection of glucose and the efficient removal of organic dyes. ACS Applied Nano Materials, 6, 9369-9375.

CoNi-MOF-graphene nagnetic nanocomposites for the electrocatalytic detection of glucose and the efficient removal of organic dyes

Abstract

The design of nanocomposite with electrocatalytic activity and recyclable development for the detection of small biomolecules and the removal of environmental pollutants has received enormous curiosity. A magnetic nanocomposite was synthesized by the hydrothermal approach comprising two building units metal-organic frameworks (MOFs) and graphene (GR). GR accumulated organic ligands through the large specific surface area, cobalt (Co) and nickel (Ni) served as coordination ions to seamlessly connect with the former for forming CoNi-MOFs-GR (CNMs-GR) to improve the conductivity of MOFs and the electrocatalytic activity of GR. The nanocomposite was utilized to construct an electrochemical sensing platform for the detection of glucose in human blood serum and the removal of organic dyes (MB, CR, and NR) in water. The CNMs-GR modified electrode exhibited good electrochemical performance toward glucose in a wide linear range of 10 μM-2900 μM with a detection limit of 1.27 μM. The maximum uptake capacity of CNMs-GR for MB, CR, and NR was respectively 184.29 mg/g, 912.47 mg/g, and 894.36 mg/g. Most obviously, this work provided a strategy for the design of an effective bifunctional nanocomposite, which not only demonstrated the enormous potential of detection of glucose but also realized the removal of organic dyes.

Keywords : Magnetic nanocomposite, electrocatalyst, adsorbent, glucose oxidation, organic dyes adsorption

5.1 Introduction

Glucose is an essential biological small molecule, which plays a very important role in the metabolism of the organism. However, diabetics cannot metabolize glucose properly, so excessive glucose will bring serious disease problems [1]. Presently, the main diagnostic method for diabetes is to measure blood sugar [2]. Enzyme-based electrochemical sensors have been deeply studied, but their applications are limited due to the influence of external factors [3,4]. The non-enzymatic glucose electrochemical sensors can disengage the limitation of the application without considering the external factors, thereby realizing accurate glucose detection [5]. Thus, non-enzymatic glucose electrochemical sensors have attracted more and more attention, and there is an urgent need for a non-enzymatic sensing device that can quickly and accurately detect glucose.

On the other hand, the environmental pollution caused by organic dyes has become a severe problem and attracted a lot of attention because of the boom of modern industry [6]. Most dyes have the characteristics of high toxicity, biodegradability, and easy residues [7]. The removal of dyes can be carried out by physical and chemical methods such as adsorption, ion exchange, deposition, bioelectrochemical technology, and oxidation [8-10]. The adsorption method is considered to be the most economical and effective way owing to its simple operation, convenience, and sustainable development [11].

Metal-organic frameworks (MOFs) have attracted considerable attention due to their uniform cavities, abundant active sites and unique chemical properties, and have been widely used in many fields, such as batteries, electrochemical sensors and organic dye adsorption [12,13]. These advantages make it more potential in the exploration of multifunctional nanomaterials. Zhang et al. [14] prepared a new POM-encapsulated MOF material by hydrothermal method, which showed excellent HER activity and dye degradation activity, but it could not be recycled. Wu and coworkers [15] reported a series of 3D MOFs with excellent OER activity and photocatalytic properties for renewable energy conversion and environmental remediation, which provided a direction for the production of multi-functional environmentally friendly catalysts. Presently, many efforts have been made to modify and enhance the characteristics of single-metal MOFs by combining one or more metals into a single MOFs [16].

Compared with single metal MOFs, bimetallic MOFs exhibit higher catalytic activity due to the generation of new defects within the same framework and the excellent synergistic effect between various metal centers [17]. However, the poor conductivity of MOFs limits their application. The compounding of MOFs with various conductive materials is a popular strategy to improve performance. Graphene (GR) has attracted widespread attention in many fields owing to its superior electrical conductivity, significant electron transport capability, ultrahigh specific surface area, and good chemical stability [18]. Recent studies have shown that composites of MOFs and GR can integrate the advantages of various components, enabling the composites to have better stability and high conductivity [19-21]. The unique structure of GR provides a variety of sites for coupling with MOFs. Moreover, the carboxyl group of GR is able to enhance the coordination bond and guide the growth of MOF to form a more favorable structure. As far as we know, the bifunctional applications of CoNi-MOFs-GR (CNMs-GR) nanocomposite have not yet been reported elsewhere. In this chapter, nickel (Ni) and cobalt (Co) with a high magnetic intensity were used as magnetic sources of MOFs, and GR with a large specific surface area and adsorption capacity was further introduced to overcome these defects.

Magnetic CNMs-GR nanocomposite was synthesized by a simple hydrothermal method, and it was further investigated for the electrocatalytic activity of glucose and the removal of three organic dyes (methylene blue (MB), congo red (CR), and neutral red (NR)). Co^{2+} are mainly used to build bimetallic MOFs with Ni^{2+} and can enhance the magnetic properties of the complexes, making CNMs-GR easy to separate in terms of dye adsorption. The structure and properties of the magnetic nanocomposite were characterized via field-emission scanning electron microscopy (FESEM), vibrating sample magnetometer (VSM), X-ray photoelectron spectroscopy (XPS), cyclic voltammetry (CV), and chronoamperometry. A strong synergy between CNMs with electrocatalytic activity and GR with a large adsorption capacity enhanced glucose oxidation and the adsorption of organic dyes. The bifunctional nanocomposite showed great promise in the construction of glucose sensing platform and wastewater treatment.

5.2 Experimental

5.2.1 Chemicals

Carboxylated graphene (GR) was ordered from Chengdu Organic Chemicals Co. Ltd., Chinese Academy of Sciences. Glucose, sodium hydroxide, $Co(NO_3)_2 \cdot 6H_2O$, $Ni(NO_3)_2 \cdot 6H_2O$, 2-aminoterephthalic acid, ethanol, N, N-dimethylformamide, and other reagents were purchased from Aladdin Chemistry Co., Ltd. (Shanghai, China).

5.2.2 Instrumentation

XPS spectra were taken from the AXIS ULTRA DLD. Magnetization hysteresis loops were obtained by vibrating sample magnetometer (VSM, Lakeshore 7404). FESEM images were obtained with a Japan JSM-7900F. All electrochemical preparations and measurements were performed using the CHI 660E electrochemical analyzer (Shanghai CH Instrument Co., Ltd., China).

5.2.3 Synthesis of CNMs-GR.

0.75 mmol $Ni(NO_3)_2 \cdot 6H_2O$ and 0.75 mmol $Co(NO_3)_2 \cdot 6H_2O$ were added in 2-aminoterephthalic acid (1.5 mmol), GR (35 mg), ultrapure water (4.0 mL), ethanol (4.0 mL), and N, N-dimethylformamide (64.0 mL). The mixture was stirred till it completely got dissolved. The final obtained solution was transferred in a 100 ml Teflon-lined stainless-steel autoclave and maintained at 140 °C for 24 h. At the completion of reaction, the product was collected with the process of centrifugation and washed repeatedly by ultrapure water and ethanol. Finally, the product (CNMs-GR) was dried at 60 °C.

5.2.4 Preparation of CNMs-GR/GCE

4.0 mg CNMs-GR was added into 2.0 mL ultrapure water and ultrasonicated for 15 min to attain uniform dispersion. Later, 8 µL of CNMs-GR dispersion was drop cast on the surface of GCE and dried at an infrared lamp. Thus, the CNMs-GR modified electrode was prepared to denote CNMs-GR/GCE. Finally, the prepared CNMs-GR/GCE was performed in electrochemical experiments in Fig. 5.1.

Fig. 5.1: Synthesis route of CNMs-GR and its applications in electrocatalysis and adsorption

5.3 Results and Discussions

5.3.1 Characterisation of CNMs

FESEM was employed for the investigation of the morphology of CNMs and CNMs-GR. Fig. 5.2A displays the spherical dispersed particles of CNMs. Fig. 5.2B and C reveal that wrinkles of GR are clearly observed and CNMs are dispersed on the GR sheet surface or embedded in the layer with close interfacial contact. To clarify the chemical compositions of CNMs-GR nanocomposite with a simple and fast method, we used the energy dispersive spectrometer (EDS) mapping equipped in the FESEM to analyze the element distribution. Although the amounts of the two metal salts feed ratio are the same, when Ni and Co coordinate with ligands, the coordination between Ni and ligands dominates during the reaction process. Therefore, there is a difference in the content ratio of Ni and Co in the product in Fig. 5.2D. As expected, the appearance of C, O, N, Co, and Ni elements could be observed without any other discernible impurities. The element mapping of CNMs-GR nanocomposite demonstrates the homogeneous distribution of elements. The FESEM and TEM images (Fig. 5.2E and F) indicate that the CNMs has an average diameter size of about 400 nm.

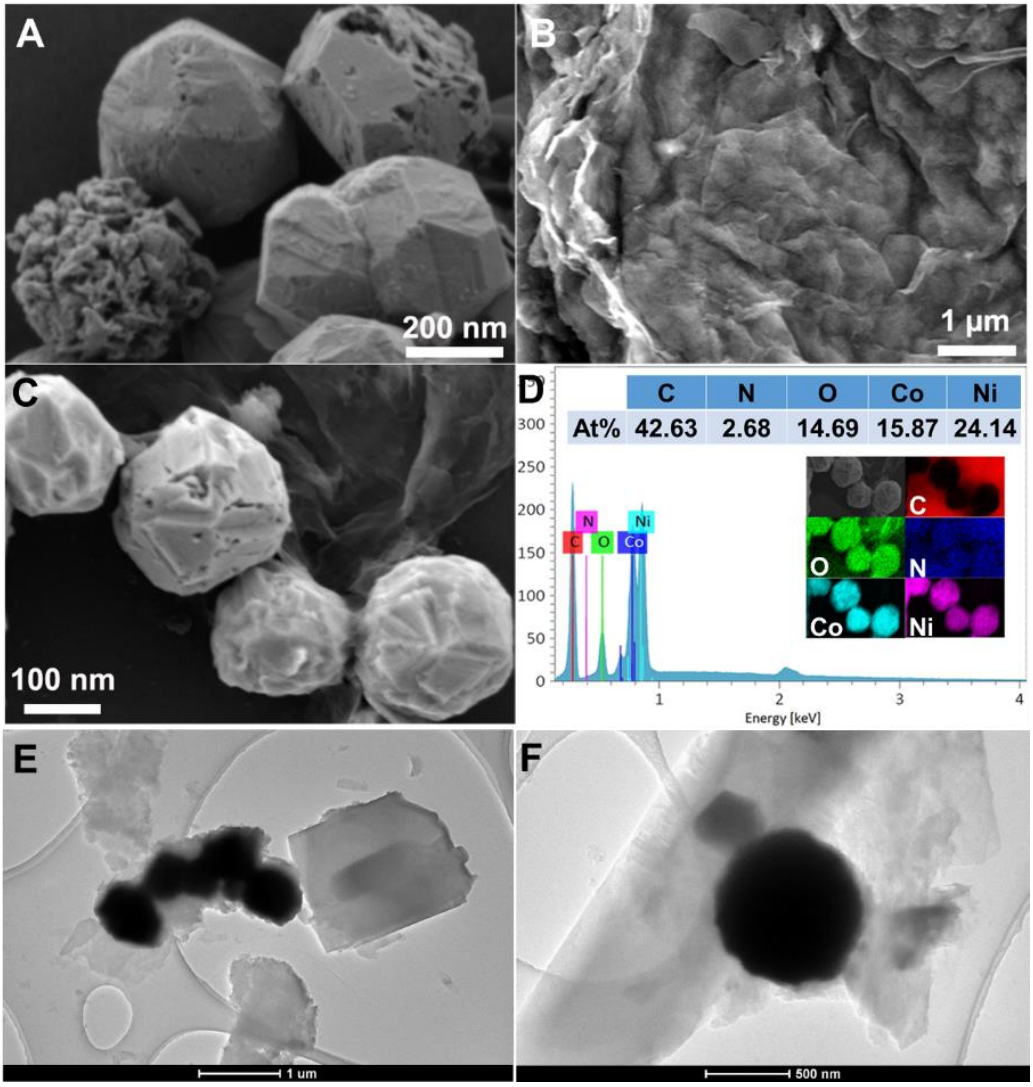

Fig.5.2: FESEM images of (A) CNMs, (B and C) CNMs-GR; (D) EDS analysis of CNMs-GR and the relevant elemental mapping images; TEM images of (E and F) CNMs-GR

XPS spectral study of CNMs-GR nanocomposite has been conducted and shown in Fig. 5.3. The peaks in the spectra demonstrate that the nanocomposites can be composed of C 1s, O 1s, N 1s, Ni 2p, and Co 2p (Fig. 5.3A), which are consistent with the results of EDS. In the C 1s spectra (Fig. 5.3B), the peaks at 284.7, 285.8, and 288.7 eV are appointed to the C-C, C=C, and C=O, (22) which could be ascribed to the existence of GR. The peaks loaded at 532.0 eV and 533.5 eV correspond to hydroxyl O and carboxylate O (Fig. 5.3C). In Fig. 5.3E, two peaks with binding energies at around 856.2 eV and 873.8 eV are corresponding to the Ni $2p_{3/2}$ and Ni $2p_{1/2}$ orbitals of Ni^{2+} [23,24]. In Fig. 5.3F, the peaks observed at 781.6 and 798.1 eV are assigned to the Co $2p_{3/2}$ and Co $2p_{1/2}$ owing to Co^{2+} [25-27].

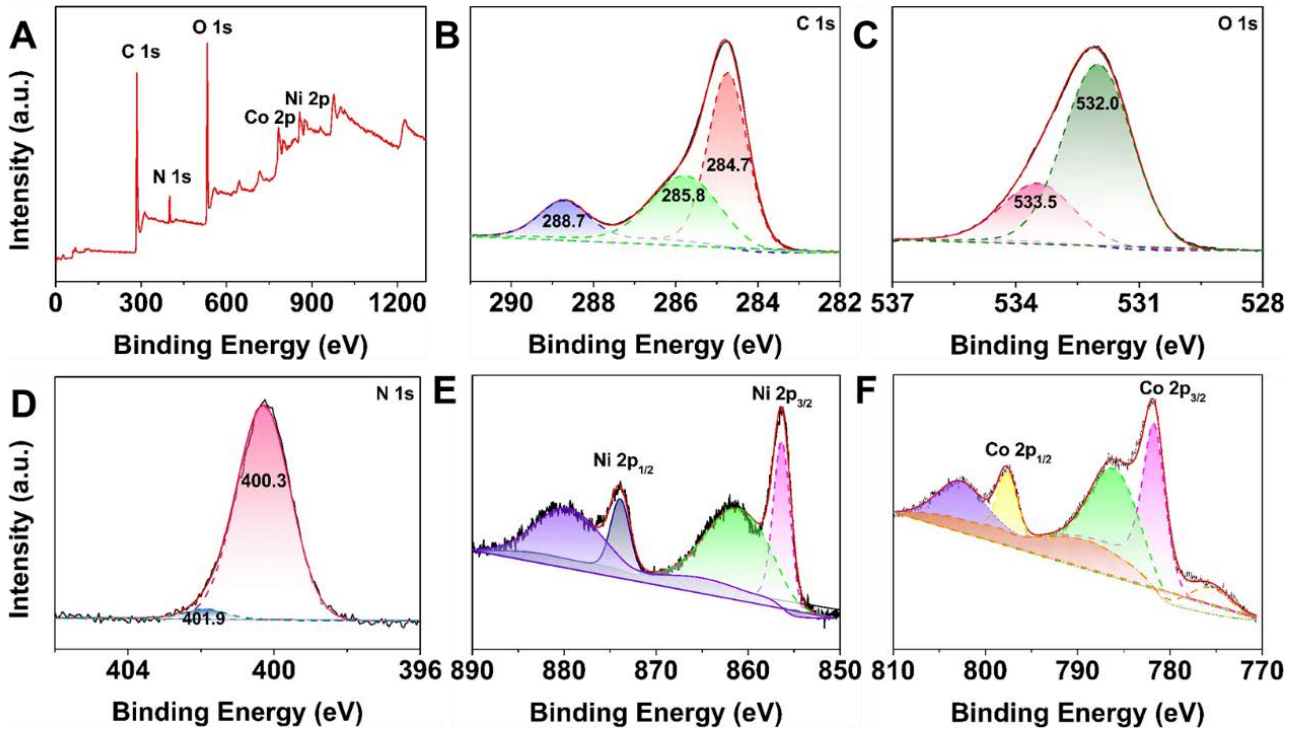

Fig. 5.3: (A) XPS survey spectra of CNMs-GR. (B-E) XPS spectra of C 1s, O 1s, N 1s, Ni 2p, and Co 2p, respectively, for CNMs-GR

The magnetization intensity of the different samples was well-studied. Fig. 5.4 depicts the superparamagnetic behavior of CNMs and CNMs-GR by using a VSM, with a saturation magnetization *Ms*=46.9 emu g^{-1} and 41.2 emu g^{-1}. The CNMs-GR has been proved relatively weaker magnetic intensity than CNMs, which is due to the addition of non-magnetic graphene.

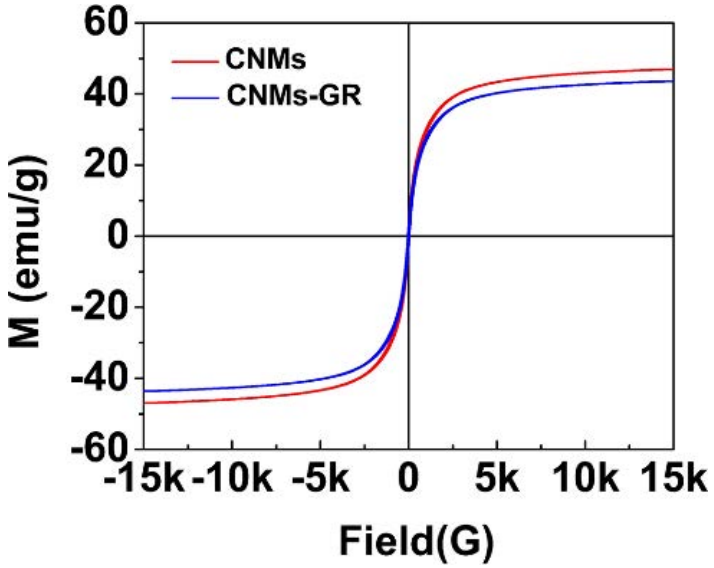

Fig. 5.4: Magnetization hysteresis loops of CNMs and CNMs-GR

5.3.2 Electrochemical Performance of CNMs-GR/GCE

The characterization of the modified GCEs is confirmed with the CV technique, and the results of the different modified GCEs are shown in Fig. 5.5A. The bare GCE exhibits a well-defined reversible redox peak. The redox peak current decreases significantly for CNMs-modified GCE because of the impediment of electron transfer. The redox peak current of CNMs-GR/GCE is significantly enhanced compared to CNMs/GCE because GR can accelerate electron transfer. Fig. 5.5B depicts the CV responses for the addition of 2.0 mM glucose in 0.1 M NaOH, comparing the electrochemical behavior of all of the modified GCEs. CNMs-GR/GCE displays much better glucose oxidation capability in comparison with the bare GCE and CNM/GCE. Fig. S6 shows the electrochemical responses for CNMs-GR/GCE in 0.1 M NaOH with and without 2.0 mM glucose. Evidently, CNMs-GR/GCE displays a pair of redox peaks with an anodic peak at around 0.63 V and a cathodic peak at 0.55 V without glucose, implying the presence of reversible Faradaic reaction of Ni^{2+}/Ni^{3+} with the assistance of OH^- [28]. In contrast, the addition of 2.0 mM glucose results in a notable rise in peak current for CNMs-GR/GCE. The results strongly illustrate the enhanced performance of GR integrated with CNMs in CNMs-GR for the electrochemical detection of glucose. In the basic medium, the coordination interaction between Ni^{2+} and the organic linker became weak, and the Ni^{2+} is released out to react with OH and further oxidized to Ni^{3+} [28,29]. Thus, the possible mechanisms for the electrochemical oxidation of glucose can be described as the following redox reactions given in Equations [28, 30, 31]:

$$Ni^{2+} \rightarrow Ni^{3+} + e^- \quad (1)$$

$$Ni^{3+} + OH^- + \text{glucose} \rightarrow Ni^{2+} + \text{glucolactone} + H_2O + e^- \quad (2)$$

The relationship between peak current and scan rate was scrutinized by CV in 0.1 M NaOH in the existence of 2.0 mM glucose. The current responses at CNMs-GR/GCE are increased with increasing various scan rates in Fig. S7. The relationship between the current response of glucose and scan rates as given below:

I_{pa} (μA)=0.113v (mV s^{-1}) – 4.61

I_{pc} (μA)=– 0.104v (mV s^{-1}) – 4.09

It reveals that the oxidation of glucose on the CNMs-GR/GCE is basically an adsorption-controlled process [32, 33].

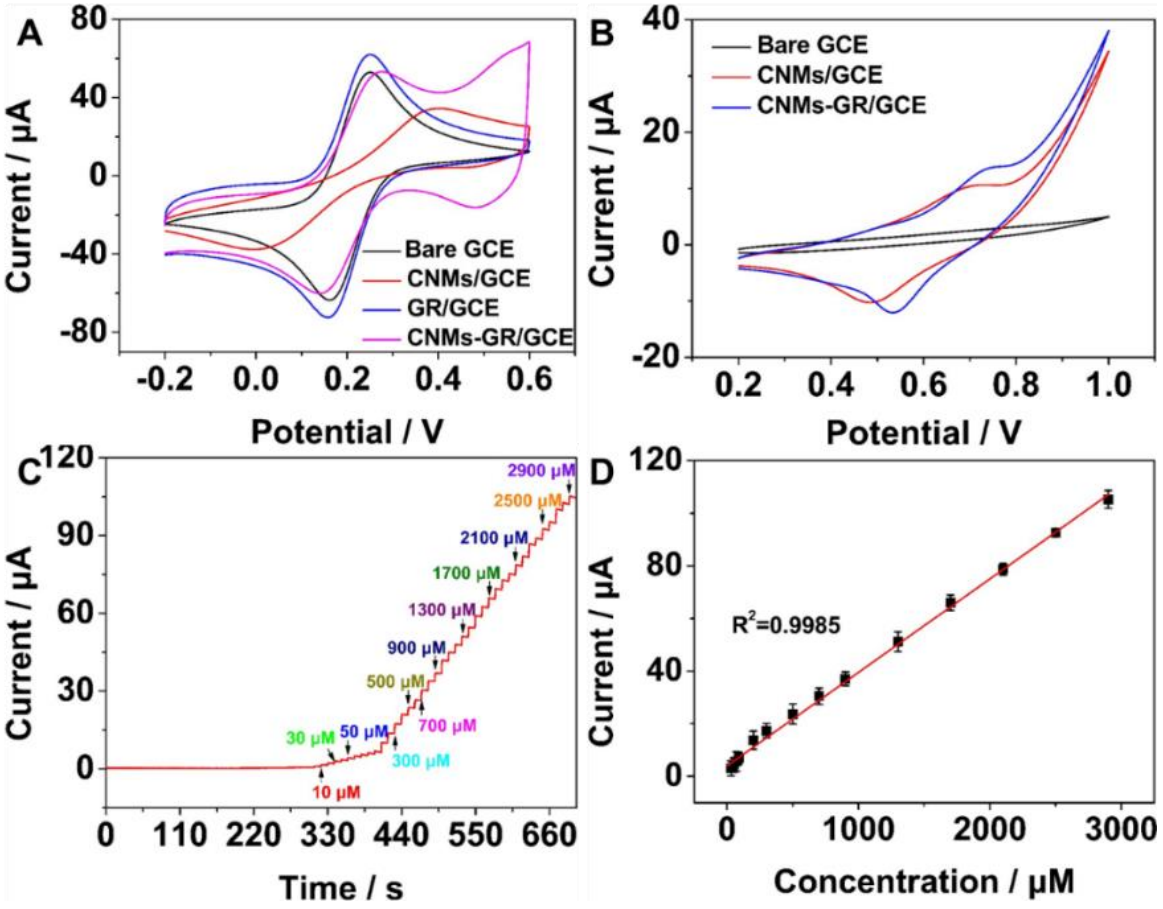

Fig. 5.5: (A) CV curves of the bare GCE, GR/GCE, CNMs/GCE, and CNMs-GR/GCE in 0.1 M KCl containing 5.0 mM $[Fe(CN)_6]^{3-/4-}$; (B) CV curves of the bare GCE, CNMs/GCE, and CNMs-GR/GCE in 2.0 mM glucose (0.1 M NaOH). (C) Chronoamperometric curves of CNMs-GR/GCE with successive addition of glucose (10 μM-2900 μM) in 0.1 M NaOH. (D) The linear relationship between the current and the glucose concentration

5.3.3 Chronoamperometric Determination of Glucose

The chronoamperometry was employed to investigate the different concentrations of glucose in 0.1 M NaOH at CNMs-GR/GCE. Fig. 5.5C describes the current response with the concentration range varying from 10 μM to 2900 μM of glucose. The excellent electrocatalytic activity of CNMs-GR is observed from the increasing current response gradually in Fig. 5.5D. The current response and the concentrations show good linearity with R^2=0.9985, the linear regression equation is I (μA)=0.0355C (μM)+3.99, and the detection limit achieves 1.27 μM (3-fold signal/noise value). The oxidation of glucose can be

attributed to the synergistic characteristics of CNMs and GR such as efficient electrocatalytic activity and good conductivity. Table 5.1 lists a comparison of several modified electrodes for glucose detection. Obviously, the method is simple, fast, and sensitive detection. Moreover, CNMs-GR/GCE displays a better sensing performance with a wider linear range which was due to the unique structure of the CNMs-GR that achieved high electrochemical performances for the electrocatalysis of glucose.

Table 5.1: Comparison of the electrochemical performance of CNMs-GR/GCE with reported sensors

Electrode	Linear range (μM)	LOD (nM)	Ref.
NiO/CuO/PANI/GCE	0.02-2.5	2.0	[34]
NiO NSs/GCE	0.1-10.0	1.16	[35]
NiO/OMC/GCE	0.002-1.0	0.65	[36]
Triple-decker/GO	0.05-8.5	0.017	[37]
PVA-NG/AgNP nanofibers	5-47000	0.56	[38]
PtNPs@UiO-66/GCE	5-14750	3.06	[39]
ZIF-$Zn_{0.5}$ $Co_{0.5}$	0-1250	9.0	[40]
2D Cu_2O-rGO-P	5-10,560	3.78	[41]
NiHCNP/PN/CNTs	0.006-3	0.1	[42]
CuO-CoO	0.002-4	1.4	[43]
CNMs-GR/GCE	1.0-2900	0.21	This work

5.3.4 Selectivity, Stability, and Reproducibility of CNMs-GR/GCE

As illustrated in Fig. 5.6A, the selectivity of CNMs-GR/GCE is evaluated in some common compounds which may be encountered during analytical detection. None of these analyses yield a significant response compared to the glucose response. The results manifest that the developed CNMs-GR/GCE shows good selectivity detection for the glucose. CNMs-GR/GCE was evaluated to obtain good stability and for the monitoring of glucose. The stability of CNMs-GR/GCE was carried out three times at each 1-day interval in 2.0 mM glucose solution by applying the CV technique. CNMs-GR/GCE displays a relatively stable performance for repetitive measurements, showing 93% retention of the initial response. The response is decreased further to 78% upon consecutive scans after 15 days in Fig. 5.6B. The reproducibility was assessed using six independent CNMs-GR/GCEs for glucose detection under identical fabrication and measurement conditions. No obvious cathodic current decay is observed in Fig. 5.6C. The obtained results implied high reproducibility for CNMs-GR/GCE. Overall, CNMs-GR/GCE displayed high reproducibility and stability for determining glucose, which was essential characteristics features for a sensor in practical application.

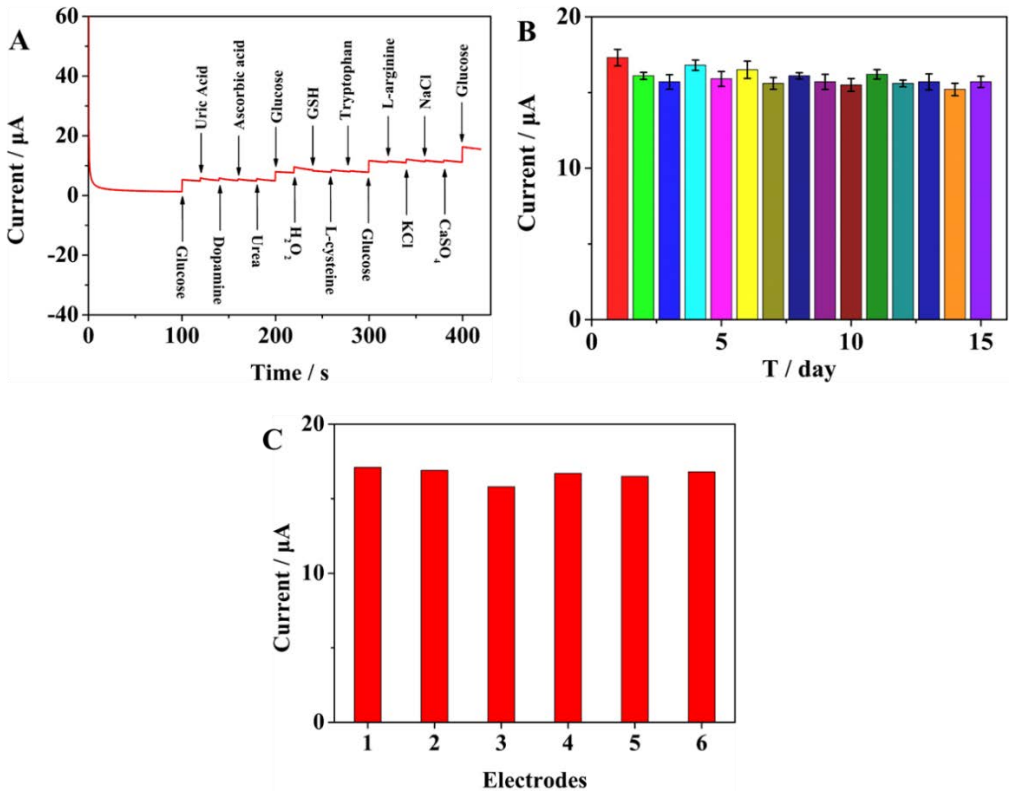

Fig. 5.6: (A) Influence of interfering substances, (B) long-term storage, and (C) reproducibility for glucose detection by CNMs-GR/GCE

5.3.5 Practical application

We verified the practical applicability of CNMs-GR/GCE by chronoamperometry measurements of glucose in human blood serum samples. Different concentrations of glucose were added into the sample diluted with sodium hydroxide solution to calculate the recovery. Table 5.2 shows the recoveries of glucose detection between 95.8% and 100.27%, and the result emphasizes the potential glucose detection ability with high selectivity in biological fluid.

Table 5.2: Determination of glucose in human serum samples (n=6)

Sample	Added (μM)	Found (μM)	RSD (%)	Recovery (%)
	10	9.58	2.61	95.8
Human serum	100	100.27	1.84	100.27
	500	499.84	1.95	99.67

5.3.6 Dye Removal Studies

The dye removal efficiency was calculated by measuring the dye concentration before and after adsorption at 25 °C. The dyes used in this study were MB, CR, and NR. A certain amount of the CNMs-GR as adsorbent was added to the aqueous dye solution, and then the adsorbent/adsorbate complex was separated by a permanent magnet. The concentrations of the remnant dye are determined based on the absorbance of solutions at 664 nm (MB), 505 nm (CR), and 528 nm (NR) with a UV-vis spectrophotometer in Fig. 5.7A. The final dye concentrations are calculated by comparing the UV-vis absorbance to the appropriate calibration curve of the dye samples diluted before analysis in Fig. S8. The removal (%) of the dyes is estimated using the following equation:

$$\text{Removal}(\%) = (1 - \frac{C}{C_0}) \times 100 \qquad (3)$$

Where C_0 (mg/L) is the initial dye concentration before removal, C (mg/L) is the concentration of the dye remaining in the solution after treatment. According to calculation, the removal efficiency of MB, CR, and NR is 98.34%, 93.95%, and 94.42%, respectively, which revealed the CNMs-GR is an effective adsorbent.

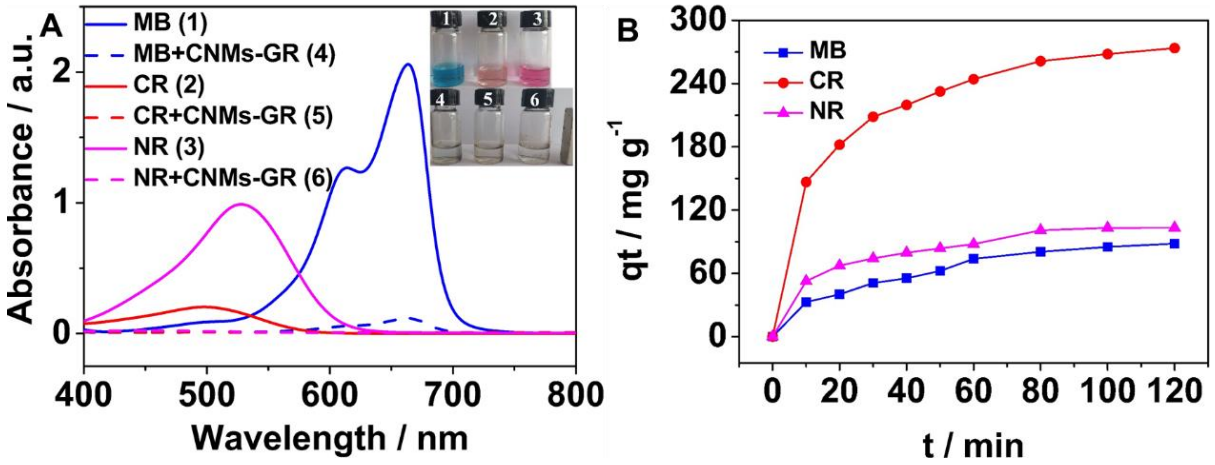

Fig. 5.7: (A) The UV-vis absorption spectra of 7.0 mg/L MB and supernatant of MB+CNMs-GR, 21.0 mg/L CR and CR+CNMs-GR, 12.0 mg/L NR and NR+CNMs-GR; Inset: The photographic pictures in the absence (1, 2 and 3) and presence (4, 5 and 6) of CNMs-GR with an external magnet; (B) The adsorption capacities of MB, CR and NR on CNMs-GR

The performance of CNMs-GR for the removal of MB, CR, and NR from ultrapure water was further investigated at 25 °C. The results indicated that the dye adsorption occurred relatively fast in the first 10 min, and it had a certain adsorption capacity in 10 to 60 min. There was no significant change in the adsorption capacity after 60 min. For the system under discussion, the adsorption capacity of the studied system is rapid at the original stage and basically maintained stable after reaching equilibrium in Fig. 5.7B. The maximum adsorption capacities for MB, CR, and NR are 73.84 mg/g, 244.21 mg/g, and 87.79 mg/g, respectively. The phenomenon is probably due to the existence of abundant adsorption sites on the surface of CNMs-GR. With the adsorption of organic dyes, the adsorption sites gradually decrease and eventually reached saturation.

As illustrated in Fig. 5.8, the adsorption isotherms of MB, CR, and NR on CNMs-GR have been studied. It can be evidently observed that the adsorption capacity of the three organic dyes has increased remarkably and stabilized with the increase of the primordial dye concentrations. The interaction of MB,

CR, and NR with CNMs-GR is also further analyzed, and it is displayed through two adsorption isothermal models, Langmuir (2) and Freundlich (3).

$$\frac{C_e}{q_e} = \frac{1}{K_L q_m} - \frac{C_e}{q_m} \quad (4)$$

$$\ln q_e = \frac{1}{n}\ln C_e + \ln K_F \quad (5)$$

Where q_e and C_e (mg·g^{-1}) are the adsorption capacity of MB, CR, and NR by CNMs−GR and the concentration of three organic dyes at equilibrium, respectively. For the Langmuir equation, q_m (mg·g^{-1}) is the maximum saturated adsorption capacity of CNMs-GR, and K_L is the Langmuir constant. For the Freundlich equation, K_F is the Freundlich constant, and n (dimensionless) is the Freundlich intensity parameter. As shown in Fig. S9 and Table S2, the R^2 of the Langmuir is closer to 1.0, so the adsorption process of the three dyes is more consistent with the molecular layer and uniform adsorption. According to the calculation, the maximum saturated adsorption capacity of MB. CR, and NR are 184.29 mg/g, 912.47 mg/g, and 894.36 mg/g, respectively. CNMs-GR has better adsorption for CR and NR than MB, which may be due to: (1) CR has a larger conjugated structure and a stronger the π-π conjugation interaction with CNMs-GR; (2) More amino groups of CR and NR are easier to form a hydrogen bond with CNMs-GR. In addition, the prepared CNMs-GR nanocomposite makes a comparison of adsorption performance with the previous study, CNMs-GR exhibits comparatively a better adsorption performance for MB, CR, and NR in Table 5.3.

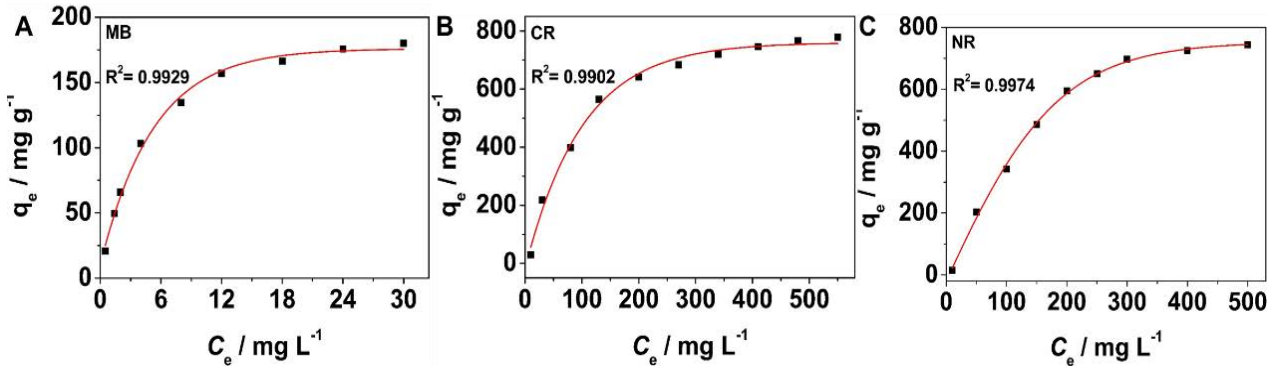

Fig. 5.8: The adsorption capacities of (A) MB, (B) CR and (C) NR on CNMs-GR

Table 5.3: Comparisons of CNMs-GR with other nanomaterials

Adsorbents	Adsorption capacity of adsorbate (mg g^{-1})			Ref.
	MB	CR	NR	
Activated carbon fibers	21.3	22.1	20.7	[44]
Magnetic Fe_3O_4@graphene	45.27	33.66	—	[45]
Fe_3O_4-clicked GO	109.5	98.8	—	[46]
Titanium peroxide	224.37	—	327.61	[47]
Fe_3O_4-MNPs-AC	78.76	—	—	[48]
pTSA-Pani@GO-CNT	—	66.666	—	[49]
3D hierarchical GO-NiFe LDH	—	489	—	[50]
CNMs-GR	184.29	912.47	894.36	This work

Reusability played a crucial role in practical applications. CNMs-GR were recycled by a magnet to investigate the reusability. CNMs-GR was repeatedly washed with ethanol to remove the adsorbed dye and reused for the adsorption experiment. As depicted in Fig. 5.9, the removal efficiency of the adsorbent is only reduced by about 8%, indicating that the magnetic CNMs-GR has remarkable absorption capacity, reusability, and stability, which is a promising dye adsorbent.

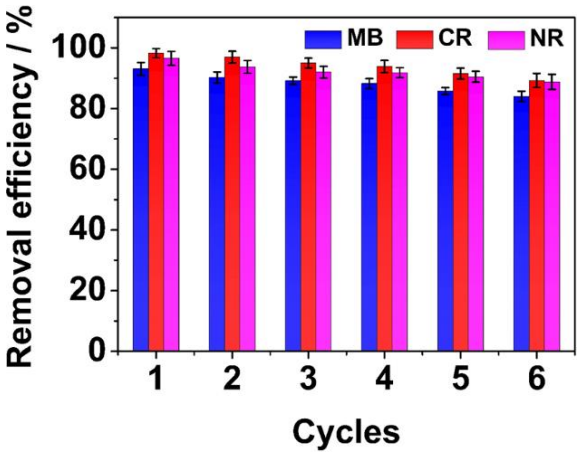

Fig. 5.9: Reusability of CNMs-GR

5.4 Conclusion

An effective bifunctional CNMs-GR nanocomposite was carefully synthesized through a facile one-pot hydrothermal synthesis procedure, and its efficient electrocatalytic activity of glucose and the removal efficiency of three organic dyes were investigated. The combination of GR and CNMs realized a more remarkable performance than either nanomaterial alone owing to the increase of specific area and the enhancement of electrocatalytic activity. The as-prepared CNMs-GR exhibited an outstanding electrocatalytic effect on glucose oxidation with a wide linear response range, low LOD, well stability, excellent selectivity, and reproducibility. Moreover, CNMs-GR/GCE was also employed to study its practicability in human blood serum samples with a satisfactory recovery of 95.8%-100.27%. CNMs-GR revealed excellent adsorption capacity and efficiency towards MB, CR, and NR with maximum adsorption up to 184.29 mg/g, 912.47 mg/g, and 894.36 mg/g, respectively. More importantly, CNMs-GR nanocomposite had the potential to construct electrochemical sensors and remove organic dyes from the wastewater based on its admirable bifunctional activity.

References

1. Waqas, M.; Wu, L. Y.; Tang, H. G.; Liu, C. Z.; Fan, Y. J.; Jiang, Z.; Wang, X. Q.; Zhong, J. P.; Chen, W. Cu_2O Microspheres Supported on Sulfur-Doped Carbon Nanotubes for Glucose Sensing. *ACS Appl. Nano Mater.* **2020**, *3*, 4788-4798.

2. Chao, H.; Zhou, Z.; He, W.; Li, M.; Yuan, X.; Su, P.; Song, J.; Yang, Y. Pt/MXene-Based Flexible Wearable Non-Enzymatic Electrochemical Sensor for Continuous Glucose Detection in Sweat. *ACS Appl. Mater. Inter.* **2022,** *14*, 20641-20651.

3. Bag, S.; Baksi, A.; Nandam, S. H.; Wang, D.; Ye, X. L.; Ghosh, J.; Pradeep, T.; Hahn, H. Nonenzymatic Glucose Sensing Using $Ni_{60}Nb_{40}$ Nanoglass. *ACS Nano* **2020**, *14*, 5543-5552.

4. Guo, S. X.; Zhang, C. H.; Yang, M.; Zhou, Y. L.; Bi, C. L.; Lv, Q. T.; Ma, N. A Facile and Sensitive Electrochemical Sensor for Non-Enzymatic Glucose Detection Based on Three-Dimensional Flexible Polyurethane Sponge Decorated with Nickel Hydroxide. *Anal. Chim. Acta* **2020**, *1109*, 130-139.

5. Wei, M.; Qiao, Y. X.; Zhao, H. T.; Liang, J.; Li, T. S.; Luo, Y. L.; Lu, S. Y.; Shi, X. F.; Lu, W. B.; Sun, X. P. Electrochemical Non-Enzymatic Glucose Sensors: Recent Progress and Perspectives. *Chem. Commun.* **2020**, *56*, 14553-14569.

6. Liu, X. B.; He, F. Y.; Bai, L. W.; Cao, X. W.; Liu, C.; Lu, W. B. A Two-Dimensional G-CoP/N,P-co-Doped Carbon Nanowire Electrode for the Simultaneous Determination of Hydroquinone and Catechol in Domestic Wastewater. *Anal. Chim. Acta* **2022**, *1210*, 339871

7. Bai, L. W.; Shi, Y. F.; Zhang, X.; Liu, X. B.; Wu, F.; Liu, C.; Jia, J. F.; Lu, W. B. A Two-Dimensional $NiMoO_4$ Nanowire Electrode for the Sensitive Determination of Hydroquinone in Four Types of Actual Water Samples. *J. Anal. Test.* **2022**, *6*, 382-392.

8. Xu, E.; Wu, Z. Z.; Ding, T.; Ye, X. Q.; Jin, Z. Y.; Liu, D. H. Magnetic $(Zn\text{-}St)_{10}Fe^0_n$ (n = 1, 2, 3, 4) Framework of Macro-Mesoporous Biomaterial Prepared via Green Enzymatic Reactive Extrusion for Dye Pollutants Removal. *ACS Appl. Mater. Inter.* **2019**, *11*, 43553-43562.

9. Far, H. S.; Najafi, M.; Hasanzadeh, M.; Rabbani, M. Self-Supported 3D-Printed Lattices Containing MXene/Metal-Organic Framework (MXOF) Composite as an Efficient Adsorbent for Wastewater Treatment. *ACS Appl. Mater. Inter.* **2022,** *14*, 44488-44497.

10. Benhalima, T.; Ferfera-Harrar, H. Eco-Friendly Porous Carboxymethyl Cellulose/Dextran Sulfate Composite Beads as Reusable and Efficient Adsorbents of Cationic Dye Methylene Blue. *Int. J. Biol. Macromol.* **2019**, *132*, 126-141.

11. Huang, Z.; Zhao, M. H.; Wang, C.; Wang, S. X.; Dai, L. Q.; Zhang, L. B. Preparation of a Novel Zn(II)-Imidazole Framework as an Efficient and Regenerative Adsorbent for Pb, Hg, and As Ion Removal from Water. *ACS Appl. Mater. Inter.* **2020**, *12*, 41294-41302.

12. Qiao, Y. X.; Liu, Q.; Lu, S.Y.; Chen, G.; Gao, S.Y.; Lu, W.B.; Sun, X.P. High-Performance Non-Enzymatic Glucose Detection: Using a Conductive Ni-MOF as an Electrocatalyst. *J. Mater. Chem. B* **2020**, *8*, 5411-5415.

13. Liu, C. S.; Sun, C. X.; Tian, J. Y.; Wang, Z. W.; Ji, H. F.; Song, Y. P.; Zhang, S.; Zhang, Z. H.; He, L. H.; Du, M. Highly Stable Aluminum-Based Metal-Organic Frameworks as Biosensing Platforms for Assessment of Food Safety. *Biosens. Bioelectron.* **2017**, *91*, 804-810.

14. Zhang, Z.; Gómez-García, C. J.; Wu, Q.; Xin, J.; Pang, H.; Ma, H.; Chai, D.; Li, S.; Zhao, C. Synthesis of a Polyoxometalate-Encapsulated Metal-Organic Framework via In Situ Ligand Transformation Showing Highly Catalytic Activity in Both Hydrogen Evolution and Dye Degradation. *Inorg. Chem.* **2022**, *61*, 11830-11836

15. Wu, R.; Wang, J.; Wang, L.; Xu, C.; Luo, R.; Shao, F.; Zhang, X.; Fan, Y. Three-Dimensional Cadmium-Organic Framework with Dual Functions of Oxygen Evolution in Water Splitting and Fenton-like Photocatalytic Removal of Organic Pollutants. *Inorg. Chem.* doi.org/10.1021/acs.inorgchem.3c00089.

16. Xue, Z.; Li, Y.; Zhang, Y.; Geng, W.; Jia, B.; Tang, J.; Bao, S.; Wang, H. P.; Fan, Y.; Wei, Z. W. Modulating Electronic Structure of Metal-Organic Framework for Efficient Electrocatalytic Oxygen Evolution. *Adv. Energy Mater.* **2018**, *8*, 1801564.

17. Jalal, N, R.; Madrakian, T.; Afkhami, A.; Ahmadi, M. Ni/Co Bimetallic Metal-Organic Frameworks on Nitrogen-Doped Graphene Oxide Nanoribbons for Electrochemical Sensing of Doxorubicin. *ACS Appl. Nano Mater.* **2022**, *5*, 11045-1058.

18. Ma, X. Y.; Hao, R. L.; Wang, Z. Y.; Xu, P. Y.; Luo, Y. C.; Zhao, Y. Nanoscale $CuFe_2O_4$ Monodispersedly Anchored on Reduced Graphene Oxide as Excellent Peroxydisulfate Catalyst for Removal of Gaseous Elemental Mercury. *Chem. Eng. J.* **2020**, *401*, 126101.

19. Lu, M. X.; Deng, Y. J.; Luo, Y.; Lv, J. P.; Li, T. B.; Xu, J.; Chen, S. W.; Wang, J. Y. Graphene Aerogel-Metal-Organic Framework-Based Electrochemical Method for Simultaneous Detection of Multiple Heavy-Metal Ions. *Anal. Chem.* **2019**, *91*, 888-895.

20. Li, Z.; Liu, C.; Maboudian, R. Synthesis and Characterization of UiO-66-NH_2 Incorporated Graphene Aerogel Composites and Their Utilization for Absorption of Organic Liquids. *Carbon* **2023**, *201*, 561-567.

21. Fei, L. Y.; Chen, C.; Lin, H, J.; Graphene Oxide Assisted Assembly of Superhydrophilic MOF-Based Membrane with 2D/3D Hybrid Nanochannels for Enhanced Water Purification. *Chem. Eng. J.* **2023**, *460*, 141694.

22. Li, J. H.; Liu, J. L.; Tan, G. R.; Jiang, J. B.; Peng, S. J.; Deng, M.; Qian, D.; Feng, Y. L.; Liu, Y. C. Fabrication of Glucose Bioelectrochemical Sensor Based on Au@Pd Core-Shell Supported by Carboxylated Graphene Oxide. *Anal. Biochem.* **2023**, *667*, 115091.

23. Xiao, X. L.; Peng, S. H.; Wang, C.; Cheng, D.; Li, N.; Dong, Y. L.; Li, Q. H.; Wei, D. G.; Liu, P.; Xie, Z. Z.; Qu, D. Y.; Li, X. Metal/Metal Oxide@Carbon Composites Derived from Bimetallic Cu/Ni-Based MOF and Their Electrocatalytic Performance for Glucose Sensing. *J. Electroanal. Chem.* **2019**, *841*, 94-100.

24. Zhu, J.; Yin, H.; Gong, J.; Al-Furjan, M. S. H.; Nie, Q. L. In Situ Growth of Ni/NiO on N Doped Carbon Spheres with Excellent Electrocatalytic Performance for Non-Enzymatic Glucose Detection. *J. Alloys Compd.* **2018**, *748*, 145-153.

25. Zou, H. H.; Tian, D. Y.; Lv, C.; Wu, S. M.; Lu, G. X.; Guo, Y. F.; Liu, Y. B.; Yu, Y.; Ding, K. J. The Synergistic Effect of Co/Ni in Ultrathin Metal–Organic Framework Nanosheets for the Prominent Optimization of Non-Enzymatic Electrochemical Glucose Detection. *J. Mater. Chem. B* **2020,** *8*, 1008-1016.

26. Jia, Z. K.; Ma, Y. S.; Yang, L. Y.; Guo, C. P.; Zhou, N.; Wang, M. H.; He, L. H.; Zhang, Z. H. $NiCo_2O_4$ Spinel Embedded with Carbon Nanotubes Derived from Bimetallic NiCo Metal-Organic Framework for the Ultrasensitive Detection of Human Immune Deficiency Virus-1 Gene. Biosens. Bioelectron. **2019**, *33*, 55-63.

27. Bai, Z. Q.; Yuan, L. Y.; Zhu, L.; Liu, Z. R.; Chu, S. Q.; Zheng, L. R.; Zhang, J.; Chai, Z. F.; Shi, W. Q. Introduction of Amino Groups into Acid-Resistant MOFs for Enhanced U(VI) Sorption. *J. Mater. Chem. A* **2015**, *3*, 525-534.

28. Gumilar, G.; Kaneti, Y. V.; Henzie, J.; Chatterjee, S.; Na, J.; Yuliarto, B.; Nugraha, N.; Patah, A.; Bhaumik, A.; Yamauchi, Y. General Synthesis of Hierarchical Sheet/Plate-Like M-BDC (M=Cu, Mn, Ni, and Zr) Metal-Organic Frameworks for Electrochemical Non–Enzymatic Glucose Sensing. *Chem. Sci.* **2020**, *11*, 3644-3655.

29. Vaidyanathan, S.; Cherng, J. Y.; Sun, A. C.; Chen, C. Y.; Bacteria-T Emplated NiO Nanoparticles/Microstructurefor an Enzymeless Glucose Sensor. *Int. J. Mol. Sci.* **2016**, 17, 1104.

30. Zhang, L.; Ding, Y.; Li, R.; Ye, C.; Zhao G.; Wang, Y. Ni-Based Metal-Organic Framework Derived Ni@C Nanosheets on a Ni Foam Substrate as a Supersensitive Non-Enzymatic Glucose Sensor. *J. Mater. Chem. B* **2017**, *5*, 5549-5555.

31. Lu, M. X.; Deng, Y. J.; Li, Y. C.; Li, T. B.; Xu, J.; Chen, S. W.; Wang, J. Y. Core-Shell MOF@MOF Composites for Sensitive Nonenzymatic Glucose Sensing in Human Serum. *Anal. Chim. Acta* **2020**, *1110*, 35-43.

32. Balasubramanian, P. He, S. B.; Deng, H. H.; Peng, H. P.; Chen, W. Defects Engineered 2D Ultrathin Cobalt Hydroxide Nanosheets as Highly Efficient Electrocatalyst for Non-Enzymatic Electrochemical Sensing of Glucose and L-cysteine. *Sens. Actuator B Chem.* **2020**, *320*, 128374.

33. Wang, J.; Xu, L.; Lu, Y.; Sheng, K.; Liu, W.; Chen, C.; Li, Y.; Dong, B.; Song, H. Engineered IrO_2@NiO core-Shell Nanowires for Sensitive Nonenzymatic Detection of Trace Glucose in Saliva. *Anal. Chem.* **2016**, *88*, 12346-12353.

34. Ghanbari, K.; Babaei, Z. Fabrication and Characterization of Non-Enzymatic Glucose Sensor Based on Ternary NiO/CuO/Polyaniline Nanocomposite. *Anal. Biochem.* **2016,** *498*, 37-46.

35. Heyser, C.; Schrebler, R.; Grez, P. New Route for the Synthesis of Nickel (II) Oxide Nanostructures and Its Application as Non−Enzymatic Glucose Sensor. *J. Electroanal. Chem.* **2018**, *832*, 189-195.

36. Luo, L.; Li, F.; Zhu, L.; Ding, Y.; Zhang, Z.; Deng, D.; Lu, B. Nonenzymatic Glucose Sensor Based on Nickel (II) Oxide/ordered Mesoporous Carbon Modified Glassy Carbon Electrode. *Colloids Surf. B* **2013**, *102*, 307-311.

37. Yu, Z. N.; Zou, L.; Chen, Y. L.; Jiang, J. Z. (Pc)Eu(Pc)Eu[trans−T($COOCH_3$)$_2$PP]/GO Hybrid Film-Based Nonenzymatic H_2O_2 Electrochemical Sensor with Excellent Performance. *ACS Appl. Mater. Inter.* **2016**, *8*, 30398−30406.

38. Xu, Z. L.; Yang, L.; Xu, C. L. Pt@UiO-66 Heterostructures for Highly Selective Detection of Hydrogen Peroxide with an Extended Linear Range. *Anal. Chem.* **2015**, *87*, 3438−3444.

39. Cheng, C. F.; Zhang, C. M.; Gao, X. H.; Zhuang, Z. H.; Du, C.; Chen, W. 3D Network and 2D Paper of Reduced Graphene Oxide/Cu_2O Composite for Electrochemical Sensing of Hydrogen Peroxide. *Anal. Chem.* **2018**, *90*, 1983-1991.

40. Kim, K.; Kim, J.; Bae, Y. S. Zn–Co Bimetallic Zeolitic Imidazolate Frameworks as Nonenzymatic Electrochemical Glucose Sensors with Enhanced Sensitivity and Chemical Stability. *ACS Sustainable Chem. Eng.* **2022**, *10*, 11702-11709.

41. Wang, Z. D.; Ma, Y.; Hao, X. G.; Huang, W.; Guan, G. Q.; Abudula, A.; Zhang, H. A Novel Electroactive Hybrid Film Electrode with Proton Buffer Effect for Detecting Hydrogen Peroxide and Uric Acid. *J. Mater. Chem. A* **2014**, *2*, 15035-15043.

42. Periasamy, A. P.; Umasankar, Y.; Chen, S. M. Nanomaterials-Acetylcholinesterase Enzyme Matrices for Organophosphorus Pesticides Electrochemical Sensors: a Review. *Sensors* **2009,** *9*, 4034-4055.

43. Nandini, S.; Nalini, S.; Sanetuntikul, J.; Shanmugam, S.; Niranjana, P.; Melo, J. S.; Suresh, G. S. Development of a Simple Bioelectrode for the Electrochemical Detection of Hydrogen Peroxide Using Pichia Pastoris Catalase Immobilized on Gold Nanoparticle Nanotubes and Polythiophene Hybrid. *Analyst* **2014**, *139*, 5800-5812.

44. Zhang, L.; Tu, L. Y.; Liang, Y.; Chen, Q.; Li, Z. S.; Li, C. H.; Wang, Z. H. Li, W. Coconutbased Activated Carbon Fibers for Efficient Adsorption of Various Organic Dyes. *RSC Adv.* **2018**, *8*, 42280-42291.

45. Madrakian, T.; Afkhami, A.; Ahmadi, M.; Adsorption and Kinetic Studies of Seven Different Organic Dyes onto Magnetite Nanoparticles Loaded Tea Waste and Removal of them from Wastewater Samples. *Spectrochim. Acta A.* **2012**, *99*, 102-109.

46. Namvari, M.; Namazi, H. Clicking Graphene Oxide and Fe_3O_4 Nanoparticles Together: an Efficient Adsorbent to Remove Dyes from Aqueous Solutions. *Int. J. Environ. Sci. Technol.* **2014**, *11*, 1527-1536.

47. Zhao, X. G.; Huang, J. G.; Wang, B.; Bi, Q.; Dong, L. L.; Liu, X. J. Preparation of Titanium Peroxide and Its Selective Adsorption Property on Cationic Dyes. *Appl. Surface Sci.* **2014**, *292*, 576-582.

48. Bagheri, A. R.; Ghaedi, M.; Asfaram, A.; Bazrafshan, A. A.; Jannesar, R. Comparative Study on Ultrasonic Assisted Adsorption of Dyes from Single System onto Fe_3O_4 Magnetite Nanoparticles Loaded on Activated Carbon: Experimental Design Methodology. *Ultrason. Sonochem.* **2017**, *34*, 294-304.

49. Ansari, M. O.; Kumar, R.; Ansari, S. A.; Ansari, S. P.; Barakat, M. A.; Alshahrie, A.; Cho, M. H. Anion Selective pTSA Doped Polyaniline@Graphene Oxide-Multiwalled Carbon Nanotube Composite for Cr(VI) and Congo Red Sdsorption. *J. Colloid Interface Sci.* **2017**, *496*, 407-415.

50. Zheng, Y. Q.; Cheng, B.; You, W.; Yu, J. G.; Ho, W. K. 3D Hierarchical Graphene Oxide NiFe LDH Composite with Enhanced Adsorption Affinity to Congo red, Methyl Orange and Cr(VI) ions. *J. Hazard. Mater.* **2019**, *369*, 214-225.

Chapter 6: Cu/Zr-MOF dual-mode detection of hydrogen peroxide

This chapter presents the synthesis of the copper/zirconium metal-organic frameworks (Cu/Zr-MOF) nanozymes by a solvothermal method. The prepared Cu/Zr-MOF is confirmed by FESEM, TEM, XPS and XRD. The results demonstrate that the Cu/Zr-MOF not only exhibits excellent electrocatalytic activity towards H_2O_2 reduction, but also shows high peroxidase-like activity. Leveraging these advantageous properties, a dual-mode colorimetric-electrochemical sensing platform is developed for accurate and sensitive detection of H_2O_2.

This Chapter is published to the journal "ACS Applied Nano Materials":

Lei, P., Wu, N., Zhou, Y., Dong, C., Liu, Y., and Shuang, S. (2024). Cu/Zr metal-organic frameworks with high peroxidase-like activity for sensitive electrochemical and colorimetric dual-mode detection of hydrogen peroxide released from living cells. ACS Applied Nano Materials, 7, 6556-6563.

Cu/Zr metal-organic frameworks with high peroxidase-like activity for sensitive electrochemical and colorimetric dual-mode detection of hydrogen peroxide released from living cells

Abstract

Hydrogen peroxide (H_2O_2) is closely associated with various diseases and is commonly used as a target for disease diagnosis and treatment, making the research on H_2O_2 detection methods crucial. Compared to currently used single-mode detection methods, dual-mode detection offers self-validation and self-correction capabilities, which help to provide more accurate detection results. Herein, an electrochemical and colorimetric dual-mode sensing platform was developed to detect H_2O_2 based on copper/zirconium metal-organic frameworks (Cu/Zr-MOF) nanozymes with high peroxidase-like activity. Cu/Zr-MOF catalyzes the reduction of H_2O_2 to generate ·OH, which oxidizes colorless 3,3',5,5'-tetramethylbenzidine (TMB) into a blue product (oxTMB), and the color change can be recognized and measured using a smartphone application. Furthermore, Cu/Zr-MOF exhibits excellent electrocatalytic reduction activity towards H_2O_2. Electrochemistry demonstrated higher sensitivity with a detection limit as low as 21.3 nM, compared to colorimetry (0.11 μM). The effective combination of the two detection modes allows the sensing platform to exhibit high accuracy, selectivity, and reliability. The dual-mode sensing platform opens a pathway for the accurate and sensitive detection of intracellular/extracellular H_2O_2 and has a broad spectrum of applications in pathological research and disease diagnosis.

Keywords: Dual-mode, electrochemistry, colorimetry, MOF nanozyme, hydrogen peroxide

6.1. Introduction

H_2O_2 is a reactive oxygen species (ROS) present in living organisms, which enables the generation of highly active hydroxyl radicals [1]. It plays a crucial role in regulating cell growth, cell differentiation, apoptosis, immune cell activation, and other biological signal transduction processes [2,3]. Excessive secretion of H_2O_2 can easily lead to oxidative stress, resulting in aging and numerous diseases, such as cardiovascular disease, atherosclerosis, Parkinson's disease, diabetes, and cancer [4,5]. H_2O_2 is produced as a byproduct of various oxidase reactions during the oxidative metabolism process in organisms, making it an essential cellular metabolite closely associated with human health [6]. Therefore, the detection of H_2O_2 release from living cells is of immense significance for comprehending cell metabolism and enabling early disease diagnosis.

Various methods, including colorimetry [7], electrochemistry [8], photoelectrochemistry [9], and fluorescence [10], have been utilized to detect H_2O_2. Although certain advancements have been achieved, most of these methods are based on single-mode construction, which can lead to issues such as high background signal, significant interference, low accuracy, and limited sensitivity [11]. In order to enhance accuracy effectively, several dual-mode sensing platforms that rely on two relatively independent signals have been developed, such as fluorescence-colorimetry [7], fluorescence-photothermal [12], and fluorescence-electrochemistry [13]. Among these techniques, colorimetric-electrochemical dual-mode detection has garnered considerable attention due to its notable advantages of high sensitivity, rapid speed, and cost-effectiveness [14]. As a result, it holds significant potential in the development of precise, efficient, and real-time H_2O_2 detection.

Metal-organic frameworks (MOFs) are a type of porous material composed of metal nodes and organic connectors [15]. Due to their easily adjustable structure, ease of functionalization, and active site opening, MOFs have become the focus of research in H_2O_2 electrochemical and colorimetric sensing. Dong et al. [16] developed a ratio electrochemical sensor using Au-Co-MOF as the detection probe for sensitive and specific detection of H_2O_2 in cells. Jose's group [15] designed an electrochemical platform based on Co-MOF deposition on a graphite electrode for H_2O_2 detection, utilizing Co to enhance the electrocatalytic activity. Wang et al. [17] prepared a Zr-MOF-PVP nanocomposite with enzyme-like

properties, which exhibited significant catalytic activity for the colorimetric detection of H_2O_2. Although these methods have achieved fast response with acceptable sensitivity for the determination of H_2O_2, single detection approaches prove vulnerable to various internal and external factors, causing significant impacts on accuracy, selectivity, and stability. Its limitation restricts the developmental potential of electrochemical and colorimetric sensing. There is growing interest in dual-mode sensing techniques that integrate two complementary methods to overcome the limitation. The approach is gaining attention for its remarkable accuracy and effective anti-interference capabilities, allowing it to meet diverse analytical requirements. To our knowledge, only a limited number of dual-mode electrochemical colorimetric methods have been used for H_2O_2 detection, and they still face challenges associated with visualization and accurate detection. Therefore, establishing a colorimetric-electrochemical dual-mode detection method based on MOFs has more significant potential for achieving high sensitivity and selective detection of H_2O_2.

Based on the above inspiration, Zr-based metal-organic frameworks containing Cu (Cu/Zr-MOF) nanozymes were successfully synthesized using the solvothermal method. We not only explored the peroxidase-like activity of Cu/Zr-MOF nanoenzyme but also discovered its excellent electrochemical reduction activity towards H_2O_2. Leveraging these performance advantages, a colorimetric-electrochemical dual-mode sensing platform was established to enable accurate and sensitive detection of H_2O_2 (Fig. 6.1). Additionally, a "Color Recognizer" application was used to collect the reaction solution’s color patterns (RGB), creating a smartphone-based sensing system. The dual-mode output of colorimetry and electrochemistry greatly enhances the selectivity and accuracy, showing promising prospects for real-time monitoring.

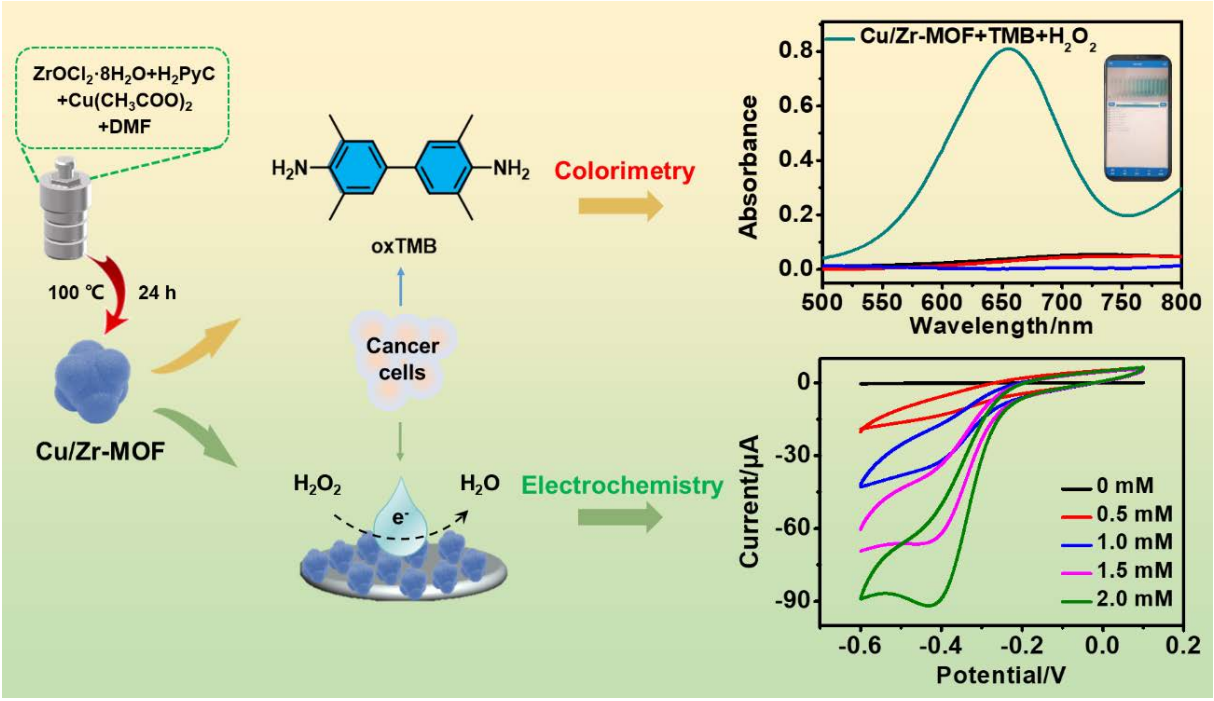

Fig. 6.1: Preparation of Cu/Zr-MOF for electrochemical and colorimetric dual-mode detection of H_2O_2

6.2 Experimental

6.2.1 Reagents

Zirconium oxychloride octahydrate ($ZrOCl_2 \cdot 8H_2O$), copper(II) acetate ($CuAc_2$), trifluoroacetic acid (TFA), 1H-pyrazole-4-carboxylic acid (H_2PyC, 97%), dimethylformamide (DMF), hydrogen peroxide (H_2O_2, 30%), 3,3,5,5-tetramethylbenzidine (TMB), and other analytical grade reagents, were purchased from Shanghai Aladdin Bio-Chem Technology Co., Ltd. Ultrapure water was used for the experiments. 0.1 M phosphate-buffered solution (PBS) was prepared using potassium dihydrogen phosphate, disodium hydrogen phosphate, and phosphoric acid. 0.2 M acetate buffer solution (NaAc-HAc) was prepared using sodium acetate and glacial acetic acid.

6.2.2 Instruments

UV-visible absorption spectra were recorded on a UV-2550 UV-visible spectrophotometer (Shimadzu Co., Kyoto, Japan). Electrochemical detection was performed using a CHI-660E electrochemical workstation (Shanghai Chenhua Instrument Co., China). The surface morphology and elemental composition of Cu/Zr-MOF were observed using a ZEISS Gemini 300 scanning electron microscope

(SEM, ZEISS, Germany) and a TF20 transmission electron microscope (TEM, FEI, USA). The crystalline of Cu/Zr-MOF was determined through XRD-7000 analysis. X-ray photoelectron spectroscopy (XPS) was used to determine the valence states of the elements present.

6.2.3 Preparation of Cu/Zr-MOF and Cu/Zr-MOF/SPE

$ZrOCl_2 \cdot 8H_2O$ (22.0 mg), $Cu(Ac)_2$ (62.0 mg), and 1H-pyrazole-4-carboxylic acid (H_2PyC) (17.0 mg) were dissolved in 20 mL of DMF by ultrasonication. Then, TFA (100 μL) was added to the solution. The mixture was transferred to the 100 mL Teflon-lined stainless-steel autoclave and left at 100 °C for 1 day. The blue crystalline material (Cu/Zr-MOF) was collected by centrifugation, washed several times with DMF and acetone, and dried at 60°C for 12 h. 5 μL of Cu/Zr-MOF suspension (2.0 mg dispersed in 2.0 mL 0.1 wt% Nafion) was dropped onto commercial screen-printed electrodes (SPE) surface and dried under infrared light to obtain Cu/Zr-MOF/SPE. The preparation of Zr-MOF is similar to that of Cu/Zr-MOF, with the only difference being the absence of copper acetate.

6.2.4 Peroxidase-Like Activity of Cu/Zr-MOF

The optimal catalytic conditions for the system were determined by studying the catalytic activity of Cu/Zr-MOF at different temperatures (30-48 °C), solution pH (3.0-7.0), catalyst concentrations (0.1-1.0 mg mL^{-1}), and reaction times (5-35 min). The typical TMB was used as colorimetric substrate to evaluate the peroxidase-like activity of Cu/Zr-MOF. Typically, 40 μL of Cu/Zr-MOF solution (1.0 mg mL^{-1}) was added to cuvette containing 30 μL of H_2O_2 (10 mM), 30 μL of TMB (10 mM), and 1.9 mL of NaAc-HAc (0.2 M, pH 5.0). The mixture was incubated at 42 °C in the dark for 20 minutes, followed by UV-visible spectrophotometric analysis to measure the absorbance at 652 nm of the system.

6.2.5 Steady-State Kinetics of the Peroxidase-Like Cu/Zr-MOF

The absorbance changes of TMB+H_2O_2+Cu/Zr-MOF system were measured by varying the concentrations of TMB or H_2O_2 to study the steady-state kinetics of the peroxidase-like reaction. To determine the affinity between Cu/Zr-MOF and the substrate TMB or H_2O_2, a series of H_2O_2 concentrations (30 μL, 10 mM) were added to the NaAc-HAc (1.9 mL, 0.2 M, pH 5.0) containing Cu/Zr-MOF (40 μL, 0.7 mg mL^{-1}) and TMB (30 μL, 10 mM); similarly, a series of TMB concentrations (30

μL, 10 mM) were added to the NaAc-HAc (1.9 mL, 0.2 M, pH 5.0) containing Cu/Zr-MOF (40 μL, 0.7 mg mL^{-1}) and H_2O_2 (30 μL, 10 mM). After incubating at 42°C for 20 min, the kinetic test was performed and the absorbance changes at 652 nm were recorded. The kinetic constants were calculated based on the Michaelis-Menten equation, $V=V_{max}[S]/(K_m+[S])$, where V is the initial velocity, [S] is the substrate concentration, V_{max} is the maximum reaction rate, and K_m is the Michaelis constant.

6.2.6 Electrochemical and Colorimetric Dual-Mode Detection of H_2O_2

Electrochemical detection. Different concentrations of H_2O_2 were added to 5.0 mL of PBS (0.1 M, pH 7.4), and quantitative analysis of H_2O_2 was performed using the chronoamperometry to investigate the relationship between the current and the concentration of H_2O_2.

Colorimetric detection. Different concentrations of H_2O_2, 40 μL of TMB (10 M), and 40 μL of Cu/Zr-MOF (1.0 mg mL^{-1}) were added to NaAc-HAc (1.9 mL, 0.2 M, pH 5.0). The mixed solution was then incubated at 42 °C in the dark for 20 minutes, and the UV-visible spectrum of the mixed solution was recorded to study the relationship between the absorbance at 652 nm and the concentration of H_2O_2. Moreover, a smartphone is used to capture images of the reaction solution, and the "Color Recognizer" application digitizes them to draw quantitative curves of G/RGB and H_2O_2 concentration, achieving quantitative analysis of H_2O_2.

6.2.7 Cell Culture and Detection of H_2O_2 in Living Cells

HeLa cells were cultured under suitable conditions. When the cells reached 90%, they were collected by centrifugation and adjusted to 1×10^6 mL^{-1} using PBS (pH 7.4). Cells were stimulated with a certain concentration of PMA to induce the release of H_2O_2 and incubated for 30 minutes. Subsequently, the above solution was added to HAc-NaAc (0.2 M, pH 5.0), TMB (30 μL, 10 mM), and Cu/Zr-MOF (0.7 mg mL^{-1}), followed by incubation at 42°C for 20 min. Finally, the absorbance of the reaction solution was measured at 652 nm. For electrochemical detection, 8 μL solution was evaluated on an electrode.

6.3 Results and Discussions

6.3.1 Characterization of Cu/Zr-MOF

The elemental composition and valence state of Cu/Zr-MOF were analyzed by XPS, and the full spectrum confirms the existence of C, O, N, Zr, and Cu in Fig. 6.2G. The elements C, N, and O belong to the ligand H_2PyC of Zr-MOF (Fig. S10A). In the C 1s spectrum, peaks at 284.7 eV, 285.6 eV, and 288.8 eV correspond to C-C, C=C, and C=O in H_2Pyc, respectively (Fig. S10B). Two peaks are observed at 531.8 eV and 532.0 eV, representing C-OH and C=O in Fig. S10C. The peaks observed at 182.8 eV and 185.2 eV are distinctive features associated with Zr $3d_{3/2}$ and Zr $3d_{5/2}$ in Fig. S10D. In the high-resolution Cu 2p spectrum (Fig. 6.2H), the peaks at 934.8 eV and 954.7 eV correspond to Cu $2p_{3/2}$ and Cu $2p_{1/2}$, and the peak at 943.3 eV presents the shake-up satellite, which are the typical peaks of Cu^{2+} [18]. The crystal structure of Cu/Zr-MOF was characterized using XRD (Fig. 6.2I). XRD patterns of all samples present the characteristic peaks of Zr-MOF [19]. There is a shoulder peak at 7°, indicating lower crystallinity of Cu/Zr-MOF, resulting in a smaller crystal size and more skeletal defects. These characterization results confirmed the successful synthesis of Cu/Zr-MOF.

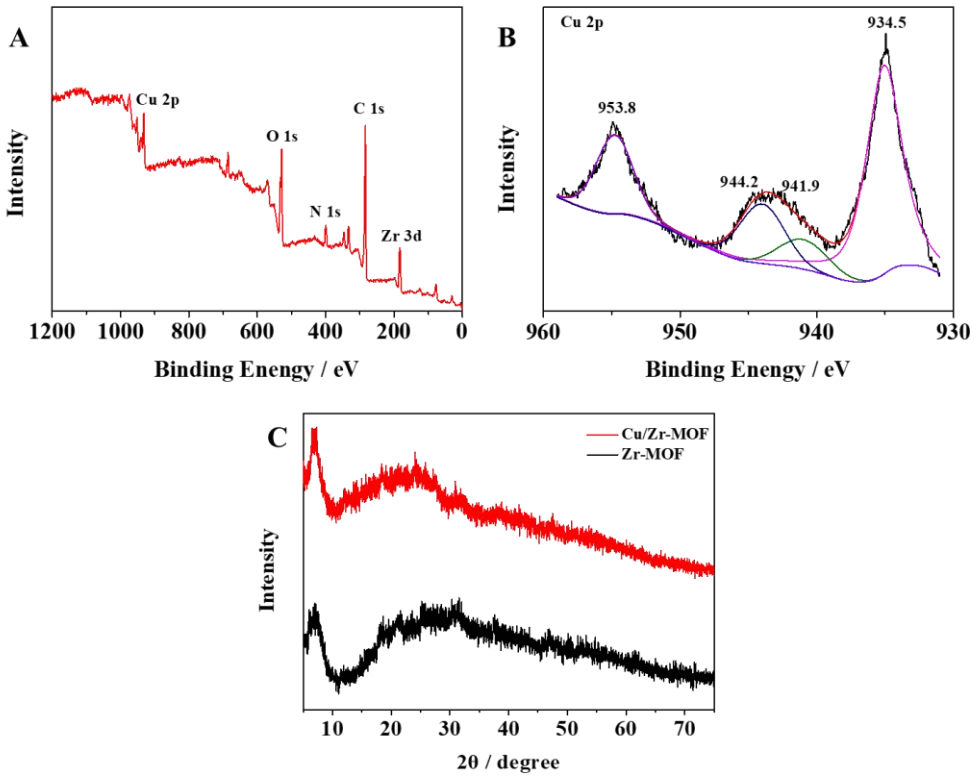

Fig. 6.2: XPS full spectrum (A) and Cu 2p (B) of Cu/Zr-MOF; XRD spectrum (C) of Cu/Zr-MOF

The characterization by FESEM and TEM facilitates the study of the surface morphology and structure of Cu/Zr-MOF. The FESEM image of Cu/Zr-MOF (Fig. 6.3A and B) has an apparent morphology of

agglomerated particles ranging from 100 to 200 nm, which is consistent with the TEM images in Fig. 6.3C. The elemental composition of Cu/Zr-MOF was determined through mapping analysis (Fig. 6.3D) and EDS (Fig. 6.3E), indicating the presence of C, N, O, Zr, and Cu elements in the material.

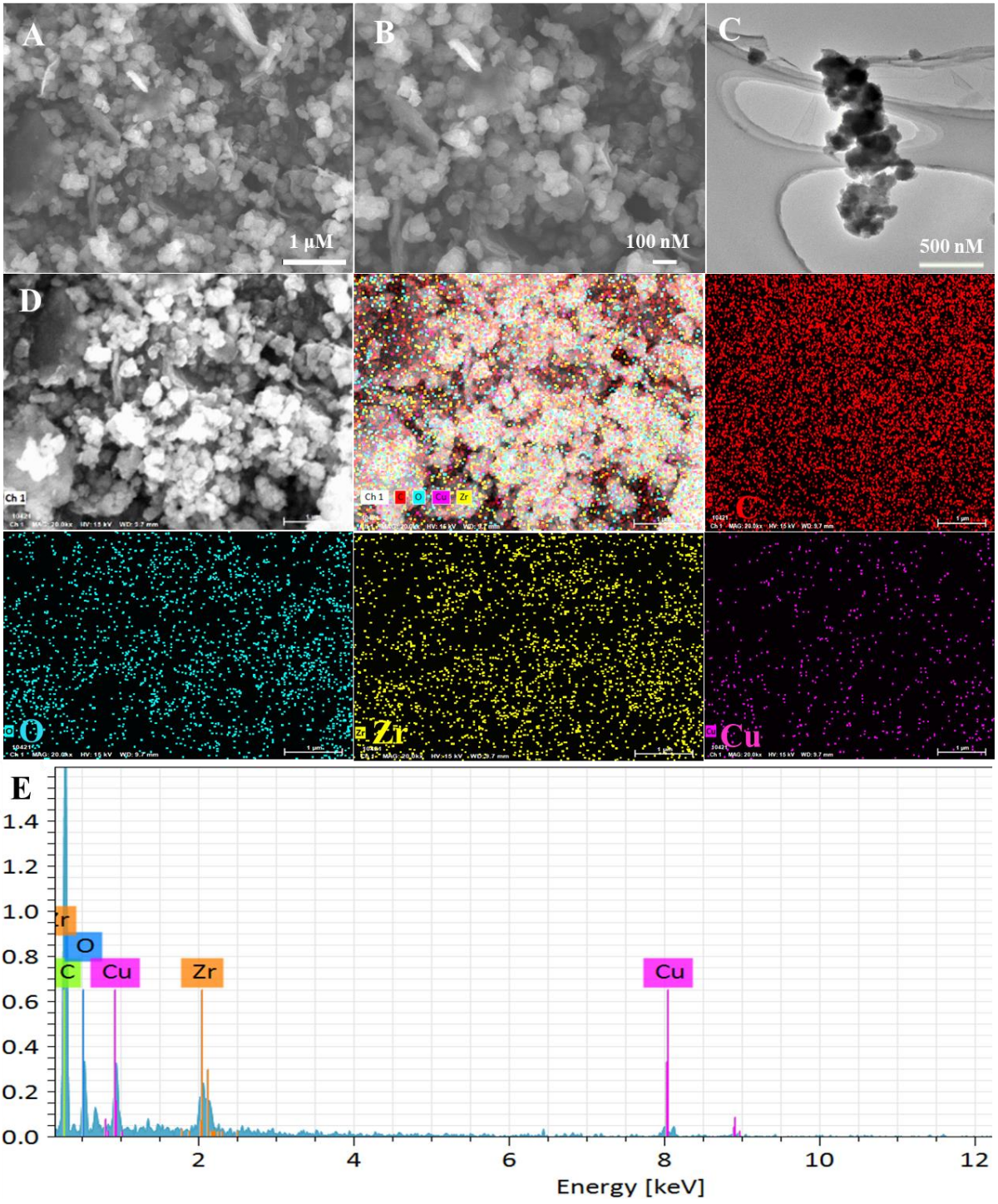

Fig. 6.3: FESEM (A and B) and TEM (C and D) images of Cu/Zr-MOF; mapping analysis (E) and EDS (F) of Cu/Zr-MOF

6.3.2 Electrocatalytic Activity of Cu/Zr-MOF

The electrocatalytic activity was evaluated based on the cyclic voltammograms (CVs) obtained at both SPE and Cu/Zr-MOF/SPE in the presence and absence of H_2O_2, as shown in Fig. 6.4A. No reduction peak is observed at SPE in the absence and presence of H_2O_2. However, Cu/Zr-MOF/SPE exhibits a more pronounced reduction peak upon the addition of H_2O_2, indicating its superior catalytic effect on H_2O_2. To further demonstrate the exceptional performance of Cu/Zr-MOF for H_2O_2, we tested it under various H_2O_2 concentrations. As depicted in Fig. 6.4B, the reduction peak current consistently increases with the progressive rise in H_2O_2 concentration. Furthermore, the peak position gradually shifts towards positive potential (from -0.46 V to -0.42 V) and the reduction peak broadened, which exemplifies the characteristic electrocatalytic reduction process of H_2O_2 [20].

The effect of different scan rates on H_2O_2 reduction is investigated on Cu/Zr-MOF/SPE, as shown in Fig. S11A. In the range of 10-190 mV s^{-1}, the peak current of H_2O_2 reduction increases with an increasing scan rate. The peak current shows a linear relationship with the square root of the scan rate (Fig. S11B), which indicates that the reduction of H_2O_2 on SPE/MOFs is diffusion-controlled. There is no significant difference in the reduction current of Cu/Zr-MOF/SPE in the N_2, air, and O_2 environments, as illustrated in Fig. S11C. However, the electrochemical reduction of H_2O_2 is easily influenced by dissolved oxygen, thus requiring deoxygenation of the solution during the detection process. The CV response of Cu/Zr-MOF/SPE to H_2O_2 was studied in PBS at pH 3.0-8.0. As shown in Fig. S11D, the reduction peak current of H_2O_2 increases with increasing pH from 5.0 to 7.4. However, the reduction peak current decreases when the pH reached 8.0. Therefore, pH 7.4 is chosen as the optimal pH. The effect of different modifications on the electrochemical behavior of H_2O_2 is investigated, as depicted in Fig. S11E. The reduction peak current of H_2O_2 reaches its maximum when the modification of Cu/Zr-MOF is 8.0 μL. When the modification exceed 8.0 μL, the surface modification film become too thick, hampering the electron exchange between H_2O_2 and the electrode surface, resulting in a reduction in the peak current. Hence, 8.0 μL is selected as the optimal modification for subsequent experiments. The current response of H_2O_2 at various applied potentials was studied by chronoamperometry, considering the impact of the applied potential on the background current [21]. As shown in Fig. S11F, the current initially increases

and then decreases as the sensing potential increases from -0.3V to -0.5V with the maximum and stable current response obtains at -0.45 V. Therefore, -0.45V is chosen as the optimal detection potential for H_2O_2 in the subsequent experiments.

According to the relevant literature and experimental results [22, 23], the possible reaction mechanism of the electrocatalytic reduction of H_2O_2 by Cu/Zr-MOF is illustrated in Fig. 6.4C. During the reaction, Cu (II) in Cu/Zr-MOF accepts electrons from the electrode surface to form Cu (I). Cu (I) is oxidized by H_2O_2, losing electrons to form Cu (II), and H_2O_2 obtains electrons to reduce to H_2O.

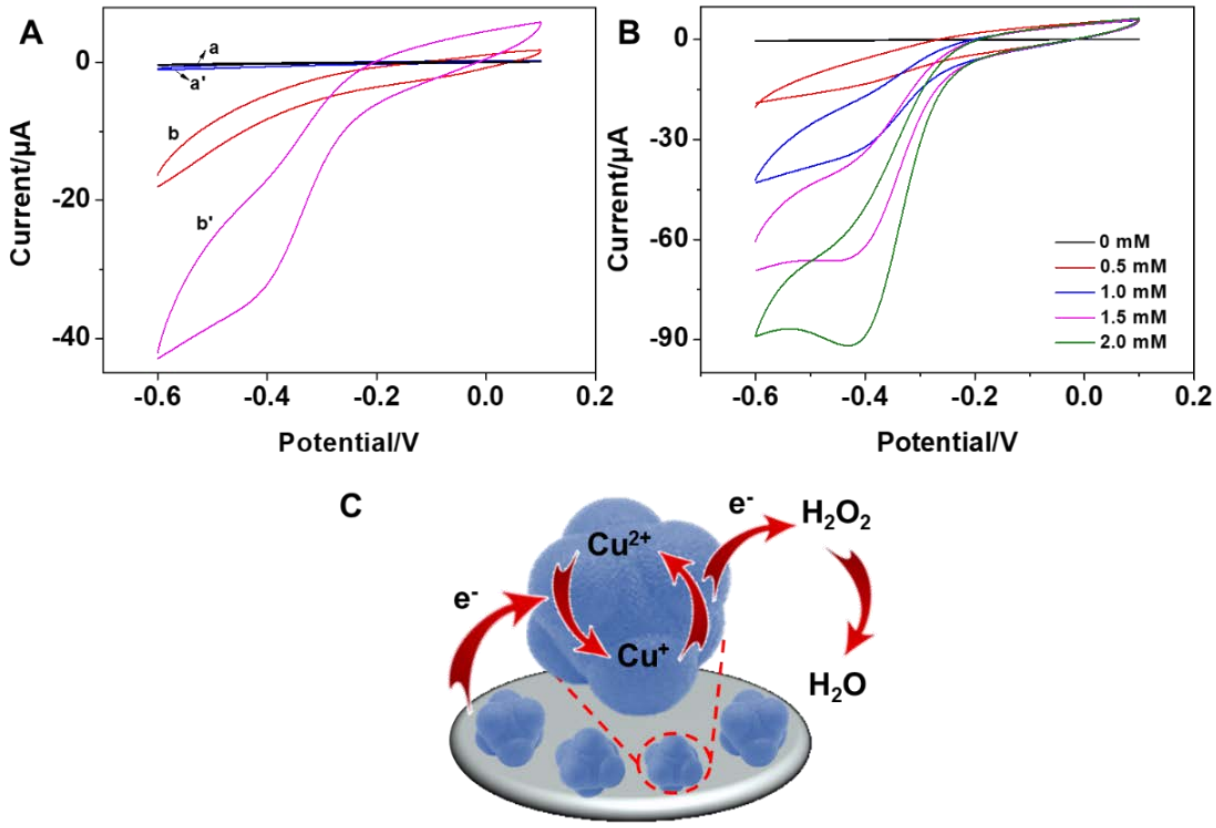

Fig. 6.4: (A) CVs of SPE (a and a') and Cu/Zr-MOF/SPE (b and b') in the presence (b and b') and absence (a and a') of 1.0 mM H_2O_2; (B) CVs of Cu/Zr-MOF/SPE in different concentrations of H_2O_2; (C) The reaction mechanism of electrocatalytic reduction of H_2O_2 with Cu/Zr-MOF/SPE

6.3.3 Peroxidase-Like Activity of Cu/Zr-MOF

The peroxidase-like activity of Cu/Zr-MOF and the absorption spectra of different reaction systems under the same conditions are investigated in Fig. 6.5A. No absorption peaks at 652 nm are observed for Cu/Zr-MOF, Cu/Zr-MOF+H_2O_2, and TMB+H_2O_2. However, when Cu/Zr-MOF, H_2O_2, and TMB

coexist, a strong absorption peak appears at 652 nm. Meanwhile, no absorption peak can be observed at 652nm for Zr-MOF (Fig. S12). These results indicate that Cu/Zr-MOF can catalyze the oxidation of TMB by H_2O_2 and exhibit peroxidase-like activity. The catalytic reaction mechanism of Cu/Zr-MOF is verified based on the reaction between terephthalic acid (TA) and ·OH in Fig. 6.5B [24]. The fluorescence signal of TA is almost negligible, but it is significantly enhanced when TA, Cu/Zr-MOF, and H_2O_2 coexist. This proves that Cu/Zr-MOF catalyze H_2O_2 to generate ·OH, which reacts with TA to produce 2-hydroxyterephthalic acid (HTA) with high fluorescence intensity.

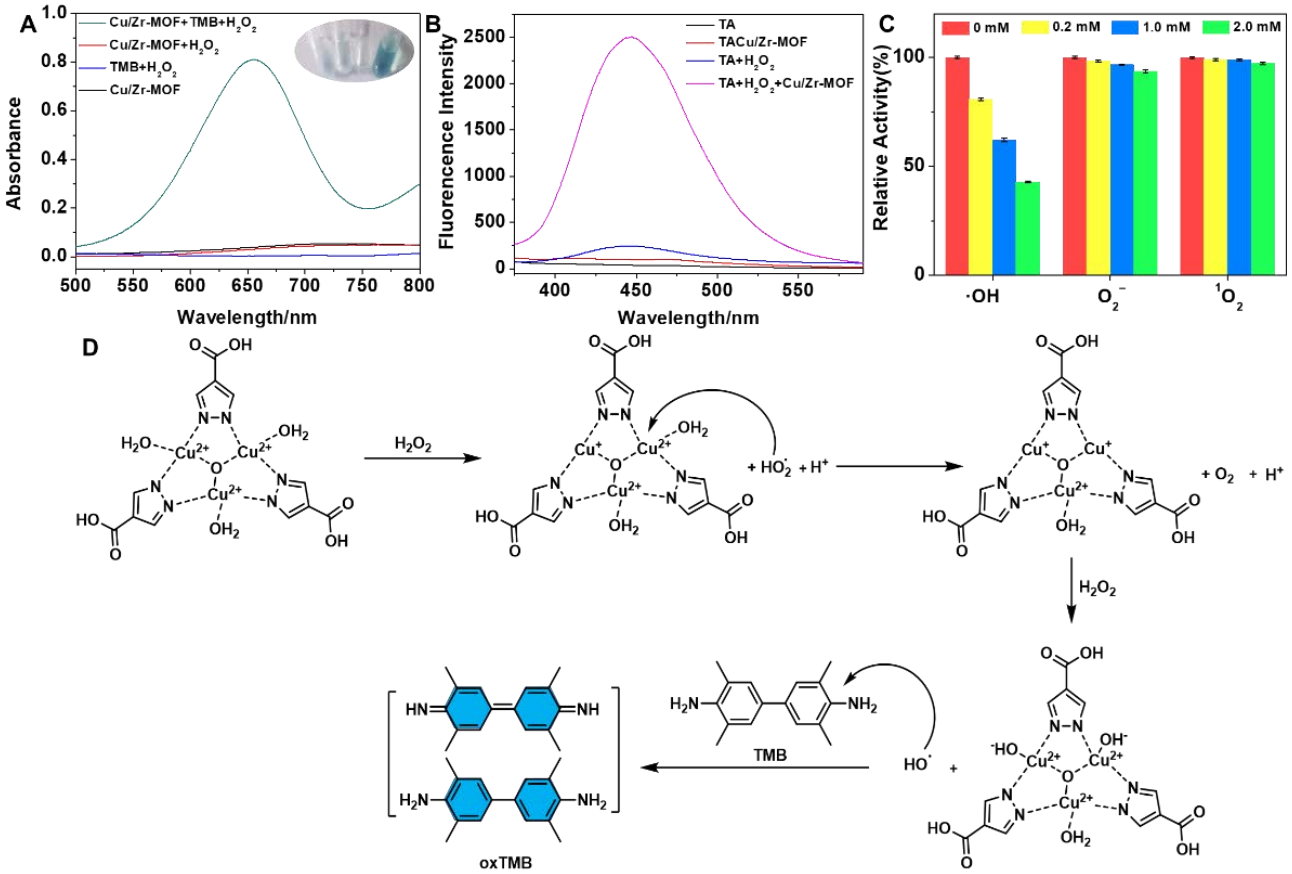

Fig. 6.5: (A) UV-vis absorption spectra of indifferent systems in NaAc-HAc (0.2 M pH=4.5) 1incubated at 42 ℃ for 20 min; (B) Fluorescence spectra of TA in the presence/absence of Cu/Zr-MOF and H_2O_2; (C) The relative activity of Cu/Zr-MOF with different radical scavenger; (D) The possible mechanism of peroxidase-like activity of H_2O_2 with Cu/Zr-MOF

Different free radical scavengers were used to explore other active oxygen species in the TMB+H_2O_2+Cu/Zr-MOF system. Various scavengers such as thiourea, p-benzoquinone (PBQ), and histidine are separately added to capture ·OH, O_2^-, and $^1O_2$ in Fig. 6.5C [25,26]. The addition of thiourea

significantly reduced the catalytic activity of Cu/Zr-MOF, indicating the presence of ·OH in TMB+H_2O_2+Cu/Zr-MOF system. The catalytic activity decreases by about 22.3% after adding P-benzoquinone (PBQ), indicating the presence of extremely few O_2^-. The effect of histidine on the catalytic activity of Cu/Zr-MOF can be ignored. Therefore, the main active oxygen specie produced by Cu/Zr-MOF catalyzing H_2O_2 is ·OH.

The presumed mechanism of Cu/Zr-MOF catalyzing the color change of TMB with H_2O_2 is illustrated in Fig. 6.5D. H_2O_2 is oxidized to $\cdot OH_2$ by Cu(II) to form Cu(I) [18]. The generated $\cdot OH_2$ reduces Cu(II) to Cu(I), which accelerates the production of ·OH [23, 27-29]. The structure of Cu/Zr-MOF facilitates sufficient contact between Cu(II) and H_2O_2, enhancing the peroxidase activity of Cu/Zr-MOF.

The effect of reaction conditions on the catalytic oxidation of TMB with H_2O_2 catalyzed by Cu/Zr-MOF was investigated. The maximum absorbance at 652 nm was set to 100%, and other absorbance and their ratios were taken as relative activities. Similar to most nanozymes [30, 31], Cu/Zr-MOF exhibits significant pH and temperature dependence. As depicted in Fig. S13A, the relative activity exhibits an initial ascent followed by a subsequent decline with increasing temperature, observing the maximum relative activity at 42°C. The observation suggests that lower temperatures are conducive to the catalytic reaction. Under acidic conditions, the relative activity demonstrates an increasing-then-decreasing trend with rising pH, reaching its highest point at pH 4.5 in Fig. S13B. The influence of Cu/Zr-MOF concentration on relative activity is illustrated in Fig. S13C, demonstrating a gradual augmentation in relative activity within the range of 0.1 to 0.7 mg/mL of Cu/Zr-MOF concentration, ultimately achieving a relatively stable state. The impact of reaction time on absorbance displays an initial increase followed by subsequent stabilization trend as the reaction time prolongs in Fig. S13D. Therefore, pH 5.0, 42℃, 0.7 mg mL^{-1}, and 20 min were selected as the optimal reaction conditions.

The steady-state kinetic analysis of the catalytic oxidation of TMB with H_2O_2 catalyzed by Cu/Zr-MOF was performed by fixing the concentration of one substrate (TMB or H_2O_2) and changing the concentration of the other substrate. The process in Fig. S14 follows the typical Michaelis-Menten kinetic model and exhibits a double reciprocal relationship within the studied substrate concentration

range, from which dynamic parameters are derived [32, 33]. Cu/Zr-MOF exhibits a fast catalytic rate and high affinity towards the substrate compared to previously reported nanozymes in Table 6.1.

Table 6.1: Kinetic parameters of Cu/Zr-MOF and other nanozymes

Nanozyme	Substrates	K_m (mM)	V_m (M/s)	Ref.
HRP	H_2O_2	3.70	8.71×10^{-8}	[34]
	TMB	0.434	10×10^{-8}	
PdNPs/N-PC-rGO	H_2O_2	0.57	3.05×10^{-8}	[35]
	TMB	0.074	4.31×10^{-8}	
Ru@G	H_2O_2	5.8	1.37×10^{-7}	[36]
	TMB	0.027	1.63×10^{-8}	
MOF-818@PMOF(Fe)	H_2O_2	0.298	0.91×10^{-8}	[37]
	TMB	0.895	6.01×10^{-8}	
Pd-Fe_3O_4_middle	H_2O_2	126.73	6.67×10^{-7}	[38]
	TMB	0.017	25.15×10^{-8}	
CoRh@G	H_2O_2	33	1.38×10^{-7}	[39]
	TMB	0.028	1.10×10^{-7}	
Cu/Zr-MOF	H_2O_2	1.290	3.82×10^{-7}	This work
	TMB	2.371	9.65×10^{-7}	

6.3.4 Electrochemical and colorimetric detection of H_2O_2

We studied the dual-mode detection of H_2O_2 by leveraging the electrocatalytic activity and peroxidase-like of Cu/Zr-MOF. As presented in Fig. 6.6A, the *i-t* curve is recorded by continuously injecting varying concentrations of H_2O_2. H_2O_2 concentration (ranging from 0.1 µM to 2500 µM) displays a linear relationship with the current signal (Fig. 6.6B). The linear equation is I_{pc}= -0.103*C*-5.00 (R^2=0.9902) with a detection limit of 21.3 nM (S/N=3). In Fig. 6.6C, the absorption spectra of the reaction system exhibit an increase in absorbance at 652 nm as the H_2O_2 concentration increases. A linear correlation exists between the H_2O_2 concentration (0.5 µM-100 µM) and absorbance with a detection limit of 0.11 µM (S/N=3) in inset Fig. 6.6C. Smartphone is utilized to record both the H_2O_2 concentration and the associated color changes (G/RGB) for H_2O_2 detection in Fig. 6.6D. The G/RGB increases proportionally with the rise in H_2O_2 concentration, resulting in a gradual transition from colorless to blue, thus demonstrating a linear correlation with the LOD of 19.26 µM.

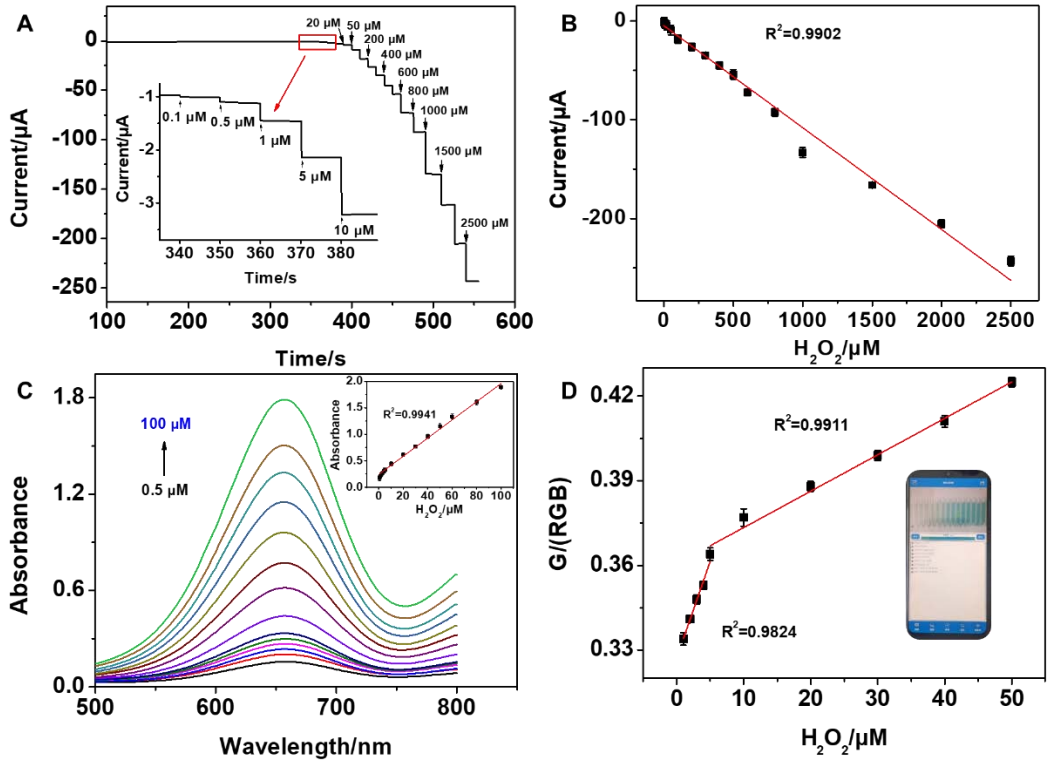

Fig. 6.6: (A) Chronoamperometric response of Cu/Zr-MOF/SPE on cumulative injection of H_2O_2 in PBS (0.1 M, pH 7.4); (B) Calibration plot of peak current as a function of concentration of H_2O_2; (C) UV-Vis absorption spectra of different H_2O_2 concentrations (Inset: the plotted linear relationships between absorbance and the corresponding H_2O_2 concentration); (D) Response of smart phone colorimetric detection system to different concentrations of H_2O_2

According to Table 6.2, the developed dual-mode detection method exhibits broader linear ranges, comparable detection limits, and superior performance compared to other methods. It is primarily attributed to the remarkable electrocatalytic performance and peroxidase-like activity of Cu/Zr-MOF nanozymes, which confers exceptional sensitivity and stability to the dual-mode sensing platform, enabling precise and sensitive detection of H_2O_2. Moreover, the obtained results can mutually verify and self-correct, significantly enhancing detection accuracy and reliability.

Table 6.2: Comparison of different sensors for the detection of H_2O_2

Material	Method	Linear range	LOD	Ref.
LIG/PB/CS	Electrochemistry	121-5000 μM	121.0	[40]
CeO_2·NPs	Electrochemistry	0.1-40 μM	0.035 μM	[41]
Bi_2Te_3	Electrochemistry	0.1-60 μM	0.016 μM	[42]
PAN-CuO	Colorimetry	0.5-125 μM	0.12 μM	[43]
Fe-N-C	Chromometry	0.5-100 mM	—	[44]
Fe-doped aminated lignin	Colorimetry	10-100 mM	54 μM	[45]
SQDs	Fluorescence	1.17-1.97 mM	30 nM	[46]
	Colorimetry	0.87-1.50 mM	60 nM	
FeSx/SiO_2	Electrochemistry	10 nM-10 μM	2.5 nM	[47]
	Colorimetry	1-100 μM	0.2 μM	
MOF-818	Chromometry	0.0133-166 mM	9.02 μM	[48]
	Electrochemistry	66 nM-3 mM	53.05 nM	

	Colorimetry	0.5-100 µM	0.11 µM	
Cu/Zr-MOF	G/RGB	1-50 µM	19.26 µM	This work
	Electrochemistry	0.1-2500 µM	21.3 nM	

6.3.5 Selectivity and Stability

The study of selectivity and stability is crucial for analytical detection. The selectivity of H_2O_2 (1.0 mM) was investigated under the presence of 10 times concentrations of potential interfering substances. No significant changes are observed in the current, absorbance, and solution color in Fig. 6.7A and B. Due to the oxidative nature of trivalent Fe^{3+} and ClO^-, a color change can be observed, but it has little impact on the electrochemical signal. Despite storage for 30 days, whereas Cu/Zr-MOF maintained a relative catalytic activity of 97.2%, and the current of Cu/Zr-MOF/SPE remained at 96.1% of the original current (Fig. 6.7C and D). The aforementioned results provide evidence for the good selectivity and stability of Cu/Zr-MOF for H_2O_2.

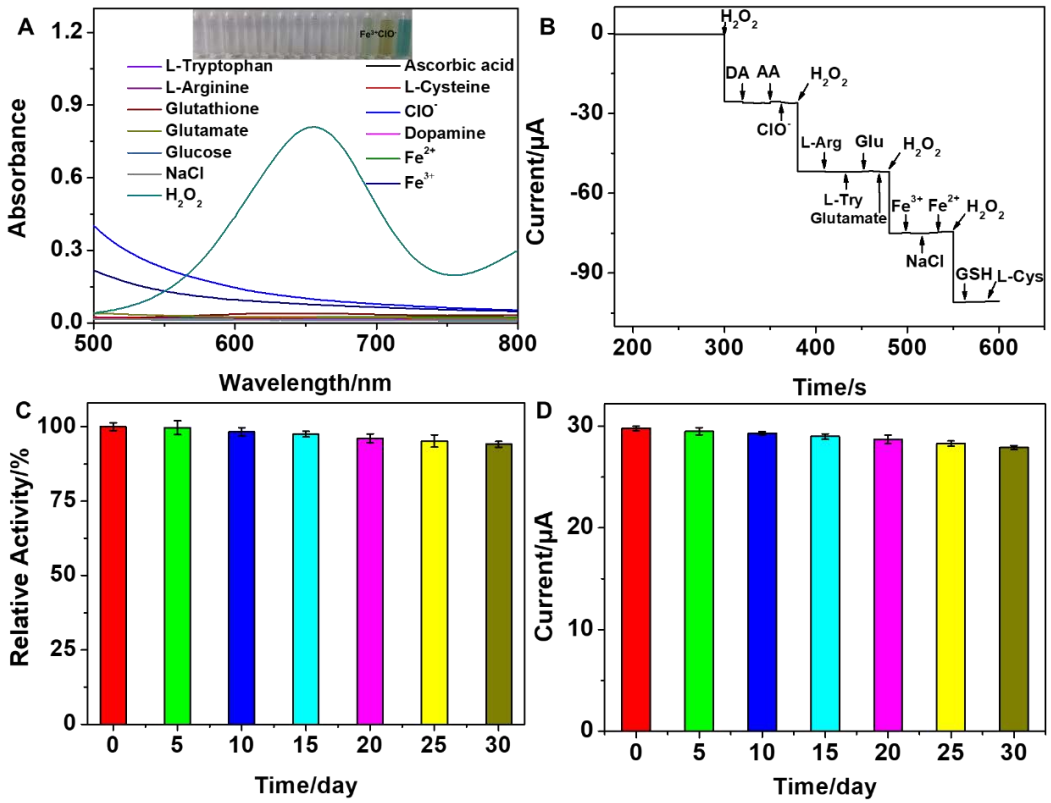

Fig. 6.7: Selectivity (A, B) and stability (C, D) of electrochemical and colorimetric H_2O_2 detection

6.3.6 Real-Time Detection of H_2O_2 Released by Living Cells

Based on the excellent sensing performance of Cu/Zr MOF, we further explored its potential applications in biology. The toxicity of Cu/Zr-MOF was evaluated on HeLa cells using the MTT assay. As shown in Fig. S15, the cell viability of all experimental groups remained above 75%, demonstrating that Cu/Zr-MOF exhibits low cytotoxicity and is suitable for application in biological systems. To confirm the feasibility of electrochemical and colorimetric dual-mode detection, it was conducted by stimulating the release of H_2O_2 from cells using PMA [49]. As shown in Fig. 6.8A, PMA can activate protein kinase *C* in HeLa cells, which then induces NADPH oxidase to generate O_2^-, ultimately resulting in the production of H_2O_2 catalyzed by superoxide dismutase. There is only a small change in current when PMA was added without cells. However, when 0.4 μM PMA is added to PBS containing cells, the current increased dramatically in Fig. 6.8B. HeLa cells are stimulated with different concentrations of PMA, resulting in a concentration-dependent response in Fig. 6.8C and D. According to the calibration curve of electrochemical and colorimetric in Fig. 6.8D, the concentration of H_2O_2 produced by HeLa cells is approximately 1.95 and 2.05 μM, with each cell producing about 2.0 pM of H_2O_2, which is consistent with previous reports [50]. These results indicate that Cu/Zr-MOF can be applied for the detection of H_2O_2 in cells and can be further utilized in pathological research.

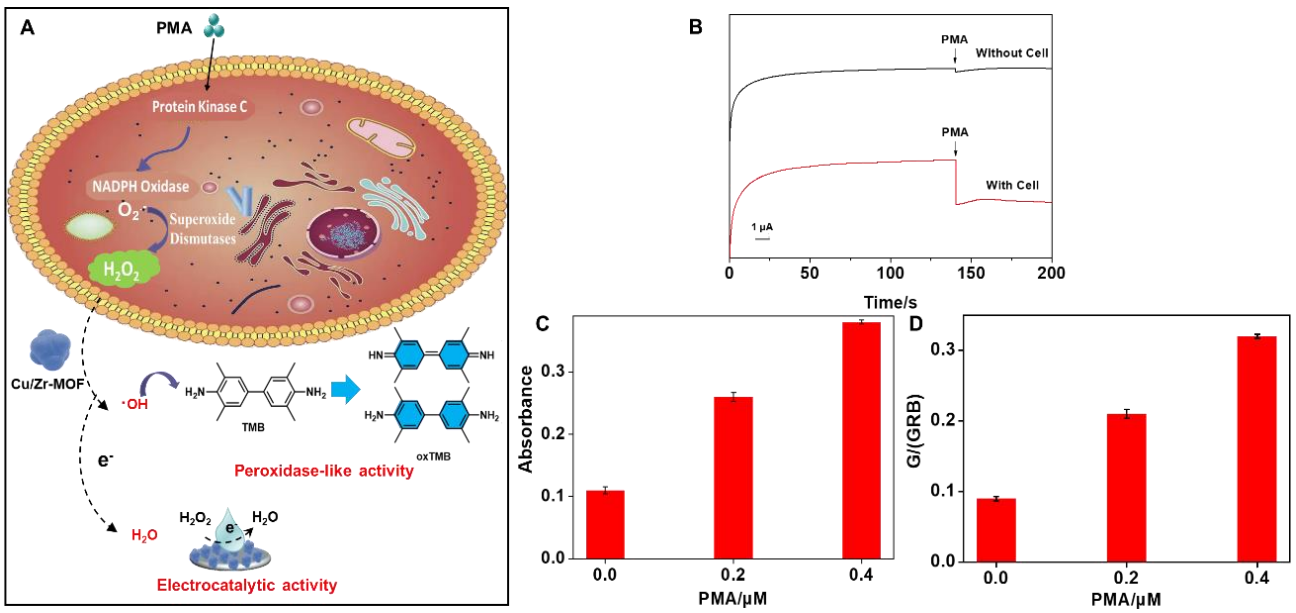

Fig. 6.8: (A) Schematic of the mechanism of H_2O_2 production in Hela cells stimulated by PMA; i-t curves (B), absorbance (C), and G/GRB (D) of HeLa cells stimulated by PMA

6.4 Conclusion

This work proposed a Cu/Zr-MOF nanozymes with excellent biocompatibility synthesized through the solvothermal method. The Cu metal center imparted Cu/Zr-MOF with outstanding electrocatalytic activity and peroxidase-like towards H_2O_2. Based on the dual catalytic activity of Cu/Zr-MOF, we constructed an electrochemical and colorimetric dual-mode sensing platform for H_2O_2 detection. Compared to colorimetry, electrochemistry exhibited higher sensitivity with a detection limit as low as 21.3 nM. In colorimetry, the change in color allowed the detection of H_2O_2 at a concentration of 0.11 μM. Utilizing a smartphone with a "Color Recognizer" application, real-time and accurate analysis by RGB analysis could be achieved without the use of laboratory instruments. The constructed dual-mode sensing platform has been successfully applied for the real-time detection of H_2O_2 released by cancer cells. This dual-mode detection proved to be more reliable and accurate than traditional single-mode detection, overcoming the limitations of each technique and expanding the application of dual-mode detection in broader areas.

References

1. Montezano, A.C.; Dulak, L.M.; Tsiropoulou, S.; Harvey, A.; Briones, A.M.; Touyz, R.M. Oxidative Stress and Human Hypertension: Vascular Mechanisms, Biomarkers, and Novel Therapies. *Can. J. Cardiol.* **2015**, *31*, 631-641.
2. Sies, H.; Hydrogen Peroxide as a Central Redox Signaling Molecule in Physiological Oxidative Stress: Oxidative Eustress. *Redox Biol.* **2017**, *11*, 613-619.
3. Mohammadi, S.S.; Vaezi, Z.; Hossein N.M. Chemiluminescent Liposomes as a Theranostic Carrier for Detection of Tumor Cells Under Oxidative Stress. *Anal. Chim. Acta* **2019**, *1059*, 113-123.
4. Liu, H.; Chen, Q.; Cheng, X.; Wang, Y.; Zhang, Y.; Fan, G. Sustainable and Scalable In-Situ Fabrication of Au Nanoparticles and Fe_3O_4 Hybrids as Highly Efficient Electrocatalysts for the Enzyme-Free Sensing of H_2O_2 in Neutral and Basic Solutions. *Sensor. Actuat. B: Chem.* **2020**, *314*, 128067.

5. Daemi, S.; Ghasemi, S.; Ashkarran, A.A. Electrospun CuO-ZnO Nanohybrid: Tuning the Nanostructure for Improved Amperometric Detection of Hydrogen Peroxide as a Non-Enzymatic Sensor. *J. Colloid Interf. Sci.* **2019**, *550*, 180-189.

6. Gu, C.; Bai, L.; Hou, T.; Zhang, L.; Gai, P.; Li, F. Dual-Mode Colorimetric and Homogeneous Electrochemical Detection of Intracellular/Extracellular H_2O_2 Based on FeSx/SiO_2 Nanoparticles with High peroxidase-Like Activity. *Anal. Chim. Acta* **2023**, *1265*, 341332.

7. Chen, X.; He, D.; Shentu, J.; Yang, S.; Yang, Y.; Wang, Y.; Zhang, R.; Wang, K.; Qian, J.; Long, L. Smartphone-Assisted Colorimetric and Near-Infrared Ratiometric Fluorescent Sensor for On-Spot Detection of H_2O_2 in Food Samples. *Chem. Eng. J.* **2023**, *472*, 14490.

8. Singh, N.; Siddiqui, H.; Goswami, M.; Kumar, S.; Ashiq, M.; Sathish, N.; Santosh, M.S.; Kumar, S. 3D-Printed Nanoscale-Thick Silver Thin Films for Electrochemical Sensing. *ACS Appl. Nano Mater.* **2023**, *6*, 3303-3311.

9. Hou, T.; Xu, N.N.; Song, X.; Yang, L.M.; Li, F. Label-Free Homogeneous Photoelectrochemical Aptasensing of $VEGF_{165}$ based on DNA-Regulated Peroxidase-Mimetic Activity of Metal-Organic-Frameworks. *Chin. Chem. Lett.* **2023**, *34*, 107907.

10. Yang, L.M.; Guo, H.; Hou, T.; Li, F. Uncovering the Interaction between Intracellular Telomerase Activity and Hydrogen Peroxide during Cancer Cell Apoptosis Utilizing a Dual-Color Fluorescent Nanoprobe. Anal. Chem. **2022**, *94*, 15162.

11. Sun, J.; Warden, A.R.; Huang, J.; Wang, W.; Ding, X. Colorimetric and Electrochemical Detection of Escherichia coli and Antibiotic Resistance Based on a p-Benzoquinone-Mediated Bioassay. *Anal. Chem.* **2019**, *91*, 7524-7530.

12. Li, S.; Wei, Z.; Xiong, L.; Xu, Q.; Yu, L.; Xiao, Y. In Situ Formation of o-Phenylenediamine Cascade Polymers Mediated by Metal-Organic Framework Nanozymes for Fluorescent and Photothermal Dual-Mode Assay of Acetylcholinesterase Activity. *Anal. Chem.* **2022**, *94*, 17263-17271.

13. Wang, X.; Lin, W.; Chen, C.; Kong, L.; Huang,Z.; Kirsanov, D.; Legin, A.; Wan, H.; Wang, P. Neural Networks Based Fluorescence and Electrochemistry Dual-Modal Sensor for Sensitive and

Precise Detection of Cadmium and Lead Simultaneously. *Sensor. Actuat. B: Chem.* **2022**, *366*, 131922.

14. Yang, Q.; Wan, C.; Wang, Y.; Shen, X.; Pang, Y. Bismuth-Based Metal-Organic Framework Peroxidase-Mimic Nanozyme: Preparation and Mechanism for Colorimetric-Converted Ultra-trace Electrochemical Sensing of Chromium ion. *J. Hazard. Mater.* **2023**, *451*, 131148.
15. Gu, C.C.; Bai, L.P.; Pu, L.; Gai, P.P.; Li, F. Highly Sensitive and Stable Self-Powered Biosensing for Exosomes Based on Dual MOF Nanocarriers. *Biosens. Bioelectron.* **2021**, *176*, 112907.
16. Dong, J.; Zheng, J.; Hou, J.; Zhao, P.; Liang, Y.; Lei, J.; Luo, X.; Hou, C.; Huo, D. Au Nanoparticle/CoFc/Metal-Organic Framework as Enzyme-Free Dual-Signal Ratiometric Electrochemical Sensor for In-Situ Determination of Cell-Secreted H_2O_2. *ACS Appl. Nano Mater.* **2023**, *6*, 11630-11639.
17. Wang, J.; Zhou, Y.; Zeng, M.; Zhao, Y.; Zuo, X.; Meng, F.; Lv, F.; Lu, Y. Zr(IV)-based Metal-Organic Framework Nanocomposites with Enhanced Peroxidase-Like Activity as a Colorimetric Sensing Platform for Sensitive Detection of Hydrogen Peroxide and Phenol. *Environ. Res.* **2022**, *203*, 111818.
18. Li, M.; Chen, J.; Wu, W.; Fang, Y.; Dong, S. Oxidase-like MOF-818 Nanozyme with High Specificity for Catalysis of Catechol Oxidation, *J. Am. Chem. Soc.* **2020**, *142*, 15569-15574
19. Yan, Y.; Bo, X.; Guo, L. MOF-818 Metal-Organic Framework-Reduced Graphene Oxide/Multiwalled Carbon Nanotubes Composite for Electrochemical Sensitive Detection of Phenolic Acids. *Talanta* **2020**, *218*, 121123.
20. Isailović, J.; Oberlintner, A.; Novak, U.; Finšgar, M.; Oliveira, F.M.; Paštika, J.; Sofer, Z.; Tasić, N.; Gusmão, R.; Hočevar, S.B. Study of Chitosan-Stabilized $Ti_3C_2T_x$ MXene for Ultrasensitive and Interference-Free Detection of Gaseous H_2O_2. *ACS Appl. Mater. Interfaces* **2023**, *15*, 31643-31651
21. Chai, X.; Ye, S.; Wang, F.; Yuan, H.; Liu, M.; Fan, F.; Zhang, L.; Zhang, X.; Wang, T.; Fu, Y. Au Nanoparticles@UiO-66 Composite Film-Coated Carbon Cloth Substrate for High-Performance H_2O_2 Electrochemical Sensing. *Inorg. Chem.* **2023**, *62*, 10694-10703

22. Huang, W.; Xu, Y.; Wang, Z.; Liao, K.; Zhang, Y.; Sun, Y. Dual Nanozyme Based on Ultrathin 2D Conductive MOF Nanosheets Intergraded with Gold Nanoparticles for Electrochemical Biosensing of H_2O_2 in Cancer Cells. *Talanta* **2022**, *249*, 12361.

23. Yu, K.; Li, M.; Chai, H.; Liu, Q.; Hai, X.; Tian, M.; Qu, L.; Xu, T.; Zhang, G.; Zhang, X. MOF-818 Nanozyme-Based Colorimetric and Electrochemical Dual-Mode Smartphone Sensing Platform for in Situ Detection of H_2O_2 and H_2S Released from Living Cells. Chem. Eng. J. **2023**, *451*, 138321.

24. Chen, J.; Xu, F.; Zhang, Q.; Li, S. N-doped MoS_2-Nanoflowers as Peroxidase-Like Nanozymes for Total Antioxidant Capacity Assay. *Anal. Chim. Acta* **2021**, *1180*, 338740.

25. Song, Y.; Huang, C.; Li, Y. Nanozyme Rich in Oxygen Vacancies Derived from Mn-Based Metal-Organic Gel for the Determination of Alkaline Phosphatase. *Inorg. Chem.* **2023**, *62*, 12697-12707.

26. Li, H.; Song, P.; Wu, T.; Zhao, H.; Liu, Q.; Zhu, X. In Situ Decorating of Montmorillonite with $ZnMn_2O_4$ Nanoparticles with Enhanced Oxidase-Like Activity and its Application in Constructing GSH Colorimetric Platform. *Appl. Clay Sci.* **2022**, *229*, 106656.

27. Mestivier, M.; Li, J.; Camy, A.; Frangville, C.; Mingotaud, C.; Benoit-Marquie, F.; Marty, J.D.; Copper-Based Hybrid Polyion Complexes for Fenton-Like Reactions. *Chem. Eur. J.* **2020**, *26*, 14152-14158.

28. Li, X.; Zhang, Y.; Tan, W.; Jin, P.; Zhang, P.; Li, K. Bioinspired Coassembly of Copper Ions and Nicotinamide Adenine Dinucleotides for Single-Site Nanozyme with Dual Catalytic Functions. *Anal. Chem.* **2023**, *95*, 2865-2873.

29. Yamaguchi, R.; Kurosu, S.; Suzuki, M.; Kawase, Y. Hydroxyl Radical Generation by Zero-Valent Iron/Cu (ZVI/Cu) Bimetallic Catalyst in Waste Water Treatment: Heterogeneous Fenton/Fenton-Like Reactions by Fenton reagents Formed In-Situ under Oxic Conditions. *Chem. Eng. J.* **2018**, *334*, 1537-1549.

30. Zhu, D.Q.; Zhang, M.L.; Pu, L.; Gai, P.P.; Li, F. Nitrogen-Enriched Conjugated Polymer Enabled Metal-Free Carbon Nanozymes with Efficient Oxidase-Like Activity. *Small* **2022**, *18*, 2104993.

31. Gai, P.P.; Pu, L.; Wang, C.; Zhu, D.Q.; Li, F. CeO_2@NC Nanozyme with Robust Dephosphorylation Ability of Phosphotriester: A Simple Colorimetric Assay for Rapid and Selective Detection of Paraoxon. *Biosens. Bioelectron.* **2023**, *220*, 114841.

32. Chai, H.; Yu, K.; Zhao, Y.; Zhang, Z.; Wang, S.; Huang, C.; Zhang, X.; Zhang, G. MOF-On-MOF Dual Enzyme-Mimic Nanozyme with Enhanced Cascade Catalysis for Colorimetric/Chemiluminescent Dual-Mode Aptasensing. *Anal. Chem.* **2023**, *95*, 10785-10794.

33. Fu, Q.; Wang, N.; Zhou, C.; Su, X. High Performance Boron Doped Peroxidase-Like Nanozyme Cu/B-NC for Detection of Epinephrine and Catalase. *Talanta* **2024**, *266*, 124991.

34. Gao, L.; Zhuang, J.; Nie, L.; Zhang, J.; Zhang, Y.; Gu, N.; Wang, T.; Feng, J.; Yang, D.; Perrett, S.; Yan, X. Intrinsic Peroxidase-Like Activity of Ferromagnetic Nanoparticles. *Nat. Nanotechnol.* **2007**, *2*, 577-583.

35. Zhang, T.; Liu, Y.; Pi, J.; Lu, N.; Zhang, R.; Chen, W.; Zhang, Z.; Xing, D. A Novel Artificial Peroxisome Candidate Based on Nanozyme with Excellent Catalytic Performance for Biosensing. *Biosens. Bioelectron.* **2022**, *196*, 113686.

36. Keoingthong, P.; Hao, Q.; Li, S.; Zhang, L.; Xu, J.; Wang, S.; Chen, L.; Tan W.; Chen, Z. Graphene Encapsuled Ru Nanocrystal with Highly-efficient Peroxidase-like Activity for Glutathione Detection at Near-Physiological pH. *Chem. Commun.* **2021**, *57*, 7669-7672.

37. Chai, H.; Yu, K.; Zhao, Y.; Zhang, Z.; Wang, S.; Huang, C.; Zhang, X.; Zhang, G. MOF-On-MOF Dual Enzyme-Mimic Nanozyme with Enhanced Cascade Catalysis for Colorimetric/Chemiluminescent Dual-Mode Aptasensing. *Anal. Chem.* **2023**, *95*, 10785-10794.

38. Duan, W.; Qiu, Z.; Cao, S.; Guo, Q.; Huang, J.; Xing, J.; Lu, X.; Zeng, J. Pd-Fe_3O_4 Janus Nanozyme with Rational Design for Ultrasensitive Colorimetric Detection of Biothiols. *Biosens. Bioelectron.* **2022**, *196*, 113724.

39. Keoingthong, P.; Xu, Y.; Li, S.; Xu, J.; Zhang, L.; Chen, Z.; Tan, W. Highly Active CoRh Graphitic Nanozyme for Colorimetric Sensing in Real Samples. *J. Phys. Chem. B* **2023**, *127*, 5453-5461.

40. Barber, R.; Davis, J.; Papakonstantinou, P. Stable Chitosan and Prussian Blue-Coated Laser-Induced Graphene Skin Sensor for the Electrochemical Detection of Hydrogen Peroxide in Sweat. *ACS Appl. Nano Mater.* **2023**, *6*, 10290-10302.

41. Liu, F.; Yang, L.; Yin, X.; Liu, X.; Ge, L.; Li, F. A Facile Homogeneous Electrochemical Biosensing Strategy based on Displacement Reaction for Intracellular and Extracellular Hydrogen Peroxide Detection. *Biosens. Bioelectron.* **2019**, *141*, 111446.

42. Zhao, F.; Zhou, S.; Zhang, Y. Ultrasensitive Detection of Hydrogen Peroxide Using Bi_2Te_3 Electrochemical Sensors. *ACS Appl. Mater. Interfaces* **2021**, *13*, 4761-4767.

43. Zheng, X.; Lian, Q.; Zhou, L.; Jiang, Y.; Gao, J. Peroxidase Mimicking of Binary Polyacrylonitrile-CuO Nanoflowers and the Application in Colorimetric Detection of H_2O_2 and Ascorbic Acid. *ACS Sustainable Chem. Eng.* **2021**, *9*, 7030-7043.

44. Jiao, L.; Xu, W.; Yan, H.; Wu, Y.; Liu, C.; Du, D.; Lin, Y.; Zhu, C. Fe-N-C Single-Atom Nanozymes for the Intracellular Hydrogen Peroxide Detection. *Anal. Chem.* **2019**, *91*, 11994-11999.

45. Li, L.; Liu, X.; Zhu, R.; Wang, B.; Yang, J.; Xu, F. Fe^{3+}-Doped Aminated Lignin as Peroxidase-Mimicking Nanozymes for Rapid and Durable Colorimetric Detection of H_2O_2. *ACS Sustainable Chem. Eng.* **2021**, *9*, 12833-12843.

46. Lu, C.; Wang, Y.; Xu, B.; Zhang, W.; Xie, Y.; Chen, Y. A Colorimetric and Fluorescence Dual-Signal Determination for Iron (II) and H_2O_2 in Food based on Sulfur Quantum Dots. *Food Chem.* **2022**, *366*, 130613.

47. Gu, C.C.; Bai, L.P.; Hou, T.; Zhang, L.; Gai, P.P.; Li, F. Dual-Mode Colorimetric and Homogeneous Electrochemical Detection of Intracellular/Extracellular H_2O_2 based on FeSx/SiO_2 Nanoparticles with High Peroxidase-Like Activity. *Anal. Chim. Acta* **2023**, *1265*, 341332.

48. Yu, K.; Li, M.; Chai, H.; Liu, Q.; Hai, X.; Tian, M.; Qu, L.; Xu, T.; Zhang, G.; Zhang, X. MOF-818 Nanozyme-Based Colorimetric and Electrochemical Dual-Mode Smartphone Sensing Platform for in Situ Detection of H_2O_2 and H_2S Released from Living Cells. *Chem. Eng. J.* **2023**, *451*, 138321.

49. Chen, S.; Zhao, P.; Jiang, L.; Zhou, S.; Zheng, J.; Luo, X.; Huo, D.; Hou, C. Cu_2O-Mediated Assembly of Electrodeposition of Au Nanoparticles onto 2D Metal-Organic Framework Nanosheets for Real-Time Monitoring of Hydrogen Peroxide Released from Living Cells. *Anal. Bio. Chem.* **2020**, 1-12.

50. Wu, P.; Cai, Z.; Gao, Y.; Zhang, H.; Cai, C. Enhancing the Electrochemical Reduction of Hydrogen Peroxide Based on Nitrogen-Doped Graphene for Measurement of Its Releasing Process from Living Cells. *Chem. Commun.* **2011**, *47*, 11327-11329.

Chapter 7: Conclusion and Recommendation

This project aims to detect various disease-related biomolecules based on electrochemical sensing technology. Carbon-based nanomaterials with excellent electrocatalytic activity were designed and prepared through methods such as hydrothermal and chemical reduction. A series of electrochemical sensors were constructed based on these materials, enabling highly sensitive and selective detection of DNA bases, dopamine, glucose, and hydrogen peroxide.

7.1 CNs for the detection of dopamine

CNs were successfully synthesized using a simple and environmentally friendly method and characterized through various techniques. Due to their large surface area, excellent electrical conductivity, and catalytic performance, the electrochemical sensing platform based on CNs exhibited outstanding electrochemical properties for detecting DA. The platform showed a wide linear range and low detection limit, as well as good selectivity, reproducibility and stability. Furthermore, the CNs/GCEs were applied in real sample analysis with satisfactory recovery, providing a new strategy for determining DA in blood.

7.2 Au/Pd-PPy/GR for simultaneous detection of DNA bases

Au-Pd/PPy/GR nanocomposites were successfully synthesized through in-situ reduction method to develop a novel sensing method for simultaneous detection of G, A, T, and C. Au-Pd/PPy enhanced conductivity, while GR further amplified electrochemical signals and improved electroactive surface area. The Au-Pd/PPy/GR/GCE exhibited excellent electrocatalytic performance in detecting G, A, T, and C, demonstrating high sensitivity, good selectivity, and long-term stability. The applicability of the electrochemical sensor was confirmed by detecting the four bases in calf-thymus DNA. More importantly, this study not only introduces a new method for detecting the four DNA bases but also paves the way for extending similar approaches to other nanocomposites, thereby broadening their applications in electrochemical detection and biotechnology.

7.3 CNMs-GR for electrocatalytic detection of glucose and removal of organic dyes

CNMs-GR magnetic nanocomposites were synthesized via a one-pot hydrothermal method, and their efficient electrocatalytic activity towards glucose oxidation and adsorption capabilities for organic dyes were investigated. The effective combination of GR and CNMs exhibited significantly enhanced performance due to the synergistic effects associated with the increased surface area and improved electrocatalytic activity compared to individual component. The CNMs-GR/GCE showed excellent electroanalytical performance for glucose with a detection limit of 1.27 μM. Furthermore, the CNMs-GR exhibited maximum adsorption capacities of 184.29 mg/g for MB, 912.47 mg/g for CR, and 894.36 mg/g for NR. This study has significant implications for the future development of dual-functional nanocomposites.

7.4 Cu/Zr-MOF dual-mode detection of hydrogen peroxide

Cu/Zr-MOF nanozymes were successfully synthesized using a straightforward solvothermal method and were developed into a dual-mode sensing platform for the electrochemical and colorimetric detection of H_2O_2. Cu/Zr-MOF exhibited excellent electrocatalytic performance and peroxidase-like activity towards H_2O_2. Compared to the colorimetric method, the electrochemical method demonstrated higher sensitivity with a detection limit as low as 21.3 nM. Moreover, a "color recognizer" application was employed to capture the color patterns (RGB) of reaction solutions to establish a smartphone-based sensing system. Most significantly, the dual-mode sensing platform has been effectively applied to the real-time detection of H_2O_2 released from cancer cells. In contrast to current single-mode detection approaches, dual-mode detection provides self-validation and self-calibration functionalities, enhancing the accuracy of results and showing promising potential for real-time monitoring applications.

7.5 Recommendation for future work

This project presented innovative sensing platforms based on nanocomposites for the successful detection of various biomolecules, including the four DNA bases, dopamine, glucose, and hydrogen peroxide. The results highlight the versatility of these platforms and demonstrate their application potential. However, several critical areas require further investigation:

(1) There is a lack of systematic research on the structure-property-performance relationships. The selection of carbon and its functional materials for nanocomposite synthesis in construction of electrochemical sensors is often based on the trial-and-error approach. The mechanisms of many carbon-based nanomaterials in electrochemical sensing are still unclear. Therefore, fundamental understanding of the sensing mechanisms is required to enable better design of the nanomaterials with tailored structures and composition for achieving higher analytical performance. This challenge may be overcome by introducing in situ characterization techniques, combined with electrochemical equipment, for the acquisition of real-time data on material properties, reaction mechanisms, and dynamic changes during electrochemical processes. Moreover, future research is expected to integrate experimental findings with theoretical calculations, establishing reaction mechanism models for structural and compositional optimization of carbon-based nanomaterials to develop low-cost and high-performance sensing devices.

(2) Although electrochemical sensors perform excellently in the detection of biomolecules in standard samples, their application in real samples still faces challenges due to matrix effects, sample complexity, and potential interferences. Carbon-based nanomaterials have exhibited high sensitivity and anti-fouling property, making them promising candidates for the development of electrochemical biosensors for rapid analysis and swift diagnosis. Future research will focus on exploring new sensing materials that can be applied in various real sample matrices, while maintaining good reliability and reproducibility. This can be achieved through innovations in synthetic methods and improvements in analytical strategies, as well as advancement in sensor design and manufacturing.

(3) The applications of carbon-based nanomaterials can be broadened by integration into new technologies such as wearable biosensors and smartphones to develop simple, rapid, accurate, and portable electrochemical sensing methods. Wearable biosensors represent an innovative technology for real-time health monitoring , connecting to smartphones via Bluetooth to facilitate data collection and analysis. These sensors can monitor various physiological indicators, including heart rate, steps, and blood oxygen levels. Future research will focus on developing new carbon-based nanomaterials

to design advanced wearable biosensing devices through multidisciplinary collaboration across materials science, biomedical engineering, data science, and software development. These collaborations will expand the practical applications of wearable biosensors in health monitoring, and enhance their role in personalized medicine and health management.

Appendix

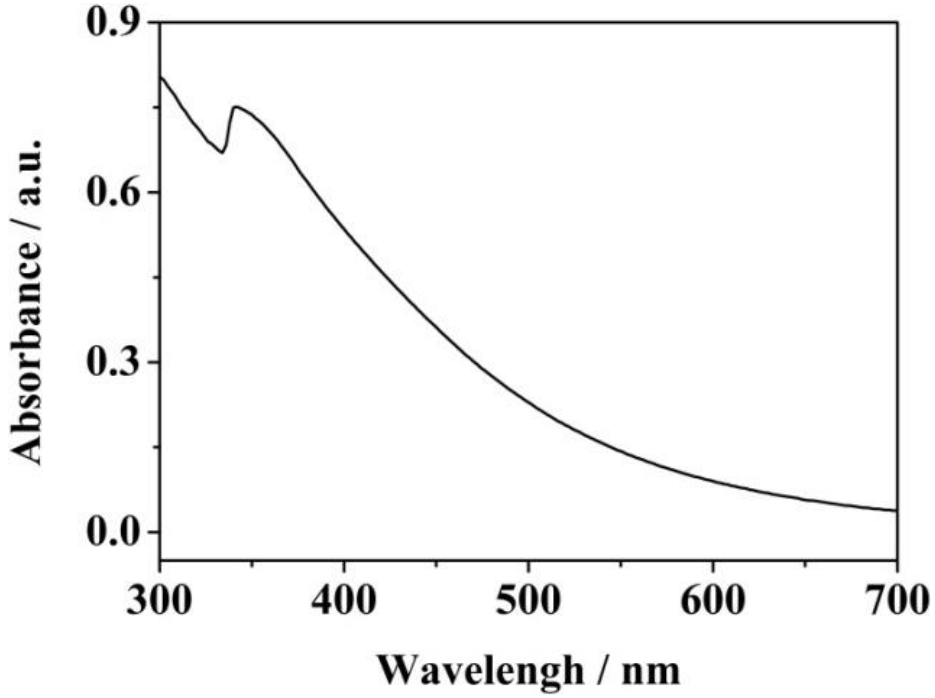

Fig. S1: UV-vis absorption spectra of CNs

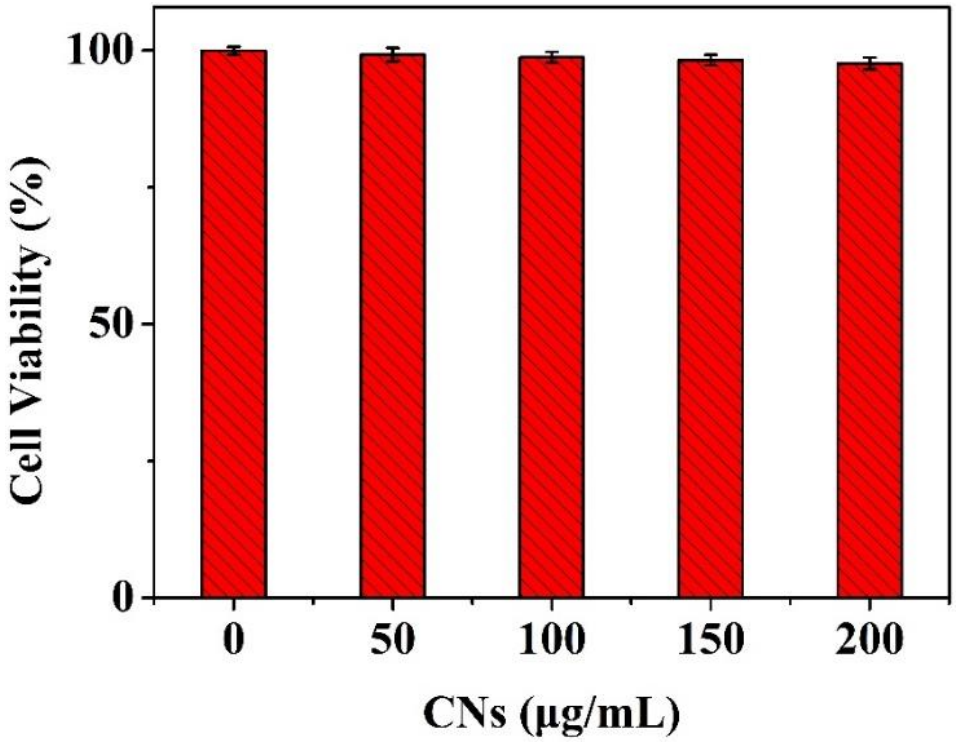

Fig. S2: Cell viability at various concentrations of CNs.

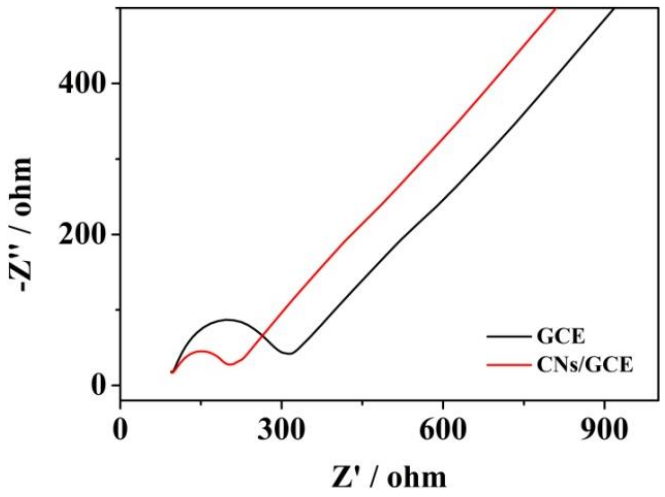

Fig. S3: EIS of 5.0 mM $[Fe(CN)_6]^{3-/4-}$ solution in 0.1 M KCl at bare GCE and CNs/GCE

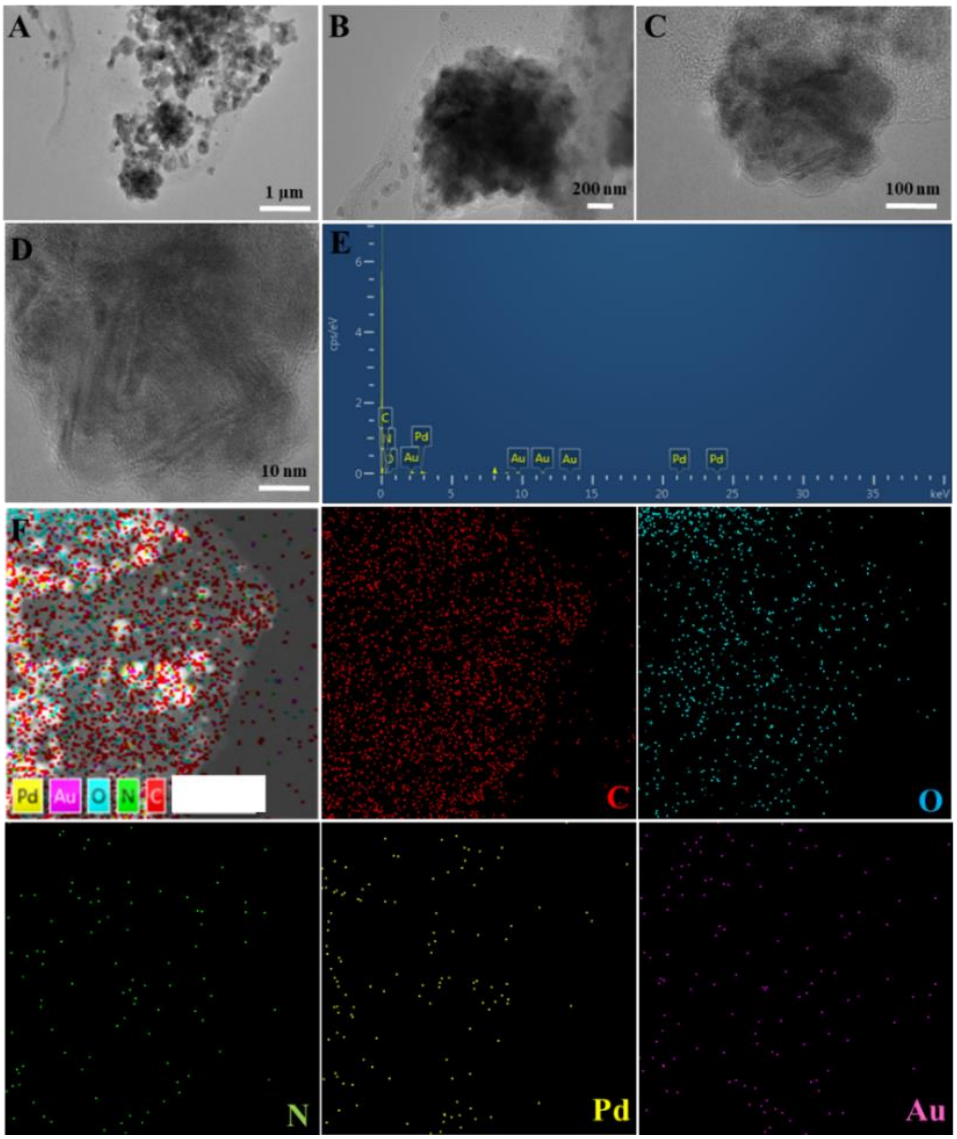

Fig. S4: (A-D) -HRTEM images, (E) EDX spectrum, (F) the elemental mapping of Au/Pd-PPy/GR

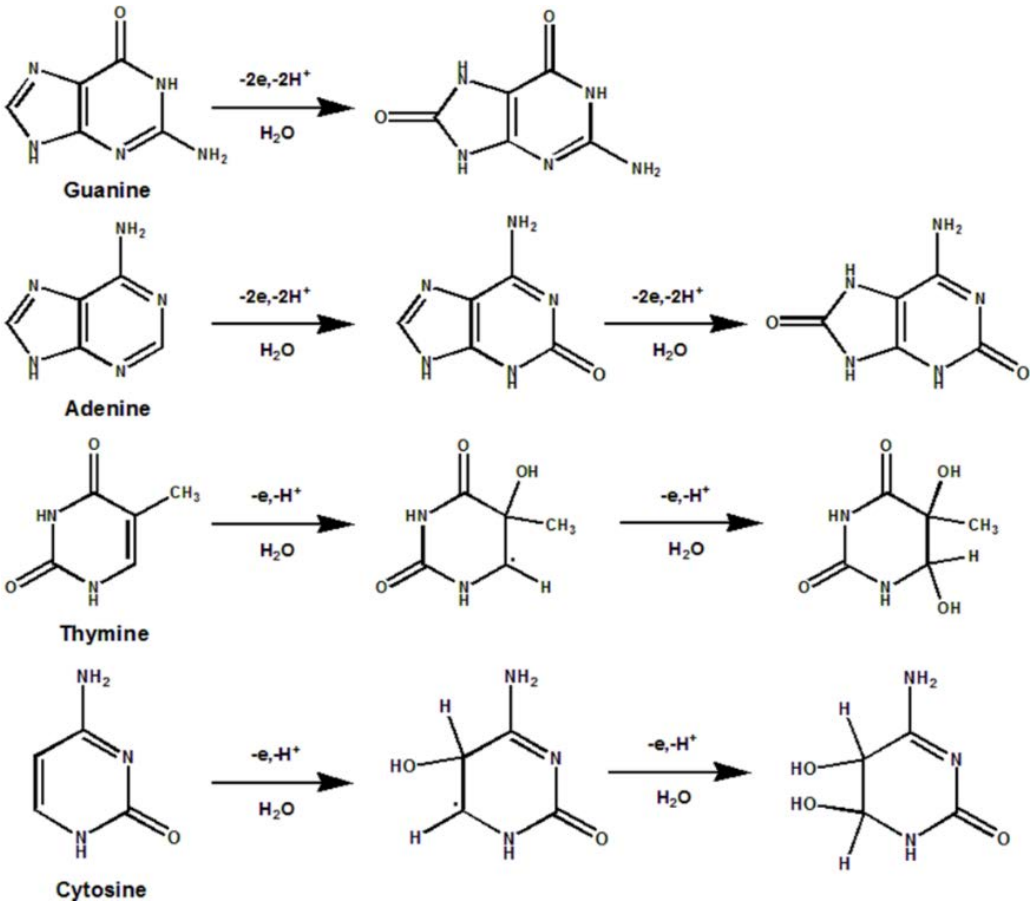

Fig. S5: The possible mechanism for the oxidation of DNA bases

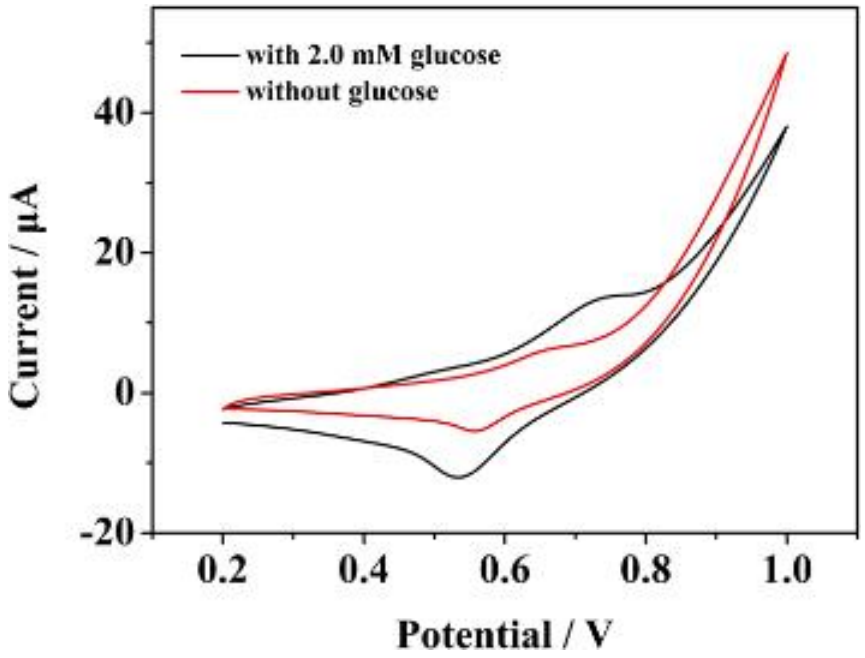

Fig. S6: CVs for CNMs-GR/GCE with and without 2.0 mM glucose in 0.1 M NaOH

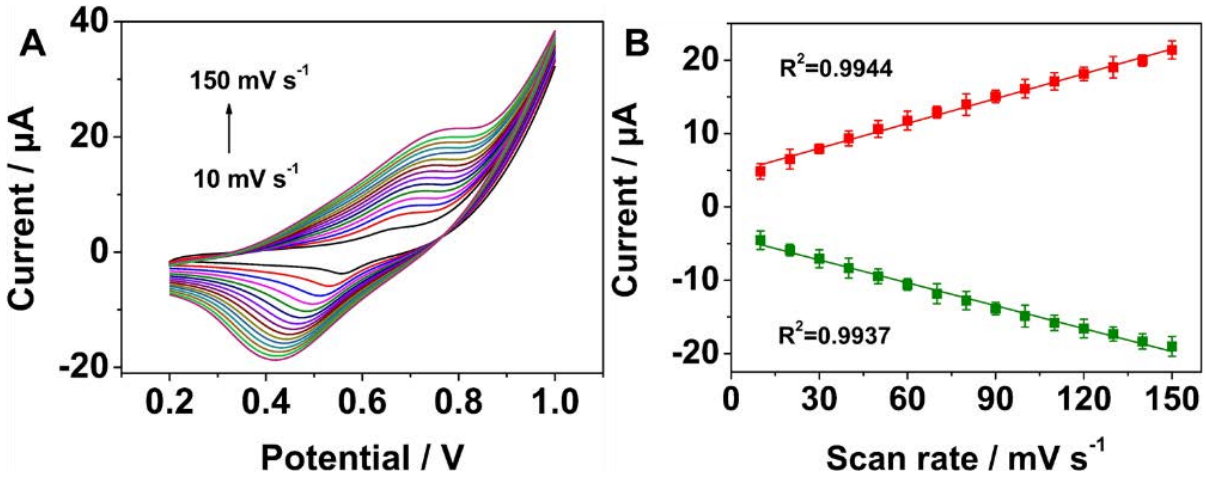

Fig. S7: (A) CV curves of CNMs-GR/GCE with 2.0 mM glucose at different scan rates in 0.1 M NaOH; (B) Plot of peak current vs scan rate

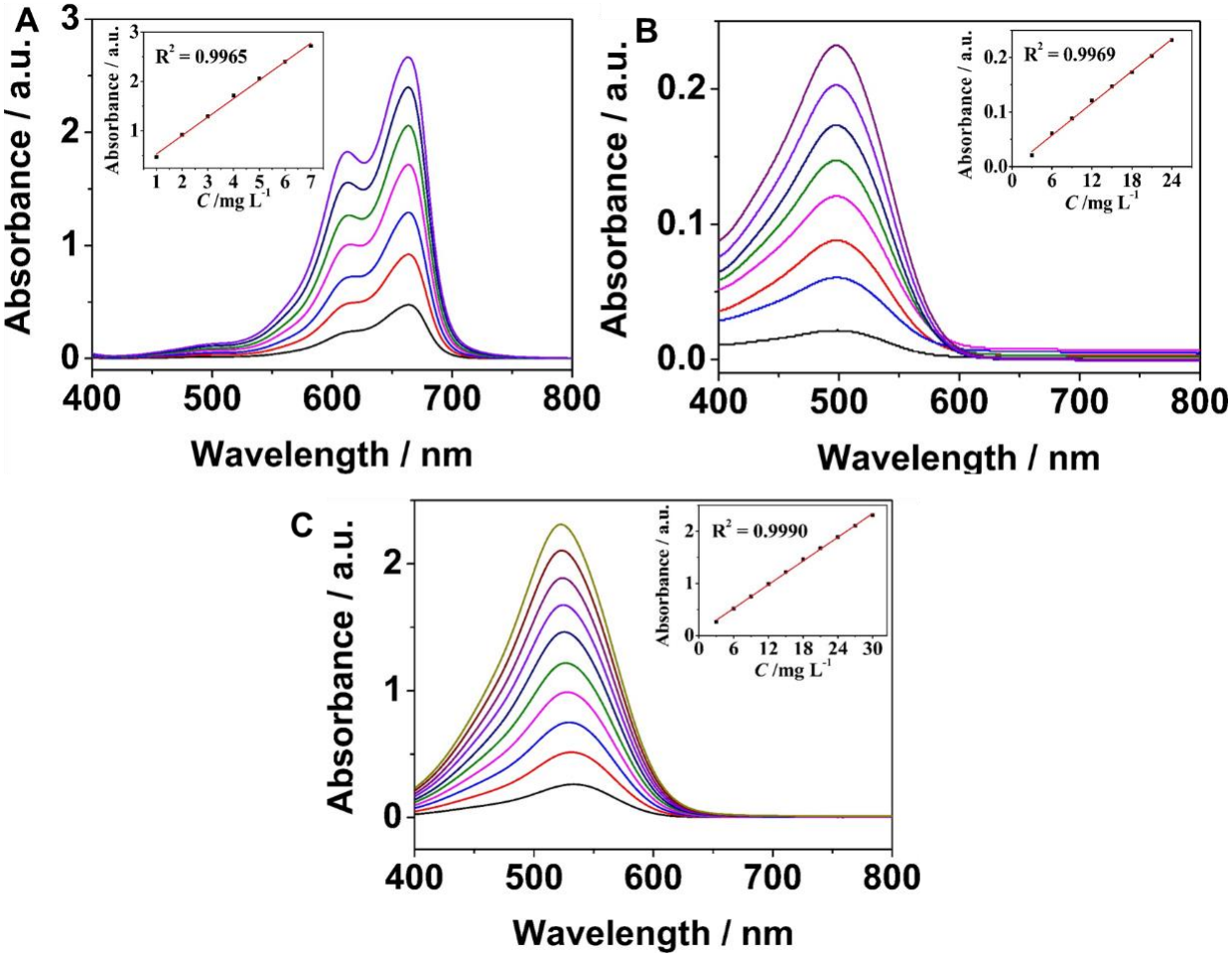

Fig. S8: Standard curves of MB, CR and NR

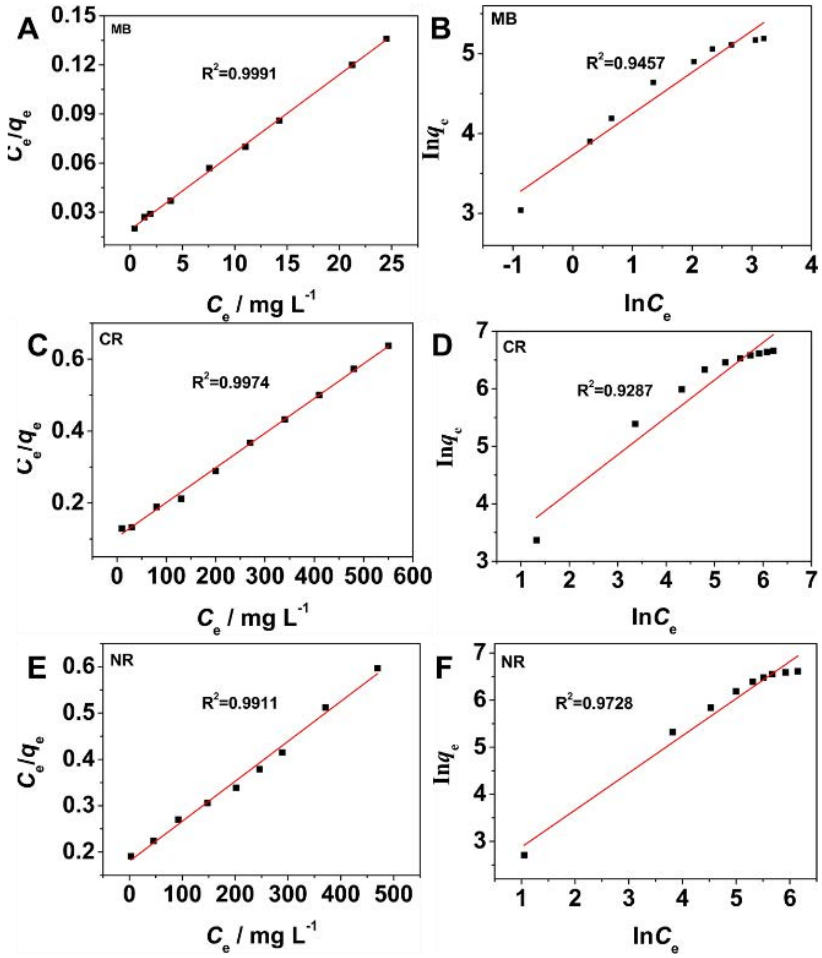

Fig. S9: Fitting of adsorption isotherm data with Langmuir model for MB (A), CR (C) and NR (E), Freundlich model for MB (B), CR (D) and NR (F) of CNMs-GR

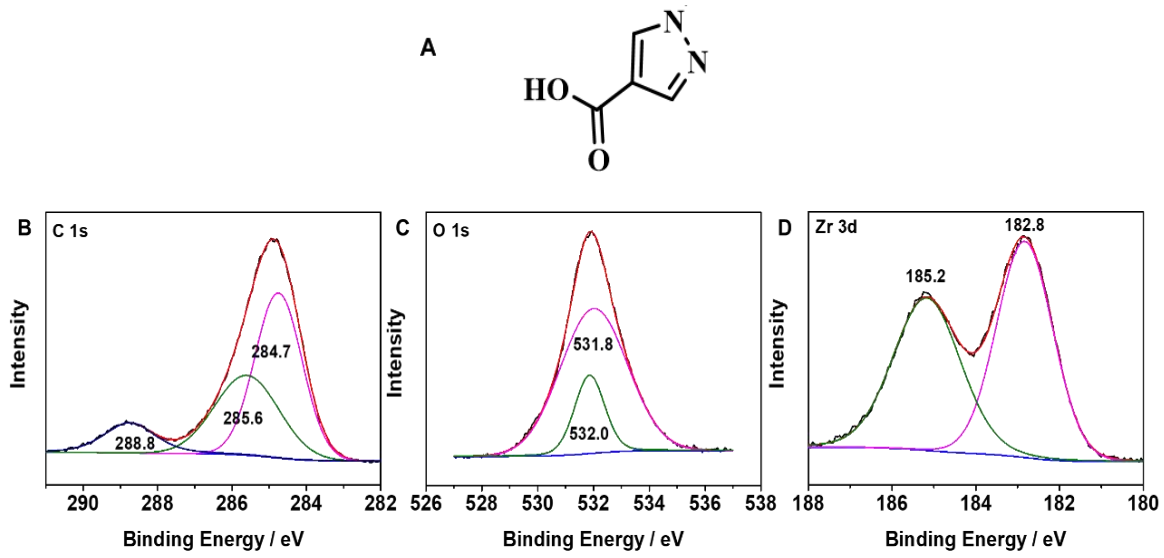

Fig. S10: (A) The structure of H_2PyC; XPS spectrum C 1s (B), O 1s (C), and Zr 3d (D) of Cu/Zr-MOF

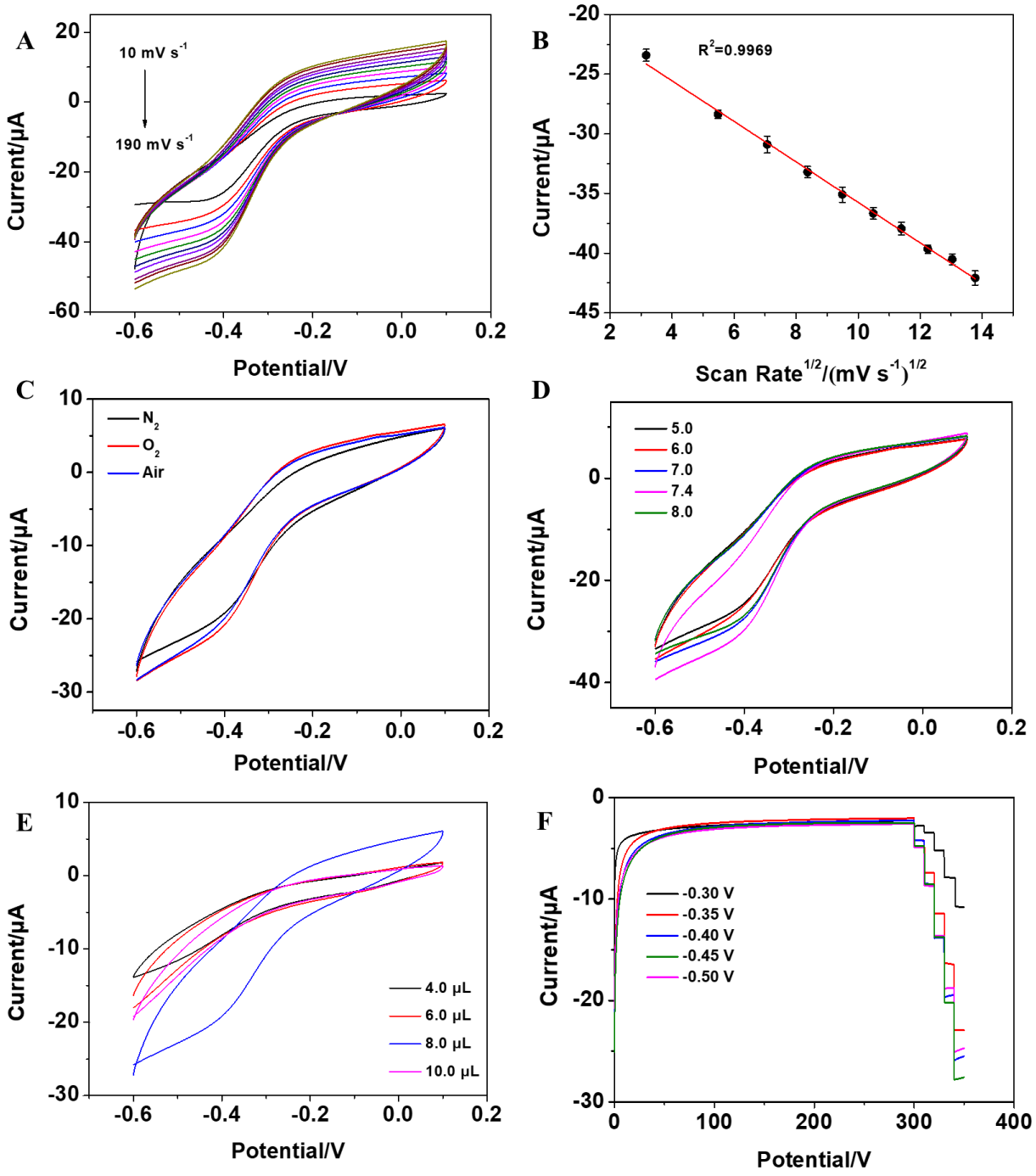

Fig. S11: (A) CV response of Cu/Zr-MOF/SPE in 0.1 M H_2O_2 at different scan rates; (B) The peak current *vs* square root of scan rates; (C) CV curves of Cu/Zr-MOF/SPE in N_2, air and O_2 with H_2O_2; Optimization study of (D) pH and (E) modification in 0.1 M H_2O_2; (F) Optimization study of the applied potential with the successive addition of H_2O_2

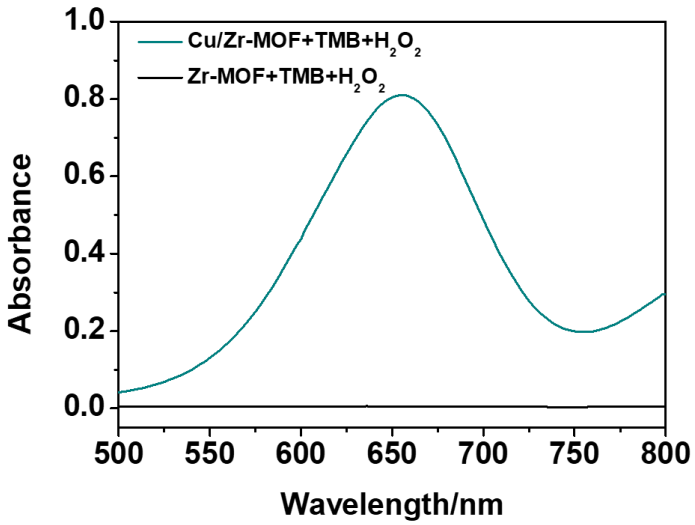

Fig. S12: (A) UV-vis absorption spectra of Cu/Zr-MOF+TMB+H_2O_2 and Zr-MOF+TMB+H_2O_2 in NaAc-HAc (0.2 M pH=4.5) incubated at 42 ℃ for 20 min

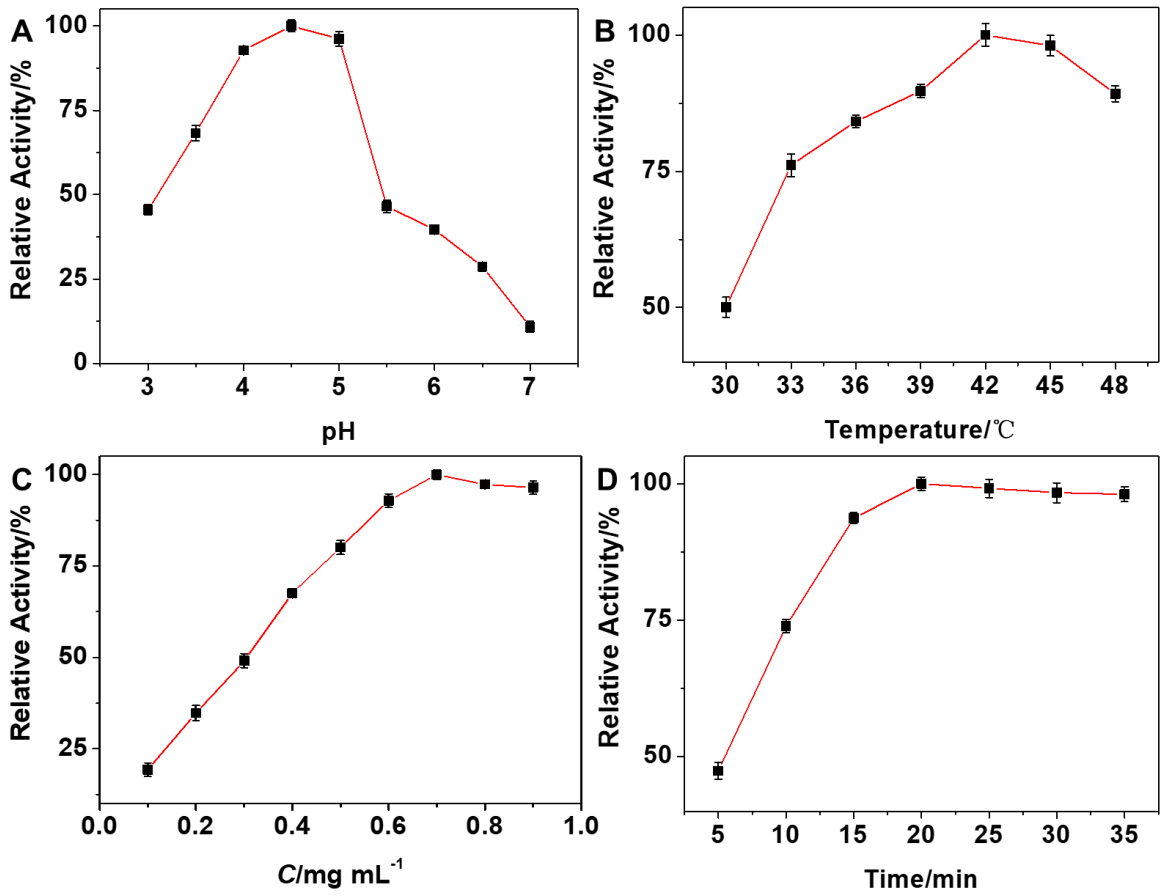

Fig. S13: Optimization of (A) pH, (B) temperature, (C) the catalyst concentration, and (D) reaction time in 0.1 M H_2O_2 on the catalytic activity of Cu/Zr-MOF towards TMB by H_2O_2

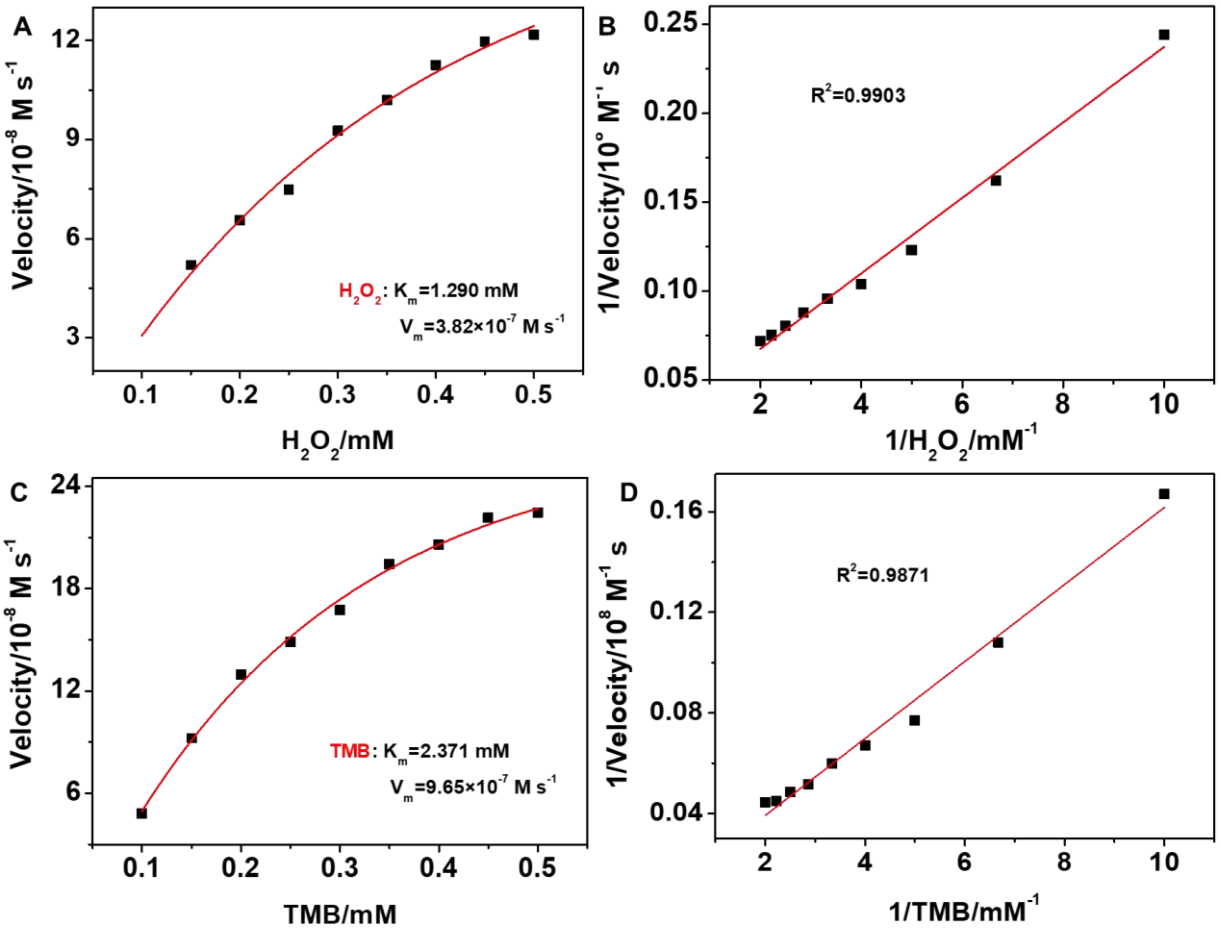

Fig. S14: (A) Velocity of the reaction measured by Cu/Zr-MOF towards various concentration of H_2O_2; (B) Double-reciprocal plots for determining the kinetic constants for H_2O_2 substrate; (C) Velocity of the reaction measured by Cu/Zr-MOF towards various concentration of TMB; (D) Double-reciprocal plots for determining the kinetic constants for TMB substrate

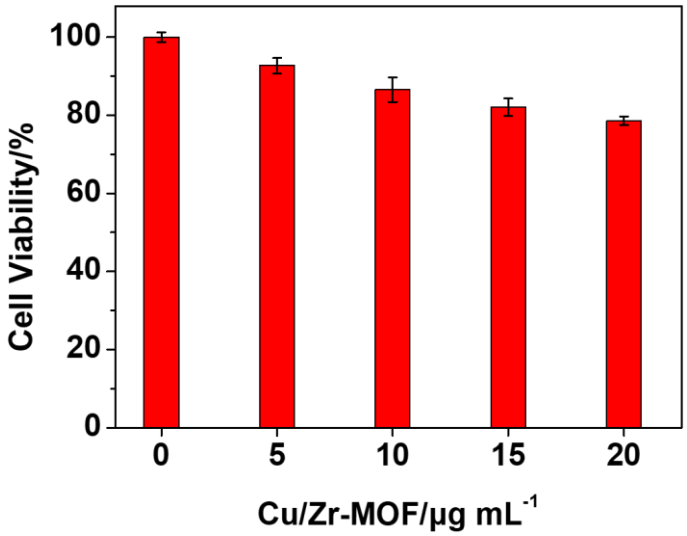

Fig. S15: Cytotoxicity of Cu/Zr-MOF

Table S1: The influence of some interfering species on the determination of DNA bases

Interferences	Relative signal change (%)			
	Guanine	Adenine	Thymine	Cytosine
Na+	2.08	1.95	2.21	1.76
K^+	–0.89	–1.28	–1.86	–1.54
Ca^+	1.82	2.15	1.64	2.03
Cu^{2+}	1.21	0.94	1.16	0.85
Cl^-	1.75	2.04	1.93	1.61
NO_3^-	–0.64	–0.82	–1.01	–0.77
SO_4^{2-}	–1.85	–2.16	–3.47	–3.21
Ascorbic acid	1.67	1.92	2.58	2.73
Uric acid	3.24	3.68	3.76	3.04
Glucose	1.94	2.15	1.87	2.31
Glutathione	0.87	1.14	0.69	0.52
Uracil	1.45	1.08	2.33	1.94
Cytosine	1.69	2.17	1.94	1.62

Table S2: Adsorption isotherm parameters of MB, CR and NR by CNMs-GR at 25 °C

Organic dyes	Langmuir model			Freundlich model		
	q_m (mg/g)	K_L (L/mg)	R^2	K_F (mg/g (L/mg)$^{1/n}$	n	R^2
MB	184.29	0.0408	0.9991	81.23	4.03	0.9457
CR	912.47	0.00211	0.9974	144.68	3.54.	0.9287
NR	894.36	0.00152	0.9911	150.40	3.82	0.9728